CRANFIELD UNIVERSITY

RYOKO MORISHIMA

ANALYSIS OF COMPOSITE WING STRUCTURES WITH A MORPHING LEADING EDGE

SCHOOL OF ENGINEERING

Department of Aerospace Engineering

PhD THESIS

Academic Year 2010-11

Supervisor: Dr. Shijun Guo

January 2011

CRANFIELD UNIVERSITY

SCHOOL OF ENGINEERING

Department of Aerospace Engineering

PhD THESIS

Academic Year 2010-11

RYOKO MORISHIMA

Analysis of composite wing structures with a morphing leading edge

Supervisor: Dr. Shijun Guo

January 2011

This thesis is submitted in partial fulfilment of the requirements for the degree of
Doctor of Philosophy

Abstract

One of the main challenges for the civil aviation industry is the reduction of its environmental impact. Over the past years, improvements in performance efficiency have been achieved by simplifying the design of the structural components and using composite materials to reduce the overall weight. These approaches however, are not sufficient to meet the current demanding requirements set for a 'greener' aircraft.

Significant changes in drag reduction and fuel consumption can be obtained by using new technologies, such as smart morphing structures. These concepts will in fact help flow laminarisation, which will increase the lift to drag ratio. Furthermore, the capability to adapt the wing shape will enable to optimise the aerodynamic performance not only for a single flight condition but during the entire mission. This will significantly improve the aircraft efficiency.

The current research work has been carried out as part of the European Commission founded Seventh Framework Program called 'Smart High Lift Device for the Next Generation Wing' (SADE), which main aim is to develop and study morphing high lift devices. The author's investigation focused on developing a design concept for the actuation mechanism of a morphing leading edge device. A detailed structural analysis has been carried out in order to demonstrate its feasibility.

In the first phase of the research the attention was directed on the preliminary design and analysis of the composite wing box. The parameters of the key structural components, such as skin, spars, ribs and stringers were set to satisfy the static stress and buckling requirements. Moreover, numerical and experimental studies were conducted to analyse the static failure and buckling behaviour of two typical composite wing structural components: a spar section and a web and base joint assembly.

In the second stage of the research, a design for the morphing leading edge actuation mechanism was developed. The actuation system was designed in such a way that the target shape was reached with minimum actuation force demand. A geometrical nonlinear FE analysis was conducted to simulate the leading edge morphing deflection and ensure that structural strength requirements were satisfied. Furthermore, the behaviour of the skin integrated with the internal actuation mechanism was modelled under the aerodynamic pressure, at different flight conditions and gust loads, in order to prove that the proposed actuation system can compete with the conventional rigid rib.

This study demonstrated that a feasible morphing leading edge design for a next generation large aircraft wing can be achieved. Developing the readiness of this technology will have a significant impact on aircraft efficiency and considerable contribution towards a more environmental friendly aviation.

Acknowledgments

I cannot believe this long journey called PhD has come to an end. It has been a very intensive but yet invaluable experience in my life, and its successful completion would not have been possible without the precious help of my supervisor, colleagues, friends and family. It is a pleasure to have an opportunity to convey my appreciation to them all.

Firstly I would like to express my deepest sense of gratitude to my supervisor Dr. Shijun Guo, for his continuous guidance and support from the very early stages of this research. His experience, passion and dedication have inspired me to challenge myself and develop as a person as well as improve my technical abilities.

I thankfully acknowledge each of the members of the research consortium with whom I enjoyed working and the European Commission for their financial support.

I would like to thank Dr. Xiang Zhang for her support especially in the first few months spent here at Cranfield. Her advices were very useful to settle down and start my research with a really positive attitude. I am grateful to Prof. Ranjan Banerjee who challenged my work every time I went to see him, teaching me to have confidence and training me to defend my thoughts. His vast knowledge and experience have motivated me to always aim towards high and rewarding achievements. I am thankful to Dr. Chak-wa Cheung for pushing me to pursue a PhD after my undergraduate studies. I can now

say that it was a very wise suggestion and this experience has given me the necessary tools to develop my career in engineering.

It is also a pleasure to acknowledge Barry Walker for his help conducting the numerous experimental tests. It would have never been possible to complete the research without his contribution.

I would like to pay a special tribute to Melanie Perera and Natalia di Matteo with whom I shared many laughs and tears. They have been supportive at any time of the day and night during all my ups and downs. My life in Cranfield would have not been the same without them. I am also thankful to Cinzia Taccoli, Marco Nunez, Guido Servetti and Shakeel Ahmed for their friendship and many lunch and coffee breaks spent together.

A special and heartfelt thank you goes to my father, mother, grandmother and my boyfriend Marco Boscolo. Their dedication, love and persistent confidence in me have taken the load off my shoulder. They have been patient to put up with me when I was stressed and they have been unselfishly happy for my successes. I would have never been able to do what I managed to achieve without their endless support.

Finally, I would also like to take this opportunity to convey my profound gratitude to everybody who have supported and encouraged me during all these years, as well as express my apologies that I cannot mention personally one by one. The successful completion of this thesis would not have been possible without them.

Table of Contents

List of Figures

List of Tables

List of Nomenclature and Symbols

BM	Bending moment	(Nm)
E_1	Longitudinal Young's Modulus	(GPa)
E_2	Transverse Young's Modulus	(GPa)
EI	Bending Rigidity	(Nm^2)
EW	Warping Rigidity	(Nm^4)
E_x	Equivalent Longitudinal Young's Modulus	(GPa)
E_y	Equivalent Transverse Young's Modulus	(GPa)
G_{12}	Ply Shear Modulus	(GPa)
GJ	Torsional Rigidity	(Nm^2)
G_{xy}	Equivalent Shear Modulus	(GPa)
k	Spring constant	-
S	Shear Strength	(MPa)
SF	Shear force	(Nm)
t	Ply Thickness	(mm)
T	Torque	(Nm)
X_c	Longitudinal Compressive Strength	(MPa)
X_t	Longitudinal Tensile Strength	(MPa)
Y_c	Transverse Compressive Strength	(MPa)
Y_t	Transverse Tensile Strength	(MPa)
ε_1	Ply Local Fibre Strain	($\mu\varepsilon$)
ε_2	Ply Local Off-Fibre Strain	($\mu\varepsilon$)

ε_x	Direct Strain in the *x*-axis	(µε)
γ_{xy}	Direct Shear Strain in the *xy*-axis	(µε)
ε_y	Direct Strain in the *y*-axis	(µε)
v_{xy}	Equivalent Poisson's Ratio	-
v_{12}	Major Poisson's Ratio	-
v_{21}	Minor Poisson's Ratio	-
θ	Twist Angle	(deg)
ρ	Density	(kg/m^3)
σ_x	Direct Stress in the *x*-axis	(MPa)
σ_y	Direct Stress in the *y*-axis	(MPa)
σ_1	Ply Local Fibre Stress	(MPa)
σ_2	Ply Local Off-Fibre Stress	(MPa)
σ_{12}	Ply Local Shear Stress	(MPa)
τ_{xy}	Direct Shear Stress in the *xy*-axis	(MPa)

Chapter 1

1. Introduction

1.1. Overview and Motivation

The current goal for the civil aviation industry is to improve the efficiency and performance of the aircraft in order to reduce the impact on the environment and also to minimise the costs incurred by the airlines without compromising all the safety aspects. Over the past years the research efforts were mainly addressed to achieve lighter structures by using composite and advanced materials, as well as by simplifying the design and reducing the number of structural components. The improvements achieved by solely using these approaches however, are not sufficient to meet the current demanding requirements set for a more eco-friendly aircraft.

Flow laminarisation offers great potential for step changes in drag reduction which leads to considerable improvements in fuel efficiency. However, the conventional commercial aircraft wing design, due to the numerous gaps between the main wing structure and the high lift device, does not provide the required high quality smooth continuous surface that laminar flow relies on. This problem could be solved by using new technologies such as morphing devices which allow seamless and gapless structures.

The state of the art wing design is characterised by a central wing box which provides stiffness and strength to the structure, in order to be able to withstand the high aerodynamic loads, and also holds most of the fuel carried by the aircraft. Replacing this rigid structure with a morphing one would cause many complications as the required rigidity would be lost, and it would be necessary to create an alternative storage for the fuel. On the other hand, if morphing structures are used to replace only the movable high lift devices, a more laminar flow can be obtained without compromising the conventional wing box concept.

Smart morphing high lift devices will also offer many more advantages in addition to flow laminarisation. As the requirements for the wing performance change during the entire flight profile, see Figure 1.1, the traditional design of an aircraft is optimised for a single operating condition, i.e. take off, cruise or landing. This leads to a non optimal performance at the off-design flight stages. However, by using morphing high lift devices the wing shape can be adapted to optimise the aerodynamic performance for any segment of the mission profile considering the aircraft changing altitude, velocity and mass, improving the overall performance efficiency.
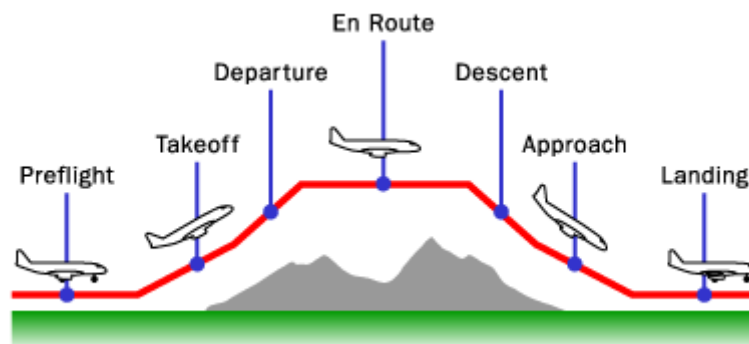
Figure 1.1 Typical commercial aircraft flight profile [1]

Furthermore, versatile high lift devices can be used to reduce off-design effect. This feature is of special relevance to laminar wings where off-design effects cause severe

problems with the transonic shock. The gapless structures will also reduce airframe noise in approach and they will increase the lift over drag ratio at take off allowing steeper climb at constant thrust and therefore further reducing noise emissions.

Several morphing wing concepts have been developed in the past however, they are mostly applied to micro air vehicles or small unmanned vehicles, and concepts for smart high lift devices for larger commercial aircraft are not readily available. Some of these designs can be taken as a starting point for the development of smart high lift devices, in particular they are mostly suitable to be used for an adaptive flap, however before a feasible morphing wing can be designed, further study and improvements are required. This sets the scene for the research on smart high lift devices for next generation wing.

1.2. The Smart High Lift Devices for the Next Generation Wing Project

The current research work was carried out as part of the European Commission funded Seventh Framework Program called 'Smart High Lift Device for the Next Generation Wing' (SADE). The main aim of this project is to develop and study morphing high lift device concepts in particular a smart leading edge and a smart single slotted flap. The seamless smart leading edge device is an indispensable enabler for laminar wings which offers a great benefit for reduction of acoustic emissions and drag. The smart single slotted flap on the other hand, with its active camber capability, increases the wing lift to drag ratio so that the overall lift produced by the new wing configuration is at least the same as the conventional one with the added advantages of increased efficiency and reduced environmental impact.

The investigation on these smart high lift devices included many technical areas of expertise, from structural analysis to aerodynamics and systems architecture. In order to study all these different aspects, thirteen partners were involved in the research activity and the numerous tasks were organised into four work packages.

Work Package 1 'Integration' – The integration of the smart high lift devices into the aircraft is simulated and assessed. A system's architecture is created for power consumption estimation and assessment of components weight. The effect of the smart high lift devices on the structure and its aeroelastic behaviour are also investigated.

Work Package 2 'Smart Leading Edge' – Morphing concepts are developed for the smart leading edge. The work covers structural, aerodynamics and actuation aspects. A design feasibility evaluation and an assessment of the maturity and readiness of the technology are also carried out.

Work Package 3 'Smart Single Slotted Flap' – The same tasks as work package 2 are performed, therefore morphing concepts for the smart flap are developed. The work covers structural, aerodynamics and actuation aspects and a design feasibility evaluation and an assessment of the maturity and readiness of the technology are also carried out.

Work Package 4 'Wind Tunnel Experiment' – The most promising concept form work package 2 is selected and designed in details for a wind tunnel model. This work package includes all the tasks involving the design manufacturing and testing of the selected smart leading edge device.

The author's research focused on the work package 2 of the SADE project and therefore a design concept for the morphing leading edge was developed and its feasibility from a structural point of view was studied.

1.3. Research Objectives

The design for the next generation wing proposed by this project uses an innovative concept to achieve a smart leading edge, to achieve a smooth seamless surface for flow laminarisation and noise reduction, and composite materials to maximise the stiffness to weight ratio. The main research objectives can be summarised as follows:

- To carry out a structural analysis of a composite wing box and its interface with the control surface, investigating in particular on the mechanical behaviour of

composite structural components and exploring new methods to increase their structural efficiency and load carrying capability;

- To develop an innovative design concept for the actuation mechanism for the morphing leading edge device of a large commercial aircraft wing;

- To conduct a static and dynamic analysis of the morphing leading edge structure and fully demonstrate its design and structural feasibility.

In order to achieve these objectives numerical and experimental studies were conducted to analyse the static failure and buckling behaviour of two typical composite wing structural components: a spar section and a web and base joint assembly. The knowledge gained from this research was then applied to the design of the composite wing box. A design for the morphing leading edge actuation mechanism was developed and a geometrical nonlinear finite element analysis was conducted to simulate the leading edge morphing deflection and ensure that the skins satisfied the structural strength requirements. To prove that the proposed actuation system can compete with the conventional rigid rib, the behaviour of the skin integrated with the internal actuation mechanism was tested under the aerodynamic pressure and gust loads.

1.4. Research Novelty and List of Publications

The research on the design and analysis of the next generation wing concept started with the study of the composite wing box of the chosen reference wing. The attention was in particular focused on finding innovative ways to improve and increase the strength and load carrying capability of the structure without adding significant weight penalty.

A novel concept for a morphing leading edge device was then developed in order to achieve a laminar flow over the wing. As previous work on a similar type of high lift device was not available, both structural analysis and modelling techniques were innovative aspects of this research. The research work conducted contributed in adding new knowledge in the area of both composite aircraft structures and morphing wing design and analysis. A detailed description of the contribution to knowledge can be

found in Section 6.3 and the following list of papers demonstrates the originality of the work:

- Guo, S., Morishima, R. Design, analysis and testing of composite sandwich T-joint structures. In: *50th AIAA/ASME/ASCE/AHS/ASC Structures, Structural Dynamics and Materials Conference*, Palm Springs, California, 4-7 April, 2009.

- Guo, S., Morishima, R., Wei, P. Sandwich T-joint structures with and without cut-out under shear loads. In: *17th ICCE Conference*, Honolulu, Hawaii, 26-31 July, 2009.

- Morishima, R., Guo, S., Dhande, R., Mills, A. Design improvement of a sandwich T-joint structure. In: *51st AIAA/ASME/ASCE/AHS/ASC Structures, Structural Dynamics and Materials Conference*, Orlando, Florida, 12-15 April, 2010.

- Morishima, R., Guo, S., Ahmed, S. A composite wing structure with a morphing leading edge. In: *51st AIAA/ASME/ASCE/AHS/ASC Structures, Structural Dynamics and Materials Conference*, Orlando, Florida, 12-15 April, 2010.

- Morishima, R., Guo, S. Optimal design of a composite wing with a morphing leading edge. In: *17th ICCE Conference*, Honolulu, Hawaii, 26-31 July, 2009.

- Morishima, R., Guo, S. Optimum design of a composite morphing leading edge for high lift wing. In: *4th SEMC Conference*, Cape Town, South Africa, 6-8 September 2010.

1.5. Structure of the Thesis

A description of the structure of the thesis is given in this section in order to guide the reader on how the research was conducted.

Chapter 2 – Literature Review

The state of the art of the design and analysis of composite morphing wing concepts is presented. A review on how the perspective of the aeroelastic effects has evolved during the past years shows a dramatic change in the design requirements of an aircraft wing.

In the past, wings were required to be as stiff as possible in order to avoid the aeroelastic effects; the current aim however is to have more flexible and lighter structures, using composite materials, and take advantage from the aeroelastic effects to increase the efficiency of the aircraft performance. The current methods to analyse, size and optimise composite aircraft wings using both classical and approximate numerical approaches are therefore herein reviewed and several concepts of adaptive wings and morphing high lift devices are described. The related development of morphing skins, active actuation systems and smart materials are also presented.

Chapter 3 – Theoretical Background

This chapter sets the theoretical framework on which the author's research was based on. The principles of the classical laminate and thin walled structures theory to analyse the behaviour of composite assemblies are firstly described. These analysis approaches were implemented into some in house computer programs which were developed to carry out preliminary structural assessments and an overview of the specific use of each program is given in this section. Finally, the finite element method approach, which was extensively used in the current research, for static and dynamic analysis of more complex composite structures is presented.

Chapter 4 – Composite Wing Box and Leading Edge Preliminary Structural Design and Analysis

This chapter shows the details of the preliminary structural design and analysis of the composite wing box for the chosen reference wing. The basic design parameters such as skin layup and thickness, stringers sizing and position were set to satisfy buckling and stress requirements, when the aerodynamic loads were applied to the structure, by conducting a parametric study. The results of an initial evaluation to estimate the morphing leading edge structure's contribution to the overall wing structural stiffness are shown. Finally in order to ensure that the wing box was fail-safe numerical and experimental studies were conducted on the static behaviour of the main load carrier structural components.

Chapter 5 – Design and Analysis of the Morphing Leading Edge

The investigation into the design and analysis of the morphing leading edge structure integrated with its actuation mechanism is discussed in this chapter. The actuation system was designed to reinforce the skin structure for carrying the externals loads while driving it to meet the morphing shape requirements. A geometrical non linear analysis was conducted to simulate the leading edge morphing deflection and ensure that the skin satisfied the structural strength requirements. In order to prove that the proposed actuation mechanism could be a practical concept, the behaviour of the skin with the integrated internal actuation mechanism was tested under the aerodynamic pressure and gust loads.

Chapter 6 – Conclusions and Future Work

The main findings of the research work on composite wing structures and the morphing leading edge are summarised in this last chapter. The contribution of the investigation conducted to the knowledge of the relevant technological field is stated and remarks to guide and motivate future investigation work are suggested.

Chapter 2

2. Literature Review

This chapter presents the state of the art of the design and analysis of composite morphing wing concepts. The first part of this section focuses on the analysis methods of composite wing structures, from simple single components (section 2.1) to more complex assemblies (section 2.2), using both classical theoretical methods and approximate numerical methods. Following this, a review on the study of the dynamic and aeroelastic behaviour of aircraft wings is presented (section 2.3). Due to the close interaction between aerodynamic loads and structural deformation these phenomena are of particular interest when designing flexible adaptable wing structures. Various concepts of adaptable wings and morphing high lift devices which allow smooth change in airfoil camber are described in section 2.4 and 2.5 respectively. Finally the potential of using morphing skins to allow adaptive wing shape change and the feasibility of using smart materials for active actuation are reviewed in section 2.6 and 2.7.

2.1. Composite Materials in Aircraft Structures

The study of composite materials started in the early 1960s when they were first developed at the Royal Aircraft Establishment at Farnborough, UK [2]. The initial application of composite materials in the aeronautical field was in the secondary structures of military aircraft, such as fairings, small doors and control surfaces. As the

technology evolved and the production costs were reduced, the use of composite materials extended to the commercial transport aircraft applications as both secondary and primary structural components such as wings and fuselage [3-4]. The composite materials usage trend for commercial transport aircraft is shown in Figure 2.1.

One of the main drives to use composite materials is their high stiffness to weight ratio; which offers potentials for great improvement in the overall performance and reduction in costs. However, their application as primary aircraft components is still today always cautiously evaluated, as they behave differently from metallic structures and the methods to accurately predict the damage mechanism and structural failure have not yet been fully explored. Many of the conventional design and analysis methods have been reviewed to include the anisotropic properties of composites and also to take in to account the additional considerations such as effect of the laminate stacking sequence, through thickness effects, interlaminar stresses and delimitation. Extensive research has therefore been conducted to study how these composite structural components react under various types of loadings and how they behave when they are assembled together.
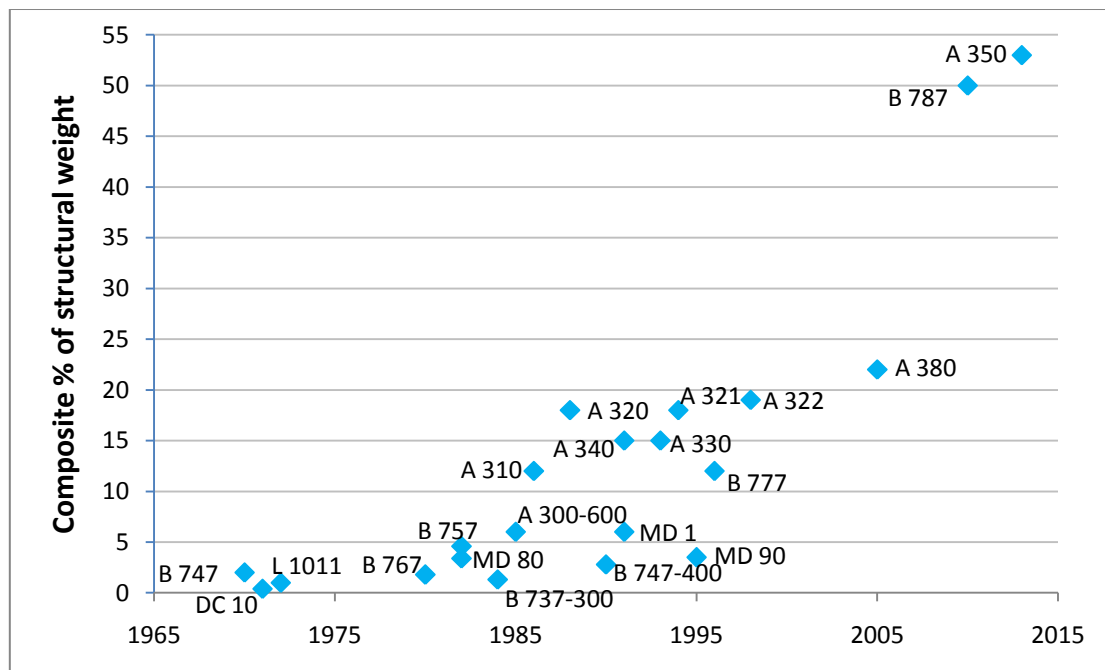
Figure 2.1 Composite usage trends in commercial transport aircraft [4-8]

2.1.1 Composite Channel Section Beam Buckling

In a wing structure, the components that carry a great portion of the bending, shear and torque loads due to the aerodynamic load are the spars, ribs and wing box skin. In the literature spar components are often modelled and studied as channel section beams. Several parameters affecting their mechanical behaviour have been investigated in the past years.

In particular, attention was focused on how the performance against buckling was affected by the location of the loading position and by the laminate fibre orientation [9-12]. These studies showed that when the load is applied through the shear centre the beam buckles in lateral-torsional mode. However, when the load is applied away from the shear centre, the warping effects are large and the warping stresses can be as high as 20% more than the flexural stresses. Further results have also demonstrated that the warping effect can nonetheless be reduced by using an appropriate fibre orientation: ±45 degrees for relatively long beams and 0 degrees for short beams. Razzaq et al. [9] also showed that the most disadvantageous loading position in a channel section is on the side of the compression flange, while the most advantageous loading position is on the tension flange in line with the shear centre.

Another method to increase the buckling stability of a channel section beam was studied in the research conducted by Tosh and Kelly [13], which used the fibre steering technique. By steering the fibres of the web panel in such a way that they followed the compression and tensile principal stresses trajectories, the stiffness of the structure was greatly increased. The deflection under an applied load was considerably reduced (168% lower) compared to that of a baseline section with a more traditional layup.

A factor that strongly influences the load carrying capability and stability of this type of primary structural components is the presence of cutouts. These are unavoidable as they allow accesses for inspection, cables and fuel lines as well as reducing the overall weight. However, despite the large literature available in the field of composite structures, few studies have been found to investigate the effect of a cut-out in the beam

web. Most researches focusing on the influence of the presence of a cutout are in fact conducted on simple panels which represent the beam web.

2.1.2 Buckling and Stress Concentration in Composite Panels with Cutouts

The presence of a cutout has always the effect of increasing the stress concentrations and lowering the load carrying capability of a structure. In a composite panel with a cutout the distribution of the applied load, especially around the cutout, is strongly dependent on the fibre orientation and it is never straight forward to predict how they affect the stress distribution. A vast number of analytical, numerical and experimental studies have therefore been conducted to determine the stress concentration around a cutout in a composite plate and how this stress distribution is affected by the cutout geometry, the type of applied loading and the laminate layup [14-19].

Cutouts have also a significant effect on the overall buckling stability of the panel [20-23]. Nemeth [24] published a comprehensive review of the research activities conducted on the buckling and postbuckling behaviour of composite plates with a cutout. This review covered many influential factors such a cutout size, shape, eccentricity and orientation; plate aspect and slenderness ratios; loading and boundary condition; plate orthotropy and anisotropy.

Extensive research has also been conducted to reduce the stress concentrations due to cutouts and also to improve the buckling stability. An approach to reduce the stress concentrations without adding structural weight was to optimise the cutout shapes and their position [25, 26]. However, when a more significant stress reduction or buckling strength improvement was required cutout edge reinforcements were often used. Several studies [27-35] showed that the most efficient type of reinforcement was to use ring doublers on each side of the panel.

In the more recent years stiffness tailoring using steered tow placement fibres has been employed to reduce the effect of cutouts [36-39]. Various techniques were also developed to optimise the fibre tow orientation trajectory using either mathematical

optimisation models [40-42], such as genetic algorithm, or multidisciplinary criterion implemented in the finite element method calculations.

2.1.3 Failure Mode of Composite Joints

The assembly of composite components is also an area of particular interest when considering composite structures. The connections or joints are potentially the weakest points and could determine the overall structural efficiency. Examples of such assemblies are the skin-to-stiffeners and skin-to-spar joints. Many researchers have investigated on the behaviour of these components and in particular on the failure mechanisms of composite laminate and composite sandwich T-joints.

Numerical [43-45] and experimental studies [46] have been conducted to determine the failure modes of composite T-joints and also to predict the presence of delamination and extent of damage when failure occurs. These studies showed that the weakest point in the structure is the triangular adhesive filled region at the root of the joint, see Figure 2.2. The failure is mainly caused by the high stresses in the filler region and consequent separation of the web panel from the base. Parametric analyses have also been carried out to determine how the failure of the composite T-joint is affected by the radius of the curvature at the web/base interface and by the laminate stacking sequence [47-49].
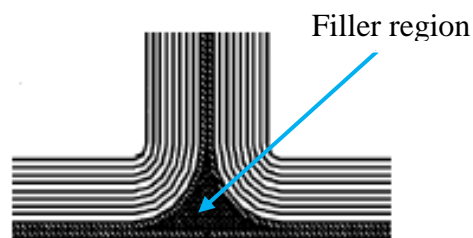
Figure 2.2 Triangular filler region between the web and base panels

Different methods have also been developed to improve the strength of these types of joints and to allow a more efficient load transfer from the joint web to the base panel.

These methods include the use of attachment laps with circular fillets connecting the web and base panels [50-53], aluminium U-shaped inserts [54], composite textile [55], Z-pinning [56], tufting [56], transverse stitching [57-59] and 3D braiding [60].

2.2. Design of Composite Wings

Knowing how single components behave, when loaded, can be useful to have a general idea on how they can affect the overall structure integrity. An aircraft is in fact made of an assembly of such components and its design involves different phases where the structure is analysed at different level of accuracy. The structural design process of an aircraft wing consists of three main phases: preliminary design, detailed design and optimisation, as shown in Figure 2.3.

Preliminary Design

- Set wing shape and general dimensions
- Estimate wing loadings
- Estimate the bending and torsional displacements

Detailed Design

- Static structural analysis of wing components (skin panels, spars, ribs)
- Static and dynamic structural analysis of the whole wing assembly

Optimisation

- Set spars and ribs position and thickness
- Set skin thickness
- Set number of stringers, position and dimension

Figure 2.3 Wing structural design process

During the preliminary design stage the general wing geometrical parameters are set and the overall displacements due to the external loadings are evaluated. During this design phase a wing box is often idealised as a thin walled box structure and its bending,

torsional and warping behaviour are studied using the thin walled closed section beam theories.

The classical analytical solutions for the thin walled structures with closed cross sections were first developed by Vlasov [61] and Gjelsvik [62]. These were then extended in order to analyse in details the effects of cross section distortion due to structural coupling effects and torsional warping [64-66]. The increasingly usage of composite materials led many researchers to develop general analytical methods to analyse composite thin walled box structures. Due to the nature of this type of materials, considerable efforts have been dedicated to study the effects of the laminate layup on the structural coupling effects [67-69] including non classical ones, such as transverse shear deflection [70-72].

In the next design phase, each component is designed in details and static and dynamic analyses are conducted for the individual components and for the whole wing structure. During this more detailed design stage however, the analysis of a wing box is often carried out using approximate methods as the geometries become more complex and exact closed form solution cannot be obtained. One of the most commonly used numerical methods is the finite element method [73, 74]. Initially this analysis method was used to develop two dimensional computational tools [75] to analyse thin walled beams, with a general cross section, using classical theories. The increase in availability of fast and cheap computers has lead to the development and wide use of commercially available three dimensional finite element codes [76-78]. These finite element method software packages offer the great advantage of accurately simulating the behaviour of complex structures reducing testing and redesign costs and identify issues before tooling is carried out.

The use of finite element methods for structural analysis made also possible to carry out complex optimisation procedures. A feedback loop is therefore created between the detailed design and the optimisation phases in order to achieve an efficient and safe structure. A wing box must be in fact optimised to satisfy multidisciplinary criteria such as stress, fatigue, buckling, flutter and weight which are controlled by a vast number of

parameter (structural size, position and materials of stringers, spars, ribs and skin panels). Various Multidisciplinary Design Optimisation (MDO) techniques, programs and software packages have therefore been developed and applied for wing box sizing and optimisation [79-85].

2.3. Structural Dynamics and Aeroelasticity

Aeroelasticity is the subject concerning the interaction between the deformation of an elastic structure in an airstream and the resulting aerodynamic force. The study of the aeroelastic phenomena involves the close interaction of three disciplines: aerodynamics, dynamics and elasticity. The interdisciplinary nature of this field is illustrated in Figure 2.4. The major disciplines of flight mechanics, structural dynamics and static aeroelasticity each result from the interaction of two types of forces, while all three forces are required to interact for dynamic aeroelastic effect to occur.
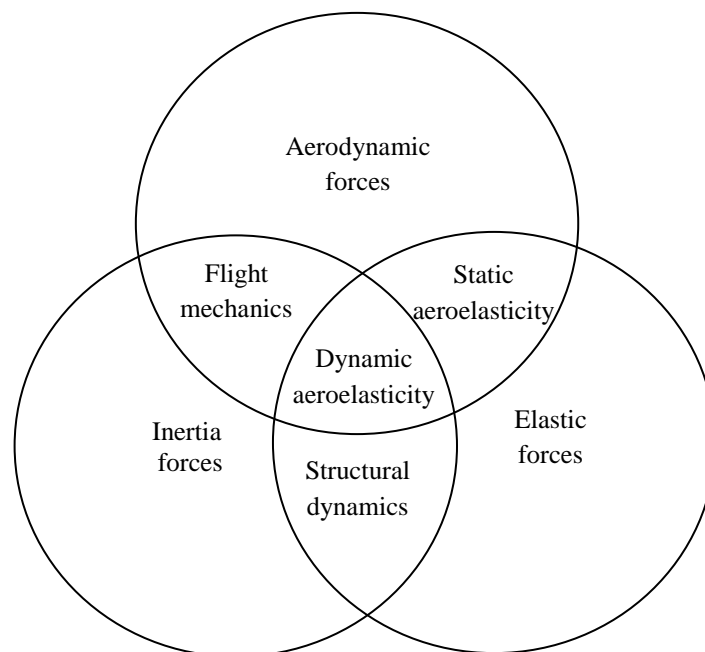
Figure 2.4 Summary of the field of aeroelasticity [86]

The field of structural dynamics addresses the dynamic deformation behaviour of continuous structures. This subject covers the determination of the natural frequency and mode shapes, response due to initial conditions, forced response in time domain and frequency response. By carrying out a structural dynamics analysis it is possible to quantitatively describe the deformation pattern at any instant in time for a continuous structural system in response to external loading [86].

Static aeroelasticity studies the interaction between the aerodynamic loading induced by a steady flow and the resulting elastic deformation of the lifting surface structure. There are two critical static aeroelastic phenomena that can be encountered, divergence and control reversal [87]. Divergence is the name given to the phenomenon that occurs when the moments due to the aerodynamic forces overcome the restoring moments due to structural stiffness resulting in the structures failure. The control reversal occurs at a specific speed at which the effect of the control surfaces, used to manoeuvre the aircraft, reverses.

Dynamic aeroelasticity studies the dynamic behaviour of a continuous structure due to the combination of inertial load and aerodynamic loads. The most characteristic and important phenomena is flutter [86, 87]. Flutter is an unstable self-excited vibration in which the structure extracts energy from the airstream. At some critical speed, known as flutter speed, the structure sustains oscillations following some initial turbulence. Below this speed the oscillations are damped, whereas above it one of the modes becomes negatively damped and unstable oscillation occur.

Aeroelastic phenomena have played an important role throughout the history of powered flight, as it severely affects the flight performance of an aircraft [88]. Because of these consequences aeroelasticity was treated as an effect to be avoided by stiffening a structure. The study of the aeroelastic effects on an aircraft were already quite well known by the 1950s, as documented in classic text books [86, 89-93] and many journal and conference papers [88, 89, 94, 95].

The concept of aeroelastic effects changed in the 1970s with the use of composite materials. These materials in fact, offered the possibility to control the directional

stiffness of a structure and consequently, take advantage of the aeroelastic coupling between bending and torsion. The wings structure started therefore to be designed with more flexible characteristics in order to take advantage of the aeroelastic effect and optimise the overall aircraft performance [96]. The use of the finite element method for structural dynamics study as well as more accurate aerodynamic models, made it also possible to analyse general complex composite structures that were idealised and simplified until then. New computational methods, both analytical and numerical, were also developed to study the effects of aeroelastic tailoring and adaptive control technology and also to analyse the interaction between the control systems and the structure (aeroservoelasticity).

2.3.1. Structural Dynamics Analysis Methods

The field of structural dynamics studies the dynamic deformation behaviour of continuous structures, determining natural frequency and mode shapes, response due to initial conditions, forced response in the time domain, and frequency response.

When a wing structure is modelled as a simple beam, its deformation pattern in response to a time dependent or frequency depended loading is studied using closed form analytical methods. Several methods have been developed to obtain exact solutions for composite wing like structures:

- Dynamic stiffness method [97-104] – where the dynamic stiffness matrix is obtained by deriving the governing differential equation of the structure using energy methods. This method has been used to study the vibration of composite beams and analyse the bending torsional coupling effects due to various types of loads.

- Modified thin walled structures theory developed by Vlasov [105] – this method allows to include the effect of the transverse shear deformation of the composite beam cross section in the vibrational displacement of the structure.

- Variational asymptotic approach [106, 107] – which allows to provide the stress and displacement fields from the structure's stiffness coefficients.

- Three high order displacement model [108] – which allows to take into account the warping effect of the cross section without the need of shear correction, by taking the cubic variation of axial strain.
- Static space based differential quadrature [109] – which uses a frequency dependent system's governing equation to study the free vibration of a composite beam structure.

Further progress for the analytical solutions was achieved when morphing structures started to be modelled and studied [110, 111], as it became essential to include parameters such as the adaptive control systems terms (e.g. actuators) and structural nonlinearities [112].

The vibration analysis of a more detailed wing model is instead often carried out using approximate methods [113, 114]. In particular, the use of the finite element method allows large three dimensional composite structures to be analysed in a relatively short period of time. Another advantage of using the finite element method for structural dynamic analysis is that both local and global vibration behaviour are computed at the same time and the interaction between the two can be analysed.

A type of vibration analysis that is of particular interest when studying aircraft structures is the response to atmospheric turbulence. As this phenomenon involves both dynamic and aerodynamic forces, it is usually treated under the subject of flight mechanics.

2.3.2. Flight Mechanics: Gust Response Analysis Methods [87]

An aircraft during a flight regularly encounters atmospheric turbulence of varying degrees of frequency and intensity. Turbulence can be considered as a movement of the air thorough which the aircraft passes. Any component of the velocity of the air that is normal to the flight path, as shown in Figure 2.5, changes the effective wing angle of attack, causing sudden increases or decreased in the lift forces. This change in

aerodynamic load generates a dynamic vibrational behaviour of the aircraft which also involves structural flexible deformation.
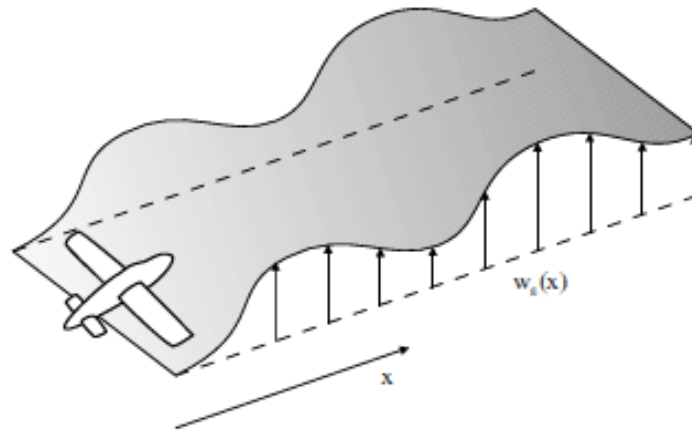
Figure 2.5 Aircraft encountering turbulence [87]

For analysis purposes turbulence is considered as one of two idealised categories: discrete gust and continuous turbulence [115]. In the discrete gust model the gust velocity varies in a deterministic manner, often in the form of a '1-cosine' shape as defined by the Airworthiness Authorities [116], whereas for a continuous turbulence model the gust velocity is assumed to vary in a random manner. When the gust is modelled with a discrete behaviour a gust load factor and a specific frequency must be determined for a certain flying altitude. The time dependent gust load shape can be written as

$$w_g(t) = w_g \left(1 - cos \frac{2\pi V}{L_g} t \right) \qquad (2\text{-}1)$$

Where

w_g is the gust load intensity

V = aircraft true airspeed at the specific altitude in m/s

L_g = gust length in m (range given in reference [116] for a certain altitude)

The frequency at the specific altitude is therefore the ratio $2\pi V/L_g$ and the highest frequency is obtained for the shorter gust length.

The gust load factor is also dependent on the aircraft flying velocity and altitude and it is defined as

$$n = 1 + \frac{K_g U_{ref} V_a}{498(W/S)} \tag{2-2}$$

Where

$K_g = \frac{0.88\mu}{5.3+\mu}$ = gust alleviation factor and $\mu = \frac{2(W/S)}{\rho cag}$ = airplane mass ratio

U_{ref} = gust velocity in ft/s (given in reference [116] for a certain altitude)

ρ = air density at the specific altitude in slug/ft^3

W = weight of the aircraft in lb

S = wing area in ft^2

c = mean aerodynamic chord in ft

g = gravitational velocity in ft/s^2

Va = aircraft equivalent velocity at the specific altitude in kts

a = lift curve slope

The continuous turbulence idealisation is on the other hand not restricted to a specific gust frequency and it is a more realistic and accurate way to represent the phenomenon of gust and is often preferred when conducting a gust response analysis of an aircraft wing.

Numerous experiments have been conducted to collect data on the nature of gust such as intensity, velocity and frequency at different altitudes [117, 118]. These data were then used to develop appropriate mathematical models to represent a continuous turbulence, such as statistical based and power spectra methods [87, 118 and 119]. Further investigations were also carried out to evaluate which aerodynamic model was most appropriate to be implemented in a gust response analysis, and also to assess wheatear to use time or frequency domain analysis methods [120]. These gust models were then applied to analyse the response behaviour of an aircraft using both analytical methods

[121], to give closed form solutions for simplified structures and numerical approaches [122] for more complex and detailed models. For both methods the results obtained provide a full time history of an aircraft elastic deformation in the event of gust encounter in order to ensure the safe design of an aircraft in terms of internal loads generated and fatigue effects.

2.3.3. Static Aeroelastic Behaviour Analysis Methods

The field of static aeroelasticity studies the interaction between the aerodynamic loading induced by a steady flow and the resulting elastic deformation of the lifting surface structure. There are two classes of design problem that are associated with static aeroelastic effects. The first one involves the potential for static instability of the structure and results in its catastrophic failure. This instability is known as 'divergence' and it can impose a limit on the flight envelop. The second class of problem is most common to all structures and is the effect of the elastic deformation on the aerodynamic loads associated with the normal operating conditions.

Classical analytical methods to study these phenomena have been well established since the 1950s [91, 92], however the necessity to develop new theories became essential when composite materials started to be widely used for aircraft primary structures. Box beam models were adapted to include the effects of anisotropy and particular attention was focused on methods to accurately compute the cross-sectional stiffness constants, as they strongly affect the aeroelastic response in terms of bending-twist and extension-twist coupling [123]. Another suitable method to analyse the aeroelastic behaviour of a composite wing was to idealise the structure using the plate modelling technique. The skins, spars and ribs were in fact modelled as single plates and then assembled to form a box structure; so that the theory of thick and anisotropy laminated plates could be used. Models with an arbitrary geometry were therefore generated with ease and analytical solutions were obtained including the transverse shear effects [124].

The development of active control technology and design of flexible wings led to the close interaction between control systems (sensors, control computers and actuators)

and deformable structures. The control system, which responds to the elastic deformation, in fact became part of the structure itself. A new field, aeroservoelasticity, was developed to study the aeroelastic behaviour of flexible structures coupled with its control system [89, 125 and 126]. A multidisciplinary design cycle, involving structures including the control systems, and aerodynamics, has become a common approach to analyse the aeroservoelastic behaviour of a wing [127-129]. Developing methods to include the effects of nonlinearities and freeplay are also considered of paramount importance as they strongly affected the accuracy of the aeroservoelastic analysis of a structure [130, 131]. The aeroservoelastic analysis of complex structures is therefore often carried out using two main analytical tools: the finite element method for structural analysis and computational fluid dynamics for aerodynamic analysis. The widespread of powerful and fast computers also facilitated the development of multidisciplinary optimisation tools to meet controllability, aerodynamic performance and structural requirements [132, 133]. Moreover, several programs [134-136] have been developed to ensure high fidelity data transfer between structural and aerodynamic analysis tools. These allow a close interaction between the two disciplines making the aeroelastic modelling more reliable and accurate during an aircraft design phase.

2.4. Adaptive Wings

In the recent years challenging targets have been set for the aviation industry to improve aircraft performance. This has been focused not only on costs reduction, but also on environmental issues. These targets however cannot be met by simply improving the engines performance and reducing the structural weight [137]. Many researchers have therefore started to consider the possibility to take advantage of the aircraft aeroelastic deflections to achieve gains in aerodynamic performance [88, 138-139]. There are two methods used to exploit these aeroelastic effects: passive aeroelastic tailoring and active aeroelastic control.

The passive aeroelastic tailoring consists in controlling the directional properties of the composite materials in order to influence the aeroelastic behaviour of the structure [140]. By tailoring the directional stiffness the coupling between bending and twisting

deformation are optimised and increase in divergence and flutter speeds can be achieved without increasing the overall structural weight [141-145]. Furthermore, taking advantage of the aeroelastic tailoring effects, innovative structural configurations with enhanced aeroelastic properties and performance, such as the forward swept wing of the X-29 [88], can be achieved.

Active aeroelastic control is achieved by using adaptive flexible structures which allow aeroelastic deflections to be used in a beneficial manner and to enhance the aerodynamic performance. The idea of a flexible camber was first introduced in the 1920's for the control of biplane wings [146]. Since then in the recent years several researches, such as the Active Flexible Wing [147], the Active Aeroelastic Wing [148-150], the Morphing Wing [151] and the Active Aeroelastic Aircraft Structures [152] programs, have been conducted to develop adaptive aeroelastic concepts. The various adaptive wing concepts focused on varying the wing shape chordwise and/or spanwise to optimise the lift to drag ratio throughout the entire flight increasing the aircraft range, to reduce the loads that are induced by gusts or manoeuvres improving aircraft performance and to control the roll manoeuvres.

2.4.1 Twisting Wing

This mechanism controls the twisting deformation of an aircraft wing in order to compensate for the aerodynamically induced twist [153]. A torque tube is placed in each wing along the full span. Each tube, which is rigidity attached near the root of the wing is moved by an actuator located in the aircraft fuselage. As changes in the aerodynamic loads on the wing occur, the torque tube is rotated to counteract the induced wing twist, as shown in Figure 2.6.
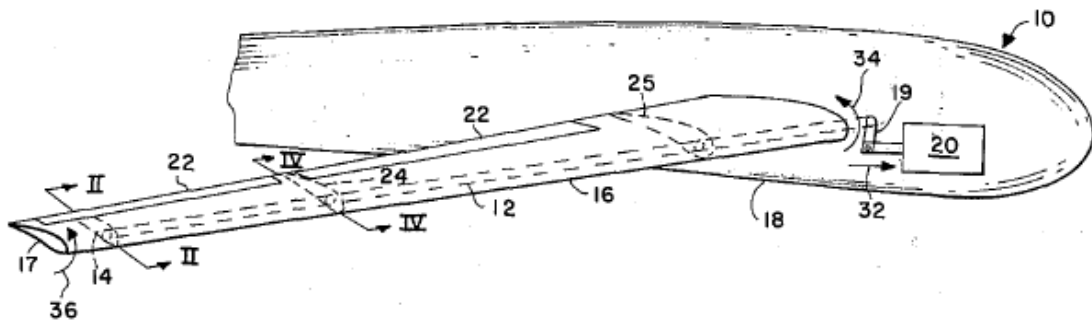
Figure 2.6 Twisting wing [153]

2.4.2 Variable Span

The concept of variable span was developed for a long range cruise missile [154, 155]. Figure 2.7 (a) shows the original wing with no extension and Figure 2.7 (b) shows the fully extended wing, with a 50% longer span. The results from this study showed that, from an aerodynamic point of view, the extended span increased the spanwise lift distribution and decreased the induced drag. From an aeroelastic point of view however, the extended wing bending stiffness was not sufficient and severe deformation occurred due to the large bending moments at the wing root.

(a)   (b)
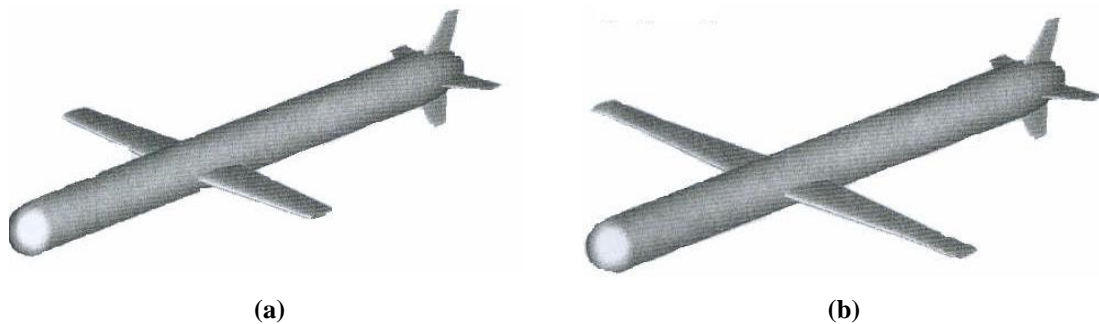
Figure 2.7 Variable span wing [154]: (a) Original span; (b) Extended span

2.4.3 Moving Spar

Two design concepts were developed to actively change the shear centre location and the torsional stiffness by moving the spars in the chordwise direction. In the first

concept [156] both front and rear spars position were changing, as shown in Figure 2.8. When the spars were further apart the maximum torsional stiffness was achieved, while when they were shifted towards the centre the torsional stiffness reached its minimum.

(a)	**(b)**
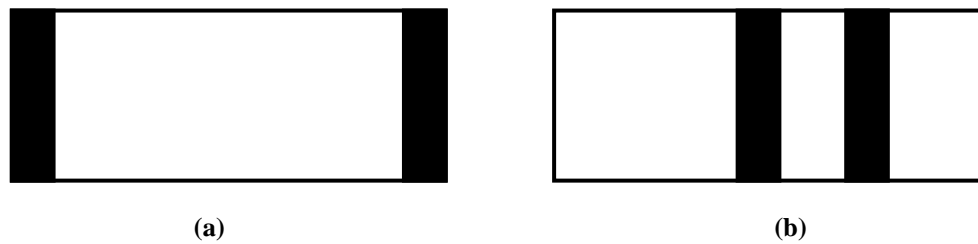
Figure 2.8 Chordwise moving spars [137]: (a) high torsional stiffness; (b) low torsional stiffness

The other concept using the same principle consisted of a conventional wing box with a third movable spar [157], as shown in Figure 2.9. By sweeping the main spar, the flexural axis of the wing was shifted, allowing the wing to be actively twisted during flight.
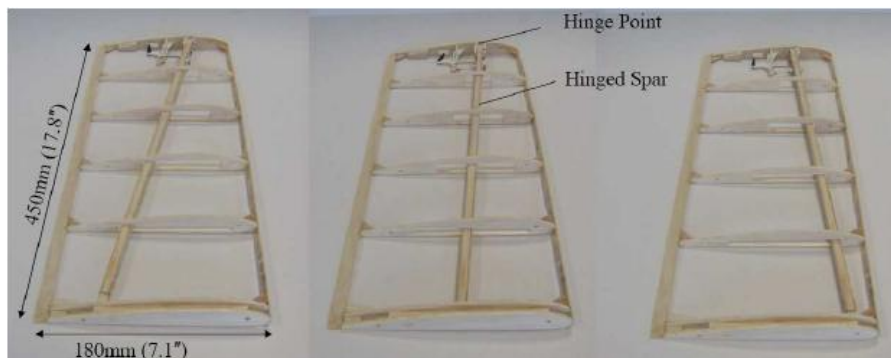
Figure 2.9 Single moving spar [157]: (a) Aft position; (b) Neutral position; (c) Forward position

Another option for the spars movement was to rotate them from vertical to horizontal [156], see Figure 2.10. This configuration allowed the active change in bending stiffness: maximum when the spars were vertical, minimum when the spars were horizontal.
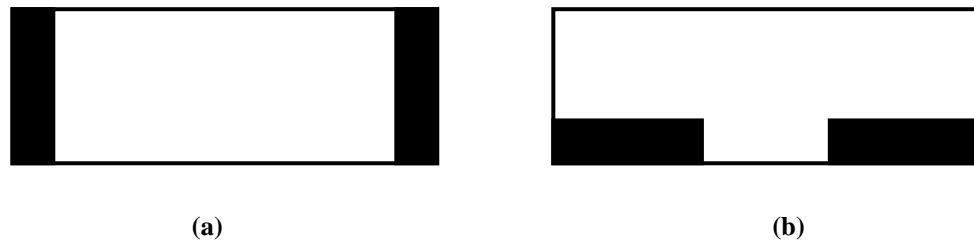
Figure 2.10 Rotating spars [137]: (a) Maximum bending stiffness; (b) Minimum bending stiffness

The feasibility of both chordwise moving and rotating spars concepts were demonstrated experimentally. It was also shown that the chordwise moving spar concept was more suitable for changing the wing shape to reduce drag, whereas the rotating spar was appropriate for rolling control since it was possible to change the position of the spar from maximum to minimum bending stiffness position in approximately 0.5 seconds.

2.4.4 Rotating Rib

The rotating rib concept [158, 159] allowed the continuous and smooth variation in camber along the wing span reducing drag and increasing lift at any particular stage of the flight mission. The conventional connection between the skin and the ribs, based on rivets, at the wing trailing edge was substituted with a discrete number of linear slides which allowed the skin to glide over the rib contour [159]. The same concept was applied at the trailing edge where the upper and lower skins met. The two skins were not rigidly connected to each other but they were allowed to glide into a linear slide bearing. When a rib was rotated by an actuator, the upper and lower skins glided over the rib contour and along the trailing edge, as shown in Figure 2.11.

The main difficulty in this concept was that a large amount of torque was required by the actuator in order to deform the skin panels and to gain friction force inside the slide bearing.
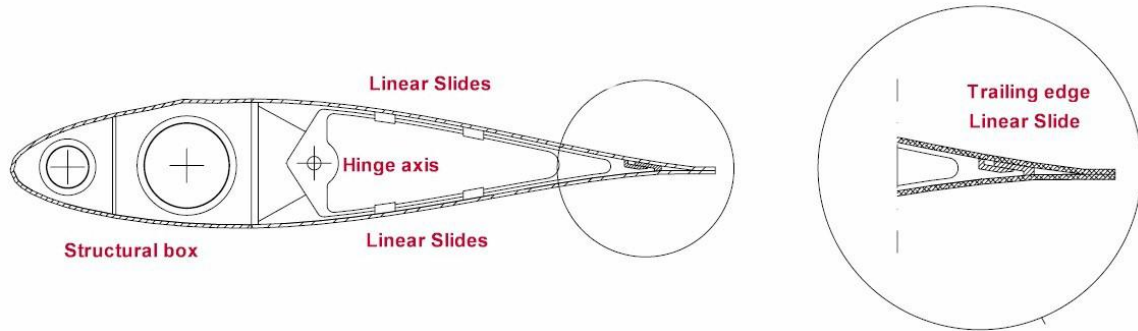
Figure 2.11 The rotating rib concept [158]

2.4.5 Belt Rib

The belt rib concept was developed with the purpose of achieving large changes in airfoil camber by using flexible components instead of more traditional moving parts [160], see Figure 2.12. The conventional rib structure was replaced by an airfoil shaped closed cell (belt) reinforced by in plane stiffeners (spokes) which were connected to the belt by hinges. Unlike a conventional rib, the belt rib concept allowed large in plane deformations in the aft section of the airfoil, increasing the lift generated by the wing. Furthermore, this concept exploited the aerodynamic and aeroelastic amplification effects in order to reduce the energy requirements of actuation system.

`
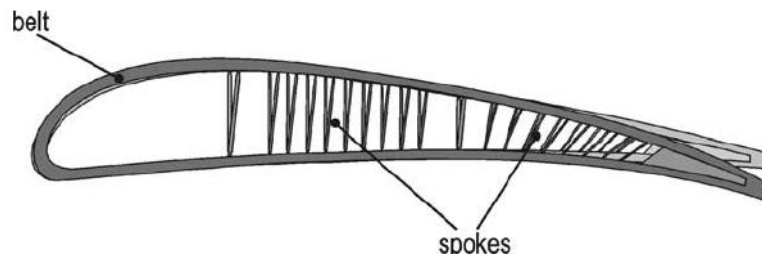
Figure 2.12 Belt rib configuration [160]

2.5. High Lift Devices

The adaptive wing concepts have proved to offer potential advantages to increase the performance of an aircraft; however these mechanisms are insufficient for the aeroelastic control of large commercial transport wings. Adaptive high lift devices and control surfaces are in fact needed to provide enough lift, obtain significant reduction in drag, and control manoeuvres. Various studies showed the advantages of using a varying camber wing on a commercial aircraft. One of the main drives to develop adaptive high lift devices is the potential to optimise the lift to drag ratio at any flight condition and therefore obtained considerable reductions in fuel consumption and costs [161, 162]. Furthermore, it has been demonstrated that by using adaptive trailing edge and leading edge devices it is possible to improve the roll effectiveness and control [163-166] as well as delaying control surface reversal [167, 168]. In this section the conventional and the more innovative adaptive trailing and leading edge systems are reviewed.

2.5.1 Conventional Trailing Edge High Lift Systems

There are many types of trailing edge flap devices that have been developed to increase the maximum lift coefficient by increasing the wing area. The conventional types use mainly a mechanical system to be operated and they can be classified in six categories.

Split Flaps

Split flaps consist of a stiffened plate on the wing lower surface, hinged just aft the rear spar [169]. As shown in Figure 2.13 (a). This type of flap was widely used in the early military airplanes. It is a good attitude and glideslope control device; however it does not produce a large lift increase. It can also be used as a speed breaker as it produces drag without losing lift.

<div align="center">(a)   (b)</div>

<div align="center">**Figure 2.13 (a) Split flap; (b) Plain flap**</div>

Plain Flaps

Plain flaps consist of hinged part of the trailing edge [169]; see Figure 2.13 (b). The best performance is achieved when the gap between the fixed wing and the movable trading edge is sealed. The deployment angle of the flap is limited to 20 degrees, beyond that, the flow separates on the upper surface.

Simple Slotted Flap

The simple slotted flap has a flap panel with a fully developed aerodynamic leading edge [170]; see Figure 2.14 (a). It is mounted on pivots on the lower wing surface and its maximum deployed position reaches 30 to 35 degrees. Due to the small overlap between the flap and the fixed trailing edge the increase in wing surface area is small and only moderate increase in lift is gained.

Single Slotted Flap

In the retracted position, Fowler flaps have a large overlap between the flap and the fixed upper wing cover. When deployed, the flap moves backwards (Fowler motion) and the wing area largely increases [170], see Figure 2.14 (b). If carefully designed a single slotted flap can be deflected up to 40 degrees and they are commonly used on light aircraft and a few transports.

(a) **(b)**
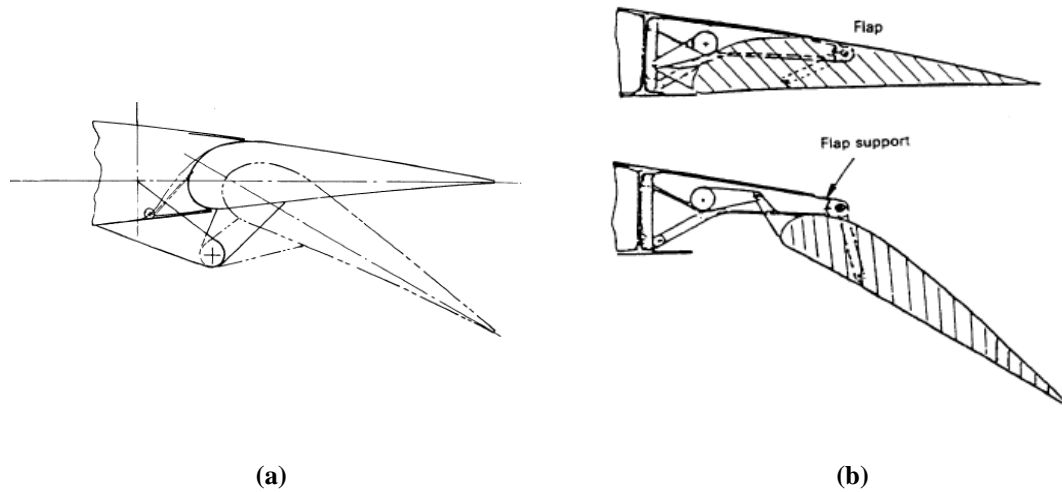
Figure 2.14 (a) Simple slotted flap [169]; (b) Single slotted flap [170]

Double Slotted Flap

Double slotted flaps are more efficient then single slotted flaps at large deflections as flow separation over the flap is postponed by the more favourable pressure distribution. Double slotted flaps are most popular for transport aircraft and various mechanical systems have been developed [169]:

- Flaps with a fixed hinge and a fixed vain, see Figure 2.15 (a)-(c)
- Flaps which are deployed using tracks, see Figure 2.15 (d)
- Flaps deployed by a four bar linkage mechanism, see Figure 2.15 (e).

(a)   (b)   (c)

(d)

(e)
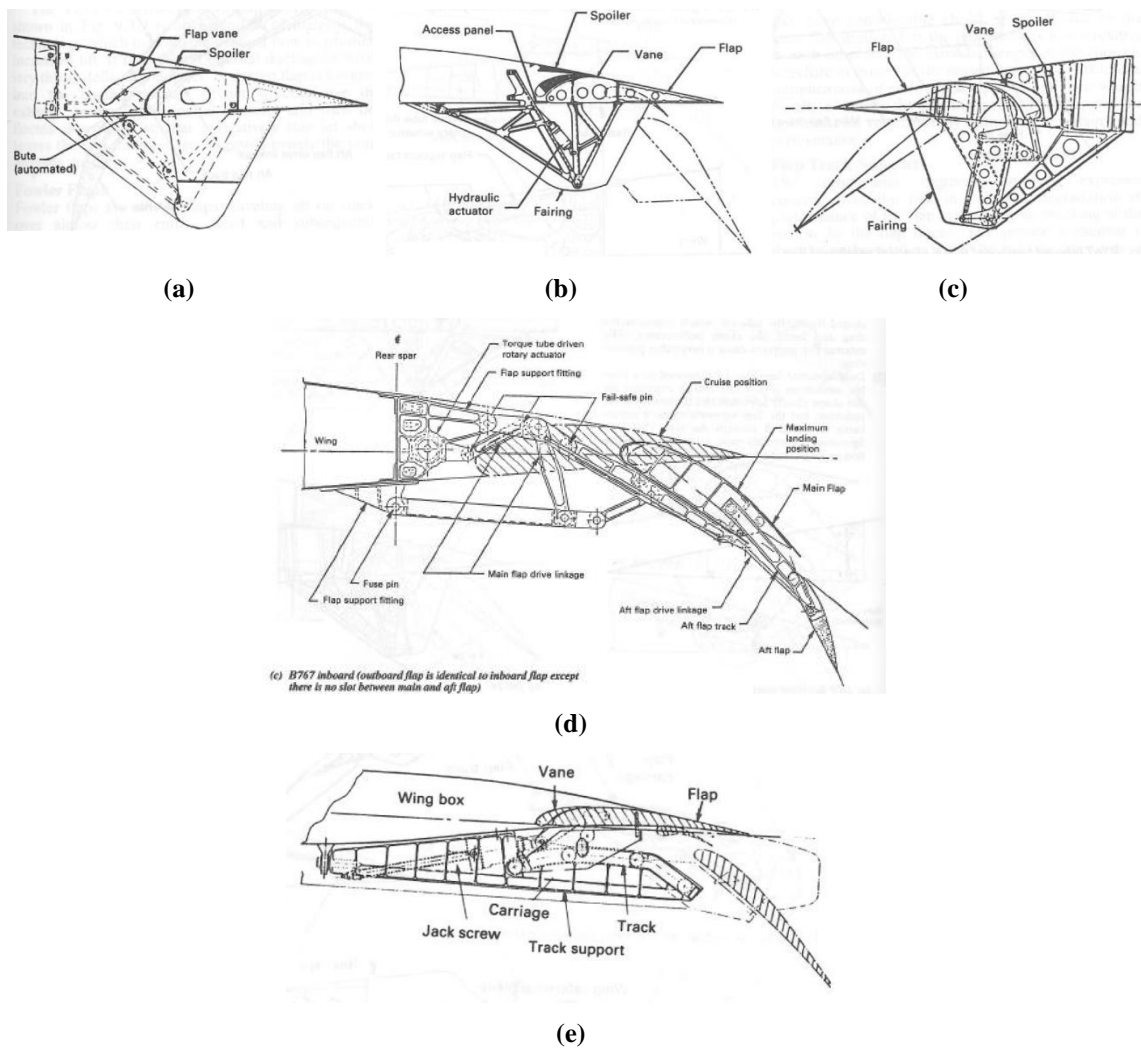
Figure 2.15 Double slotted flaps [169]: (a)-(c) Hinged type; (d) Linkage type; (e) Track type

The linkage type of double slotted flap reaches a shape that closely approximates to the aerodynamic optimum and is the most suitable for application on long range transport aircraft.

Triple Slotted Flaps

A triple slotted flap has three overlapping components and can provide significantly large Fowler motion, and the three slots allow the deflection of the aft flap to reach 80

degrees [170]. Because of the high number of components this flap mechanism is complex and heavy, as shown in Figure 2.16.
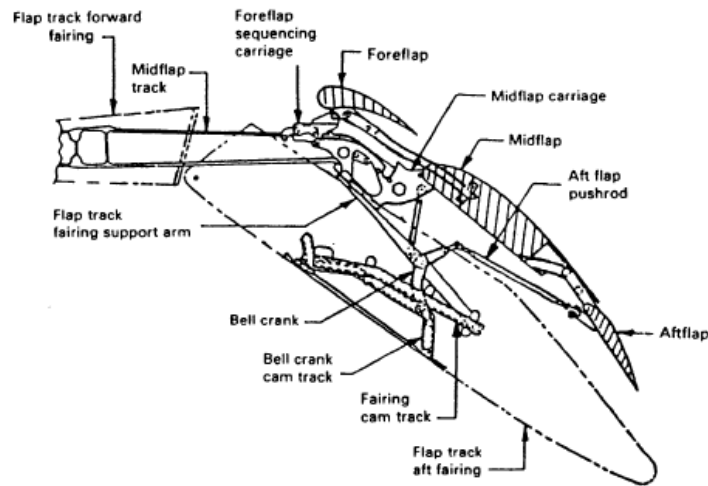
Figure 2.16 Triple slotted flap [170]

2.5.2 Adaptive Trailing Edge Devices

Most of the adaptive trailing edge devices that have been developed are mainly used for morphing wing concepts; however they can also be applied for flap trailing edges. A common aim in the development of these morphing devices is to obtain a smooth camber change in order to optimise the aerodynamic performance. Several concepts have been developed, manufactured and tested.

Finger Rib Concept

The finger rib concept consists of a rib which has a front rigid section, until the rear spar of the wing box, and a flexible section at the trailing edge. The flexible part is made of a number of separate plates combined together with revolute joints [171]. These joints allow the deflection of each segment and therefore ensure a smooth camber change of the trailing edge, see Figure 2.17 (a). The movable parts of the ribs are actuated using a

transmission beam, which is moved from the horizontal to the vertical position to camber and de-camber the wing shape, see Figure 2.17 (b).

(a) **(b)**
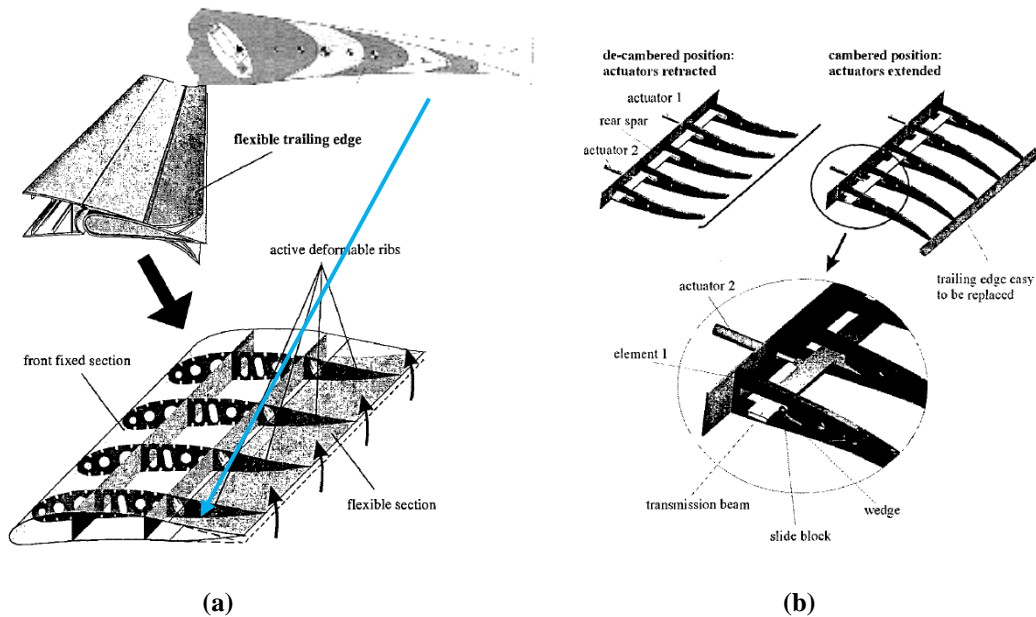
Figure 2.17 Finger rib concept [171]: (a) Morphing rib; (b) Actuating transmission beam

Sandwich Flexible Trailing Edge

The sandwich flexible trailing edge device is made of an aramid honeycomb core and silicone skin with an aluminium trailing edge tip [172]. The honeycomb core provides stiffness in the thickness direction and gives resistance to the aerodynamic loads. A fibreglass laminate is placed in the centre of the device in order to provide a hard point to attach an aluminium tip and connect the actuator driven eccentuator which controls the trailing edge deformation, see Figure 2.18.
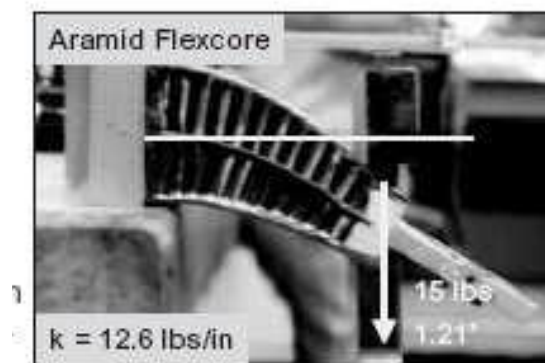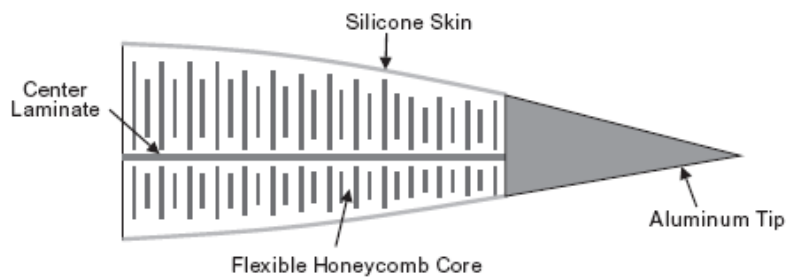
Figure 2.18 Flexible flap deflection mechanism [172]

Eccentuator Beam Mechanism

The eccentuator beam mechanism uses a transmission technique called 'eccentuation'. The eccentuator consists of a bent beam that converts a rotary input motion into a vertical and lateral translation at the output end. This output end slides on a bearing surface which is forced to move upwards or downwards depending on the direction of the rotation of the beam, see Figure 2.19 (a). With a pair of eccentuators it was possible to achieve a precise control of both structural bending and twisting, see Figure 2.19 (b). This morphing concept allows an effective control of the trailing edge deflection with a simple and reliable actuation mechanism [172-177].
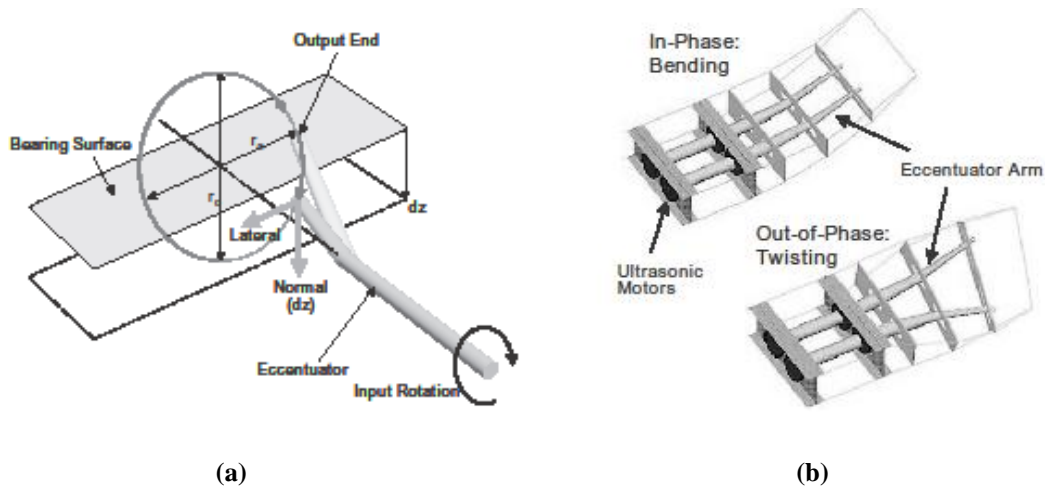
Figure 2.19 Eccentuator concept [172]: (a) Input and output ends, (b) Bending and twist control

2.5.3 Conventional Leading Edge High Lift Systems

A leading edge high lift device is used on an aircraft to delay the stall at high angles of attack. A wing leading edge consists of a fixed leading edge structure, with or without slats. If slats are used, when retracted, they form the front profile of the wing ahead of the fixed leading edge. There are several types of leading edge devices and they change the camber of the airfoil by deploying the slats or by deflecting the fixed leading edge.

Hinged Leading Edge (Droop Nose)

In a hinged droop nose the leading edge structure is rigidly deflected by a hinge placed near the front spar [170]. The tight radius curvature on the upper wing surface however causes flow separation. For this reason this concept has only been used for supersonic fighter airplanes where a high leading edge sweep angle triggers a stable vortex on the upper surface eliminating the negative effects of the hinged leading edge.

Fixed Slot

A fixed slot device consists of a slat fixed at a certain position leaving a gap between the slat and the main wing leading edge [170]. This type of high lift systems meets the main requirement of delaying stall at high angles of attack, however the fixed gap causes high drag at cruise condition and therefore it cannot be used on commercial airliners.

(a)   **(b)**

(c)
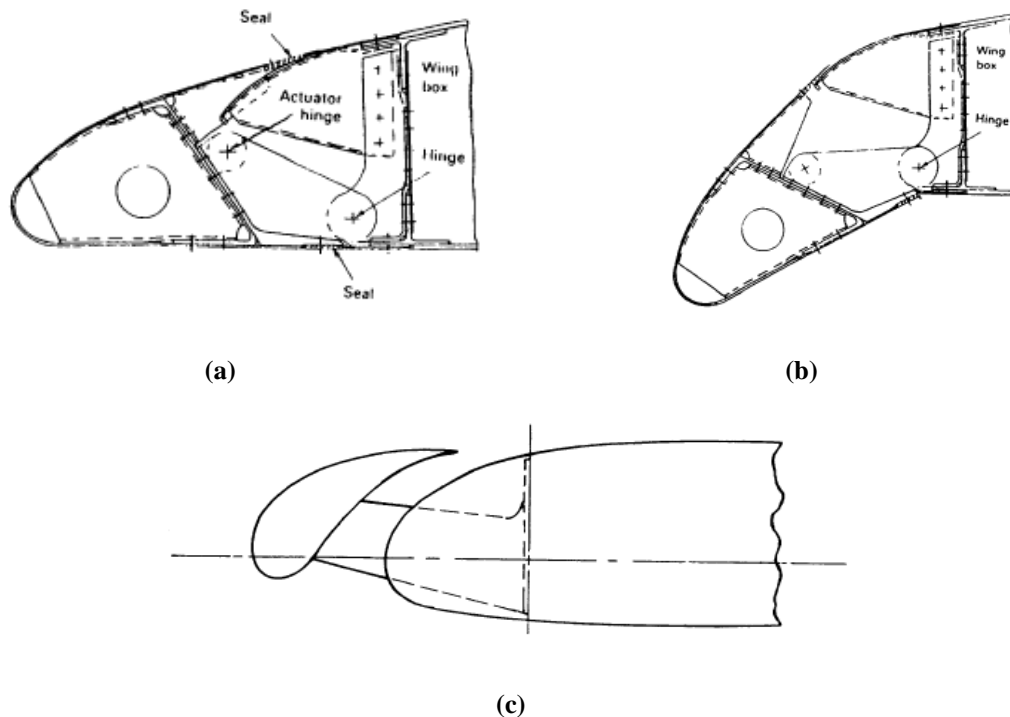
Figure 2.20 (a) Hinged leading edge; (b) Deflected hinged leading edge; (c) Fixed slot [170]

Simple Krueger Flap

The simple Krueger flap consists of a panel on the lower surface of the leading edge. A hinge near the nose curvature, see Figure 2.21 (a), allows the panel to rotate downward and then forward into a position where its forward edge seals against the lower surface of the fixed wing leading edge [170]. This type of Krueger flap is the simplest leading edge device in use on high performance airliners; however its major disadvantage is the inability to vary the angle of attack.

Folding Bull Nose Krueger Flap

The folding bull nose Krueger flap is an improved design of the simple Krueger flap. The folding bull nose is a panel along the Krueger flap length which is hinged to the aft end in the stowed position. The end of the panel, closer to the front spar, is curved and it is connected with a slave linkage that rotates to deploy the bull nose as the main Krueger panel deploys. This type of flap mechanism is more tolerant to changes in angle of attack and therefore the flow on the upper surface of the Krueger panel is attached over a wider angle of attack range.
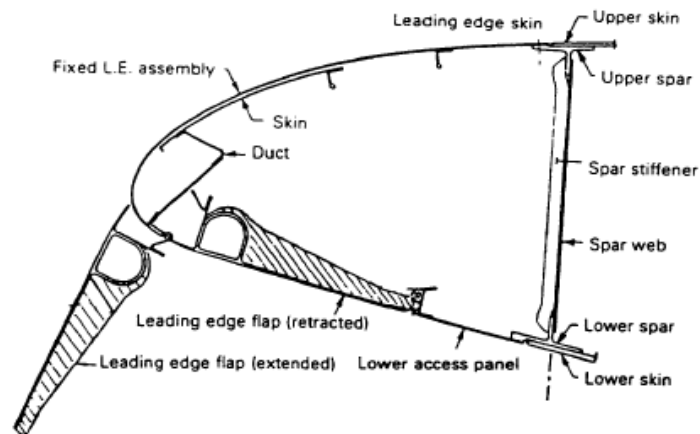
(a)
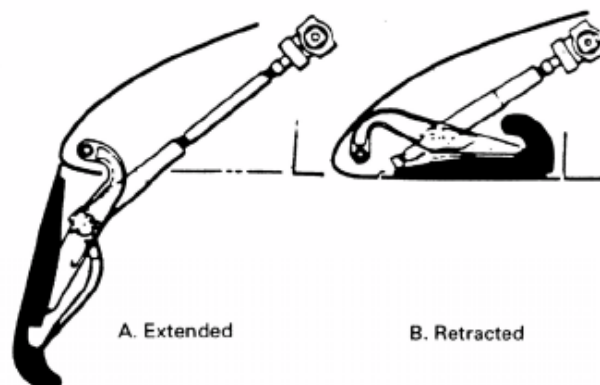
(b)

Figure 2.21: (a) Simple Krueger flap [169 and 170]; (b) Folding bull nose Krueger flap [169]

Variable Camber Krueger Flap

The variable camber (VC) Krueger flap was developed as an attempt to improve the shape of the simple deployed Krueger flap. The VC Krueger flaps uses a flexible skin (stiffened fibre glass) as the main Krueger panel in order to be able to obtain a curved surface when deployed improving considerably the aerodynamic performance [170]. This mechanism is however much more complex compared to the simple Kruger flap device. Furthermore, this system requires twice as many panels as a normal Krueger flap so that the distortion of the fibre glass panels, during the high cruise aerodynamic loads, is avoided. This design is mainly used in the inboard section of commercial aircraft wings.
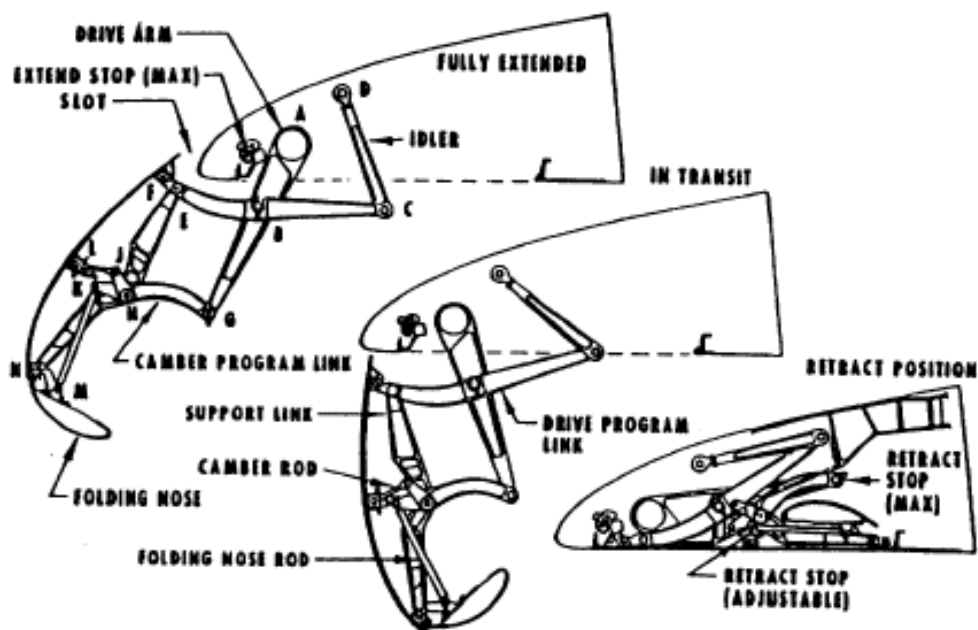
Figure 2.22 Variable camber Krueger flap [170]

2.5.4 Adaptive Leading Edge Devices

The conventional leading edge devices so far reviewed can only be used to increase the high lift performance at landing and takeoff. The increase in lift was achieved over the years by making the mechanisms more complex and therefore heavier. With the new

drive to obtain lighter and simpler structures to reduce drag, fuel consumption and noise, these conventional devices found their limitations. The feasibility of more innovative morphing leading edge devices started to be investigated. Although these type of devices can potentially be used to improve the aerodynamic performance, not only at takeoff and landing but also during cruise, not many of them have been put into practice.

Statkus Variable Camber Leading Edge Mechanism

The leading edge mechanism developed by Statkus used two sets of four bar mechanisms to control the nose camber variation [178]. The first set of four bars controls the horizontal and vertical movement, see Figure 2.23. The second set controls the angular rotation, see Figure 2.23.
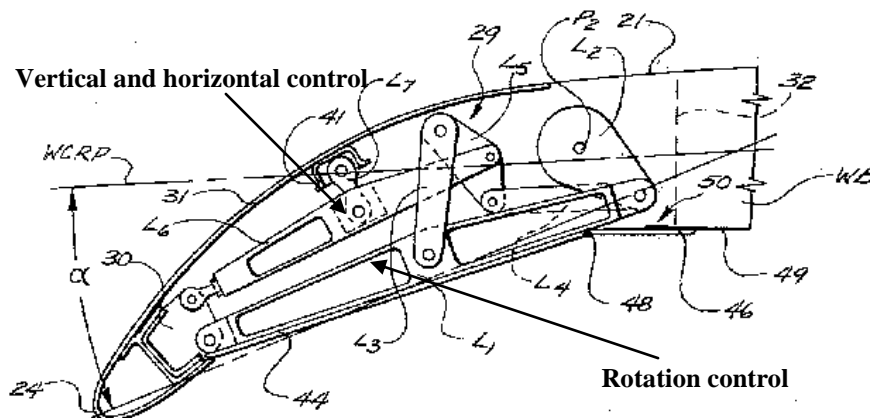
Figure 2.23 Droop nose developed by Statkus [178]

Dornier Droop Nose

The droop nose developed by Dornier [179] presented a concept that allowed both change in camber and change in nose radius. The change in radius during deployment is an effective way to enhance the aerodynamic performance as it controls the pressure suction peak at high angles of attack [180]. A main bar was connected to a pivot point at

the lower end of the front spar. When rotated, this bar pushed a plate on the lower skin deflecting the nose downward. At the same time this bar pushed a section of the upper skin increasing the nose radius, see Figure 2.24. This concept was also used by the German Aerospace Centre (DLR) to develop a seamless gapless leading edge high lift device [179].
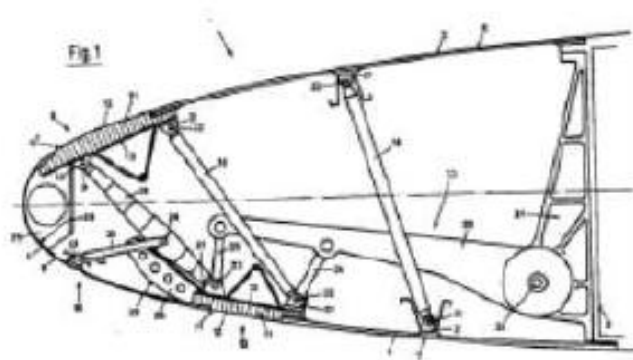
(a)
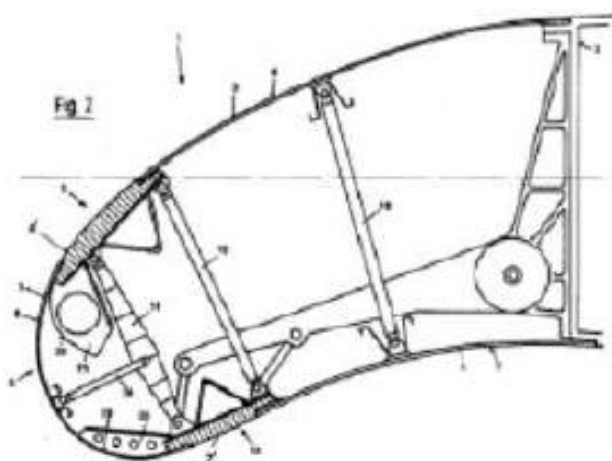
(b)

Figure 2.24 Dornier droop nose mechanism: (a) Neutral position; (b) Deflected position [179]

Airbus Droop Nose

The droop nose device developed for the inboard wing of the A380 allows the nose structure to deflect without any gaps [181]. It has of four hinged arms, two of which are driven by actuators while the other two move passively. Rotary actuators are used to deploy the leading edge device. This mechanism considerably decreased the drag and helps the wing to stall inboard before stalling outboard.
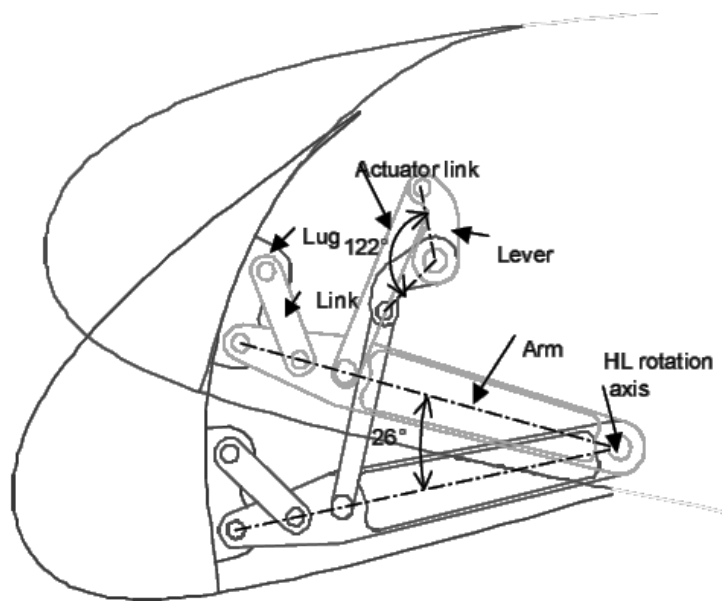
Figure 2.25 Droop nose developed by Airbus [181]

Bent Tube Mechanism

The banana tube mechanism is similar to the eccentric beam concept developed for the DARPA project related to a morphing trailing edge device [172-177]. This mechanism uses a bent beam which is shaped according to the leading edge required deflection [182]. When the beam is rotated the airfoil takes the shape of the tube itself allowing a variable camber, see Figure 2.26.
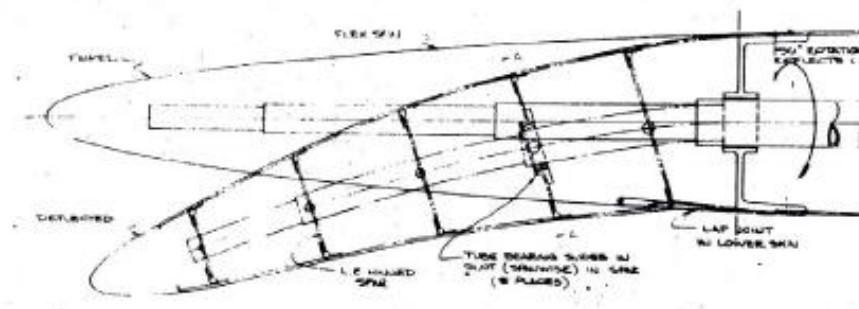
Figure 2.26 Bent tube concept [182]

The majority of current mechanism only allow a morphing deflection with no change in nose radius necessary to enhance the aerodynamic performance. The Dornier droop nose concept allowed this change in nose radius but a simple mechanism was preferred for the current design.

2.6. Morphing Skins

Morphing adaptable structures require much more flexible skins then the conventional ones. Morphing skins are therefore necessary in order to achieve a smooth and continuous surface that simultaneously deforms and carries loads. Two types of flexible materials are reviewed: one that allow change in area and the other that allows change in stiffness.

2.6.1 Materials Allowing Change in Surface Area

There are two main categories of materials which allow a change in surface area: stretchable and deployable structures. Examples of stretchable structures are the auxetic materials and the Hexcel Flex-Core material. The main characteristic of auxetic materials is that they have a negative Poisson's ratio and therefore, they become narrower when they are compressed and they become wider when they are elongated. Other interesting properties of auxetic materials are the high energy absorption, fracture toughness and resistance to indentation. Exploiting these properties in auxetic matrices could lead to composite materials with minimal fibre pull-out failure i.e. failure of the matrix/fibre interface [183].

The Hexel's Flex-Core is a material with cellular structures that can be formed into small radii curvatures without the deformation of the cell walls, loss of mechanical properties or experiencing anti elastic behaviour, see Figure 2.27. This type of material could be covered with a thin skin and be used as a morphing skin solution [183]. These type of materials offer a potential for morphing skins however their technology readiness make them inapplicable for the current study which aims to a achieve a practical solution.
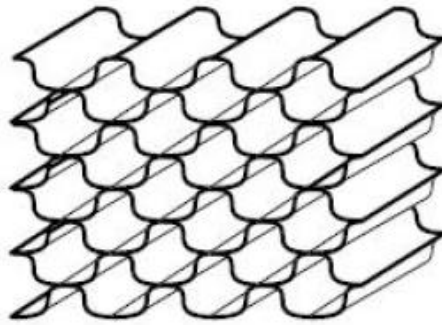
Figure 2.27 Flex-Core cellular structure [183]

2.6.2 Materials Allowing Change in Shape due to Stiffness Tailoring

When composite materials are used, the stiffness of the material can be tailored in such a way to ensure a certain change in the structural shape. For example in extreme anisotropic materials, the fibres are orientated so that a desired stiffness is obtained in the required direction. Elastomer matrix could also be used in the manufacturing process of a composite prepreg (using glass fibres), in order to tailor the stiffness of the material. Segmented structures and in particular fibre steering are used to obtain a flexible skin (like fish scales) which allow a certain type and direction of deformation when a load is applied to the structure [183], see Figure 2.28.
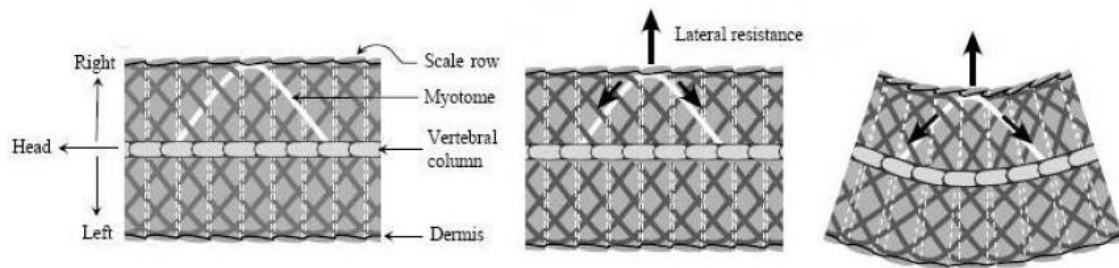
Figure 2.28 Example of segmented structure [183]

A multilayered skin is made of multiple thin layers of conventional material that are not bonded together. In this configuration the transverse shear stresses are not transmitted from one layer to another and therefore the bending stiffness is reduced compared to that of a monolithic skin. This allows a large bending curvature without affecting the skin load carrying capabilities, although reinforcements may be needed to compensate the reduction in bending stiffness.

The use of shape memory alloys also allows large structural deformation thanks to its capability of changing the stiffness properties at different conditions. Certain shape memory polymers can elongate up to 1100% and their mechanical properties can be varied over a very wide range.

These solutions allow a relatively large skin deformation however their stiffness is too low to withstand the high aerodynamic loads to which a large commercial aircraft is subject to.

2.7. Active Actuation and Smart Materials

A vast number of actuating systems have been developed and tested for the actuation of adaptive wings and these include strain actuators and smart material actuators [184-186]. It has in fact been demonstrated that distributing strain actuators along the whole wing span it is possible to induce relatively large bending and twisting deformations

[187]. The most commonly used smart material for actuating systems are the shape memory alloys (SMA) [188] and piezoelectric materials [187, 189-192].

2.7.1 Piezoelectric Materials

Piezoelectricity is the ability of certain crystals and ceramics to produce voltage when strain is applied (direct effect) and undergo deformation when an electric field is applied across them (converse effect). Piezoelectric materials can therefore be used as both sensors and actuators. The equations governing the direct and indirect effects can be found in reference [193]. The most widely used piezoceramic and piezopolymer materials are lead zirconate-titanates (PZT) and plyvinylide fluorides (PVSF's) [193].

When manufactured, a piezoelectric material has electric dipoles arranged in random directions. The responses of these dipoles to an externally applied electric field would tend to cancel one another. Therefore, in order to obtain a useful macroscopic response, the dipoles are permanently aligned with one another through a process called poling. A piezoelectric material has a characteristic Curie temperature. When it is heated above this temperature, the dipoles can change their orientation in the solid phase material. In poling, the material is heated above its Curie temperature and a strong electric field is applied. The direction of this field is the polarisation direction and the dipoles shift into alignment with it. The material is then cooled below its Curie temperature while the poling field is maintained, with the results that the alignment of the dipoles is permanently fixed. The material is then said to be poled.

The working temperature of the PZT is usually well below its Curie temperature. If the material is heated above its Curie temperature when no electric field is applied, the dipoles will revert to random orientations. Even at lower temperature, the application of too strong electric field can cause the dipoles to shift out of the preferred alignment established during poling. Once depoled, the piezoelectric material loses the properties of dimensional response to an electric field. Table 2.1 summarise the advantages and disadvantages of piezoelectrics.

Table 2.1 Advantages and disadvantages of piezoelectrics [194]

Advantages	Disadvantages
• Relatively insensitive to temperature • Linear response at low excitation levels • Lightweight and flexibility as sensors and actuators in a large variety of applications; • Broadband frequency response.	• Significant hysteresis under large electric field • Brittleness and small tensile strength • Piezoelectric effect generated through poling can decay, leading to aging effects and performance degradation.

Piezoelectric are currently used for small morphing applications, however due to the effect generate by the poling decay and the small deflection achieved they are not yet suitable for a commercial aircraft application.

2.7.2 Shape Memory Alloys

A shape memory alloy (SMA) has the unique property of "remembering" a certain deformed shape and to recover that shape at higher temperatures. The shape that a SMA memorises can be assigned through annealing. At room temperature the SMA is in a martensite phase and its undeformed crystal structure is twinned. Application of extensional stress at this condition causes the crystals to detwinning and hence to plastic deformation of the material. Through an application of heat the plastic deformation is recovered and the material is in austenite phase [193].

Figure 2.29 shows the shape memory effect for one way and two way memory. With two-way memory, the metal "remembers" two shapes, each of which can be recovered at a different temperature.
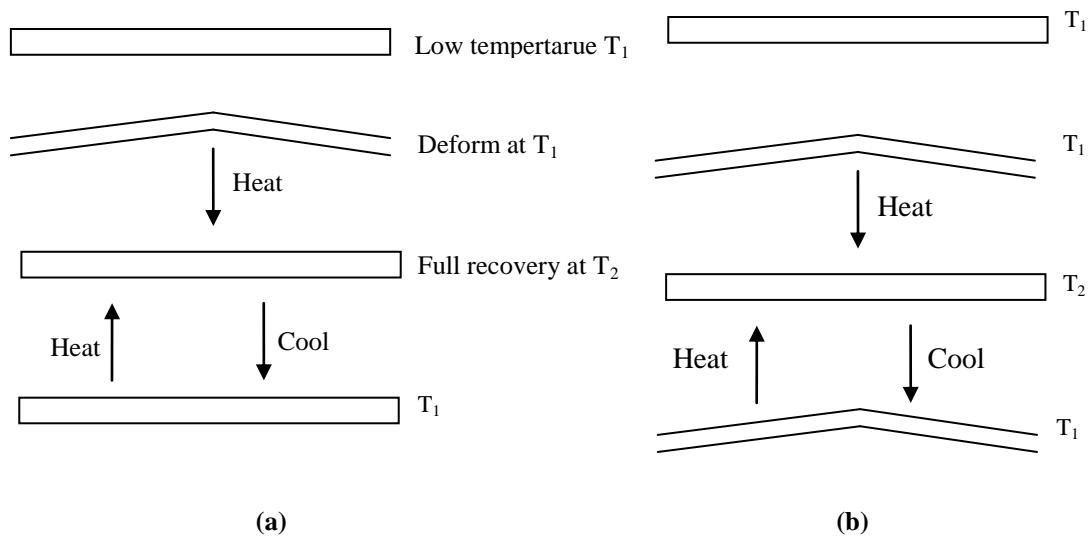
Figure 2.29 Shape memory alloy effect [194]: (a) One way; (b) Two ways

Table 2.2 summarises the advantages and disadvantages of shape memory alloys.

Table 2.2 Advantages and disadvantages of shape memory alloys [194]

Advantages	Disadvantages
• Small size, suitable for internal material-based mechanisms for single unit actuators	• Slow response time
	• Nonlinear hysteresis and thermomechanical response and therefore difficult to model
• Excellent cycling performance in repeated loading	• High energy requirements for actuation
• Flexible actuation signal	• Limited to a certain thermal range

Shape memory alloys thermal effect are currently too unpredictable and due to the limited thermal range and small deflection achieved they are not yet suitable for a commercial aircraft application, although their potential has been proved on micro air vehicles.

Chapter 3

3. Composite Structures Theoretical Background and Analysis Tools

Composite materials are made of continuous or discontinuous fibres embedded in a matrix. The directional nature of these fibres in the ply, introduces a directional dependence to the composite layer properties. Materials with direction dependent properties are called anisotropic materials. A special case of anisotropy is the existence of two perpendicular plane of symmetry in the material properties. These materials are classified as orthotropic. The mechanical behaviour of composite materials differs from that of isotropic materials, since two directions must be considered for the strength and stiffness properties.   This chapter describes how orthotropic composite structural components can be studied using classical laminate (Section 3.1) and thin walled structures theories (Section 3.2). Some computer programs developed to carry out preliminary structural design using these principles are also described. Finally the use of the finite element model to analyse more complex composite structures is presented (Section 3.3).

3.1. Structural Analysis of Composite Aircraft Components

A particular characteristic of composite materials is that stiffness and strength properties depend on the direction of the fibres in the laminate. The behaviour of these materials,

when loaded, is therefore different from isotropic materials and many more parameters must be considered to predict them. This section presents a brief insight on the classical lamination theory to calculate the stiffness properties of composite orthotropic laminates. Three computer programs, based on this theory, developed to calculate laminate stresses and strains and to carry out buckling analysis, are also described.

3.1.1. Stiffness of Orthotropic Laminates Using the Classical Lamination Theory [195]

For unidirectional fibre reinforced lamina, there are two perpendicular planes of symmetry that define the principal axes of the material properties. These principal axes correspond to the direction of the fibres and a direction transverse to the fibres, and are denoted by the subscripts 1and 2 respectively. This coordinate system is a local system associated with the single lamina. A global coordinate system, attached to a fixed reference point, is instead used when the whole laminate is considered, see Figure 3.1.
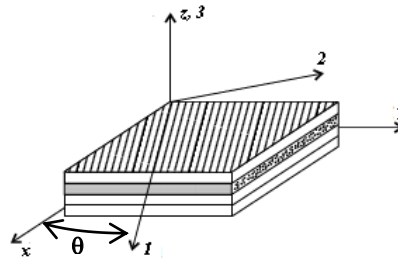
Figure 3.1 Global and local coordinate system

For a thin orthotropic ply, with no applied forces in the out of plane direction, the stress-strain relationship in the principal material direction is defined as:

$$\begin{Bmatrix} \sigma_1 \\ \sigma_2 \\ \tau_{12} \end{Bmatrix} = \begin{bmatrix} Q_{11} & Q_{12} & 0 \\ Q_{11} & Q_{22} & 0 \\ 0 & 0 & Q_{66} \end{bmatrix} \begin{Bmatrix} \varepsilon_1 \\ \varepsilon_2 \\ \gamma_{12} \end{Bmatrix}$$

(3-1)

where the Q_{ij}'s are the reduced stiffness and are given in terms of the elastic moduli in the 1 and 2 direction, E_1 and E_2, the shear modulus in the 1-2 plane G_{12}, and the major Poisson's ratio v_{12}.

$$Q_{11} = \frac{E_1}{1 - v_{12}v_{21}}, \qquad Q_{22} = \frac{E_2}{1 - v_{12}v_{21}}$$

$$Q_{12} = \frac{v_{12}E_2}{1 - v_{12}v_{21}} = \frac{v_{21}E_1}{1 - v_{12}v_{21}}, \qquad Q_{66} = G_{12}$$

(3-2)

The major Poisson's ratio is defined as the negative ratio of the strain in the 2 direction, ε_2, to the strain in the 1 direction, ε_1. The minor Poisson's ratio is instead defined as the inverse of the major Poisson's ratio and it is related to the elastic properties through:

$$v_{21} = \frac{E_2}{E_1}v_{12}$$

(3-3)

The stresses and strains expressed in the local coordinate system can be transformed to the reference system by using the following relationship:

$$\begin{Bmatrix} \sigma_1 \\ \sigma_2 \\ \tau_{12} \end{Bmatrix} = \mathbf{T} \begin{Bmatrix} \sigma_x \\ \sigma_y \\ \tau_{xy} \end{Bmatrix} \text{ and } \begin{Bmatrix} \varepsilon_1 \\ \varepsilon_2 \\ \varepsilon_{12} \end{Bmatrix} = \mathbf{T} \begin{Bmatrix} \varepsilon_x \\ \varepsilon_y \\ \varepsilon_{xy} \end{Bmatrix}$$

(3-4)

where ε_{xy} and ε_{12} are the tensor shear strain, which correspond to half of the engineering shear strains, γ_{xy} and γ_{12}, and the transformation matrix $\mathbf{T}$ is expressed in terms of the sine and cosine of the angle between the axis 1 and x, see Figure 3.1.

$$\mathbf{T} = \begin{bmatrix} m^2 & n^2 & 2mn \\ n^2 & m^2 & -2mn \\ -mn & mn & m^2 - n^2 \end{bmatrix}, m = \cos\theta \text{ and } n = \sin\theta$$

(3-5)

In order to convert the strain transformation relation from tensor strain to engineering strain, the transformation matrix is pre- and post-multiplied by a matrix $\mathbf{R}$ and the inverse of $\mathbf{R}$, where

$$\begin{Bmatrix} \varepsilon_x \\ \varepsilon_y \\ \gamma_{xy} \end{Bmatrix} = \mathbf{R} \begin{Bmatrix} \varepsilon_x \\ \varepsilon_y \\ \varepsilon_{xy} \end{Bmatrix}, \mathbf{R} = \begin{bmatrix} 1 & 0 & 0 \\ 0 & 1 & 0 \\ 0 & 0 & 2 \end{bmatrix} \tag{3-6}$$

The transformation matrix for the engineering strains is therefore given by

$$\mathbf{T}_e = \begin{bmatrix} m^2 & n^2 & mn \\ n^2 & m^2 & -mn \\ -2mn & 2mn & m^2 - n^2 \end{bmatrix} \tag{3-7}$$

Substituting the transformation matrix $\mathbf{T}_e$ for the stresses and engineering strain into Eq.

(3-1) the stress-strain relationship in the global coordinate system is expressed as

$$\begin{Bmatrix} \sigma_x \\ \sigma_y \\ \tau_{xy} \end{Bmatrix} = \mathbf{T}^{-1}\mathbf{Q}\mathbf{R}\mathbf{T}\mathbf{R}^{-1} \begin{Bmatrix} \varepsilon_x \\ \varepsilon_y \\ \gamma_{xy} \end{Bmatrix} = \begin{bmatrix} \overline{Q}_{11} & \overline{Q}_{12} & \overline{Q}_{16} \\ \overline{Q}_{12} & \overline{Q}_{22} & \overline{Q}_{26} \\ \overline{Q}_{16} & \overline{Q}_{21} & \overline{Q}_{66} \end{bmatrix} \begin{Bmatrix} \varepsilon_x \\ \varepsilon_y \\ \gamma_{xy} \end{Bmatrix} \tag{3-8}$$

In a laminate with N orthotropic layers perfectly bonded together with an infinitely thin bond line and continuous in-plane deformations across the bond line the strain distribution can be defined as

$$\begin{Bmatrix} \sigma_x \\ \sigma_y \\ \tau_{xy} \end{Bmatrix} = \begin{Bmatrix} \varepsilon_x^0 \\ \varepsilon_y^0 \\ \gamma_{xy}^0 \end{Bmatrix} + z \begin{Bmatrix} \kappa_x \\ \kappa_y \\ \kappa_{xy} \end{Bmatrix} \tag{3-9}$$

where the superscript '*0*' represents the mid plane strain, and κ is the curvature of the laminate. The stresses in the kth ply can be expressed in terms of the reduced stiffness of that particular ply by substituting Eq. (3-9) into the stress-strain relationship Eq. (3-8),

$$\begin{Bmatrix} \sigma_x \\ \sigma_y \\ \tau_{xy} \end{Bmatrix}_{(k)} = \begin{bmatrix} \overline{Q}_{11} & \overline{Q}_{12} & \overline{Q}_{16} \\ \overline{Q}_{12} & \overline{Q}_{22} & \overline{Q}_{26} \\ \overline{Q}_{16} & \overline{Q}_{21} & \overline{Q}_{66} \end{bmatrix}_{(k)} \left(\begin{Bmatrix} \varepsilon_x^0 \\ \varepsilon_y^0 \\ \gamma_{xy}^0 \end{Bmatrix} + z \begin{Bmatrix} \kappa_x \\ \kappa_y \\ \kappa_{xy} \end{Bmatrix} \right) \tag{3-10}$$

The laminate in-plane forces and moments per unit width applied to a point in the laminate are obtained by through thickness integration of the stresses in each ply

$$\begin{Bmatrix} N_x \\ N_y \\ N_{xy} \end{Bmatrix} = \int_{-h/2}^{h/2} \begin{Bmatrix} \sigma_x \\ \sigma_y \\ \tau_{xy} \end{Bmatrix}_{(k)} dz, \qquad \begin{Bmatrix} M_x \\ M_y \\ M_{xy} \end{Bmatrix} = \int_{-h/2}^{h/2} \begin{Bmatrix} \sigma_x \\ \sigma_y \\ \tau_{xy} \end{Bmatrix}_{(k)} z dz \qquad (3\text{-}11)$$

Substituting the stress-strain relationship of Eq. (**3-10**) into Eq. (**3-11**) the following constitutive relation for the laminate can be defined

$$\begin{Bmatrix} N_x \\ N_y \\ N_{xy} \\ M_x \\ M_y \\ M_{xy} \end{Bmatrix} = \begin{bmatrix} \begin{bmatrix} A_{11} & A_{12} & A_{16} \\ A_{12} & A_{22} & A_{26} \\ A_{16} & A_{26} & A_{66} \end{bmatrix} & \begin{bmatrix} B_{11} & B_{12} & B_{16} \\ B_{12} & B_{22} & B_{26} \\ B_{16} & B_{26} & B_{66} \end{bmatrix} \\ \begin{bmatrix} B_{11} & B_{12} & B_{16} \\ B_{12} & B_{22} & B_{26} \\ B_{16} & B_{26} & B_{66} \end{bmatrix} & \begin{bmatrix} D_{11} & D_{12} & D_{16} \\ D_{12} & D_{22} & D_{26} \\ D_{16} & D_{26} & D_{66} \end{bmatrix} \end{bmatrix} \begin{Bmatrix} \varepsilon_x^0 \\ \varepsilon_y^0 \\ \gamma_{xy}^0 \\ \kappa_x \\ \kappa_y \\ \kappa_{xy} \end{Bmatrix} \qquad (3\text{-}12)$$

where [A], [B], and [D] matrices are the laminate stiffness matrix and are defined in terms of the ply stiffness as

$$A_{ij} = \sum_{k=1}^{N} \left(\overline{Q}_{ij} \right)_{(k)} (z_k - z_{k-1})$$

$$B_{ij} = \frac{1}{2} \sum_{k=1}^{N} \left(\overline{Q}_{ij} \right)_{(k)} (z_k^2 - z_{k-1}^2) \qquad (3\text{-}13)$$

$$D_{ij} = \frac{1}{3} \sum_{k=1}^{N} \left(\overline{Q}_{ij} \right)_{(k)} (z_k^3 - z_{k-1}^3)$$

The matrices [A] and [D] represent the laminate membrane and bending stiffness respectively while the matrix [B] represents the coupling stiffness. These three matrices therefore, determine the stiffness of a laminate in different directions and describe the response of a laminate to in-plane forces and moments.

3.1.2. Composite Laminate Stiffness Properties Calculation Using CoALA

CoALA is a Cranfield University in house FORTRAN program developed to perform composite laminate analysis based on the classical lamination theory described above. This program offers a quick method to calculate the laminate properties of both symmetric and unsymmetrical composite orthotropic materials. The input file contains the ply mechanical properties, the ply configuration, the layup configuration and loading characteristics. The program uses these input data to compute the following laminate properties:

- Laminate stiffness matrices [A], [B] and [D]
- Equivalent elastic constants in the membrane and bending modes
- Ply residual and resultant strains in the local material local coordinate system
- Ply residual and resultant stress in the local material local coordinate system
- Ply failure index and probable cause of ply in-plane mode of failure (fibre direction, transverse direction, shear)

This program was used in the current research study to calculate laminate stiffness properties and equivalent elastic constants.

3.1.3. Composite Laminated Plates with a Circular Cutout

Aircraft structural component often contain cutouts which can cause severe stress concentrations. Classical methods to calculate the stress around a circular cutout in a composite laminate plate is available from textbooks [195], however in application to the present research work the ESDUpac A8501 was used [196]. This ESDUpac is a FORTRAN program which calculates the elastic stress and strain distribution around the perimeter of a circular cutout in a homogeneous orthotropic flat plate subject to any combination of in-plane loads, as shown in Figure 3.2. One of the requirements to use this program is that the cutout must be large in comparison to the plate thickness i.e. for diameters greater than five times the laminate thickness.
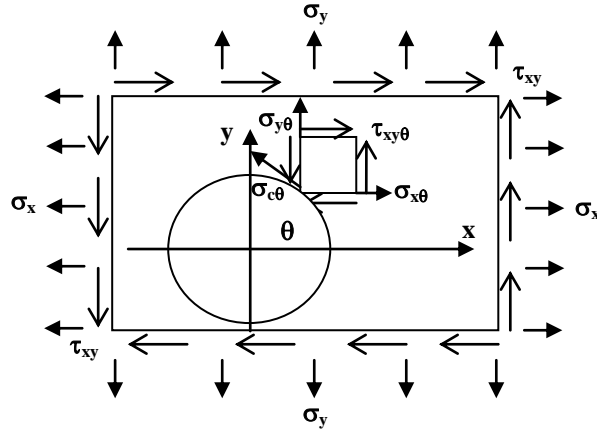
Figure 3.2 Direct stress and circumferential stresses around the circular cutout [196]

The circumferential stress around a cutout in an orthotropic plate subject to biaxial and shear loading, is calculated as [196]

$$\sigma_{c\theta} = \frac{(\sigma_x + \sigma_y)\mu - \sigma_y\xi + \tau_x\lambda}{(1 + \beta_1^2 - 2\beta_1\cos 2\theta)(1 + \beta_2^2 - 2\beta_2\cos 2\theta)} \tag{3-14}$$

where

$$\mu = (1 + \beta_1)(1 + \beta_2)(1 + \beta_1 + \beta_2 - \beta_1\beta_2 - 2\cos\theta)$$

$$\xi = 4\{\beta_1 + \beta_2 - (1 + \beta_1\beta_2)\cos 2\theta\} \tag{3-15}$$

$$\lambda = 4(\beta_1\beta_2 - 1)\sin 2\theta$$

and

$$\beta_1 = (\alpha - 1)/(\alpha + 1)$$
$$\tag{3-16}$$
$$\beta_2 = (\delta - 1)/(\delta + 1)$$

The terms α and δ are expressions in terms of the laminate equivalent elastic constants:

$$\alpha = \left[\left\{ \frac{E_y}{2G_{xy}} - v_{yx} \right\} + \left[\left\{ \frac{E_y}{2G_{xy}} - v_{yx} \right\}^2 - \frac{E_y}{E_x} \right]^{\frac{1}{2}} \right]^{\frac{1}{2}}$$

$$\delta = \left[\left\{ \frac{E_y}{2G_{xy}} - v_{yx} \right\} - \left[\left\{ \frac{E_y}{2G_{xy}} - v_{yx} \right\}^2 - \frac{E_y}{E_x} \right]^{\frac{1}{2}} \right]^{\frac{1}{2}}$$

(3-17)

Using transformation equations the direct stresses and shear stresses in the *x*- and *y*-directions can be defined in terms of the circumferential stress as

$$\sigma_{x\theta} = \sigma_{c\theta} \sin^2 \theta$$
$$\sigma_{y\theta} = \sigma_{c\theta} \cos^2 \theta$$
$$\tau_{xy\theta} = \sigma_{c\theta} \sin \theta \cos \theta$$

(3-18)

Hence, the *x*- and *y*- strains around the cutout edges are

$$\varepsilon_{x\theta} = \frac{1}{E_x} \left(\sigma_{x\theta} - \sigma_{y\theta} v_{xy} \right)$$

$$\varepsilon_{y\theta} = \frac{1}{E_x} \left(\sigma_{y\theta} - \sigma_{x\theta} v_{yx} \right)$$

$$\gamma_{xy\theta} = \frac{\tau_{xy\theta}}{G_{xy}}$$

(3-19)

The theory used for this program is only valid for infinite plates; however the results obtained can be considered accurate for plates that have a boundary no closer than 1.5 cutout diameter away from the hole perimeter [196]. The effect of interlaminar stresses and load shedding near the edges of the cutout were not included in the program, nevertheless the stresses and strains obtained proved to be a realistic approximation to assess the strength of various lay-ups with regards to in-plane failure of fibres and/or matrix. For these reasons this readily available program was considered an appropriate

analysis tool to study the effect of the presence of a circular cutout in composite structural components.

3.1.4. Buckling of Stiffened Panel Using the ESDUpac A0301

Thin composite panels such as wing skin covers are often subject to buckling concern. Stiffeners of various cross-sections are therefore used to improve the stability of these structures. The buckling analysis methods of simple composite panels can be found in textbooks [195], and they are developed using the laminated composite theories, to calculate the structural stiffness properties, and plates and shells theories to predict the buckling loads. These methods however are not suitable to assess the buckling stability of stiffened panels.

The ESDUpac A0301 is a computer program which calculates initial compressive buckling loads for long flat composite stiffened panels [197]. The method on which the program is based is the finite strip method, which is suited to analyse prismatic structures that show periodic deformation patterns under loading. The major input of the formulation of the buckling problem is the stiffness of the strip elements of the panel. This in fact determines the relationship between the stresses and strains when the structure is loaded. The other input required is the geometry of the panel and of the stiffeners. The program then calculates the buckling load, stress and strain. Because of its relatively simple and quick running procedure this program was considered the most suitable tool to carry out buckling analysis of composite stiffness panel structures in the preliminary design stages.

3.2. Composite Thin-Walled Structural Analysis [198]

An aircraft can be considered as an assembly of panels ranging from open to multicell closed sections subject to bending, shear, torsional and axial loads. Because the thickness of these panels is small compared to the cross sectional dimensions, these structures are often treated as thin-walled beams. Exploiting the thin-walled nature of aircraft structures simplifying assumption can be made when calculating stresses and

displacements. The stress across the thickness of the plates can in fact be considered constant and furthermore the squares and higher order power of the thickness term can be neglected when computing the sectional properties. A detailed analysis of open and closed isotropic thin-walled beams under various types of loadings can be found in [198]. In this section however composite thin-walled structures are considered and the methods to analyse the behaviour of open and closed section beams under bending and torsion are shown. Two computer programs developed to calculate the stiffness properties, stresses and strains of composite closed single and double cell thin-walled beams are also presented.

3.2.1. Bending of Open or Closed Thin-Walled Section Beams [198]

The stresses due to the bending moments M_X and M_Y are calculated in the same manner for both closed and open sections. These moments are taken to be positive when each induces a tensile stress in the positive *XY* quadrant of the *GXY* axis system. *G* is the centroid of the section and passes through the neutral axis of the section *NA*. The neutral axis is inclined at an angle α with respect to the *X*-axis. Each laminate *x*-axis is parallel to the global *Z*-axis.
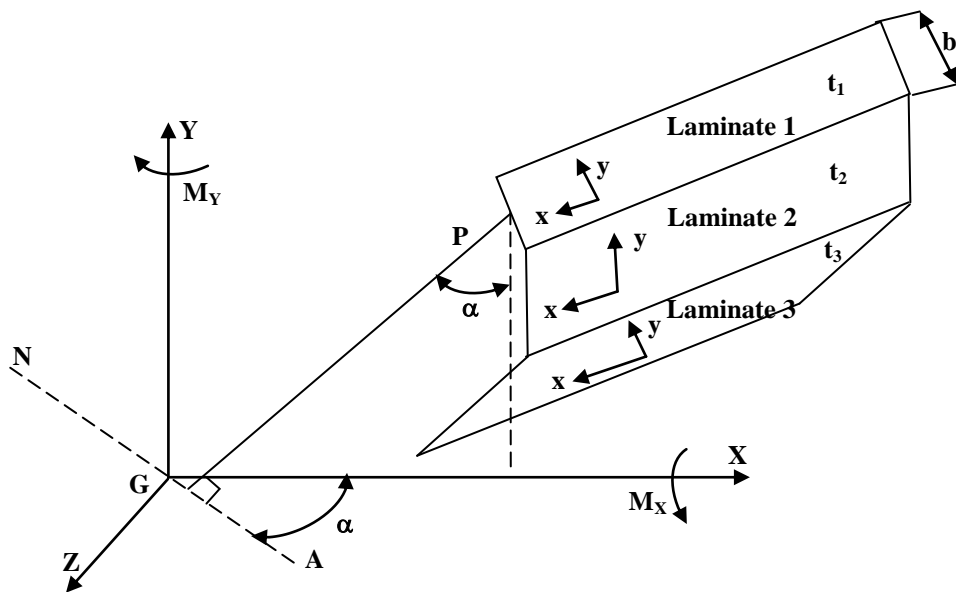
Figure 3.3 Global and local coordinate system for an arbitrary section under bending loads

The analysis is carried out by first considering each panel separately, for example the Laminate 1 with thickness t_1 and a small element of area δA is selected, see Figure 3.3. This area is at a distance P from the neutral axis and it is defined as

$$P = X \sin \alpha + Y \cos \alpha \tag{3-20}$$

The direct stress σ_z, on the element area δA, at a distance P from the neutral axis is given by the expression

$$\sigma_Z = E_Z \frac{P}{R} \tag{3-21}$$

where E_Z is the elastic modulus in the global Z-direction and R is the radius of the curvature at the section. Since the Z-axis and laminate x-axis are parallel the stresses and the elastic modulus in the global Z-direction can be defined as

$$\sigma_Z = \sigma_x, \qquad E_Z = E_x \tag{3-22}$$

Substituting the expression for P from Eq. (3-20) into Eq. (3-21) the following relationship is obtained

$$\sigma_Z = \frac{E_Z}{R} (X \sin \theta + Y \cos \theta) \tag{3-23}$$

The resultant moments M_X and M_Y are given by the expressions

$$M_X = \int_A \sigma_Z Y \, dA$$

$$M_Y = \int_A \sigma_Z X \, dA \tag{3-24}$$

Where A is the area integration limits for the panel considered. Substituting Eq. (3-23) into Eq. (3-24) the expression for the moment forces can be rewritten as

$$M_X = \int_A \frac{E_Z}{R}(X \sin \alpha + Y \cos \alpha)Y \, dA$$

$$M_Y = \int_A \frac{E_Z}{R}(X \sin \alpha + Y \cos \alpha)X \, dA$$

(3-25)

or by expanding

$$M_X = \frac{\sin \alpha}{R} E_Z \int_A XY \, dA + \frac{\cos \alpha}{R} E_Z \int_A Y^2 \, dA$$

$$M_Y = \frac{\sin \alpha}{R} E_Z \int_A X^2 \, dA + \frac{\cos \alpha}{R} E_Z \int_A XY \, dA$$

(3-26)

However the integral terms are by definition the cross sectional properties of the beam

$$\int_A XY dA = I_{XY}$$

$$\int_A Y^2 dA = I_{XX}$$

$$\int_A X^2 dA = I_{YY}$$

(3-27)

Eq. (3-26) therefore becomes

$$M_X = \frac{\sin \alpha}{R} E_Z I_{XY} + \frac{\cos \alpha}{R} E_Z I_{XX}$$

$$M_Y = \frac{\sin \alpha}{R} E_Z I_{YY} + \frac{\cos \alpha}{R} E_Z I_{XY}$$

(3-28)

Remembering that $E_Z = E_x$ and that E_Z is likely to vary from each laminate, the cross sectional properties can be redefined to include the effective elastic modulus in the member Z-direction as

$$I'_{XY} = E_Z I_{XY}$$

$$I'_{XX} = E_Z I_{XX} \tag{3-29}$$

$$I'_{YY} = E_Z I_{YY}$$

Substituting Eq. (3-29) into Eq. (3-28) the expressions for bending moments become

$$M_X = \frac{\sin \alpha}{R} I'_{XY} + \frac{\cos \alpha}{R} I'_{XX}$$

$$M_Y = \frac{\sin \alpha}{R} I'_{YY} + \frac{\cos \alpha}{R} I'_{XY} \tag{3-30}$$

Solving the two expressions in Eq. (3-30) simultaneously it is obtained that

$$\frac{\sin \alpha}{R} = \frac{M_Y - M_X I'_{XY}/I'_{XX}}{I'_{YY}\left(1 - I'_{XY}{}^2/I'_{XX}I'_{YY}\right)} = \frac{M'_Y}{I'_{YY}}$$

$$\frac{\cos \alpha}{R} = \frac{M_X - M_Y I'_{XY}/I'_{YY}}{I'_{XX}\left(1 - I'_{XY}{}^2/I'_{XX}I'_{YY}\right)} = \frac{M'_X}{I'_{XX}} \tag{3-31}$$

where

$$M'_Y = \frac{M_Y - M_X I'_{XY}/I'_{XX}}{\left(1 - I'_{XY}{}^2/I'_{XX}I'_{YY}\right)}$$

$$M'_X = \frac{M_X - M_Y I'_{XY}/I'_{YY}}{\left(1 - I'_{XY}{}^2/I'_{XX}I'_{YY}\right)}$$

Substituting Eq. (3-31) into Eq. (3-23) the following expression for stress is obtained

$$\sigma_Z = E_Z \left(\frac{M'_Y}{I'_{YY}} X + \frac{M'_X}{I'_{XX}} Y \right) \tag{3-32}$$

σ_Z is therefore the normal stress acting on the Laminate 1 in the beam Z-direction due to the applied moments M_X and M_Y. The axial force intensity on the Laminate 1 is given by

$$N_x = \sigma_x t \tag{3-33}$$

where t is the laminate thickness.

When all the n laminates of the section are considered the sectional properties become

$$I'_{XY} = \sum_{i=1}^{n} (E_Z I_{XY})_i$$

$$I'_{XX} = \sum_{i=1}^{n} (E_Z I_{XX})_i \tag{3-34}$$

$$I'_{YY} = \sum_{i=1}^{n} (E_Z I_{YY})_i$$

The direct stresses at a point in the laminate due to bending moments can then be obtained using Eq. (3-32) by substituting the value of E_Z of the considered laminate.

3.2.2. Shear of Open and Closed Thin-Walled Section Beams [198]

The shear stresses around the cross section of both open and closed sections, due to applied shear forced, are defined in terms of the shear flow q. The shear forces S_X and S_Y are positive when they act in the positive X- and Y- directions respectively. It is also assumed that the shear forces are applied through the shear centre R, so that no twist is generated. The shear flow is in this case calculated for an arbitrary section made of an assembly of flat laminated plates arranged so that each laminate x- axis is parallel to the section global Z-axis, as shown in Figure 3.4.
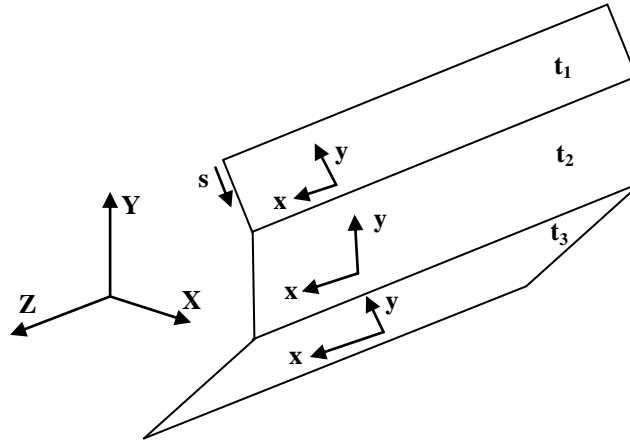
Figure 3.4 Global and local coordinate system of an arbitrary section under shear loading
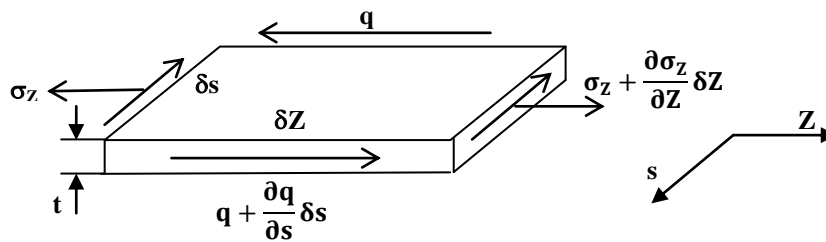
Figure 3.5 Shear and direct stresses due to applied shear load

By taking the stress condition at a point on small wall section of a single laminate, the equilibrium state can be described as

$$\frac{\partial q}{\partial s} + t\frac{\partial \sigma_Z}{\partial Z} = 0 \tag{3-35}$$

The direct stress σ_Z is given by Eq. (3-32) and by substituting it into Eq. (3-35) the following is obtained

$$\frac{\partial q}{\partial s} = -E_Z\left(\frac{M'_X}{\partial Z}\frac{tY}{I'_{XX}} + \frac{M'_Y}{\partial Z}\frac{tX}{I'_{YY}}\right) \tag{3-36}$$

where $M'_X = \frac{M_X - M_Y I'_{XY}/I'_{YY}}{\left(1 - I'_{XY}{}^2/I'_{XX}I'_{YY}\right)}$ and therefore differentiating with respect to Z

$$\frac{\partial M'_X}{\partial Z} = \frac{\dfrac{\partial M'_X}{\partial Z} - \dfrac{\partial M'_Y}{\partial Z}\dfrac{I'_{XY}}{I'_{YY}}}{\left(1 - I'_{XY}{}^2/I'_{XX}I'_{YY}\right)}$$

(3-37)

However from the bending theory [198]

$$\frac{\partial M_X}{\partial Z} = S_Y$$

$$\frac{\partial M_Y}{\partial Z} = S_X$$

(3-38)

and thus

$$\frac{\partial M'_X}{\partial Z} = \frac{S_Y - S_X I'_{XY}/I'_{YY}}{\left(1 - I'_{XY}{}^2/I'_{XX}I'_{YY}\right)} = S'_Y$$

(3-39)

Similarly

$$\frac{\partial M'_Y}{\partial Z} = S'_X$$

(3-40)

Hence Eq. (3-36) can be rewritten as

$$\frac{\partial q}{\partial s} = -E_Z\left(\frac{S'_Y}{I'_{XX}}tY + \frac{S'_X}{I'_{YY}}tX\right)$$

(3-41)

Integrating Eq. (3-41) with respect to s from the origin $s = 0$ to any point s on Laminate 1 the shear flow q becomes

$$q_s = -E_Z\left(\frac{S'_Y}{I'_{XX}}\int_0^s tY\,ds + \frac{S'_X}{I'_{YY}}\int_0^s tX\,ds\right) + q_{s=0}$$

(3-42)

Eq.(3-42) can be used to obtain the shear flow distribution around each laminate in both open and closed thin-walled sections. The method to determine q_s is different for open and closed sections, therefore they are considered separately.

Open Section

For an open section, the shear flow is zero a t the open edge of the beam. Therefore if the origin $s = 0$ is taken at the open edge $q_{s=0} = 0$ and Eq. (3-42) becomes

$$q_s = -E_Z \left(\frac{S'_Y}{I'_{XX}} \int_0^s tY \, ds + \frac{S'_X}{I'_{YY}} \int_0^s tX \, ds \right)$$

(3-43)

Single Cell Closed Section

In a closed section the complete shear flow consists of the sum of the shear flow q for and open section and $q_{s=0}$. The shear flow when $s = 0$ is however unknown since there are no open edges. In order to calculate this term an imaginary cut is created in the closed section, and this point is considered as the origin for s, as shown in Figure 3.6. The open section shear flow is calculated as shown in Eq. (3-43)
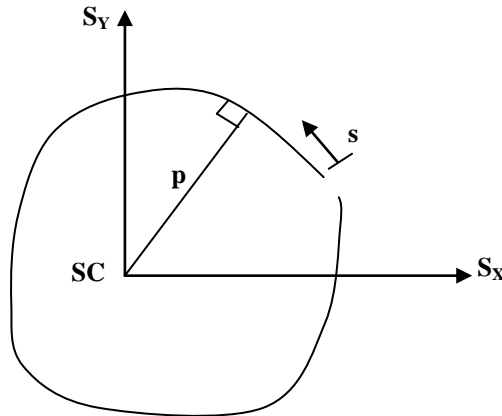
Figure 3.6 Imaginary cut in a close section and origin of *s*

The $q_{s=0}$ value is obtained by equating the moments on the section due to the applied shear forces S_X and S_Y, and the resultant shear flow distribution. If the moments are taken about the shear centre (where the shear forces are applied) the following is obtained

$$0 = \oint pq \, ds = \oint (pq_{open} + pq_{s=0}) ds$$

$$= \oint pq_{open} \, ds + \oint pq_{s=0} ds$$

(3-44)

However $q_{s=0}$ is constant and depends on the position of the cut, thus Eq. (3-44) gives

$$0 = \oint p q_{open} \, ds + q_{s=0} \oint p \, ds \tag{3-45}$$

The integral $\oint p \, ds = 2A$, where A is the area enclosed by the mid line of the closed section, thus

$$q_{s=0} = -\frac{\oint p q_{open} ds}{2A} \tag{3-46}$$

The resultant shear flow distribution is then the sum of the q_{open} and $q_{s=0}$ distributions.

3.2.3. Torsion of Open and Closed Thin-Walled Section Beams [198]

The torsional load applied to a structure can be classified under two categories: free torsion which allow the section to warp freely, and restrained torsion in which the warping in the section is restrained at some point inducing a torsional-bending behaviour. In this section only free torsion is consider for both close and open sections.

Open Section

From basic theory [198], the rate of twist of a beam subject to a torque T is related by the relationship

$$T = GJ \frac{d\theta}{dZ} \tag{3-47}$$

Where Z is the axis along the beam length, G is the shear modulus and J is the torsion constant.

In a composite laminate the shear modulus G corresponds to the bending equivalent shear modulus G_{xy} which is obtained with the knowledge of the laminate thickness t and the term d_{33} from the laminate bending compliance matrix (inverse of the laminate bending stiffness matrix [D])

$$G_{xy}^b = 12(t^3 d_{33}) \tag{3-48}$$

The section property *J* for an open section can be defined as

$$J = \sum \frac{bt^3}{3} \; or \; J = \frac{1}{3} \int_{sec} t^3 ds \tag{3-49}$$

where *b* is the width of the element

Considering that the shear modulus may vary from element to element the torsional stiffness of a composite section is

$$GJ = \sum G_{xy}^b bt^3 / 3 \tag{3-50}$$

Applying the St Venant theory [198] the in plane shear stress, in an open section, induced by the torque can be calculated as

$$\tau_{xy} = 2G_{xy}^b n \frac{d\theta}{dZ} \tag{3-51}$$

Where *n* is the distance from the mid plane of the element and varies from –*t/2* and +*t/2*. Thus the maximum shear stress occurs at the two outer surface of the element.

When subject to free torsion an open section beam is subject to thickness and cross section warping, w_s and w_s respectively. The thickness warping can be defined as [198]

$$w_t = ns \frac{d\theta}{dZ} \tag{3-52}$$

where *ns* represent the area swept when the beam is twisted as shown in Figure 3.7.
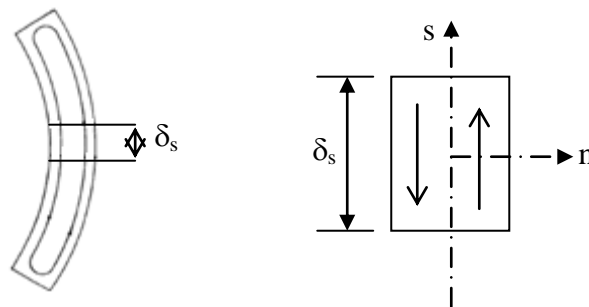
Figure 3.7 Shear lines in a thin-walled section beam

The cross section warping is defined as

$$w_s = -\frac{d\theta}{dZ} \int_0^s p_R \, ds \tag{3-53}$$

The integral term however can be defined as

$$A_R = \frac{1}{2} \int_0^s p_R \, ds \tag{3-54}$$

where A_R is the area swept by a generator rotating about the centre of twist from the point of zero warping, as sown in
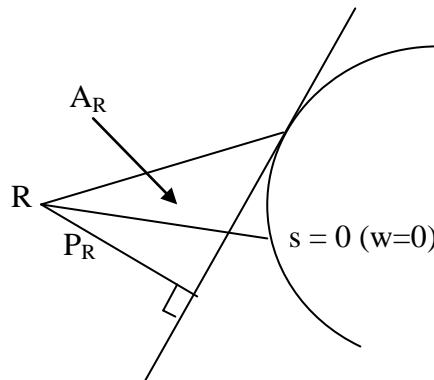
Figure 3.8 Warping of an open section beam

The cross section warping can therefore be defined as

$$w_s = -2A_R \frac{d\theta}{dZ} \tag{3-55}$$

or in terms of the applied torque as

$$w_s = -2A_R \frac{T}{\sum G_{xy}^b bt^3 / 3} \tag{3-56}$$

Single Cell Closed Section
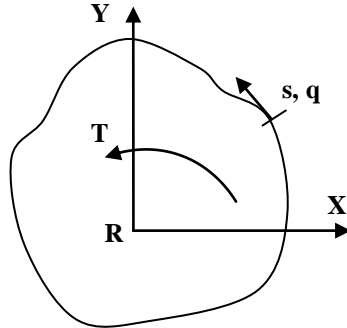
Figure 3.9 Shear flow distribution in a closed section beam subject to torsion

The application of a pure torque to a closed section beam results in the development of a constant shear flow in the beam wall [198]. The shear stress however may vary around the cross section since the wall thickness is free to vary as a function of *s*. The relationship between the applied torque *T* and this constant shear flow is

$$T = \oint pq \, ds \tag{3-57}$$

since the shear flow is constant and $\oint p \, ds = 2A$

$$T = 2Aq \tag{3-58}$$

which is known as the Bredt-Batho formula. The rate of twist in an isotropic material is defined as

$$\frac{d\theta}{dZ} = \frac{q}{2A} \oint \frac{ds}{Gt} \tag{3-59}$$

where *G* is the section shear modulus. However, for a composite material the shear modulus for each ply varies with respect to the global axis and it must be therefore defined for each lamina. The laminate shear modulus, to be used for a torsional analysis of a closed section, is the membrane shear modulus G^m_{xy} which is defined in terms of the term a_{33} form the laminate compliance membrane matrix (inverse of the membrane stiffness matrix [A])

$$G_{xy}^m = 1/(ta_{33})$$ (3-60)

The expression for the rate of twist for a composite section therefore becomes

$$\frac{d\theta}{dZ} = \frac{q}{2A} \oint \frac{ds}{G_{xy}^m t}$$ (3-61)

Using the relationship in Eq. (3-58) the rate of twist can be expressed in terms of the applied torque T

$$\frac{d\theta}{dZ} = \frac{T}{4A^2} \oint \frac{ds}{G_{xy}^m t}$$ (3-62)

Rearranging Eq. (3-62) it is obtained that

$$T = \frac{4A^2}{\oint \frac{ds}{G_{xy}^m t}} \frac{d\theta}{dZ}$$ (3-63)

Remembering the torque and twist rate relationship in Eq. (3-47) the torsional stiffness for a single cell closed composite section can be defined as

$$GJ = \frac{4A^2}{\oint \frac{ds}{G_{xy}^m t}}$$ (3-64)

The warping distribution around the cross section can be defined as [198]

$$w_s - w_s = \int_0^s \frac{q_s}{G_{xy}^m t} ds - \frac{A_{0s}}{A} \oint \frac{q_s}{G_{xy}^m t} ds - Y_R \frac{d\theta}{dZ}(X_s - X_0) + X_R \frac{d\theta}{dZ}(Y_s - Y_0)$$ (3-65)

where A_{0s} is the area generated from the origin for s to any point s around the cross section. The last two terms in Eq. (3-65) relates the warping displacement to an arbitrary origin which undergoes axial displacement due to warping. If the origin coincides with the centre of twist R of the section then Eq. (3-65) can be simplified to

$$w_s - w_s = \int_0^s \frac{q_s}{G_{xy}^m t} ds - \frac{A_{0s}}{A} \oint \frac{q_s}{G_{xy}^m t} ds$$ (3-66)

3.2.4. Closed Cell Thin-Walled Beam Stiffness Calculation Using the VABS Program

VABS, variational asymptotical beam sectional analysis, is an efficient high-fidelity cross sectional analysis code [75, 199, 200]. This computer program uses the variational asymptotic method to split a three dimensional nonlinear elastic problem onto a two dimensional linear cross sectional analysis and a one dimensional non linear beam problem. The geometry of the cross section is given as an input to the VABS program in the form of a finite element mesh. This allows the program to analyse arbitrary cross sectional shapes. When modelling composite materials each laminate is modelled separately, therefore for each element the composite material properties and ply angles are specified. Figure 3.10 shows an example of a beam cross section made in composite materials, where each ply is modelled as an element and they are assembled to form laminated panels which are assembled into a structure.
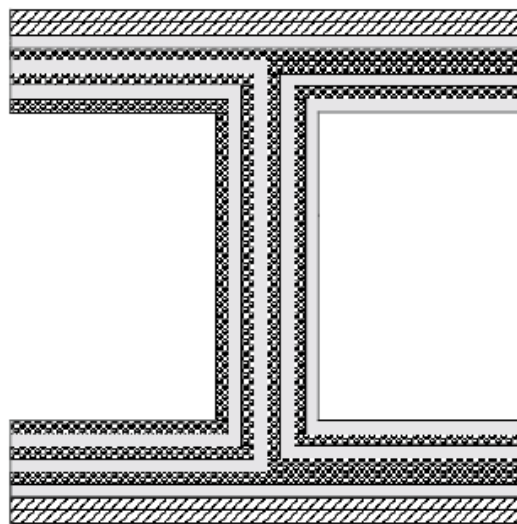
Figure 3.10 I beam configuration and layup [200]

Using the geometrical and material data the program calculates the following cross sectional properties

- The 6 x 6 cross sectional mass matrix
- The 4 x 4 stiffness matrix constructed using the classical stiffness model
- The 6 x 6 stiffness matrix constructed using the generalised Timoshenko model
- The 5 x 5 stiffness matrix constructed using the generalised Vlasov model

In addition the three dimensional displacement, strain and stress fields are recovered for the global behaviour of a one dimensional beam analysis using the classical model, the generalised Timoshenko model or the generalised Vlasov model.

This program was developed mainly to analyse blade sections, e.g. for helicopter rotors or wind turbine, and therefore it presents some limitations to calculate the properties of vary large cross sections. However, this program is an extremely useful tool to obtain a quick and accurate estimate of the stiffness properties of closed cell thin-walled beams to be used for preliminary structural design and analysis.

3.2.5. Stress Analysis of Stiffened Thin-Walled Beams Using the TWbox Program

The structures considered so far consisted of simple plates, however in aircraft structures most panels are reinforced by stiffeners. In order to simplify the analysis of these structures, it can be assumed that the shear loads are carried by the skins only; while the direct stresses are mainly carried by the stringers. Since the stress is constant across the stringer cross section it is possible to replace them with a concentrated area known as booms located along the mid line of the skin [198]. Figure 3.11 shows how a typical wing structure can be idealised for analysis simplification.
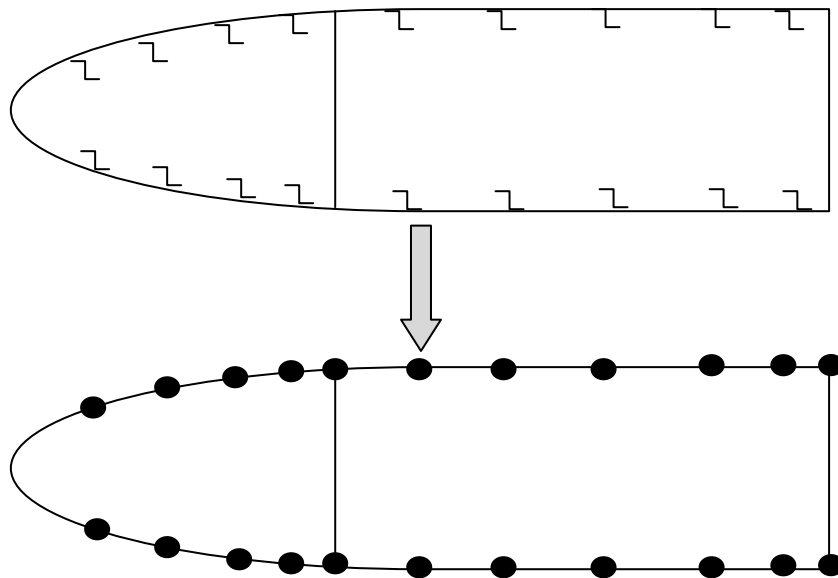
Figure 3.11 Idealisation of wing section [198]

The direct stress carrying capability of the skin can be taken into account by increasing the area of each boom by an area equivalent of the direct stress carrying capacity of the adjacent skin panels. Figure 3.12 (a) shows the actual stress distribution in an arbitrary panel while Figure 3.12 (b) shows how this distribution would be idealised when considering a structure made of panels and booms.

(a)   **(b)**
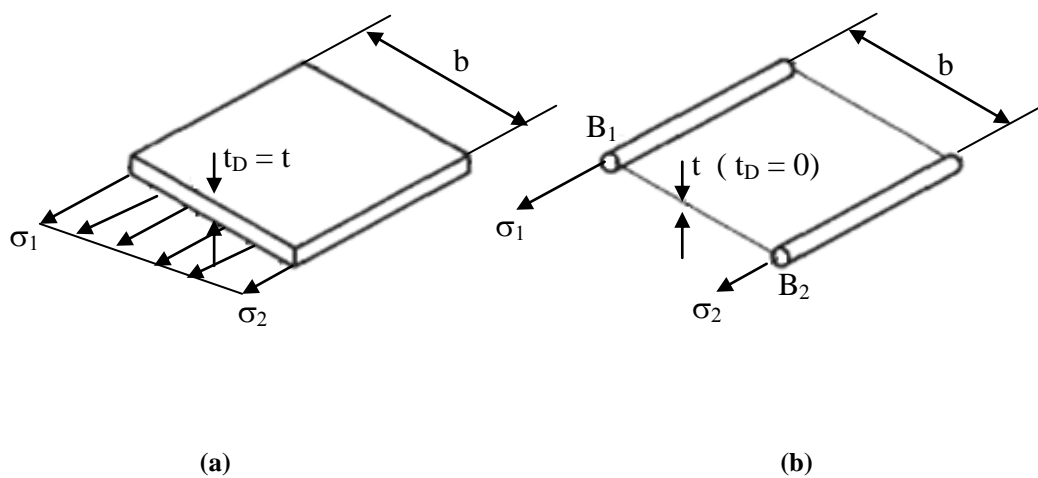
Figure 3.12 Idealisation of a panel [198]

In Figure 3.12 (a) the direct stress carrying thickness t_D is equal to the actual thickness t while in Figure 3.12 (b) $t_D = 0$. In the actual panel the direct stress distribution in the actual panel varies linearly from an unknown value σ_1 to an unknown value σ_2. In the idealised panel this distribution is lost, however the direct stress in both panels must be the same. By equating the moments due to the direct stresses it is possible to obtain expressions for the boom areas B_1 and B_2. Thus, taking moments about the right-hand edge of each panel

$$\sigma_2 t_D \frac{b^2}{2} + \frac{1}{2}(\sigma_1 - \sigma_2)t_D b \frac{2}{3}b = \sigma_1 B_1 b \tag{3-67}$$

Hence

$$B_1 = \frac{t_D b}{6}\left(2 + \frac{\sigma_2}{\sigma_1}\right) \tag{3-68}$$

Similarly

$$B_2 = \frac{t_D b}{6}\left(2 + \frac{\sigma_1}{\sigma_2}\right) \tag{3-69}$$

In Eq. (3-68) and (3-69) the ratio of σ_1 and σ_2, if unknown, can be frequently assumed. The direct stress distribution in Figure 3.12 (a) is caused by a combination of axial load and bending moment. For axial load only $\sigma_1/\sigma_2 = 1$ and $B_1 = B_2 = t_D b/2$; for a pure bending moment $\sigma_1/\sigma_2 = -1$ and $B_1 = B_2 = t_D b/6$. Thus, different idealisations of the same structure are required for different loading conditions.

This skin and boom idealisation was employed to develop the TWbox program [201] which calculates the shear and direct stresses of stiffened composite single and double cell thin-walled beams. This program also enables to analyse both constant cross section and tapered beams. The inputs required by the program are

- Number of booms
- Booms *xy* coordinate at the two ends of the beam
- Booms area
- Equivalent elastic modulus of the laminated composite
- In plane forces and torque applied

Using these data the program calculates the beam bending stiffness, the direct stress in the booms, the cross section basic shear flow and the shear stress in each section of the panels. This program is a useful tool when setting the initial sizes of a composite wing, in particular to assess whether the strength of the stiffened skin is enough to support the applied aerodynamic loadings.

3.3. Finite Element Analysis

Aircraft structural analysis is carried out by replacing the actual structure with an idealised approximated model. At different levels of the design process the structure can be more or less accurate. At some stage in the design however, an accurate estimate of components loads and stresses is needed and in this case the idealised structure must be a close representation of the actual structure. Standard methods presented in the previous sections become inadequate as they cannot cope with the necessary degree of complexity. The finite element method is then used to analyse complex continuous structures [202, 203].

In the finite element method the continuous structures are artificially idealised into a number of elements interconnected at the nodes and the matrix method of analysis is applied to determine forces and displacements. These finite elements can be two or three dimensional and the structural idealisation can be carried out in many different ways, depending on the type of problem, the accuracy of the solution and time available for computation. Commercially available software has made this analysis method more accessible. This section presents the approached used by the finite element software package NASTRAN to carry out non linear static, buckling and dynamic analyses.

3.3.1. Non Linear Static Analysis Using NASTRAN [204]

A linear static analysis assumes a linear relationship between applied load and displacement. As the stiffness of a structure does not change the problem can be solved in a single step. For a system to be liner it has to satisfy the following assumptions:

- The structure is only subject to small displacement when the load is applied

- The stress and strain relationship in the materials is linear

- The boundary conditions remain constant

If one of these conditions is not satisfied nonlinear effects must be introduced; which can be geometric, material or boundary condition nonlinearities.

In a static nonlinear problem the stiffness of the structure depends on the displacement and the response is not longer a linear function of the applied load. As the structure deflects under the applied load, the stiffness changes, therefore the structure's response changes as well. As a result, nonlinear problems require an incremental solution scheme where the displacement is calculated in steps and at each time the stiffness is updated. Each step uses the results from the previous step as a starting point. The stiffness matrix is therefore generated and decomposed several times during the analysis.

A linear finite element static system is expressed as

$$F = \boldsymbol{K}u \tag{3-70}$$

However a nonlinear system is expressed as

$$F - R = \boldsymbol{K}^T \Delta u = r \tag{3-71}$$

Where $\mathbf{K}$ is the elastic stiffness matrix, $\mathbf{K^T}$ is the tangent stiffness matrix in a nonlinear system, Δu is the displacement vector, F is the applied load vector and r is the residual.

The nonlinear static analysis requires the solution of the non linear equilibrium equation Eq. (3-71) which can be obtained in NASTRAN selecting an appropriate method: full Newton-Raphson, modified Newton-Raphson, Newton-Raphson with strain correction or the secant method [203].
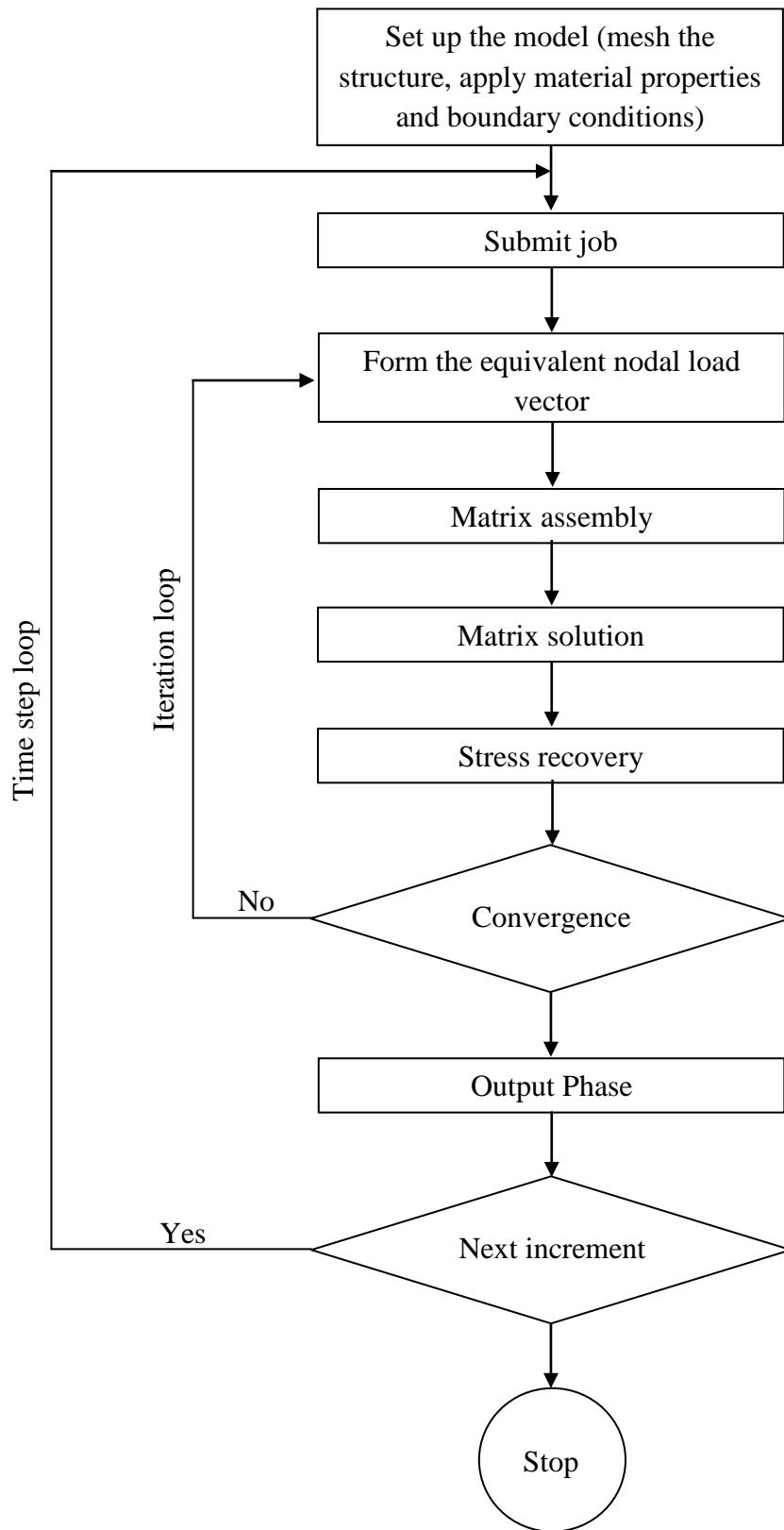
Figure 3.13 Static nonlinear solution flow sequence [204]

Figure 3.13 shows a flow chart of the nonlinear solution sequence using NASTRAN. The total load is applied to the model gradually in increments. For each load step, the solution is achieved after one or more iterations. If the behaviour of the model is generally linear only a few iterations are required to solve that load step. However if the model behaviour is complex many iterations are needed and for each iteration the stiffness matrix is reassembled and a solution is calculated. At the end of each iteration a check is carried out to ensure that the solution has converged. If the convergence is not satisfied the iteration is repeated with the new information and the stiffness matrix is reassembled and the solution is recalculated. This process is repeated until convergence is achieved when the next incremental load is then applied. The load increments are applied until the full load of the model is solved.

3.3.2. Linear Buckling Analysis Using NASTRAN [205]

A buckling analysis is used to determine the load at which the structure becomes instable, i.e. when the structure continues to deflect without an increase in magnitude of loading. When carrying out a linear buckling analysis, in the finite element method the stiffness of a structure is determined as the sum of the linear stiffness matrix and differential stiffness matrix [205]. The differential stiffness matrix, which is a function of the geometry, element type and applied loads, represents the linear approximation of reducing the linear stiffness matrix in the case of a compressive load, and increasing the linear stiffness matrix in the case of a tensile load. The linear and differential stiffness matrices for each element are denoted as $[k_a]_i$ and $[k_d]_i$, respectively. For the whole structure the linear stiffness matrix can be then represented as

$$[K_a] = \sum_i^n k_{a_i} \qquad (3\text{-}72)$$

Similarly, the system differential stiffness matrix can then be represented as

$$[K_d] = \sum_i^n k_{d_i} \qquad (3\text{-}73)$$

The overall system stiffness matrix is then defined as

$$[K] = [K_a] + [K_d] \tag{3-74}$$

The total potential energy of the structure is equal to

$$[U] = \frac{1}{2}\{u\}^T[K_a]\{u\} + \frac{1}{2}\{u\}^T[K_d]\{u\} \tag{3-75}$$

In order for the system to achieve static equilibrium, the total potential energy must have a stationary value, i.e. the following must be satisfied

$$\frac{\partial[U]}{\partial u_i} = [K_a]\{u\} + [K_d]\{u\} = \{0\} \tag{3-76}$$

where u_i is the displacement of the i-th degree of freedom.

Eq. (3-76) can be also be written as

$$\Big[[K_a] + P_a\big[\overline{K_d}\big]\Big]\{u\} = 0 \tag{3-77}$$

where $K_d = P_a\big[\overline{K_d}\big]$ and P_a is the applied load. In order for Eq. (3-77) to have a non trivial solution, the following relationship must be true:

$$\Big|[K_a] + P_a\big[\overline{K_d}\big]\Big| = \{0\} \tag{3-78}$$

where $| \quad |$ stands for the determinant of the matrix. Eq. (3-78) is satisfied for only certain values of P_a and these values are the critical buckling loads.

A real structure has an infinite number of degrees of freedom. The finite element model approximates the behaviour of the structure with a finite number of degrees of freedom. The number of buckling loads obtained using the finite element method is then equal to the number of the degrees of freedom of the model, i.e.

$$P_{cr_i} = \lambda_i P_a \tag{3-79}$$

Substituting Eq. (3-79) in Eq. (3-78)

$$\left|[K_a] + \lambda_i\overline{[K_d]}\right| = \{0\} \tag{3-80}$$

Eq. (3-80) is in the form of an eigenvalue problem. Once the eigenvalues λ_i are obtained the buckling loads can then be obtained using Eq. (3-79).

The NASTRAN software offers three methods to solve the eigenvalue problem of Eq. (3-80): the inverse power method, the enhanced inverse power method and the Lanczos method.

The inverse power method [205] is a tracking method as it attempts to extract the lowest eigenvalue and eigenvector in a desired range. Only one mode or root is determined at a time and each root is found using an iterative process. Because the eigenvalue calculation strongly depends on the chosen range, the inverse power method can miss some modes, and it is therefore an unreliable method to solve the bucking problem.

The enhanced inverse power method is similar to the inverse power method except that is uses Sturm sequence logic [205] to ensure that all modes are found within the specified eigenvalue range. The Sturm sequence gives the number of modes below each trial eigenvalue.

The Lanczos method overcomes the limitations and combines the best features of the other two methods. It is and efficient method and if an eigenvalue cannot be extracted within the specified range a diagnostic message is issued. This method computes accurate eigenvalues and eigenvectors, i.e. displacement plots at the various buckling loads can be visualised using a post-processing software. This method is the most recommended method when carrying out linear buckling analysis using NASTRAN.

3.3.3. Dynamic Analysis Using NASTRAN [206]

In a dynamic analysis the loads are applied to the structure as a function of time and consequently, the induced responses (displacements, velocities, accelerating forces and

stresses) are also time dependent. This time-varying characteristic makes dynamic analysis more complicated than static analysis. Three types of dynamic analysis can be performed with NASTRAN:

- Real eigenvalue analysis: used to determine the undamped free vibration behaviour of a structure. The results of an eigenvalue analysis indicate the frequency and shape at which the structure tends to vibrate.
- Linear frequency response analysis: an efficient method for finding the steady-state response to sinusoidal excitation. In a frequency response analysis, the loading is a sine wave for which the frequency, amplitude and phase are specified.
- Linear transient response analysis: the most general method of computing the response to time varying loads. The loading in a transient response is known at every point in time.

Real Eigenvalue Analysis

The equation of motion of a structure with no damping and applied loading describes its undamped free vibration behaviour and in a matrix form is defined as

$$[M]\{\ddot{u}\} + [K][u] = 0 \tag{3-81}$$

where $[M]$ is the mass matrix and $[K]$ is the stiffness matrix. To solve Eq. (3-81) a harmonic solution can be assumed

$$\{u\} = \{\phi\} \sin \omega t \tag{3-82}$$

where $\{\phi\}$ is the eigenvector or mode shape and ω is the circular natural frequency. This harmonic form of the solution indicates that all the degrees of freedom of the structure vibrate in synchronous manner. The structural configuration does not change its basic shape during motion but only its amplitude changes.

Differentiating Eq. (3-82) and substituting it in Eq.(3-81) the following is obtained

$$-\omega^2[M]\{\phi\}\sin\omega t + [K]\{\phi\}\sin\omega t = 0 \qquad \text{(3-83)}$$

which, after simplifications, becomes

$$([K] - \omega^2[M])\{\phi\} = 0 \qquad \text{(3-84)}$$

For Eq. (3-84) to have a non trivial solution, the following relationship must be true:

$$|[K] - \omega^2[M]| = \{0\} \qquad \text{(3-85)}$$

where | | stands for the determinant matrix. Eq. (3-85) is in the form of an eigenvalue problem which is satisfied by a set of discrete eigenvalues ω^2_i. To each eigenvalue there is a corresponding eigenvector ϕ_i which satisfies Eq. (3-85). Each eigenvalue and eigenvector therefore defines a free vibration mode of the structure. The *i*-th eigenvalue is related to the *i*-th natural frequency, f_i, by

$$f_i = \frac{\omega_i}{2\pi} \qquad \text{(3-86)}$$

This eigenvalue problem is solved by NASTRAN in the same manner as the buckling eigenvalue problem discussed in section 3.3.2. The same three methods, the inverse power, the enhanced inverse power and the Lanczos, can be used. Similarly to the bucking analysis case however, the preferred and most suitable method to solve the eigenvalue problem is the Lanczos method.

Linear Frequency Response Analysis

A frequency response analysis is a method to compute structural response to steady state oscillatory excitation. For this type of analysis the responses computed for the grid nodes are expressed as complex numbers defined by the magnitude and phase or by the real and imaginary components. These quantities are graphically presented by Figure 3.14.
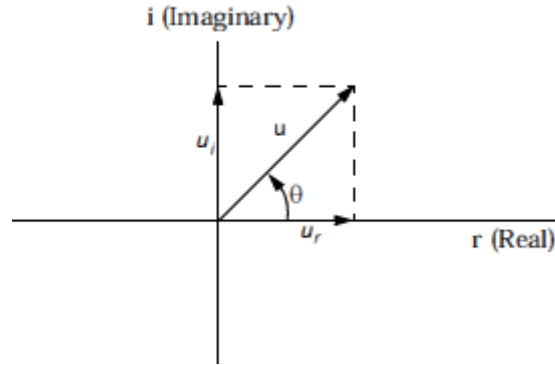
Figure 3.14 Frequency response complex representation [206]

where

$$u = \text{magnitude} = \sqrt{u_r{}^2 + u_i{}^2}$$

$$\theta = \text{phase angle} = \tan^{-1}(u_i/u_r)$$

$$u_r = \text{real component} = u\cos\theta$$

$$u_i = \text{imaginary component} = u\sin\theta$$

There are two methods to carry out a frequency response analysis: a direct method and a modal method. In the direct frequency response analysis the structural response is computed at discrete excitation frequencies by solving a set of coupled matrix equations using complex algebra. The damped forced complex vibration equation of motion with harmonic excitation can be expresses as

$$[M]\{\ddot{x}(t)\} + [B]\{\dot{x}(t)\} + [K]\{x(t)\} = \{P(\omega)\}e^{i\omega t} \tag{3-87}$$

where $[M]$ is the mass matrix, $[B]$ is damping matrix and $[K]$ is the stiffness matrix. The solution to Eq. (3-87) is expected to be harmonic and of the form

$$\{x\} = \{u(\omega)\}e^{i\omega t} \tag{3-88}$$

where $\{u(\omega)\}$ is a complex displacement vector. Taking the first and second derivatives of Eq. (3-88), the following is obtained

$$\{\ddot{x}\} = -\omega^2\{u(\omega)\}e^{i\omega t} \tag{3-89}$$

$$\{\dot{x}\} = i\omega\{u(\omega)\}e^{i\omega t} \tag{3-90}$$

When Eq. (3-89) and Eq.(3-90) are substituted in Eq.(3-87) the expression of the equation of motion becomes

$$[M]\{x(t)\} + [B]\{x(t)\} + [K]\{x(t)\} = \{P(\omega)\}e^{i\omega t} \tag{3-91}$$

which after dividing by $e^{i\omega t}$ simplifies to

$$[-\omega^2 M + i\omega B + K]\{u\{\omega\}\} = P(\omega) \tag{3-92}$$

The equation of motion is then solved by inserting the forcing frequency ω. This expression represents a system of equations with complex coefficients if damping is included or the applied loads have phase angles. The equations of motions at each input frequency are then solved in a manner similar to a static problem.

In the modal frequency response analysis, when the damping is proportional (and in this study case it was 3% of the critical damping), the mode shapes of the structures are used to uncouple the equations of motion. First of all the variables are transformed from a physical coordinates $\{u(\omega)\}$ to modal (generalised) coordinates $\{\xi(\omega)\}$ by assuming

$$\{x\} = [\phi]\{\xi(\omega)\}e^{i\omega t} \tag{3-93}$$

The mode shapes $[\phi]$ are used to transform the problem in terms of the behaviour of the modes as opposed to the behaviour of the grid points. Eq. (3-93) represents an approximation as not all the modes are used. Temporarily all damping are ignored, which results in the undamped equation for harmonic motion

$$-\omega^2[M]\{x\} + [K]\{x\} = \{P(\omega)\} \tag{3-94}$$

at forcing frequency ω.

Substituting the modal coordinates in (3-93) for the physical coordinates in Eq. (3-94) and dividing $e^{i\omega t}$, the following is obtained

$$-\omega^2[M][\phi]\{\xi(\omega)\} + [K][\phi]\{\xi(\omega)\} = \{P(\omega)\} \qquad (3\text{-}95)$$

Now this is the equation of motion in terms of the modal (generalised) coordinates. This expression however, is still a coupled equation. In order to uncouple this equation Eq. (3-95) is premultiplied by $[\phi^T]$ to obtain

$$-\omega^2[\phi]^T[M][\phi]\{\xi(\omega)\} + [\phi]^T[K][\phi]\{\xi(\omega)\} = [\phi]^T\{P(\omega)\} \qquad (3\text{-}96)$$

where

$[\phi]^T[M][\phi]$ = modal (generalised)mass matrix

$[\phi]^T[M][\phi]$ = modal (generalised)stiffness matrix

$[\phi]^T\{P\}$ = modal (generalised) force vector

The final step uses the orthogonality property of the mode shapes to formulate the equation of motion in terms of the generalised mass and stiffness matrices, which are diagonal matrices. These diagonal matrices do not have the off-diagonal terms that couple the equations of motion. Therefore, in this form the modal equations of motion are uncoupled. In this form the equations of motion can be written ad a set of uncoupled single degree of freedom system as

$$-\omega^2 m_i \xi_i(\omega) + k_i \xi_i(\omega) = p_i \xi_i(\omega) \qquad (3\text{-}97)$$

where

m_i = i-th modal mass

k_i = i-th modal stiffness

p_i = i-th modal force

Once the individual modal response $\xi_i(\omega)$ are computed, the physical responses, which are in a complex form, are recovered as the summation of the modal responses using

$$\{x\} = [\phi]\{\xi(\omega)\}e^{i\omega t} \qquad (3\text{-}98)$$

Linear Transient Response Analysis

A transient response analysis is conducted to study the behaviour of a structure subject to a time varying excitation. Similarly to the frequency response analysis the transient response, with NASTRAN, can be calculated using direct and modal methods. Other common methods to solve the dynamic equation of motion of a multi degree of freedom system are the Newmark Beta and Wilson Theta methods. Both these methods use an implicit formulation and assume that the acceleration of the system varies linearly between two instants of time. With the methods adopted by NASTRAN this assumption is not necessary and the results are more accurate.

In the direct transient analysis the structural response is calculated by solving a set of coupled equations using direct numerical integration. The dynamic equation of motion in matrix form is expresses as

$$[M]\{\ddot{u}(t)\} + [B]\{\dot{u}(t)\} + [K]\{u(t)\} = \{P(t)\} \tag{3-99}$$

The structural response is solved at discrete times, typically with a fixed integration time step $\varDelta_t$. By using a central finite difference representation for the velocity and acceleration at discrete times,

$$\{\dot{u}_n\} = \frac{1}{2\Delta t}\{u_{n+1} - u_{n-1}\} \tag{3-100}$$

$$\{\ddot{u}_n\} = \frac{1}{\Delta t^2}\{u_{n+1} - 2u_n + u_{n-1}\} \tag{3-101}$$

and averaging the applied force over three adjacent time points, the equation of motion can be expressed as

$$\begin{aligned}\left[\frac{M}{\Delta t^2}\right](u_{n+1} - 2u_n + u_{n-1}) &+ \left[\frac{B}{2\Delta t}\right](u_{n+1} - u_{n-1}) \\ + \left[\frac{K}{3}\right](u_{n+1} + u_n + u_{n-1}) &= \frac{1}{3}(P_{n+1} + P_n + P_{n-1})\end{aligned} \tag{3-102}$$

Collecting terms, the Eq. (3-102) can be written as

$$[A_1]\{u_{n+1}\} = [A_2] + [A_3]\{u_n\} + [A_4]\{u_{n-1}\} \tag{3-103}$$

where

$$[A_1] = \left[\frac{M}{\Delta t^2} + \frac{B}{2\Delta t} + \frac{K}{3}\right] \; ; \quad [A_2] = \frac{1}{3}(P_{n+1} + P_n + P_{n-1})$$

$$[A_3] = \left[\frac{2M}{\Delta t^2} - \frac{K}{3}\right] \; ; \qquad [A_4] = \left[-\frac{M}{\Delta t^2} + \frac{B}{2\Delta t} - \frac{K}{3}\right]$$

The matrix $[A_1]$ is defined as the dynamic matrix and matrix $[A_2]$ is the applied force averaged over three adjacent time points. The transient solution is obtained by decomposing $[A_1]$ and applying it to the right hand side of Eq. (3-103). In this form the solution behaves like a succession of static solutions with each time step performing a forward back substitution on a new load vector.

In the modal transient response, when the damping is proportional (and in this study case it was 3% of the critical damping), the mode shapes of the structure are used to uncouple the equation of motion. The variable of the equation of motion are expressed in terms of modal (generalised) coordinates using

$$\{u(t)\} = [\phi]\{\xi(t)\} \tag{3-104}$$

The mode shaped $[\phi]$ are used to transform the problem in terms of the behaviour of the modes as opposed to the behaviour of the grid points. Temporarily ignoring the damping the equation of motion becomes

$$[M]\{\ddot{u}(t)\} + [K]\{u(t)\} = \{P(t)\} \tag{3-105}$$

Substituting Eq. (3-104) into Eq. (3-105) the following equation is obtained

$$[M][\phi]\{\ddot{\xi}(t)\} + [K][\phi]\{\xi(t)\} = \{P(t)\} \tag{3-106}$$

In order to uncouple the equations of motion each term is multiplied by $[\phi^T]$ to obtain

$$[\phi]^T[M][\phi]\{\ddot{\xi}\} + [\phi]^T[K][\phi]\{\xi\} = [\phi]^T\{P(t)\} \tag{3-107}$$

where

$[\phi]^T[M][\phi]$ = modal (generalised)mass matrix

$[\phi]^T[M][\phi]$ = modal (generalised)stiffness matrix

$[\phi]^T\{P\}$ = modal (generalised) force vector

The final step uses the orthogonality property of the mode shapes to formulate the equation of motion in terms of the generalised mass and stiffness matrices, which are diagonal matrices. These diagonal matrices do not have the off-diagonal terms that couple the equations of motion. Therefore, in this form the modal equations of motion are uncoupled. In this form the equations of motion can be written ad a set of uncoupled single degree of freedom system as

$$m_i \xi_i(t) + k_i \xi_i(t) = p_i(t) \tag{3-108}$$

where

$m_i = i$-th modal mass

$k_i = i$-th modal stiffness

$p_i = i$-th modal force

Once the individual modal (generalised) response $\xi_i(\omega)$ are computed, the physical responses, which are in a complex form, are recovered as the summation of the modal responses using

$$\{u(t)\} = [\phi]\{\xi(t)\}$$

$$\tag{3-109}$$

The modal transient response allows a quicker computation of the structural response and when analysing a large structure this method is the most appropriate. However, when high frequencies excitations are applied, the frequencies used for the modal transient analysis may lose accuracy. The selection of the appropriate analysis method strongly depends on the type of problem and accuracy needed [206].

Chapter 4

4. Composite Wing Box and Leading Edge Preliminary Design and Analysis

The main aim of this research study is to achieve a feasible design for a morphing leading edge to be used as a high lift device on a short range commercial aircraft. However, before setting the details of the actuation system it was of paramount importance to ensure that the main wing box structure was able to withstand the external loads. This section presents the details of the preliminary structural design and analysis of the wing box of the reference wing.

Firstly the reference wing geometry details are described in Section 4.1, followed by an estimated calculation of the aerodynamic loading and external forces due to the generated lift (Section 4.2). An initial evaluation was then carried out to estimate the morphing leading edge structure's contribution to the overall wing structural stiffness (Section 4.3). Subsequently, the wing box basic design parameters, such as skin layup and thickness; stringers' position, size and layup, were set conducting a parametric analysis (Section 4.4 and 4.5). The details of these parameters were chosen in such way that structural buckling and stress safety limits were met.

Furthermore, in order to ensure that the wing box components were fail safe a comprehensive study was conducted on the static behaviour of spar/rib structures.

Attention was focused on the effect of the presence of cutouts, methods to reduce the stress concentration around the edges of these cutouts, buckling of web panels (Section 4.6) and failure modes of spar/rib to skin joints (Section 0).

4.1. The Reference Baseline Wing

The reference baseline wing used in the current research was designed for a short range commercial aircraft and its general geometrical details were provided by one of the Project Partners. The wing dimensions, shape and performance were comparable with that of an A320 wing. The wing area was 172 m^2 and the semi-span was 19.8 m (17% more than the A320 wing span), as shown in Figure 4.1. A section, located in the outboard wing, at 8.3 m from the root with a chord of 4 m, was taken as the wing reference section to carry out design and structural analysis. The provided wing geometrical design parameters are summarised in Table 4.1.
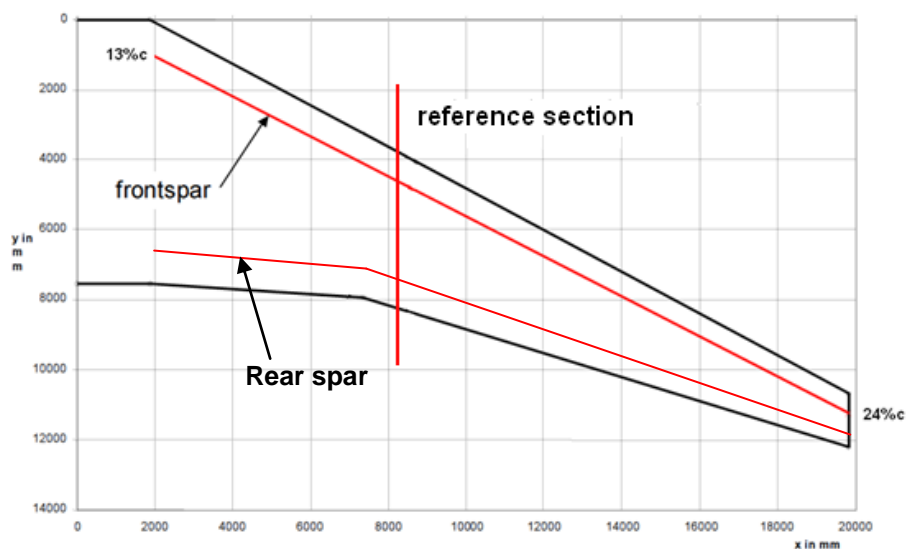
Figure 4.1 Reference wing planform [207]

Table 4.1 Baseline wing geometrical parameters [207]

Area (m^2)	172
Aerodynamic mean chord (m)	5.15
Span (m)	39.65
Aspect ratio	9.14
Taper ratio	0.2
Root chord/percentage relative thickness (m)	16
Kink chord/percentage relative thickness (m)	11.5
Tip chord/percentage relative thickness (m)	10.5
Sweep angle outer wing (deg)	28
Dihedral (deg)	5

The wing structure was supported by two spars and thirty one ribs. The front spar followed a line parallel to the leading edge and at the root it was placed at 13% of the root chord and at the tip at 24% of the tip chord. Similarly, the rear spar followed the trailing edge line and at the root it was place at 40% of the root chord and at the tip at 33% of the tip chord. The pitch along the spar between each rib was 0.6 m. Before the engine mount the ribs were oriented in line with the air flow, while in the outboard section they were perpendicular to the front spar. The spars and the ribs together with the skin panels formed the centre wing box, which in a wing structure is the main load carrier. More detailed information about skin, spars and ribs thickness; stringers size and materials were not readily available and they were therefore set as part of the preliminary design study and they are presented in the following sections.

4.2. Wing Weight and Aerodynamic Loading Estimation
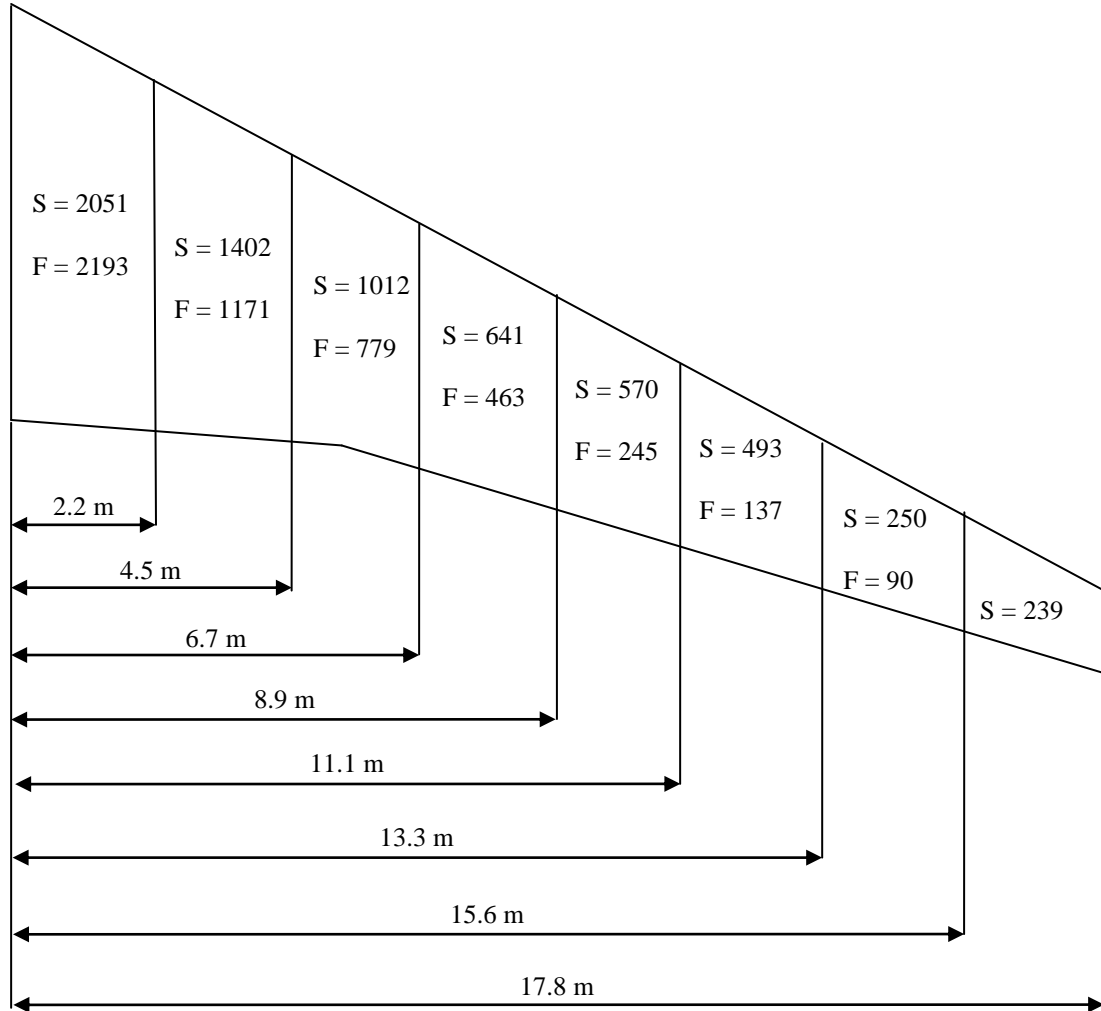
Figure 4.2 Wing structural and fuel mass spanwise distribution (mass in kilograms, S = structural mass, F = fuel mass)

The wing loading, specifically shear force, bending moment and torque, due to the lifting force were calculated using the Wingloads program [208]. The lift force was assumed to have a spanwise elliptical distribution and to be applied at the quarter chord. The shear force at a certain section was then calculated as the sum of the lift force acting from that particular point to the wing tip. The bending moment was then obtained by multiplying the shear force by its distance to the wing root. Similarly, the

torque was calculated by multiplying the shear force by its distance to the wing elastic axis. At these preliminary design stages the total lift force generated at take off was assumed to be just above the maximum takeoff weight. Using the flight conditions data available (air speed and density) the total lift was estimated to be 475 kN. The actual shear force and bending moment acting on the wing however were calculated by subtracting the weight of the wing itself. The structural and fuel mass for the reference wing were calculated by scaling the corresponding loads for an A320. Figure 4.2 shows the distribution of the structural and fuel mass along the span (from root to tip without considering the wing box section). The total mass of a half span wing was approximately 12 tonnes (which is equivalent to 115 kN). Figure 4.3 shows the total shear force, bending moment and torque spanwise distribution, including the limit load factor of 2.5 [116].
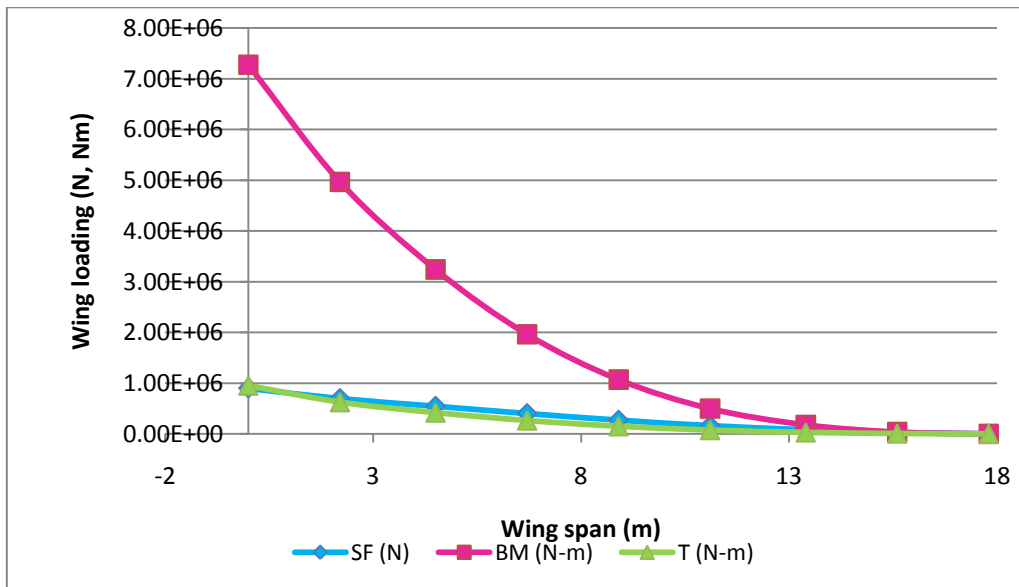
Figure 4.3 Shear force, bending moment and torque spanwise distribution

Interpolating the data from Figure 4.3 the shear force at the reference section was 429.42 x 10^3 N, while the bending moment and torque were 219.52 x 10^4 Nm and 292.72 x 10^3 Nm respectively. These loads were used as force input to set some of the wing geometrical parameters in the following sections.

4.3. Wing Box and Leading Edge Stiffness Evaluation

One of the first requirements to achieve a feasible design for a morphing leading edge is that its skin must be flexible enough to be deflected. This implies that its stiffness properties are much lower than that of the wing box skin. Thus, before starting to design the morphing leading edge structure, it was necessary to estimate the leading edge contribution to the overall wing stiffness and also to evaluate how a reduction in leading edge stiffness could affect the overall structural rigidity. The cross sectional properties, bending rigidity (*EI*), torsional rigidity (*GJ*), and warping rigidity (*EW*) were calculated using the computer program VABS, which was described in section 3.2.4. Because of the limitations on the geometrical size that could be handled by the program a 1 to 25 scaled model was used to study the influence of the leading edge.

The analysis was carried out at the wing reference section, see Figure 4.1, and its dimensions were reduced to 25% of the original. For this stiffness evaluation study both wing box and leading edge skins were made of a generic carbon fibre material. Figure 4.4 shows a simplified model of the wing box and leading edge cross section.

Section where material properties was reduced
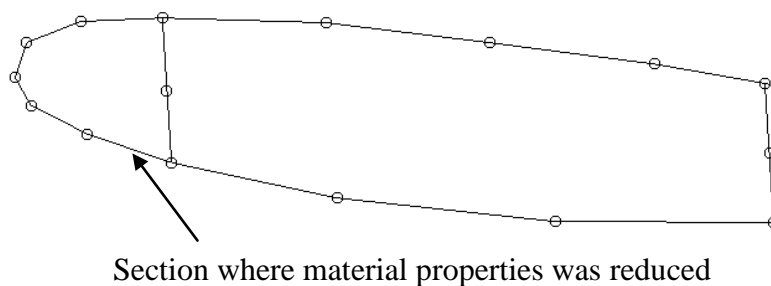
Figure 4.4 Simplified wing box and leading edge structural model

In order to evaluate the influence of the leading edge stiffness reduction, the stiffness properties of 50% of the lower part of the leading edge skin was varied, as shown in Figure 4.4. A two dimensional study was firstly conducted and the bending, torsional

and warping rigidities were calculated. Figure 4.5 shows the variation in the overall structural bending and torsional rigidities when the leading edge stiffness properties were reduced from 100% to 25%. In the figure the change in stiffness properties is expressed in percentage reduction. The two curves indicate that the leading edge stiffness reduction did not have a strong influence on the overall structural rigidities. In fact, even when the elastic and shear moduli of the leading edge panel were reduced by 75% (maintaining only 25% of the original stiffness) the torsional and bending rigidities only decreased by 2%.
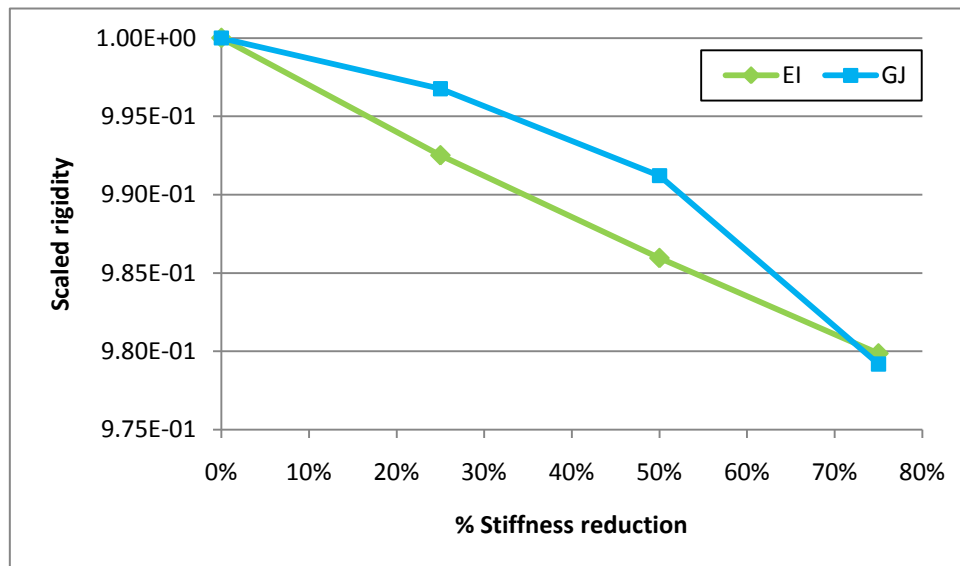
Figure 4.5 Bending and torsional rigidity variation due to the leading edge stiffness reduction

Figure 4.6 shows that the influence of the leading edge stiffness reduction on the structural warping rigidity was also not significant. In fact, when the leading edge stiffness properties were reduced by 75% the overall warping rigidity decreased by 10%.
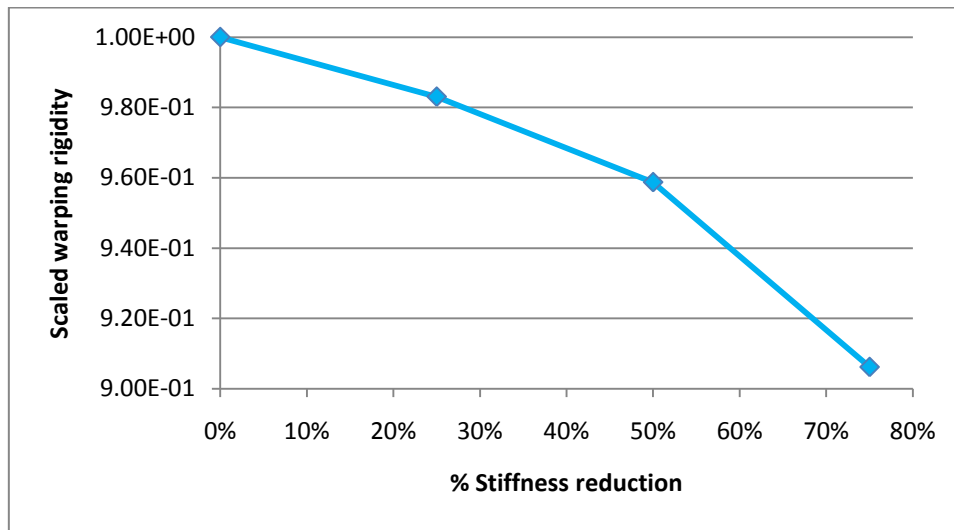
Figure 4.6 Warping rigidity variation due to the leading edge stiffness reduction

A three dimensional study was also conducted and the twist angle (θ) was calculated varying the stiffness of the leading edge lower panel. Figure 4.7 shows that when the leading edge stiffness was reduced by 75% the twist angle increased by 2% which follows the variation in overall structural torsional rigidity.
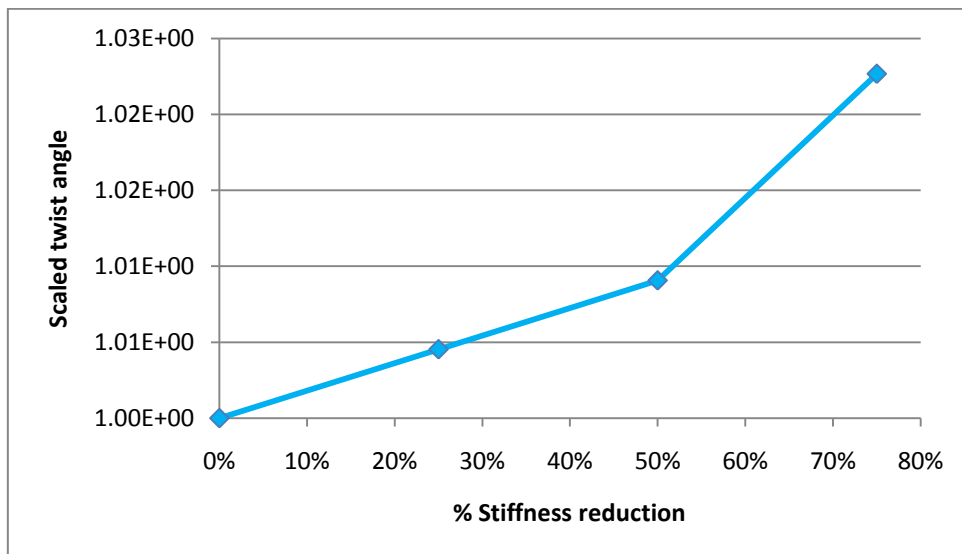
Figure 4.7 Twist angle variation due to the leading edge stiffness reduction

Table 4.2 *EI*, *GJ*, *EW* and θ variation for single and double structure due to stiffness reduction

	Leading edge stiffness	EI (Nm^2)	GJ (Nm)	EW (Nm^4)	θ (deg)
	100%	2.14 E+03	2.16 E+03	1.77 E+02	6.62 E-01
	75%	2.12 E+03	2.16 E+03	1.74 E+02	6.65 E-01
2 cell	50%	2.11 E+03	2.14 E+03	1.70 E+02	6.68 E-01
	25%	2.09 E+03	2.12 E+03	1.60 E+02	6.77 E-01
	Rubber	2.09 E+03	2.08 E+03	1.48 E+02	6.90 E-01
1 cell	-	2.12 E+03	1.63 E+03	3.79 E+02	8.80 E-01

Table 4.2 shows a summary of the variation of the structural rigidities and twist angle due to the leading edge stiffness properties reduction. Comparing the double cell, 100% stiffness case, and the single cell it can be seen that the rigidity when the leading edge is included is not much higher than that when only the wing box is considered. This shows that most of the wing rigidity is provided by the wing box. Moreover, a case when the composite lower panel of the leading edge structure was substituted with rubber was also considered. The comparison with the 100% stiffness case showed that if the concern is focused solely on the overall structural rigidity, part of the lower skin of the leading edge could be made with an extremely flexible material to allow its morphing deformation. However, in the actual case the structure also needs to be strong enough to withstand the external loads. These two comparisons were useful to understand that during the leading edge design, the trade off between structural stiffness and strength could be studied without having to always take into account the effect on the overall wing rigidity. Thus, in order to simplify the analysis, the trade off between structural stiffness and strength for the leading edge was studied separately from the wing box, which is subsequently presented and discussed in details. The design of the wing box as main load carrier is instead presented in following sections of this chapter.

4.4. Wing Box Skin Preliminary Design

This section presents how the wing box skin panel thickness and the stringers geometry were set at the wing reference section, where the wing box length was 1.855 m, the

front and rear spars were 0.438 m and 0.364 m in height respectively as shown in Figure 4.8.
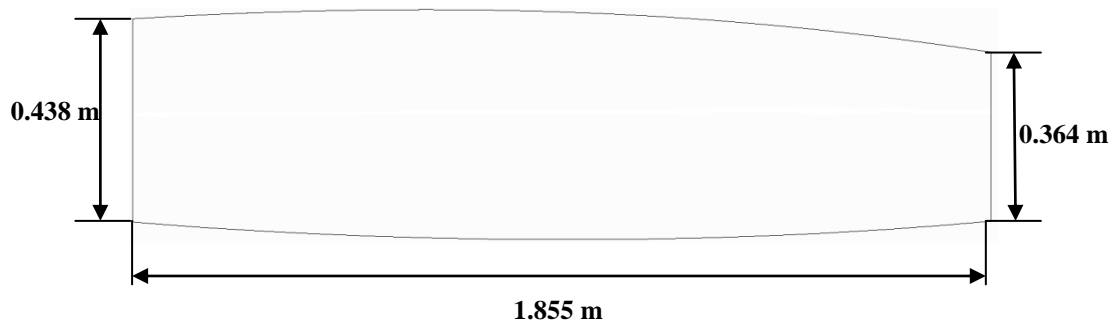
Figure 4.8 Wing box geometry at the reference section

Comparing the commercially available types of material for aircraft primary structures applications, it was found that the Hexcel Intermediate Modulus (IM) and High Strength (HS) carbon fibre materials were the most suitable [209]. Considering the strength and weight ratio as the selection criteria [210], the IM carbon fibre prepreg was the most advantageous as it had, in fact, high tensile and shear strength and modulus at lower density. Table 4.3 shows the mechanical properties of the HexTow IM7 carbon fibre which was used for the wing box skin panels and stringers.

Table 4.3 Mechanical properties of HexTow IM7 [211]

E_1 (GPa)	E_2 (GPa)	G_{12} (GPa)	v_{12}	X_t (MPa)	X_c (MPa)	Y_t (MPa)	Y_c (MPa)	S (MPa)	ρ (kg/m^3)
164	10	5	0.3	2723	1689	101	223	74	1780

Two different thicknesses were used for the skin and stringers; 0.25 mm and 0.184 respectively. The stringers ply were thinner in order to be able to obtain a suitable layup for relatively thin laminates, while obeying the stacking sequence rules, and also to achieve finer changes in thickness to reduce the overall weight when carrying out optimisation analysis. For both skin panels and stringers the laminate was made of 60% of 0º plies (spanwise), 30% of ±45º plies and 10% of 90º plies [210].

Scaling from the data available for an A320 wing, at the reference section, fourteen stringers were used to reinforce the wing box skin panels. To maximise the effect of the stringers against buckling due to the aerodynamic loads I-shaped stringers were used on the upper wing cover. T-shaped stingers were instead used on the lower skin, since the risk of buckling was lower compared to the upper surface.
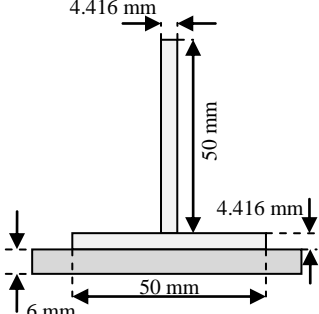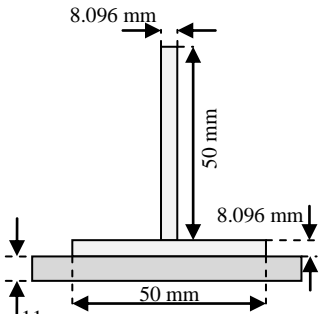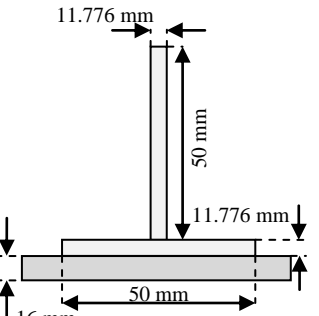
The ESDUpac A0301, described in section 3.1.4, was used to calculate the buckling load of the stiffened upper and lower wing box skin panels. Various combinations of skin and stringers laminate thickness were used, their effect on the buckling load was evaluated and finally an appropriate solution, which satisfied the panel stability requirements, was selected. At the reference section, the load to which the upper skin panel had to withstand against buckling was calculated as

$$P_{US} = \frac{BM_{reference\,section}}{airfoil\,height} = \frac{219.52 \times 10^4 (Nm)}{0.438\,(m)} = 5011.87\,kN \qquad (4\text{-}1)$$

To assess the buckling of the lower skin cover the applied load was calculates as

$$P_{LS} = \frac{(Wing\,mass_{reference\,section})(g)(distance\,from\,root)}{airfoil\,height}$$

$$= \frac{3128.63(kg) \times 9.81(m/s^2) \times 6.3(m)}{0.438} = 441.46\,kN \qquad (4\text{-}2)$$

Table 4.4 Skin thickness and stringers sizing

1	4.416 mm 50 mm 4.416 mm 50 mm 6 mm	Skin and stringers 24 layers: $[0_2/45/90/-45/0_2/45/90/-45/0_2]_s$ Buckling load: 164 kN
2	8.096 mm 50 mm 8.096 mm 50 mm 11 mm	Skin and stringers 44 layers: $[0_2/45/90/-45/0_2/45/90/-45/0_2/45/90/-45/0_2/45/90/-45/0_2]_s$ Buckling load: 953 kN
3	11.776 mm 50 mm 11.776 mm 50 mm 16 mm	Skin and stringers 64 layers: $[0_2/45/90/-45/0_2/45/90/-45/0_2/45/90/-45/0_2/45/90/-45/0_2/45/90/-45/0_2]_s$ Buckling load: 2874 kN

4		Skin and stringers 64 layers: $[0_2/45/90/-45/0_2/45/90/-45/0_2/45/90/-45/0_2/45/90/-45/0_2/45/90/-45/0_2/45/90/-45/0_2]_s$ Buckling load: 3356 kN
5		Skin and stringers 74 layers: $[0_2/45/90/-45/0_2/45/90/-45/0_2/45/90/-45/0_2/45/90/-45/0_2/45/90/-45/0_2/45/90/-45/0_2]_s$ Buckling load: 5574 kN

Table 4.4 shows the results of this parametric study summarising the skin and stringers components' thicknesses, their layup and the corresponding buckling load. The arrangement 2 and 5 satisfied the lower and upper wing box panel buckling requirements, respectively and were therefore chosen for the current study.

The stringers geometry and skin thickness data were then used to construct an idealised model of the wing box made of panel and booms as described in section 3.2.5., and as shown in Figure 4.9. The TWbox program was used to calculate the wing box shear and direct stresses.
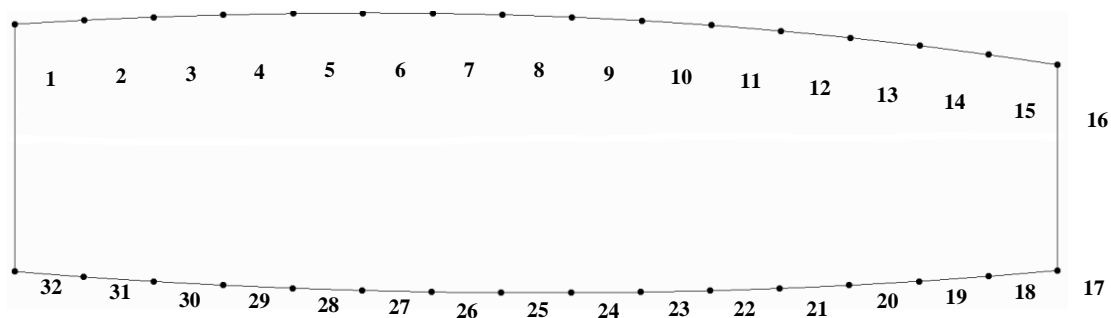
Figure 4.9 Wing box structure's panels and booms idealisation

The maximum shear stress on the upper and lower panels were in sections 2-3 and 30-31 respectively, while the maximum direct stress concentration occurred in booms 6 and 28. The direct stress was assumed to be equally distributed between the stringers' components and the skin. Table 4.5 summarise the stresses and failure index results obtained. The results showed that, including the design requirement safety factor of 1.5, the wing box skin stresses were within the material allowable.

Table 4.5 Wing box shear and direct stresses (including the load factor 1.5)

		Shear		Direct	
		Stress (MPa)	Failure index	Stress (MPa)	Failure index
Upper surface	Skin	-12.56	0.17	-53.10	0.03
	Stringer flange (skin)	-	-	-53.10	0.03
	Stringer web	-	-	-53.10	0.03
	Stringer flange	-	-	-53.10	0.03
Lower surface	Skin	21	0.28	131.66	0.05
	Stringer flange (skin)	-	-	131.66	0.05
	Stringer web	-	-	131.66	0.05

This section therefore presented how the parameters for the wing box skin design were determined to satisfy both buckling and stress criteria. In particular, the skin thickness for the upper and lower skins was set to 18.5 and 11 mm respectively, and the stringers dimensions of the upper and lower skins were set for those described as case 2 and 5 in Table 4.4.

4.5. Leading Edge Skin Preliminary Structural Analysis

The leading edge at the reference section was 0.86 m in chordwise length and 0.44 m in height, as shown in Figure 4.10.
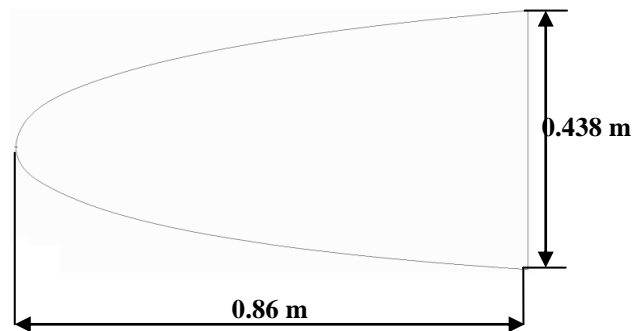
Figure 4.10 Leading edge geometry at the wing reference section

The LE skin was reinforced by eight metallic I-shaped stringers on both upper and lower skin panels and their flange and web were 12 mm in length and 3 mm in thickness. In the initial design two types of materials were selected for the leading edge skin: a metallic option, aluminium 2024-T81, and glass fibre. The aluminium skin was 2 mm in thickness while the glass fibre skin was 3 mm in thickness made of 12 layers arranged in a symmetrical layup $[\pm45/0_3/90]_s$. Table 4.6 and Table 4.7 show the mechanical properties of glass fibre and aluminium.

Table 4.6 Mechanical properties of glass fiber [212]

E_1 (GPa)	E_2 (GPa)	G_{12} (GPa)	v_{12}	X_t (MPa)	X_c (MPa)	Y_t (MPa)	Y_c (MPa)	S (MPa)	ρ (kg/m^3)	t (mm)
39	8.6	3.8	0.28	1080	620	39	128	89	2100	0.25

Table 4.7 Mechanical properties of Aluminum 2024-T81 [213]

E (GPa)	G (GPa)	v_{12}	X (MPa)	S (MPa)	ρ (kg/m^3)
72.4	28	0.33	450	295	2780

The stress on the leading edge skin, due to the aerodynamic loading, was calculated using the same method as the one applied for the wing box skin, i.e. employing the TWbox program. A double cell idealised model of the leading edge and wing box was created and it is shown in Figure 4.11.
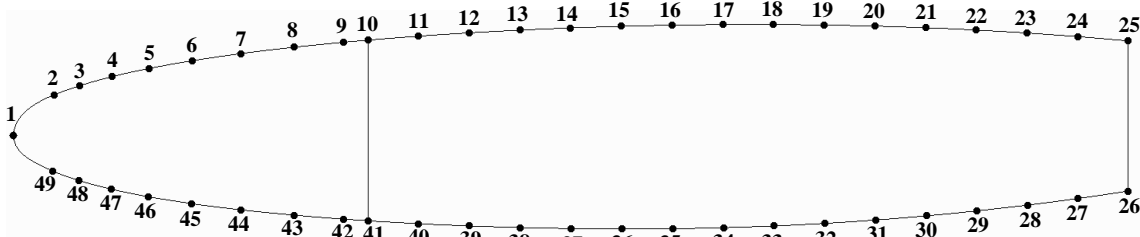
Figure 4.11 Wing box and leading edge structure's panels and booms idealisation

The wing box structure was included in this analysis in order to be able to apply the shear force through the aerodynamic centre and the bending moment thought the elastic centre. The stresses induced on the leading edge structure are summarised in Table 4.8.

Table 4.8 Leading edge shear and direct stresses (including the load factor 1.5)

		Shear		Direct	
		Stress (MPa)	Failure index	Stress (MPa)	Failure index
Glass fibre	Upper surface	37.83	0.43	-16.55	0.03
	Lower surface	38.67	0.43	12.36	0.01
Aluminium	Upper surface	57.60	0.12	-37.95	0.08
	Lower surface	53.32	0.18	72.11	0.16

The results showed that for the glass fibre skin the maximum shear stress on the upper surface was 37.83 MPa and it occurred in the panel 3-4. Whereas, the maximum shear stress on the lower surface was 38.67 MPa in the panel 47-48. The direct stress was assumed to be equally distributed between the stringers' components and the skin and therefore the maximum stress on the upper and lower skins were -16.55 MPa and 12.36

MPa in booms 8 and 43. The failure index results proved that the stress level in the structure was within the material allowable. For the aluminium skins the stresses were slightly higher compared with the glass fibre skin, however they were still well below the material allowable. The maximum shear stresses on the upper and lower panels were 57.60 MPa and 53.32 MPa respectively in section 3-4 and 47-48, while the maximum direct stresses were -37.95 MPa and 72.11 MPa in booms 8 and 43. This preliminary structural analysis set a thickness for the leading edge skin which could withstand the aerodynamic external loads; however a more detailed study was required to ensure that the skin could bear the morphing deflection. This analysis was carried out using the finite element method and it will be presented in a later chapter. The details of the spar and rib design are instead discussed in the following section.

4.6. Structural Analysis of a Spar Section and Rib and Improvements to Increase the Loading Carrying Capability

On an aircraft wing the aerodynamic loads act directly on the skin covers and they are transmitted to the ribs and spars as shear loads. These components are therefore of paramount importance and must be designed to withstand the high external loads. In addition, the web section of ribs and spars often include cutouts, which considerably lower the efficiency of the structure. The stress concentration caused by these cutouts must be always checked and methods to reinforce them must be implemented. This section presents the stress and buckling analysis of a composite C-section beam, under a shear load, carried out using numerical and experimental methods. This type of beam is a particularly appropriate representation of a spar section. However the structural analysis of the C-section web can be also applied to a rib. In particular, the study was conducted to evaluate the effect of various cutout shapes and cutout and flange reinforcements to reduce stress concentrations and increase buckling stability.

4.6.1. The C-Section Beam [214, 215]

The C-section beam considered for this study case had a constant cross section and it was 0.65 m in length, 0.2 m in height and 0.1 m in width, as shown in Figure 4.12. The beam web had single or double cutouts. For the single cutout case the hole was either circular or diamond shaped, for the double cutouts case one was circular and the other was diamond shaped.
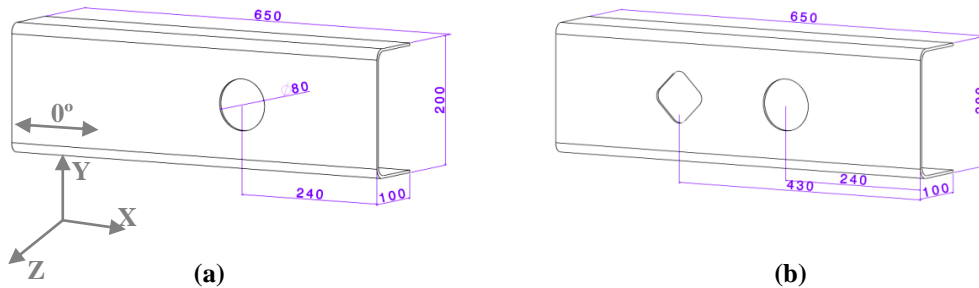
Figure 4.12 The C-section beam with (a) Single cutout and (b) Double cutouts (units in mm)

The beam web and flanges were 4 mm in thickness made of 16 layers of carbon epoxy prepreg (Hexply M21/T800) arranged in a symmetrical layup $[\pm45/0/\pm45/90/\pm45]_s$. The mechanical properties of the laminate are given in Table 4.9.

Table 4.9 Mechanical properties of M21/T800S prepreg [216]

E_1 (GPa)	E_2 (GPa)	G_{12} (GPa)	v_{12}	X_t (MPa)	X_c (MPa)	Y_t (MPa)	Y_c (MPa)	S (MPa)	ρ (kg/m^3)	t (mm)
172	10	5	0.3	3939	1669	50	250	79	1580	0.25

A pair of rings (doublers) was used to reinforce the perimeter of the cutouts and Figure 4.13 shows the doublers geometry and dimensions for both circular and diamond cutouts.
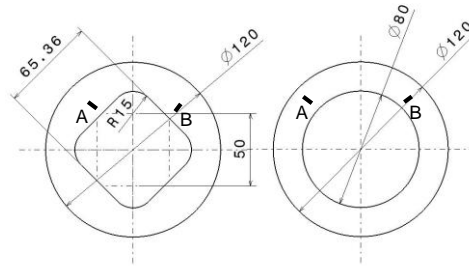
Figure 4.13 Diamond and circular cutout reinforcements dimensions

Three types of reinforcement rings were used to compare their efficiency in improving the structure's performance: one in steel alloy, one in carbon fibre laminate and one in carbon fibre steered tow placement. The steel rings were made of T300 series stainless steel, which mechanical properties are listed in Table 4.10, and they were 1.5 mm thick. The outer and inner diameters were 120 and 80 mm respectively. The composite laminate rings were 2 mm in thickness and 20 mm in width and were made of 8 plies of the same material as the beam, with a symmetrical stacking sequence $[0/\pm45/90]_s$. The fibre tow rings were also made of the carbon fibre prepreg and they were made of 6 plies with a total thickness of 1.5 mm.

Table 4.10 Mechanical properties of T300 series stainless steel [217]

E (GPa)	G (GPa)	ν_{12}	X (MPa)	S (MPa)	ρ (kg/m^3)
193	86	0.29	505	-	8000
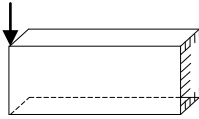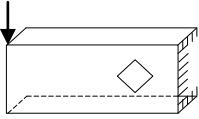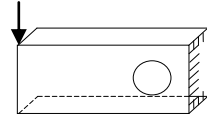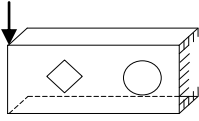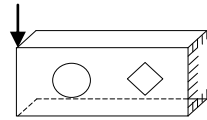
Various design cases were considered depending on the cutout shape and type of reinforcement. These cases are summarised in Table 4.11 which also shows the analysis method used: numerical or experimental. Each beam had one end fully clamped while at the opposite end it was loaded with a vertical load of 20kN through the shear centre. The different cases can be categorised under three main groups:

- *Group 1 – Single cutout*: the C-section beams in this group had a single cutout, either circular or diamond shaped, with the exception of case 1.0 which did not

contain any cutouts. Four different scenarios were studied to include two cutout shapes and two types of edge reinforcement: 1.1) unreinforced diamond cutout; 1.2) unreinforced circular cutout; 1.3) circular cutout reinforced by composite laminate rings; 1.4) circular cutout reinforced by composite tow ring.

- *Group 2 – Double cutouts with the circular one close to the clamped end*: the C-section beams in this group had both circular and diamond cutouts. The circular cutout was closer to the clamped end and the attention on stresses and strains was focused around this cutout since it was subject to more severe loads than the outboard cutout. Three cases were studied: 2.1) unreinforced cutouts; 2.2) both cutouts were reinforced by composite laminate rings; 2.3) both cutouts were reinforced by steel rings.

- *Group 3 – Double cutouts with the diamond one close to the clamped end:* The C-section beams in this group had both circular and diamond cutouts, with the diamond one closer to the clamped end. The attention was in this case focused on the diamond cutout. The three cases were: 3.1) unreinforced cutouts; 3.2) both cutouts were reinforced by composite laminate rings; 3.3) both cutouts were reinforced by steel rings.

Table 4.11 Summary of study cases

Case	Description		Study Method
1.0	C-section beam with no cutout		FEA
1.1	Single diamond cutout, no reinforcement		FEA
1.2	Single circular cutout, no reinforcement		FEA, Test
1.3	Single circular cutout, with laminate reinforcement rings		FEA
1.4	Single circular cutout, with fibre tow reinforcement rings		FEA, Test
2.1	Double cutouts, no reinforcement		FEA
2.2	Double cutouts, with laminate reinforcement rings		FEA, Test
2.3	Double cutouts, with steel reinforcement rings		FEA, Test
3.1	Double cutouts, no reinforcement		FEA
3.2	Double cutouts, with laminate reinforcement rings		FEA
3.3	Double cutouts, with steel reinforcement rings		FEA

The stress and buckling analyses were carried out using the commercially available finite element code MSC PATRAN/NASTRAN. The C-section flanges and web panel were modelled using shell elements (QUAD4), as they were appropriate to model thin composite plates. The reinforcement rings were also created using shell elements and the offset command was employed to separate the surfaces representing the beam web and the ring. A typical FE model had 11460 shell elements.

The stress concentration in shear loaded panels with cutouts usually occurs around the perimeter of the hole at the ±45° positions. In this current study the stresses and strains were therefore measured at these positions, marked as *A* and *B* in Figure 4.13.

4.6.2. Stress Analysis Numerical Results

The stress concentration around the cutout for the different design cases was calculated using the linear static analysis implemented in the finite element code NASTRAN. The effect of the different reinforcement rings was studied and their effectiveness for stress reduction was compared.

Single Cutout without Reinforcement (Cases 1.1 and 1.2)

Figure 4.14 a and b show the maximum fibre and off fibre stresses around the dimond cutout for the design case 1.1.The maximum fibre direction stress was 325 MPa and it occured in the 0º layer while the maximum off fibre stress was 18.1 MPa and it occured in the 90º layer.

(a)   (b)
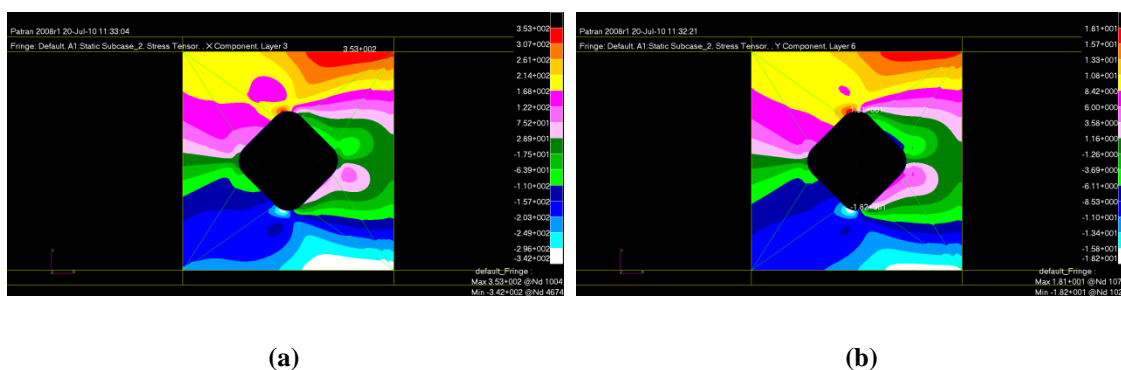
Figure 4.14 Case 1.1 stress distributions: (a) Fibre direction; (b) Off fibre direction

Figure 4.15 (a) and (b) shows the maximum fibre and off fibre direction stresses for the desing case 1.1. The maximum fibre direction stress was 329 MPa and it occured in the outer layer where the fibres were in the 45º direction, whereas the maximum off fibre stress was 18.5 MPa and it occured in the second layer where the fibres were in the -45º direction. The maximum stress concentration points for the two cases were different: for the circular cutout the maximum stress concentration occurred at the 130° position, while for the diamond this occurred at the 100° position.

<div align="center">(a)   (b)</div>
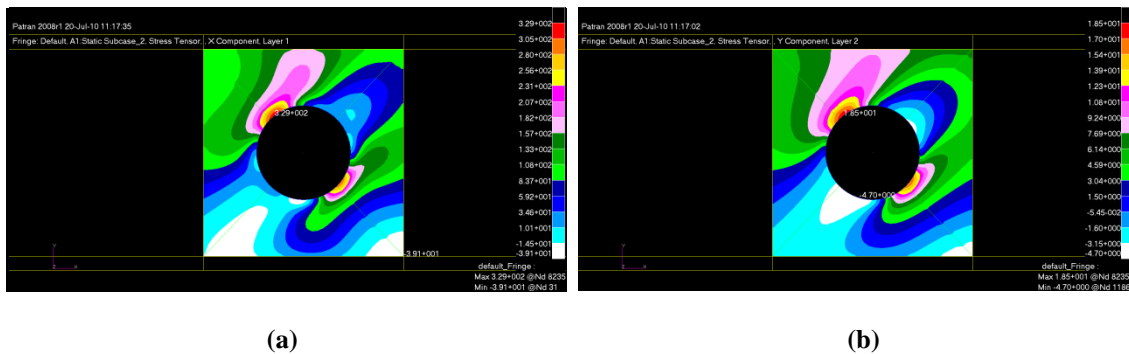
Figure 4.15 Case 1.2 stress distributions (MPa): (a) Fibre direction; (b) Off fibre direction

Table 4.12 shows the maximum strain and stress components in the global coordinates system and the maximum stresses in the material direction. These results show that all stress and strain components were lower around the diamond cutout. Without taking into consideration the impact on the manufacturing process the diamond cutout was found to be a better design for reducing stress concentration. In particular, the stress around the diamond cutout was lower because its edges were aligned with the direction of the fibres, which were mainly orientated in the ±45 degree direction.

Table 4.12 Maximum stresses and strains around unreinforced diamond and circular cutout case 1.1 and 1.2

Case	ε_x (µε)	ε_y (µε)	γ_{xy} (µε)	σ_x (MPa)	σ_y (MPa)	τ_{xy} (MPa)	σ_1 (MPa)	σ_1 (MPa)
1.1	2070	1270	1660	353	198	179	325	18.1
1.2	2190	1550	1770	372	264	188	329	18.5

Single Cutout with Reinforcement Rings (Cases 1.3 and 1.4)

Figure 4.16 shows the web and ring through thickness average fibre direction stresses at point A, shown in Figure 4.13, for cases 1.2, 1.3 and 1.4. The web principal stress was significantly reduced when the reinforcement rings were applied; a reduction of 31% and 43% was obtained when laminate rings and fibre tow rings were used respectively. Table 4.13 shows all the average through thickness stress and strain components for the design cases of group 1.
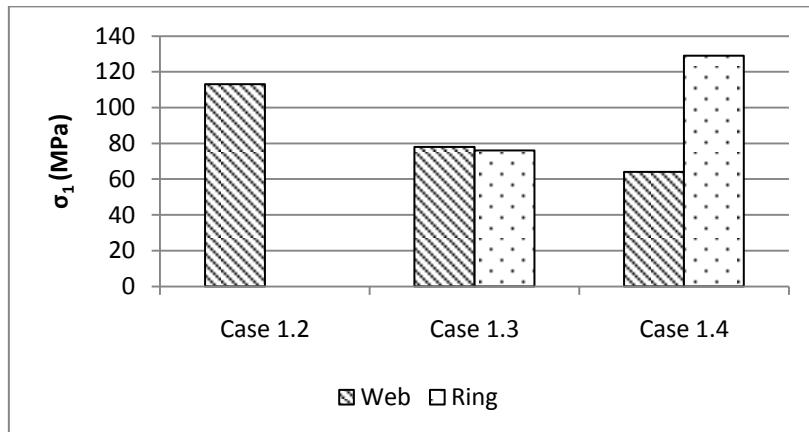
Figure 4.16 Web and ring principal stresses at point A for cases 1.2-1.4

Table 4.13 Cases 1.1 – 1.4 calculated average stresses and strains at point A

Case	ε_x (με)	ε_y (με)	γ_{xy} (με)	σ_x (MPa)	σ_y (MPa)	τ_{xy} (MPa)	σ_l (MPa)	Ring weight (g)
1.1	733	183	1182	51	35	41	92	-
1.2	1054	157	1258	70	43	43	113	-
1.3	642	164	960	45 (web)	31 (web)	33 (web)	78 (web)	19.9
				50 (ring)	26 (ring)	24 (ring)	76 (ring)	
1.4	700	45	494	45 (web)	22 (web)	17 (web)	64 (web)	14.9
				59 (ring)	50 (ring)	51 (ring)	129 (ring)	

The stress analysis results suggested that the reduction in web stress was strongly dependent on the load transfer capability of the reinforcement rings. In fact, as more loads were carried by the reinforcement rings, the stresses on the web were further reduced. From Figure 4.16 it is possible to notice that the stress on the fibre tow rings was much higher than that of the laminate rings, leading to a much lower stress level in the web. This difference in load transfer capability can be explained and quantified by the difference in elastic modulus of the laminate and fibre tow rings. The stiffness ratio of the rings can be defined as:

$$r = \frac{E_{1t}t_t}{E_{1l}t_l} \tag{4-3}$$

where t_t and t_l are the thicknesses and E_{1t} and E_{1l} the equivalent elastic moduli of the fibre tow and laminate rings respectively. The subscript '*1*' indicates the modulus in the fibre direction. The modulus of the fibre tow varied depending on the position around the cutout perimeter. The average value at point A was approximately 151 GPa and the laminate ring equivalent elastic modulus was 64.7 GPa (obtained using the program CoALA described in Section 0). The thickness of the fibre tow ring was 1.5 mm while the laminate ring thickness was 2 mm. From Eq. (4-3) the stiffness ratio was calculated to be 1.75. This ratio was nearly the same as the fibre direction stress ratio of the two

rings, which was 1.70. The greater effectiveness of the fibre tow rings was therefore due to their higher stiffness and better performance in the fibre direction.

For all the three cases, stresses in each laminate ply in the beam web and in the reinforcement rings were calculated. Figure 4.17 shows the ply by ply fibre direction stress in the web, while Figure 4.18 shows the fibre direction stress in each ring ply. In terms of stress relief around the cutout, the fibre tow ring reduced more stress in the 45° ply, whereas it was less effective in reducing the stresses in the 0° ply stress. The laminate ring on the other hand, reduced the stress in the 0° ply more than the 45° ply. Figure 4.18 shows that the stress distribution across the plies in the laminate ring was similar to that of the beam web. This was due the similarity of the laminate properties of the two components.
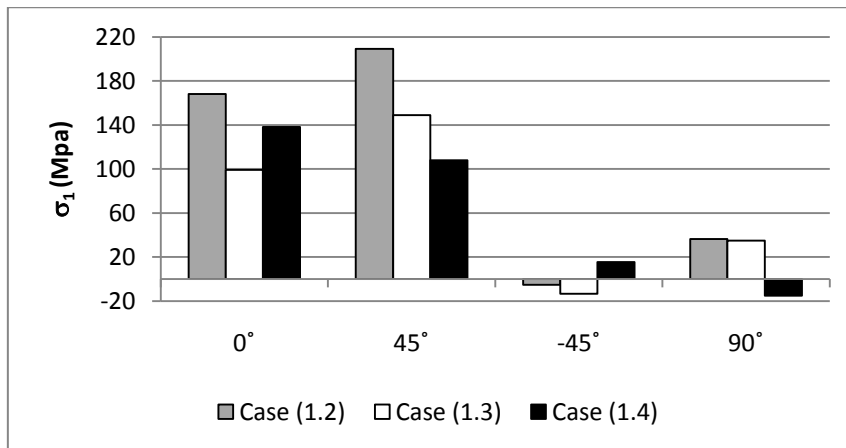
Figure 4.17 Design case 1.2 – 1.4 web ply by ply fibre direction stress
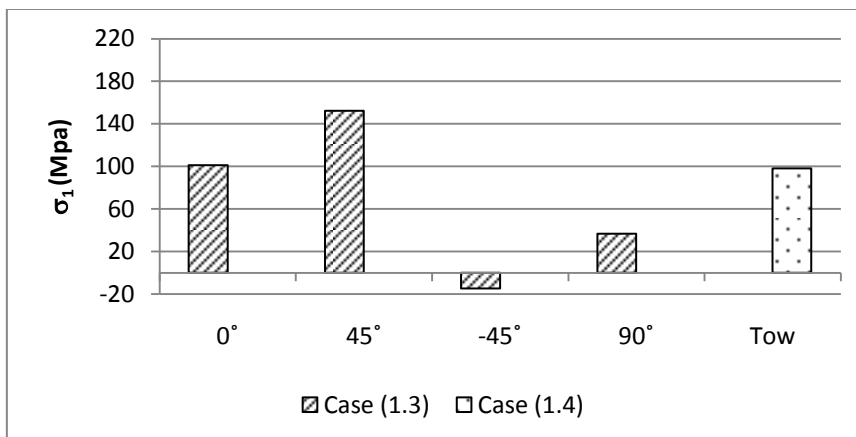
Figure 4.18 Design case 1.3 and 1.4 rings ply by ply fibre direction stress

Double Cutouts with Circular Cutout near the Clamped End (Cases 2.1, 2.2 and 2.3)

Figure 4.19 shows the web and ring fibre direction stresses at point A for cases 2.1, 2.2 and 2.3. When the laminate rings were applied, the web stress was reduced by 42%, while a 49% reduction was obtained when steel rings were applied. Table 4.14 summarises the through thickness average stress and strains components for the three design cases.
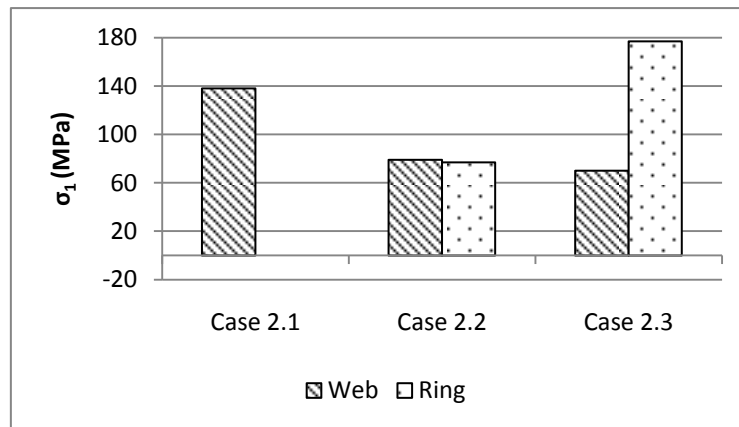
Figure 4.19 Web and ring fibre direction stresses at point A for cases 2.1-2.3

The stiffness ratio of the steel and laminate rings was calculated using Eq. (4-3). The elastic modulus and thickness of the steel and laminate rings were 193 GPa (E_{Ia}) and 1.5 mm (t_a) and 64.7 GPa (E_{Ib}) and 2 mm (t_b) respectively. The stiffness ratio was therefore 2.24, which compared well with the ring fibre direction stress ratio of 2.30. This showed that steel rings were much more effective than composite laminate rings. However, the steel rings were approximately 3.8 times heavier showing a significant disadvantage when trade off between load carrying capability and structural weight was considered.

Table 4.14 Cases 2.1 – 2.3 calculated average stresses and strains at point A

Case	ε_x (με)	ε_y (με)	γ_{xy} (με)	σ_x (MPa)	σ_y (MPa)	τ_{xy} (MPa)	σ_1 (MPa)	Ring weight (g)
2.1	1126	323	1634	80	56	56	138	-
2.2	643	167	964	45 (web)	32 (web)	33 (web)	79 (web)	19.9
				50 (ring)	27 (ring)	24 (ring)	77 (ring)	
2.3	517	184	892	38 (web)	28 (web)	31 (web)	70 (web)	75.4
				129 (ring)	76 (ring)	70 (ring)	177 (ring)	

Figure 4.20 shows the ply by ply fibre direction stress distribution for cases 2.1, 2.2 and 2.3. In terms of the stress relief in the beam web around the cutout, the steel rings were more effective than the laminate rings due to its much higher stiffness and its effectiveness was in all laminate orientation due to its isotropic properties. Figure 4.21 shows that in the laminate ring most of the load was carried by the 0° and 45° plies and that the -45° and 90° plies were less effective.
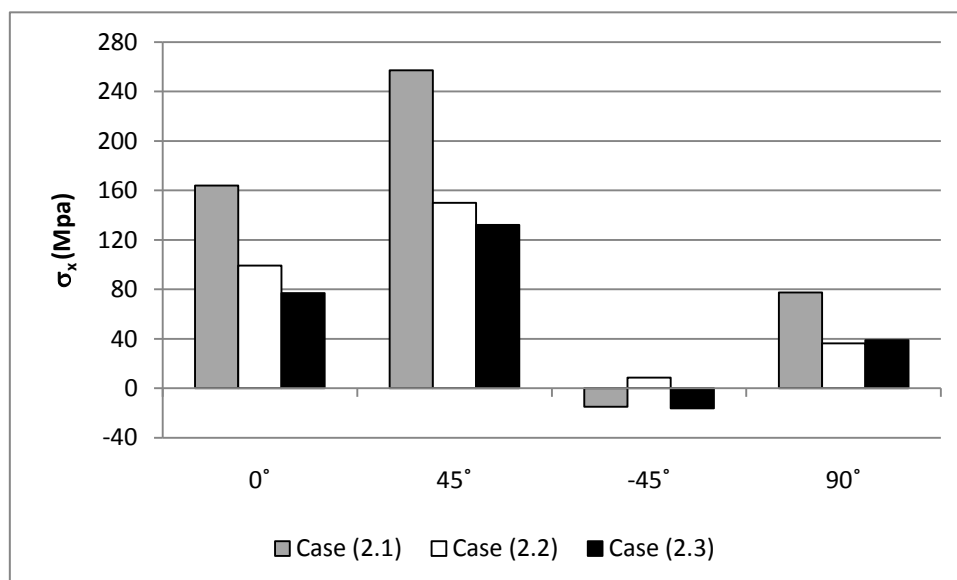
Figure 4.20 Design case 2.1 – 2.3 web ply by ply fibre direction stress
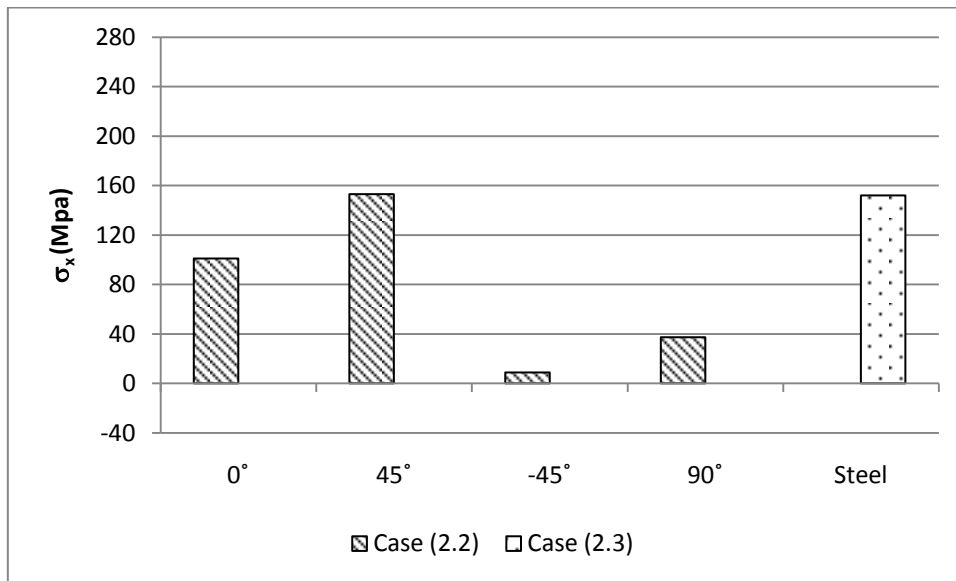
Figure 4.21 Design case 2.2 and 2.3 rings ply by ply fibre direction stress

Double Cutouts with Diamond Cutout near the Clamped End (Cases 3.1, 3.2 and 3.3)

Figure 4.22 shows the web and ring fibre direction stresses at point A for cases 3.1, 3.2 and 3.3. The steel rings had, as for the previous cases, a greater effect on web stress reduction. The stress magnitude was in fact reduced by 41% when steel rings were applied, while with laminate rings a 27% reduction was obtained.
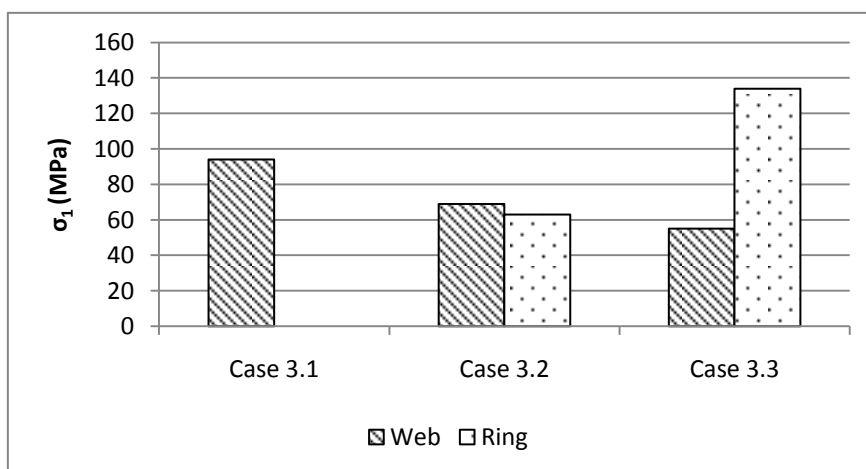
Figure 4.22 Web and ring fibre direction stresses at point A for cases 3.1-3.3

Table 4.15summarises the average through thickness stress and strains components for the three design cases. The ply by ply fibre direction stresses for cases 3.1 – 3.3 on both web and rings were similar to that of cases 2.1 – 2.3 and as discussed previously the steel rings were more effective than the laminate ones due to their higher stiffness however, presented a considerable weight penalty.

Table 4.15 Cases 3.1 – 3.3 calculated average stresses and strains at point A

Case	ε_x ($\mu\varepsilon$)	ε_y ($\mu\varepsilon$)	γ_{xy} ($\mu\varepsilon$)	σ_x (MPa)	σ_y (MPa)	τ_{xy} (MPa)	σ_1 (MPa)	Ring weight (g)
3.1	791	154	1634	54	35	41	94	-
3.2	414	197	964	33 (web)	27 (web)	33 (web)	69 (web)	23.1
				34 (ring)	23 (ring)	24 (ring)	63 (ring)	
3.3	321	162	892	26 (web)	22 (web)	27 (web)	55 (web)	87.7
				82 (ring)	58 (ring)	62 (ring)	134 (ring)	

4.6.3. Validation: Test and Theoretical Results

Five beam samples were manufactured, by the School of Applied Science in Cranfield University, and tested. These samples matched the design cases 1.2, 1.4, 2.2, 2.3 and 3.2. Figure 4.23 show two beam samples mounted on the test rig one with a single cutout (case 1.4) and one with double cutouts (case 3.2). Strains were measured at point A and B (see Figure 4.13) by strain gauge rosettes attached on both sides of the cantilever beam.

<div align="center">

(a)   (b)
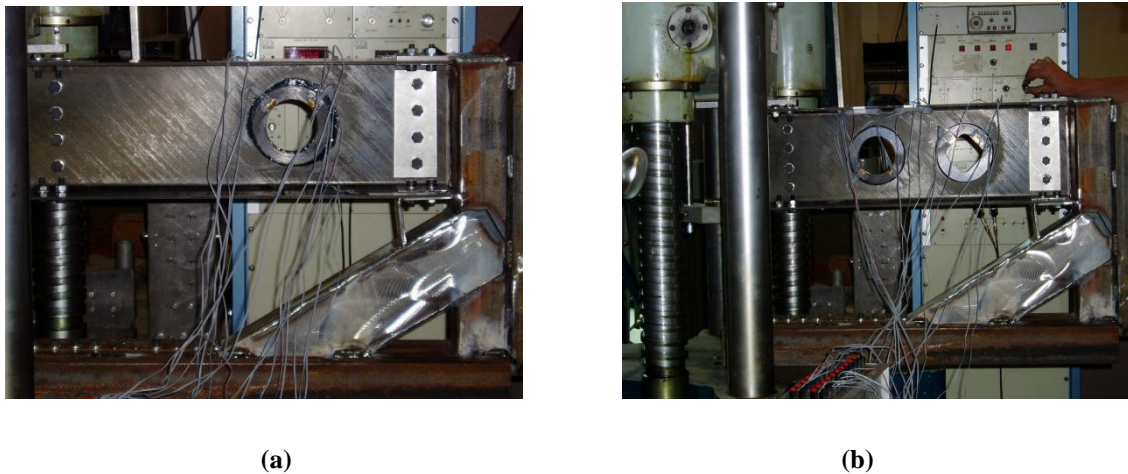
Figure 4.23 Test samples for: (a) Case 1.4, (b) Case 3.2

</div>

A comparison between experimentally measured and FE calculated strains is given in Table 4.16. The FE strains in the global x-direction (ε_x), which is the most concerned strain component for a beam under bending deflection, were in fairly good agreement with the test results. The relative error in ε_x for case 1.2 was 6% and for case 1.4 was 1.1%. However, for the double cutout cases the difference between test and numerical results was higher: 19.5% difference for case 2.2 and 29.2% for case 3.2. Satisfactory agreement was also obtained for the y-direction and shear strain components despite occasional discrepancy between the FE and experimental results. The discrepancy between the test and numerical results was probably due to the warping of the beam that occurred during the experiment. In the FE model in fact, the beam was subject to pure bending deflection due to the applied shear force, however during the test the beam was

subject to larger twist, as it was not possible to apply the load exactly in the shear centre.

Table 4.16 Comparison of measured and calculated strains at point A (units in $\mu\varepsilon$)

Cases	Measurement			FEA		
	ε_x	ε_y	γ_{xy}	ε_x	ε_y	γ_{xy}
1.2	991	355	1589	1054	157	1258
1.4	692	93	486	700	45	474
2.2	580	246	1660	643	167	964
2.3	416	245	1049	517	184	892
3.2	293	240	1062	414	197	968

Figure 4.24 and Figure 4.25 show that the comparison between the test and FE global *x*- and *y*-direction stresses was generally good.
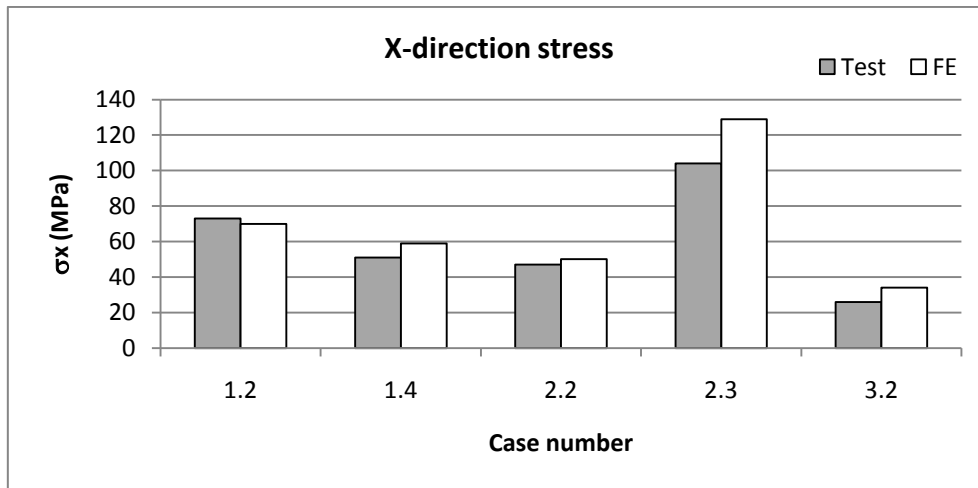
Figure 4.24 Test and numerical *x*-direction stress comparison
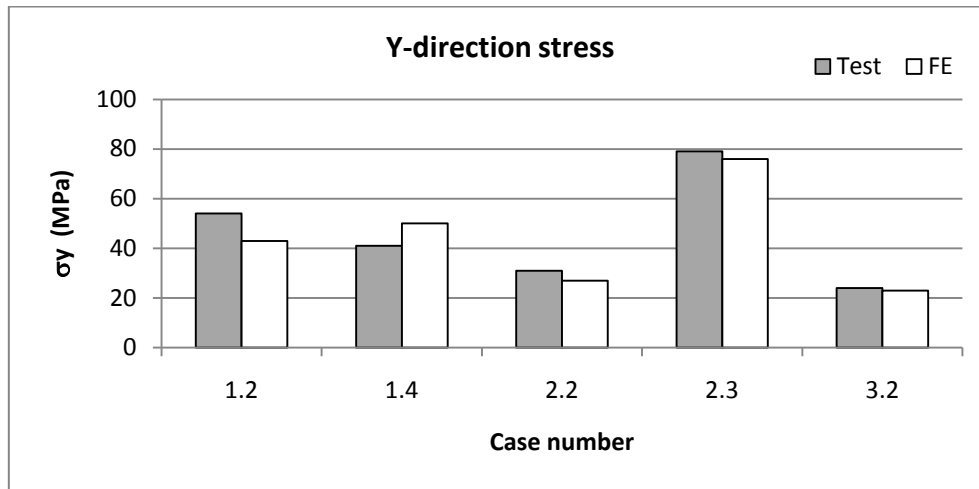
Figure 4.25 Test and numerical *y*-direction stress comparison

The stresses and strains around an unreinforced cutout were also calculated applying an analytical method using the ESDUpac A8501 described in Section 3.1.3. Table 4.17 summarises the stresses and strains at point A for case 1.2 obtained using the FE method, the experimental test and the ESDU program. Although the theoretical results were calculated for a flat plate and therefore only relatively accurate, they provided a good baseline for comparison.

Table 4.17 Numerical, experimental and theoretical stress comparison for case 1.2

	ε_x ($\mu\varepsilon$)	ε_y ($\mu\varepsilon$)	γ_{xy} ($\mu\varepsilon$)	σ_x (MPa)	σ_y (MPa)	τ_{xy} (MPa)
FE Model	1054	157	1258	70	43	43
Test	991	355	1589	73	54	55
ESDU	578	578	1585	55	55	55

4.6.4. Buckling Analysis

The buckling behaviour of the different C-section beams (Cases 1.0 – 3.3) was studied in order to investigate on the effect of cutouts and cutout reinforcement on the beam

flange and web stability. The Buckling Load Factors (BLFs) were obtained using the NASTRAN linear buckling solution, by solving the eigenvalue problem as described in Section 3.3.2.

The buckling analysis results showed that the beam critical region was the lower flange, which was in compression under the applied load. Figure 4.26 shows a typical first buckling mode of the C-section beam with a cutout.
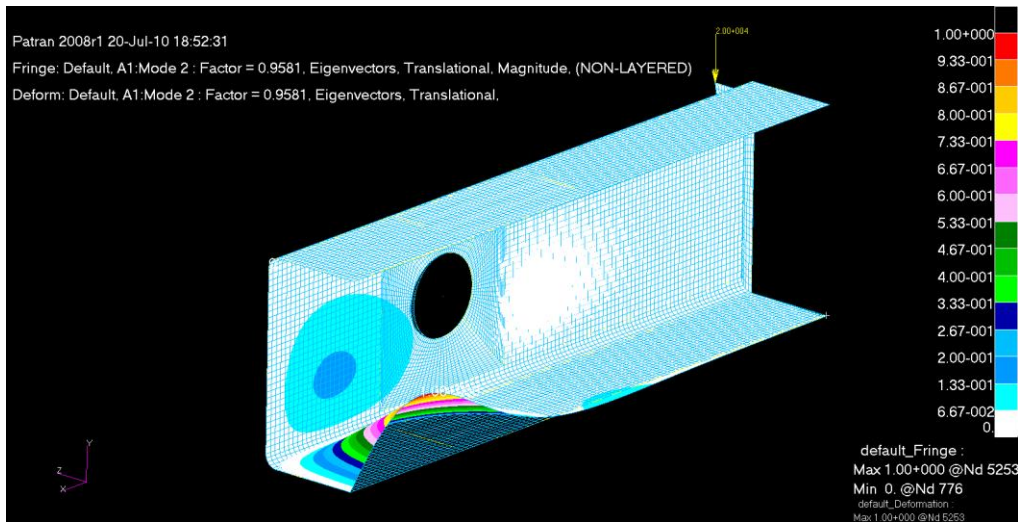
Figure 4.26 First buckling mode of a C-section beam with a cutout

Figure 4.27 shows the flange first mode BLFs for all design cases including that of a C-section beam with no cutout (Case 1.0). Comparing the unreinforced cutout cases, i.e. cases 1.1, 1.2, 2.1 and 3.1 with case 1.0 it is noticeable that the presence of a cutout/s generally increased the flange buckling stability and in particular the C-section beam with double cutouts (case 3.1) had the highest BLF.

This effect can be explained if the stress and load redistribution is considered. When a cutout is in fact introduced in the beam web the shear stress in the structure is altered: higher stresses are concentrated around the cutout relieving and consequently reducing the stress in the flange. An additional cutout would cause even higher stresses in the

web and lower stresses in the flange; the *x*-direction stresses in the flange for case 1.1 (single diamond cutout) and 3.1 (double cutout with diamond near the clamped end) were -415 MPa and -359MPa respectively whereas the *x*-direction stresses in the beam web were 354 MPa and 391 MPa respectively. Figure 4.27 also shows that the reinforcement rings increased the flange load carrying capability; however their effect was not significant.
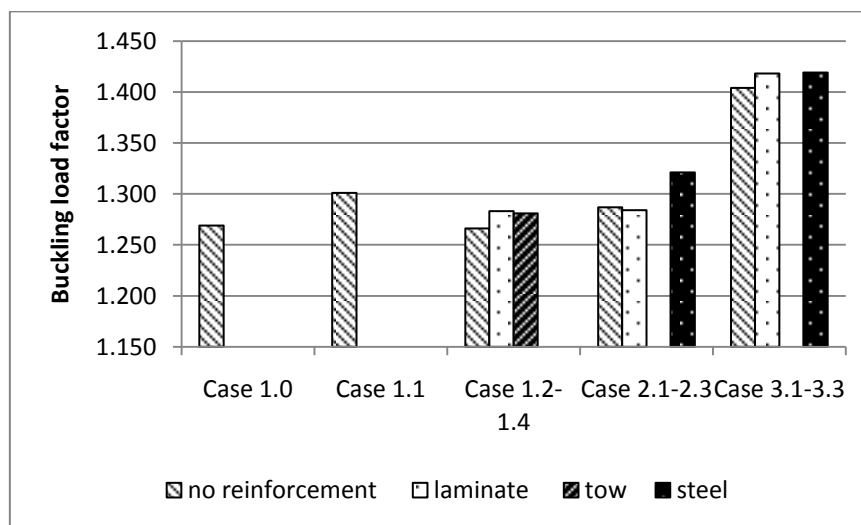
Figure 4.27 Cutout and reinforcement effect on flange buckling

The buckling analysis also illustrated that the web buckling occurred at much higher modes than the flange buckling. Figure 4.28 shows the BLF for case 1.0 – 3.3 and the respective mode number at which web buckling first occurred. This graph indicates that cutout/s, without any edge reinforcement, significantly decreased the web buckling stability. This was due to the higher stress concentrations caused by the presence of the cutout/s. For all reinforced cases however, the BLF was higher than that for a beam without a cutout (case 1.0), demonstrating that the cutout reinforcement rings were not only effective to reduce the stress concentrations but also to increase the beam web structural stability.
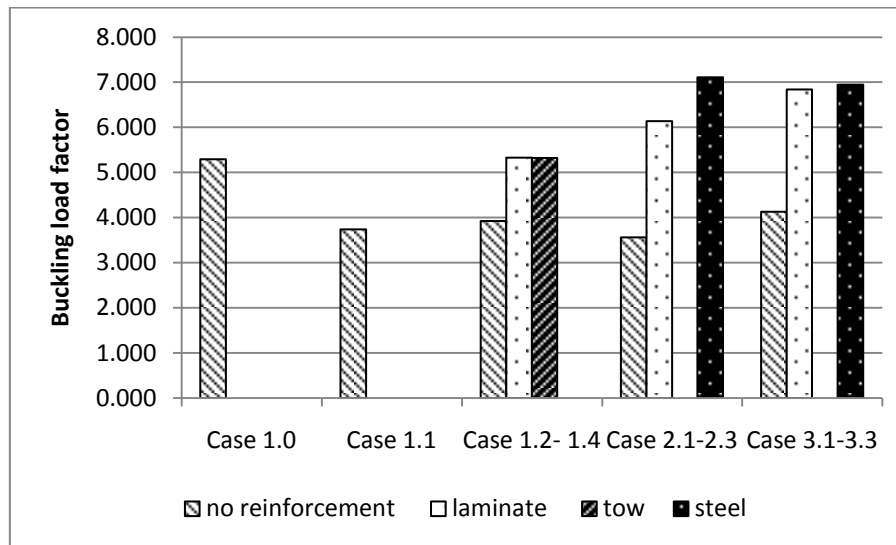
Figure 4.28 Effect of cutout ring reinforcement on the web buckling

In the C-section beam the most critical region affecting the overall structural stability was the beam flange. Four types of flange reinforcements were therefore designed, modelled and numerically tested in order to increase the C-section beam load carrying capability. The effect of the four reinforcements was firstly tested on cases 1.0 – 1.4 and the most effective flange reinforcement was then applied to the other design cases.

All four reinforcements consisted of L-shaped stiffeners. They were made of the same material and had same laminate stacking sequence as the composite beam. The reinforcement R1 was 10 mm by 10 mm in cross-section, 4 mm in thickness and 176 mm in length and it was positioned on the web, 85 mm from the centre of the cut-out towards the clamped end. The reinforcement R2 was 10 mm by 10 mm in cross-section, 4 mm in thickness and 200 mm in length and connecting the top and bottom flanges and it was positioned at the maximum buckling point (this position varied for each case). The reinforcement R3 was 10 mm by 10 mm in cross-section, 4 mm in thickness and 200 mm in length and it was placed on the critical flange, aligned with the cutout position. The reinforcement R4 was 5 mm by 5 mm in cross-section, 4 mm in thickness and 400 mm in length and it was placed on the critical flange, aligned with the cutout position. Figure 4.29 shows the position of the four reinforcements for case 1.2.
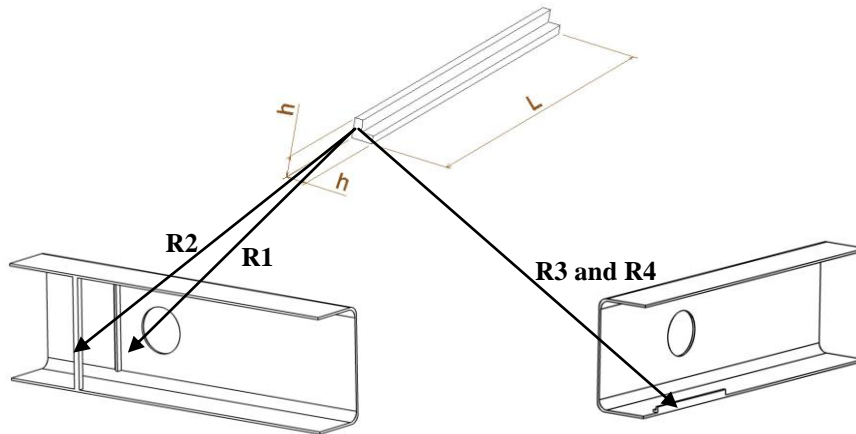
Figure 4.29 Flange buckling reinforcement position

The buckling load factor for cases $1.0 - 1.4$ with and without the four flange buckling reinforcements is shown in Figure 4.30. Since the flange was the most critical region for the C-section beam buckling, the edge flange reinforcements (R3 and R4) were the most efficient types of stiffeners to increase the overall beam stability. As the flange buckling occurred close to the clamped end a relatively larger cross-section stiffener placed in this region (reinforcement R3) proved to be more effective than a longer stiffener with a smaller cross-section (reinforcement R4). The reinforcement R3 was therefore applied to the other C-section beam design cases.
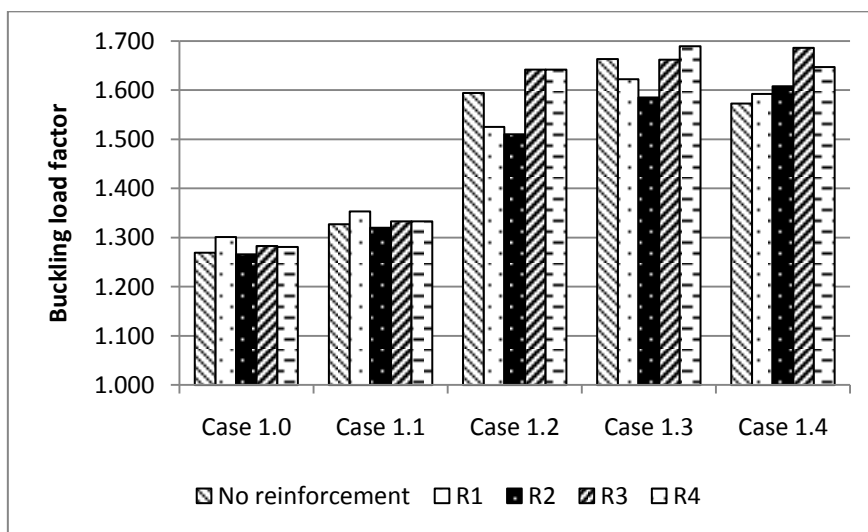
Figure 4.30 Flange reinforcement effect on the bucking behaviour of cases 1.0-1.4

Table 4.18 summarises the first mode BLFs for all design cases 1.0 − 3.3 with reinforced and unreinforced flanges and shows that this type of reinforcement increased the load carrying capability by up to 25%. Reinforcing the critical flange region was therefore demonstrated to be considerably effective for this type of C-section beam design.

Table 4.18 First mode BLFs for cases 1.0 – 3.3with reinforced and unreinforced flange

Case	Unreinforced Flange	Reinforced Flange	Increment rate (%)
1.0	1.269	1.663	23.69
1.1	1.301	1.622	19.79
1.2	1.266	1.585	20.13
1.3	1.283	1.662	22.80
1.4	1.281	1.689	24.16
2.1	1.287	1.602	19.66
2.2	1.284	1.709	24.87
2.3	1.321	1.764	25.11
3.1	1.404	1.789	21.52
3.2	1.418	1.894	25.13
3.3	1.419	1.88	24.52

4.6.5. Reference Wing Spar and Rib Sizing

The stress and buckling analysis results showed how a typical spar section behaves under a shear loading. The thickness of the C-section beam web and the layup used gave a large margin of safety for both stress concentration and buckling. A similar layup was therefore considered to be appropriate for the current reference wing application.

The shear load applied at the wing reference section was interpolated from the graph in Figure 4.3 and it was 429 kN. This load was 21 times larger than the load applied to the C-section beam sample. The spar web cross section supporting this load however was much larger than that of the C-section beam, as the spar height was 0.44 m compared to 0.2 m. Because the stresses in the C-section beam were significantly lower than the

material allowable and also the web buckling load was considerably higher than the applied one, the thickness of the spar web was not required to be increased proportionally to the applied lift induced shear load. The thickness of the spar web was therefore set to be 12mm and the laminate was made of 48 layers arranged in a symmetrical layup $[\pm45/0/\pm45/90/\pm45/\pm45/0/\pm45/90/\pm45/\pm45/0/\pm45/90/\pm45]_s$. Thus, at the wing reference section the spar cross sectional area was nearly 7 times larger than that of the C-section beam web.

The structural behaviour of a rib panel subject to shear loads was also assumed to be similar to that of the C-section beam web. The C-section beam analysis results could be therefore used to set an appropriate thickness for the rib panel at the wing reference section. In addition, as the shear load applied to the rib was in the same order of magnitude as the load applied to the spar section, the same laminate thickness and layup as the spar web were set for the rib.

Following this study the wing box sizing at the wing reference section was completed. The upper and lower skins were made of an intermediate modulus carbon fibre prepreg. The upper surface was 18.5 mm in thickness and it was reinforced with I-shaped stringers (55 mm x 50 mm x 50 mm). The lower cover was 11 mm in thickness and T-shaped stringers (50 mm x 50 mm) were used to prevent buckling. The front spar, the rear spar and the ribs were instead made of a high strength carbon fibre prepreg and they were 12 mm in thickness. These data set the preliminary parameters to ensure a safe structure, however the interaction between these components was also needed to be studied. In particular, the strength of the joint between components has a strong influence on the overall structural strength. The next section presents an example of the mechanical behaviour of a simple assembly of composite components.

4.7. Failure Analysis of a Spar to Skin Joint and Methods to Improve Its Structural Performance

The efficiency of a structure often depends on the strength of its joints where the different components are connected to form a load path. In a wing structure particular attention must be paid at the skin-to-rib and skin-to-spar joints which are subject to large loadings. A vast literature is available on the mechanical and failure behaviour of such typical composite joints and they have been reviewed in section 2.1.3. The use of a combination of composite sandwich and laminated materials, to form the structures' joints, presents significant advantages such as increase in bending rigidity without adding considerable weight penalty. However, the mechanical behaviour of these types of components has not yet been largely explored. This section presents a detailed failure analysis of a composite sandwich T-joint with a composite monolithic base panel. The structural failure modes were studied using the finite element method under both pulling and shear loads and these numerical results were validated by experimental tests. Design improvements for easier manufacturing processes without compromising the structural strength were also suggested and analysed.

4.7.1. The Sandwich T-Joint Structure

Two types of T-joint structures were manufactured and modelled to study their failure mode: one without cutout and one with a circular cutout near the joint region of the web panel. The two structures were made of the same material and had the same dimensions. The T-joint structure was made of two flat panels, a base panel and a web panel joined at a right angle to each other by two L-shaped cleats. The base panel was 160 mm in width and 240 mm in length; the web was 144 mm in height and 240 mm in length as shown in Figure 4.31.

(a)   (b)
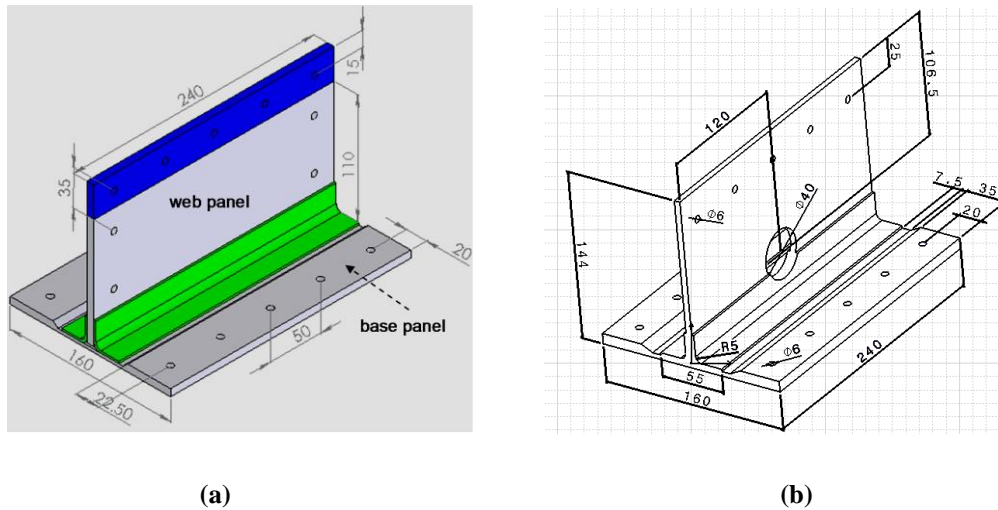
Figure 4.31 Sandwich T-joint geometry details: (a) Without cutout; (b) With cutout

The web panel was made of a 5 mm thick foam bonded to 1 mm thick composite laminate faces, which were made of 4 plies of carbon-epoxy prepreg (MTM46/HTS) in a symmetrical layup $[\pm 45]_s$. Each of the base composite faces was made of 8 plies of the same carbon-epoxy prepreg arranged in a symmetrical layup of $[\pm 45/0/90]_s$ with a thickness of 2 mm. The sandwich base panel had a foam drop off in the joint region where the composite faces were merged into a monolithic laminate. Two L-shaped cleats were bonded to the web faces and the monolithic base laminate to join the two panels together and allow a more efficient load transfer. The cleats were made of plain wave carbon cloths with a total thickness of 2 mm. The joint triangle gap between the web, base panel and cleats were filled with epoxy resin. The material properties of the carbon fibre prepreg used for the sandwich faces and cleats are summarised in Table 4.19, while the foam and adhesive material properties are shown in Table 4.20.

The commercial package MSC PATRAN/NASTRAN was used to create the FE model of the T-joint and its non linear static solution was used to carry out the stress and failure analysis. The sandwich core and the epoxy resin, used to fill the gaps around the joint region, were modelled using 3D solid elements (Hex8 Isomesh); whereas 2D shell elements (QUAD4) were used to model the composite faces, the cleats and the adhesive layers between the core and the composite faces.

Table 4.19 Carbon fibre prepreg mechanical properties

Material	E_1 (GPa)	E_2 (GPa)	G_{12} (GPa)	ν_{12}	X_t (MPa)	X_c (MPa)	Y_t (MPa)	Y_c (MPa)	S (MPa)
Sandwich faces	128.3	9	3.95	0.32	2278	1352	33.9	210	98.1
Cleats	139.6	139.6	52.5	0.3	2278	1352	2278	1352	98.1

Table 4.20 Foam and adhesive material properties

	Foam	Gap filling adhesive	Cleat adhesive	Sandwich adhesive
E *(MPa)*	60	4237	2750	3000
G *(MPa)*	30	1461	1058	-
ν	-	0.3	0.3	0.3
Shear strength (MPa)	1.3	28.9	24.1	36
Tensile strength (MPa)	1.5	46	35.2	-

4.7.2. The Sandwich T-Joint Structure under a Pulling Load [218]

Figure 4.32 (a) shows the T-joint sample mounted on the test rig for the pulling test. Both base and web panels were bolted to steel test rig components. The pulling load was applied upwards through the web panel. Figure 4.32 (b) shows the loads and boundary conditions applied to the FE model. The base was clamped at the 5 bolt locations. In order to simulate the test conditions accurately, the displacement of the upper face of the sandwich base near the thickness drop-off was constrained in the z-direction. The pulling load was applied to the web panel at the 5 bolting positions.

<div align="center">
(a)   (b)
</div>
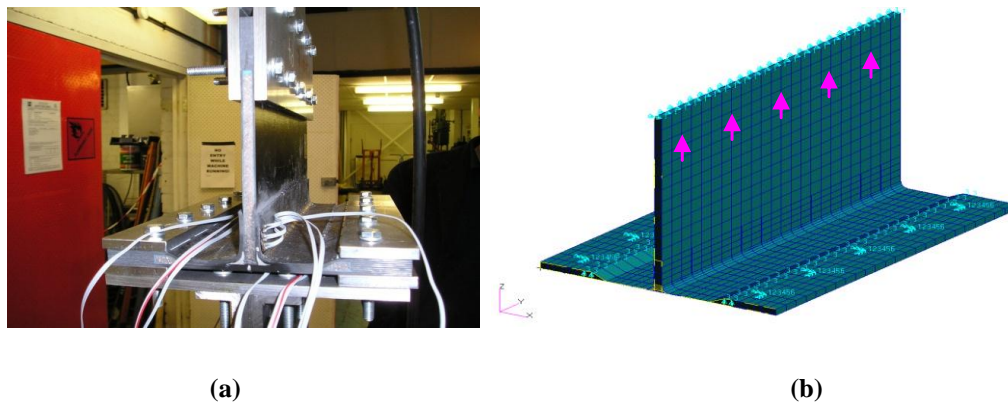
Figure 4.32 T-joint sample: (a) Pulling test set up; (b) FE model loads and boundary conditions

Several strain rosettes were mounted to the test samples to measure the strain at different locations on the bottom surface of the base panel and the cleat as shown in Figure 4.33 (a). Figure 4.33 (b) shows the position and direction of the strain gauges on the bottom surface of the base panels of the test samples with and without cutout. These data were used for FE result comparison.

<div align="center">
(a)   (b)
</div>
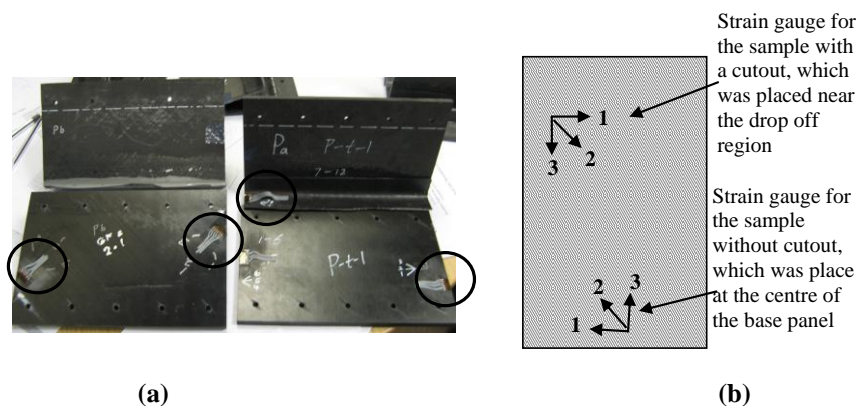
Figure 4.33 (a) Strain gauge location; (b) Strain gauge arrangement and direction

Three test samples without cutout and two samples with cutout were tested under a pulling load. For all 5 cases, the load was applied until the web panel was completely pulled away from the base panel, as shown in Figure 4.34 (b). Table 4.21 summarises the test and FE failure load and strain measurement results. For the strain comparison the measurements of gauge 2 (see Figure 4.33 (b)) were compared with the FE analysis

results. The strain gauge readings were very sensitive to the gauge position; therefore each test measurement was compared with the one obtained by FE analysis.

Table 4.21 Pulling test and FE failure load and strain measurement comparison

	Test Sample	Test Failure Load (kN)	FE Failure Load (kN)	Test Strain ε_2 ($\mu\varepsilon$)	FE Strain ε_2 ($\mu\varepsilon$)
T-joint without cutout	Pa	18.9	20	-1695	-1720
	Pb	16.6	20	800	921
	Pc	17.8	20	241	489
T-joint with cutout	Pd	14.2	16.5	518	646
	Pe	13.2	16.5	223	277

The initial failure load prediction for the T-joint without cutout was 22 kN. Under this load the in-plane shear stress of the inner ply of the composite cleat was 170 MPa, which exceeded the material allowable stress of 98.1 MPa. The cleat adhesive also failed under this pulling load due to the combination of high tensile and shear stresses near the edge of the base panel where the von Mises stress was 27.3 MPa.

(a)   (b)

Figure 4.34 Manufacturing defects: (a) Initial adhesive paste crack; (b) Excess of adhesive paste

The test samples, however, contained some manufacturing defects. Before the experiment, paste adhesive cracks at the triangular region of the joint were noticed, as shown in Figure 4.34 (a) and after the test excessive paste adhesive between the cleat and the base panel composite face was observed, as shown in Figure 4.34 (b). These manufacturing defects were implemented in the FE model and it was found that under these conditions the structural failure occurred at 20 kN.

Three types of failure were observed at these conditions: cleat failure, cleat adhesive failure and paste adhesive failure. The composite cleat failed due to high in-plane shear stresses at the curvature region, where the shear stress was 154 MPa, as shown in Figure 4.35 (a). The cleat adhesive failed near the edges of the panel, as shown in Figure 4.35 (b), due to the combination of high tensile and shear stresses near the edge of the base panel where the von Mises stress was 24.4 MPa. Failure also occurred in the region with excessive adhesive paste, as shown in Figure 4.35 (c). The von Mises stress in this region was 41.5 MPa. Due to the large bending, induced by the pulling load, the monolithic panel stress in the off fibre direction was relatively high. The stress level was however, within the material allowable stresses as shown in Figure 4.35 (d): the maximum off fibre stress was 22.7 MPa at the centre of the panel.

The initial failure load prediction for the T-joint with the cutout was 18 kN, 18% lower than the failure load of the T-joint without the cutout. Under this load the in-plane shear stress of the inner ply of the composite cleat was 153 MPa, which exceeded the material allowable stress of 98.1 MPa. The cleat adhesive also failed under this pulling load due to the combination of high tensile and shear stresses near the edge of the base panel, where the von Mises stress was 33.7 MPa.

(a)

(b)

(c)

(d)
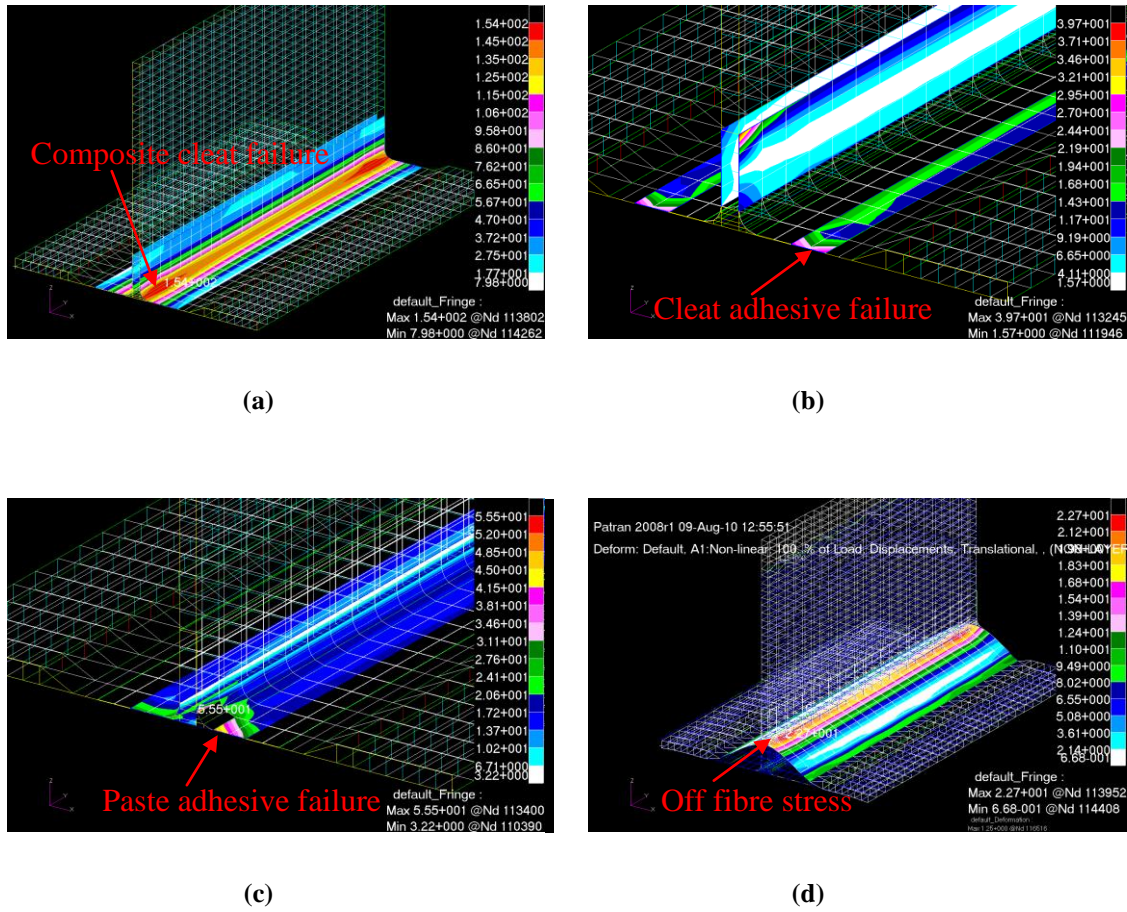
Figure 4.35 T-joint without cutout stress (MPa) at 20 kN: (a) Composite cleat shear stress; (b) Cleat adhesive von Mises stress; (c) Paste adhesive von Mises stress; (d) Composite monolithic panel off fiber stress

When the effect of manufacturing defects was considered the T-joint failure load was 16.5 kN. As for the previous case without cutout, the structural failure was due to: cleat failure, cleat adhesive failure and paste adhesive failure. The composite cleat failed due to high in-plane shear stresses at the curvature region, where the shear stress was 139 MPa, as shown in Figure 4.36 (a). The cleat adhesive failed near the edges of the panel, as shown in Figure 4.36 (b), due to the combination of high tensile and shear stresses near the edge of the base panel where the von Mises stress was 25.9 MPa. Failure also occurred in the region with excessive adhesive paste, as shown in Figure 4.36 (c), where the von Mises stress was 44.1 MPa. The pulling load caused also in this case, a large bending of the base panel, however the off fibre stress at the centre of the monolithic panel was below the material allowable and it was 20 MPa.

(a)

(b)

(a)

(b)
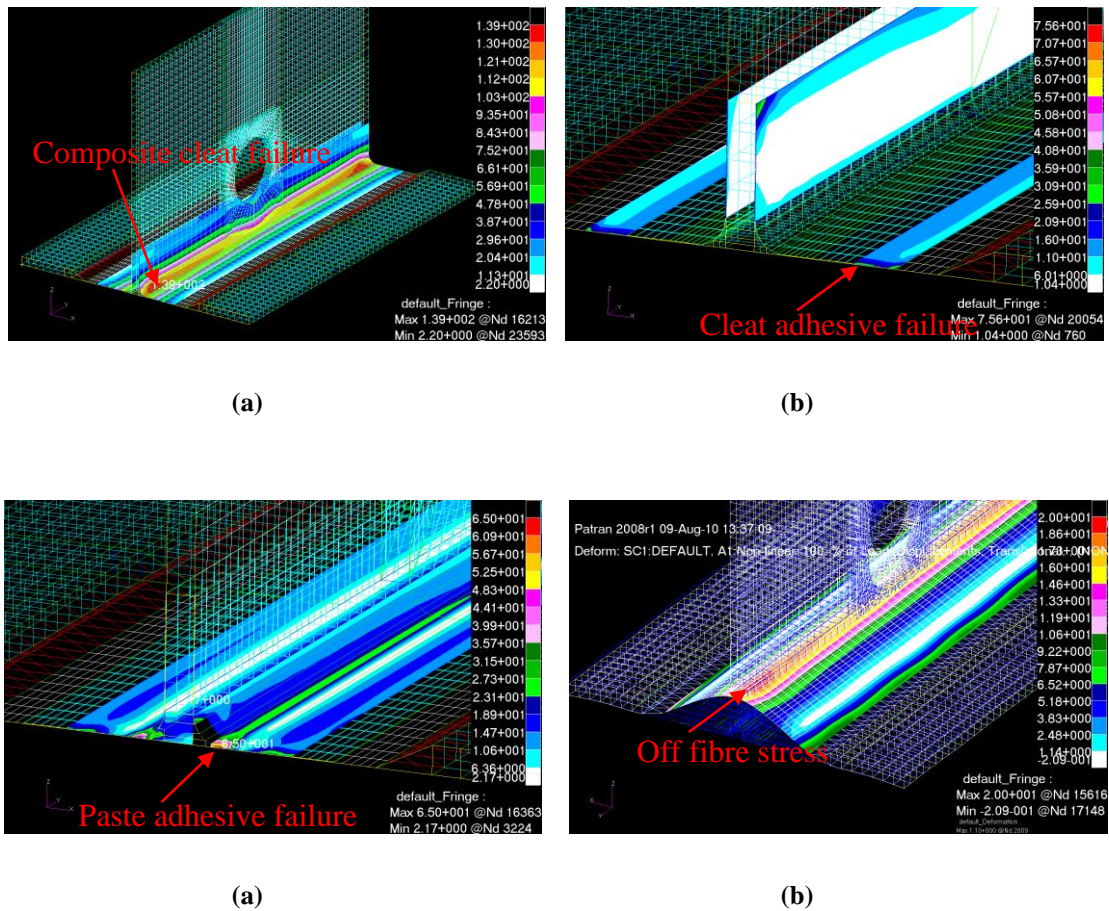
Figure 4.36 T-joint with cutout stress (MPa) at 18 kN: (a) Composite cleat shear stress; (b) Cleat adhesive von Mises stress; (c) Paste adhesive von Mises stress; (d) composite monolithic panel off fiber stress

4.7.3. The Sandwich T-Joint Structure under a Shear Load [219]

Two types of test rigs were manufactured to carry out the shear tests. Figure 4.37 (a) shows the T-joint sample test setup under shear load, mounted on the initially designed L-shaped test rig. The T-joint sample base panel was bolted to a steel flat panel mounted to the test machine and the web was bolted to an L-shaped steel test rig. The shear load was produced by pulling the upper end of the L-shaped rig upwards. Due to excessive deformation of the L-shaped test rig after the first test, a modified triangle shaped test rig as shown in Figure 4.37 (b) was used to replace the L-shaped test rig.

(a)   (b)
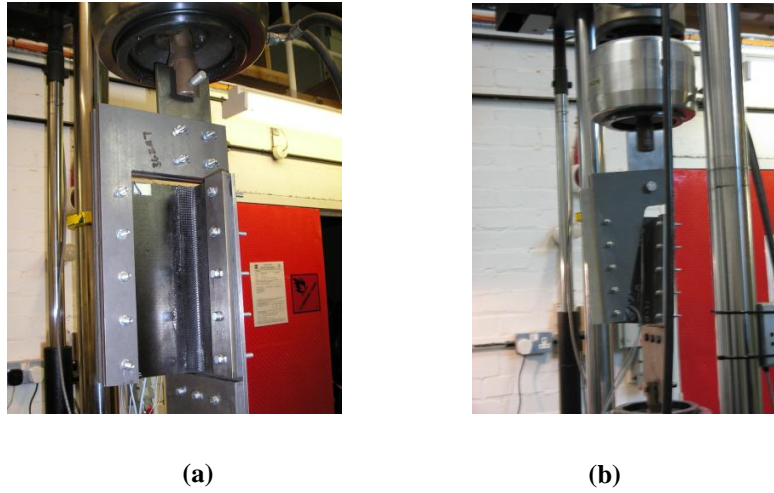
Figure 4.37 Rigs for shear test: (a) Original L-shape test rig; (b) Modified test rig

Figure 4.38 (a) shows the load and boundary conditions set in the FE model when the L-shaped test rig was used. The base was clamped at the 5 bolt locations and the shear load was applied through the 5 bolts on the web. The top edge of the web panel was constrained in the x-direction. During the test, an in-plane bending moment was induced on the web panel due to the complementary shear load. In the FE model, this in-plane bending moment was simulated by applying forces in opposite directions along the z-axis at the bolt positions as shown in Figure 4.38 (a). Figure 4.38 (b) shows the loads and boundary conditions applied to the FE model with the modified test rig. In this case, the load distribution at the bolt positions was updated according to the modified test rig shape.

→ Shear load
→ Reaction load due to bending

(a)   (b)
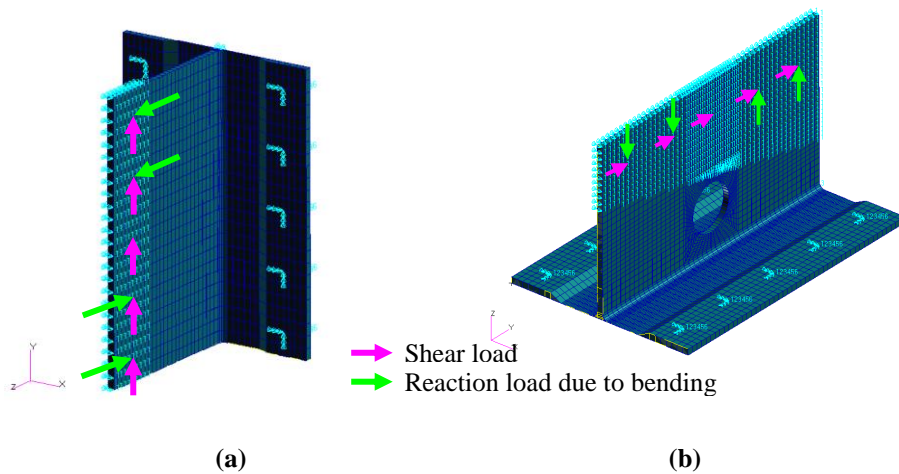
Figure 4.38 Loads and boundary conditions set in the FE model: (a) L-shape rig; (b) Modified rig

Figure 4.39 shows the strain gauge position on the web panel for the shear test samples. For the samples without cutout, the shear force was applied relatively to the off-fibre direction of the web face outer layer as shown in Figure 4.39 (a); whereas for the samples with the cutout the shear force was applied in the fibre direction of the web outer layer as shown in Figure 4.39 (b).

(a)   (b)
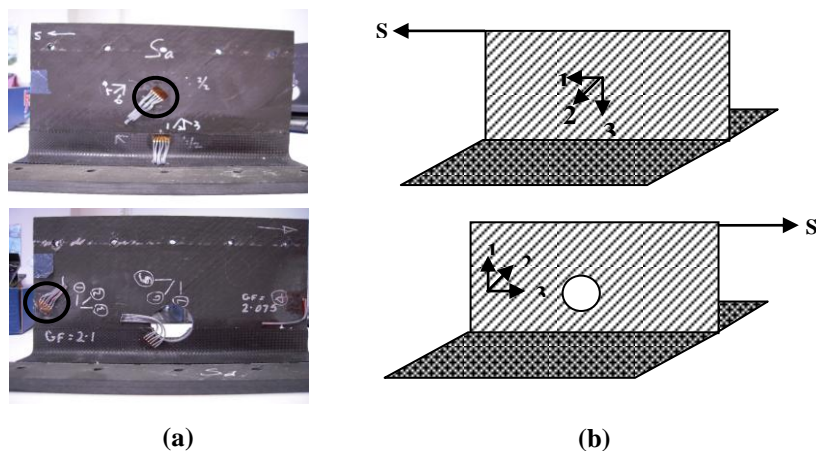
Figure 4.39 Web panel strain gauge arrangement

Three samples without the cutout (samples Sa, Sb and Sc) and two samples with the cutout (samples Sd and Se) were tested under a shear load. The first sample was tested using the L-shaped test rig. All the other samples were tested using the modified test rig. The test results shows that the sample Sa failed due to the web buckling and high tensile stress in off fibre direction in the first layer of the web face, see Figure 4.40 (a). Fibre peel off was observed near the edges of the web panel where buckling occurred. For the other two samples without cutout, the actual failure mode of the joint was not reached as severe damage around the bolting position occurred; see Figure 4.40 (b).

The samples with the cutout failed due to web buckling around the cutout, see Figure 4.40 (c). In this case however, although the web composite face off fibre stress was high, fibre peel off was not observed. This showed that the direction of the applied shear force relative to the material orientation of the composite web panel has an influence on

the structural performance of the joint. Designing the web panel in such a way that the shear load is applied in the fibre direction of the outer layer of the web composite face could be beneficial to avoid fibre peel off.

(a)

(b)   **(c)**
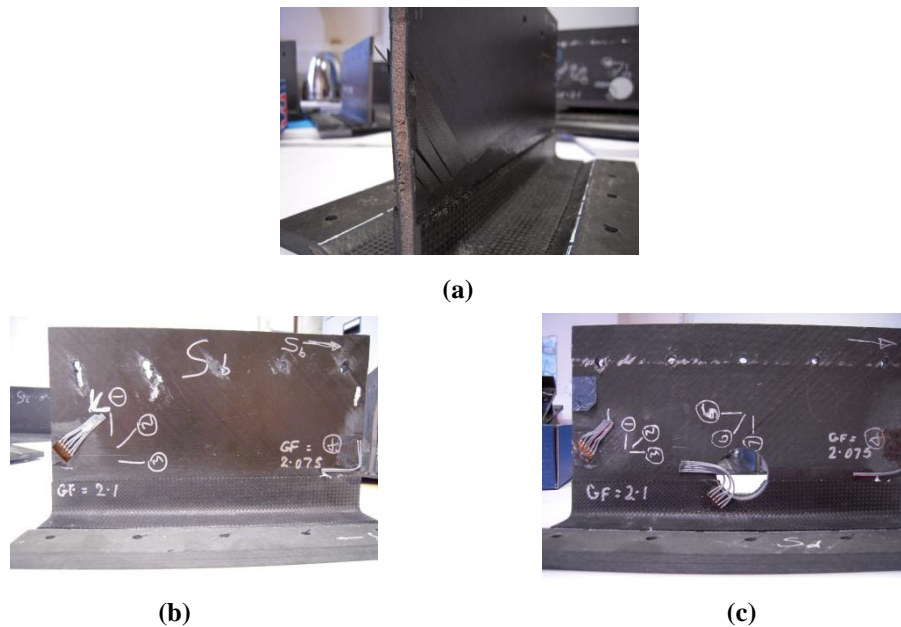
Figure 4.40 Test sample failure: (a) Sample Sa; (b) Sample Sb and (c) Sample Sd

The strain measurements of gauge 2 (see Figure 4.40) were compared with those obtained from the FE analysis, see Table 4.22. It is noted that the strain gauge readings for the test samples Sb and Sc were not compared due to the unexpected extensive bearing failure of the bolt and hole.

Table 4.22 Shear test and FE failure load and strain comparison

	Test Sample	Test Failure Load (kN)	FE Failure Load (kN)	Test Strain (με)	FE Strain (με)
T-joint without cutout	Sa	41.7	43	-2771.6	-2895
	Sb/ Sc	27.4/35.4	-	-	-
T-joint with cutout	Sd	35.1	37	-576.6	-329
	Se	35.7	37	-390.6	-329

The FE analysis for sample Sa showed that the T-joint web panel buckled at 40.5 kN as shown in Figure 4.41 (a). The web composite face, however, failed at 43 kN. At this loading level, the tensile stress of the outer ply in the off-fibre direction was 34.8 MPa as shown in Figure 4.41 (b), which exceeded the material allowable strength of 33.9 MPa.

(a)   (b)

Figure 4.41 T join in shear using the test rig 1: (a) Web buckling at 40.5 kN; (b) Web outer ply off fibre stress at 43 kN

When the FE analysis was carried out without considering the bolt bearing failure by using the modified test rig, the bucking load was 54 kN. In this case the buckling occurred more towards the centre of the web, as shown in Figure 4.42 (a). The ply failure in the off-fibre direction due to high tensile load acting on the upper part of the structure occurred in the outer layer of the composite face at 58 kN when $\sigma_2 = 33.3$ MPa, see Figure 4.42 (b).

(a)   (b)
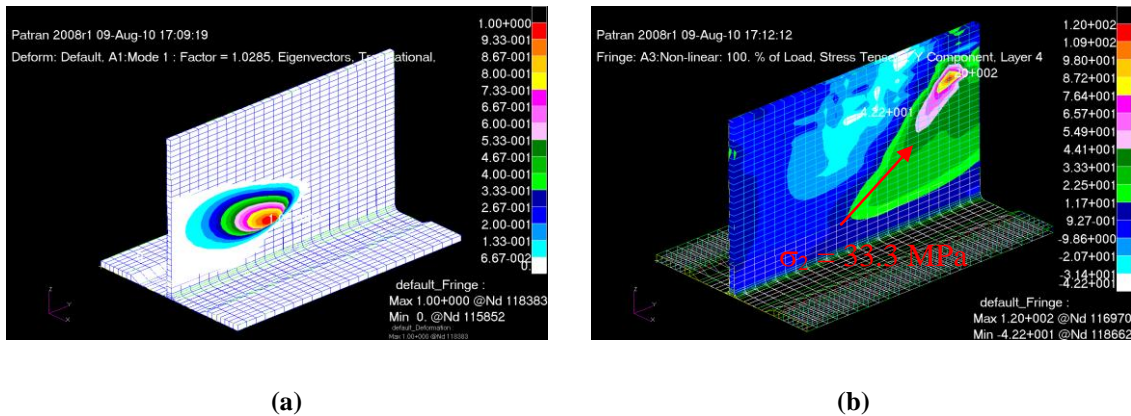
Figure 4.42 T joint in shear using the test rig 2: (a) Web buckling at 54 kN; (b) Web outer layer off fibre stress at 58 kN

For the T-joint with the cutout using the modified test rig, the predicted failure load under shear was 37 kN, 31% lower than the case without the cutout (samples Sb/ Sc). The structure failure was caused by both web buckling and stress concentration around the cutout, as shown in Figure 4.43. The maximum stress around the cutout occurred in the outer ply in the off-fibre direction and it was 36 MPa, see Figure 4.43 (b).

(a)   (b)
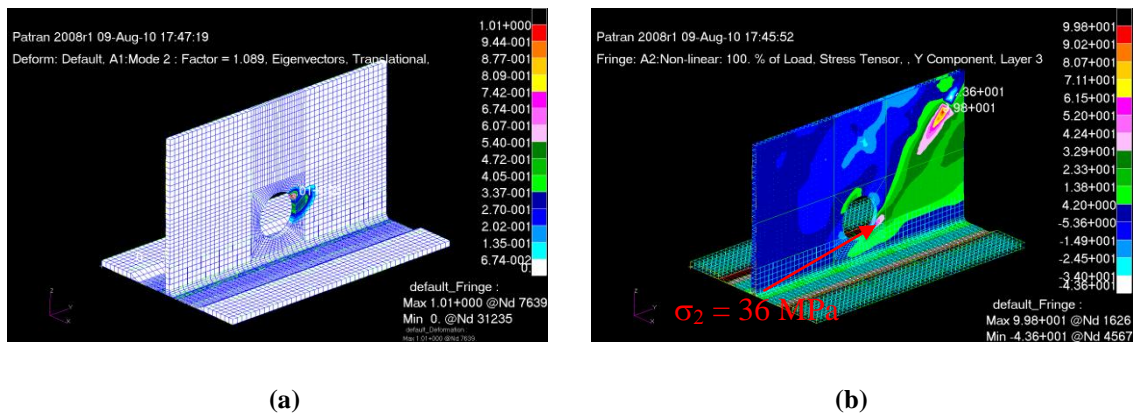
Figure 4.43 T-joint with cutout in shear at 37 kN: (a) Web buckling; (b) Web outer ply off fibre stress (Units MPa)

4.7.4. Alternative Design for the T-Joint Structure [220]
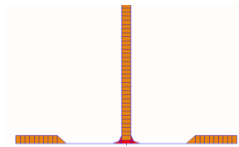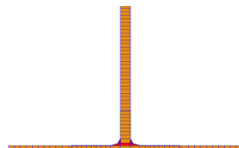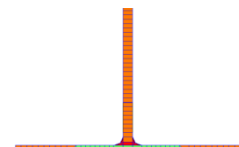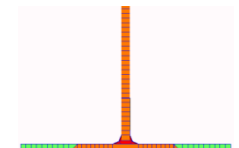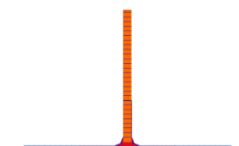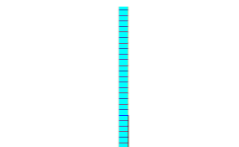
A simple sandwich T-joint without dropping the base core would make the manufacture process much cheaper and easier and at the same time the bending stiffness of the base panel could be improved. Five alternative designs with different base or web core materials were modelled and analysed to evaluate the new design. Table 4.24 presents a summary of the different design cases. Case 1 was the baseline T-joint with the base drop off, Cases 2 − 5 were the alternative designs with different base materials, glass fibre or aluminium honeycomb, and were evaluated under pulling. Cases 2 − 4 and 6 were the alternative designs with different base and web materials and were evaluated under shear. The boundary and loading conditions applied to the alternative cases were the same as the one described in Section 4.7.2 for pulling and Section 4.7.3 for shear.

The mechanical properties of the glass fibre and aluminium honeycomb are shown in Table 4.23.

Table 4.23 Honeycomb mechanical properties

Material	E (MPa)	G(MPa)	X (MPa)	S (MPa)
HRP-1/4-6.5 (Glass fibre)	827	172	6.34	3.1
1/16-5052-0.0015 (Aluminium)	4481.59	1447.9	18.27	7.92

Table 4.24 Summary of design cases

Case	Description	
1	T-joint with central monolithic panel: baseline model with the sandwich base foam drop off.	
2	T-joint with foam core: both web and base are made of sandwich composite panels with a foam core.	
3	T-joint with honeycomb central insert: the core of the central part of the sandwich base is made of fibre glass honeycomb (green region).	
4	T-joint with localised honeycomb insert: the sides of the core of the sandwich base are made of fibre glass honeycomb (green region).	
5	T-joint with foam and honeycomb core: the core of the web panel is made of foam while the base core is made of aluminium honeycomb. (This model was evaluated only under pulling)	
6	T-joint with foam and honeycomb core: the core of the base panel is made of foam while the web core is made of aluminium honeycomb. (This model was evaluated only under shear)	

Evaluation under Pulling

Table 4.25 shows a summary of the evaluation of the different design cases: the alternative designs, Cases 2-5, are compared with the baseline T-joint with the base drop-off. For all cases the structure, under the applied pulling load, deformed in a similar manner and only the magnitude of deflection differed. Figure 4.44 shows the *z*-direction displacement for Case 5 when the failure load was applied to the structure. When the centre of the base core was made of foam (Cases 2 and 4) the failure load was much lower than case 1. The stiffness of the core was too low to withstand the applied pulling load and also the deformation was relatively higher than the other cases. This indicates that the high bending stiffness advantage that a sandwich panel should have was not fully exploited. Higher failure load was in fact achieved when the centre of the core was made of honeycomb and in particular when the aluminium honeycomb was used.
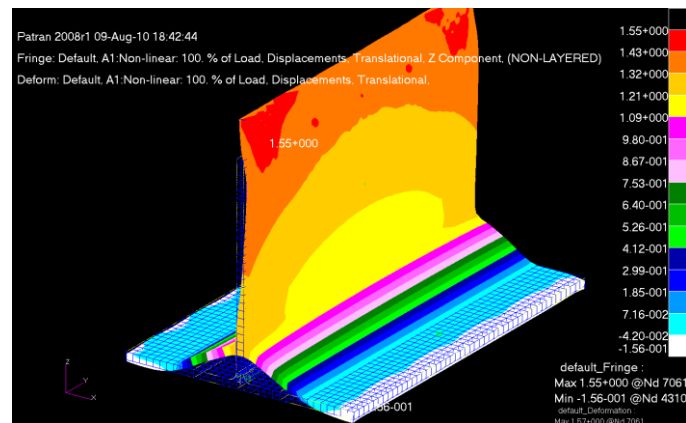
Figure 4.44 Design Case 5 *z* – direction displacement at 20 kN

For the design Cases 2 and 4 the structure failure was due to the combination of high tensile *z*-component stresses and through thickness shear stresses in sandwich base core, see von Mises stresses in Table 4.25. For Cases 3 and 5 the structure failure was due to the high through thickness shear stress in the honeycomb core and high in plane shear stress in the composite cleat, as shown in Figure 4.45 (a) and (b). In all design cases, as

shown in Table 4.25, the stress of the sandwich base composite faces or monolithic panel was not critical. The highest level of stress was concentrated at the joint of the structure and at the sides of the base near the clamped region, as shown in Figure 4.46.

(a)   (b)
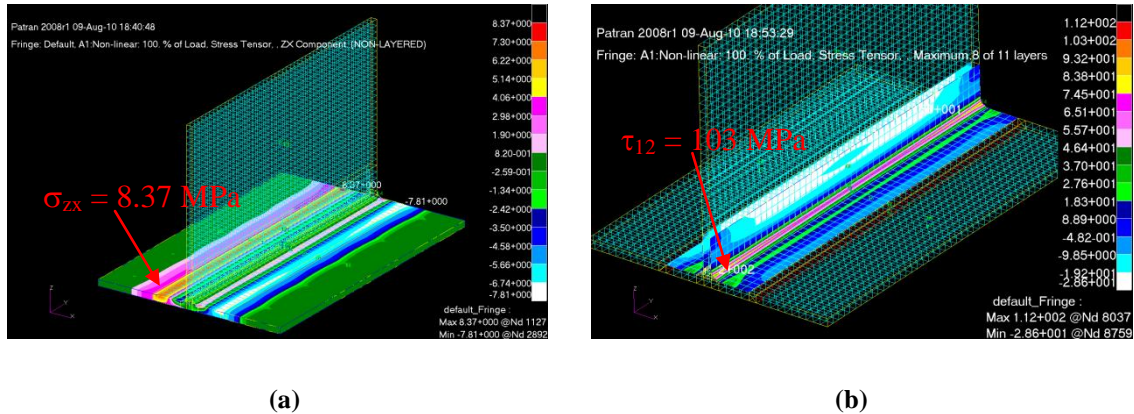
Figure 4.45 Case 5 structural failure at 20 kN: (a) Honeycomb core failure; (b) Cleat failure
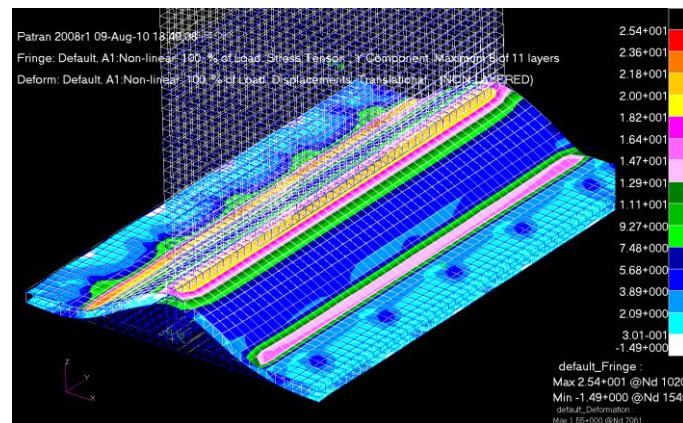
Figure 4.46 Case 5 base composite faces off fibre stress at 20 kN

Table 4.25 shows that Case 5 is the best configuration among the four alternative designs. Although its failure load is slightly lower than the original T-joint with the base drop off, it represents a good trade off between structural strength and manufacturing ease.

Table 4.25 Design cases comparison under pulling

	Design Cases				
	1	2	3	4	5
Failure Load (kN)	22	1.5	15	2	20
z-displacement (mm)	1.38	0.2	1.34	0.22	1.55
Cleat adhesive von Mises stress (MPa)	24.4	2.26	22.2	2.82	27.1
Base core von Mises stress (MPa)	-	1.32	-	1.52	-
Base core z-stress	-	-	6.75	-	7.7
Base core zx- stress (MPa)	-	-	5.51	-	8.37
Base composite off fibre stress (MPa)	24.9	2.87	22.1	3.07	25.4
Failure index	1.01	0.17	0.95	0.2	1.04
Cleat in-plane shear stress (MPa)	99.3	14.9	87.6	18.1	103

Evaluation under Shear

Table 4.26 shows a summary of the evaluation of the different design cases: the alternative designs, Cases 2-4 and 6, are compared with the baseline design of the T-joint, case 1. The primary cause of failure of the T-joint structure for Cases 2-4 was the web buckling, as it occurred for the baseline Case 1, see Figure 4.47. This buckling however, did not cause the fibre or matrix failure of the composite sandwich faces. Another cause of failure was the high shear stress in the cleat adhesive near the edge of the web flange of the cleat; see Figure 4.48 (b). When the web core was made of aluminium honeycomb the structure was much stronger. The failure load was higher than that of the baseline and also the buckling load was considerably higher. The causes of failure for this design case were the high shear stress in the web honeycomb core and high shear stress in the cleat adhesive, see Figure 4.48 (a) and Figure 4.48 (b).
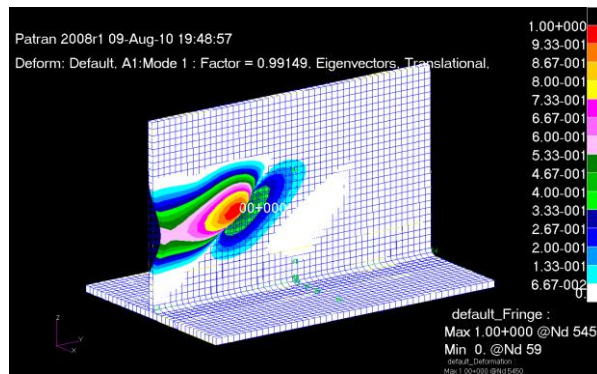
Figure 4.47 Design Case 2 web buckling at 30 kN

Table 4.26 Design cases comparison under shear

	Design Cases				
	1	2	3	4	6
Failure load (kN)	43	30	30	30	50
Buckling load factor	0.94	1.0	1.0	1.0	7.7
Cleat adhesive shear stress (MPa)	29.9	27.1	27.1	27.1	39.8
Web core shear stress (MPa)	11.1	10.0	10.1	10.0	13.9
Web core z-stress (MPa)	0.95	1.09	0.52	0.41	14.3
Web composite off fibre stress (MPa)	34.8	29.4	29.4	29.4	30.4
Failure index	1.02	0.62	0.67	0.67	0.85
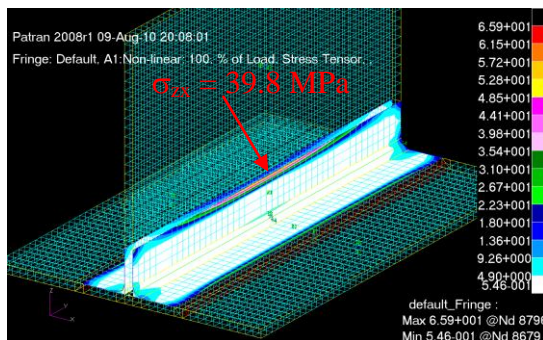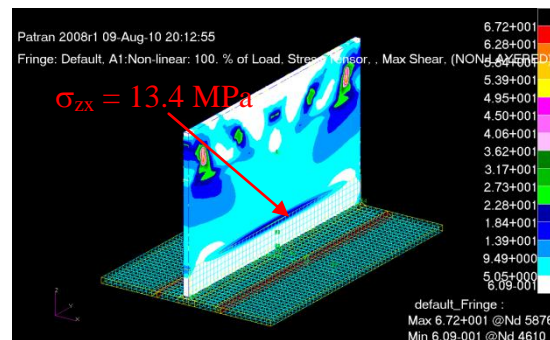
(a)   (b)

Figure 4.48 Design Case 6 at 50 kN (a) Cleat adhesive shear stress; (b) Web core shear stress

Table 4.26 shows that Case 6 is the best configuration among the four alternative designs for the T-joint structure under a shear load. Its failure load is higher than that of the baseline and therefore both structural and manufacturing advantages are greater for this alternative design case.

This section showed how pulling shear loads are transmitted across a structure's joint and how failure initiates and propagates in the various components of the joint. The analyses of the sandwich joint also pointed out an important design aspect. It was in fact demonstrated that by choosing an adequate layup surface fibre peel off can be avoided or delayed in a composite joint component subject to both shear load and bending. Furthermore, it was also shown that by increasing the local stiffness of the joint the global performance of the structure can greatly be improved.

Although the study case did not represent a particular section of the reference wing it provided illustrative results from which the behaviour of the skin-to-spar and the skin-to-rib joints under the applied external loads can be generally assumed.

This section concludes the preliminary design study of the composite reference wing. In the following chapter the design of the morphing leading edge is discussed and its feasibility is studied.

Chapter 5

5. Design and Analysis of the Morphing Leading Edge

Conventional transport aircraft leading and trailing edge high lift devices consist of movable control surfaces which increase the lift generated by the wing when they are in their extended position at takeoff and landing. The current demands to increase the lift to drag ratio, reduce noise emissions and fuel consumption require however a more laminar flow which cannot be achieved by these existing high lift systems. The conventional devices in fact do not provide the required high quality continuous surface that laminar flow relies on. Seamless morphing technology is therefore considered a potential solution to achieve the required increase in aerodynamic efficiency. This chapter presents the design and analysis of a gapless morphing leading edge which offers the potential of obtaining a more laminar flow over the wing. The gapless structure also enables a significant reduction in airframe noise and the laminar flow enables to reduce the drag over the wing airfoil. Furthermore, this increase in lift to drag ratio leads to a steeper climb at constant thrust reducing the noise footprint at takeoff.

Section 5.1 [221, 222] presents the reference wing section geometrical details and the structural requirements to obtain the desired morphed leading edge deflected shape. The design of the actuation mechanism and the FE modelling of the structure with integrated actuation system is also describes in the same section. The aerodynamic pressure distribution was obtained at different flight conditions and the actuation forces required

to deflect the leading edge and overcome the external loads were calculated at landing condition (Section 5.2) [223]. The results of the leading edge structure's static analysis due to the external pressure load are then presented in Section 5.3 [221] while Section 5.4 summarises the non linear static analysis results of the wing box and leading edge structure. Finally the morphing leading edge dynamic response behaviour is described in Section 5.5 [221].

5.1. The Reference Wing with the Morphing Leading Edge

The study of the morphing leading edge structure was carried out at the wing reference section, where the wing chord was 4 m, as shown in Section 4.1. When the leading edge structure was analysed on its own a unit span section was considered, while when the wing box structure was also analysed a 2 m tapered section was considered.

5.1.1. The Wing Box and Morphing Leading Edge Geometry and Materials

The leading edge at the reference section was 0.86 m chordwise, 1 m spanwise and 0.44 m in height, as shown in Figure 5.1. The leading edge skin was reinforced by eight metallic I-shaped stringers on both upper and lower skin panels, with 0.12 m pitch distance, and their flange and web were 12 mm in length and 3 mm in thickness. In the initial design two types of materials were selected for the leading edge skin: a metallic option, aluminium 2024-T81 (Al), and glass fibre (GF). The aluminium skin was 2 mm in thickness while the glass fibre skin was 3mm in thickness made of 12 layers arranged in a symmetrical layup $[\pm45/0_3/90]_s$. Table 5.1 and show the mechanical properties of glass fibre and aluminium.

The wing box at the reference section was 1.855 m, the front and rear spars were 0.438 m and 0.364 m in height respectively. The upper wing cover was reinforced by fourteen I-shaped stringers (55 mm x 50 mm x 50 mm) while the lower skin was reinforced by fourteen T-shaped stringers (50 mm x 50 mm), as shown in Figure 5.2. Both skin and stringers were made of carbon fibre prepreg (HexTow IM7), which mechanical properties are shown in Table 5.1; however the skin laminate plies were 0.25 mm thick

while the stringers laminate plies were 0.184 mm thick. The upper skin was made of 74 layers arranged in a symmetrical layup $[0_2/45/90/-45/0_2/45/90/-45/0_2/45/90/-45/0_2/45/90/-45/0_2/45/90/-45/0_2/45/90/-45/0_2/45/90/-45/0_2]_s$ with a total thickness of 18.5 mm. The upper skin stringers' web and flange laminates had the same layup as the skin but the total thickness was 13.616 mm. The lower skin was made of 44 layers arranged in a symmetrical layup $[0_2/45/90/-45/0_2/45/90/-45/0_2/45/90/-45/0_2/45/90/-45/0_2]_s$ and the total thickness was 11 mm. The stringers reinforcing the lower wing cover had the same layup as the skin but the flange and web thickness was 8.096 mm.
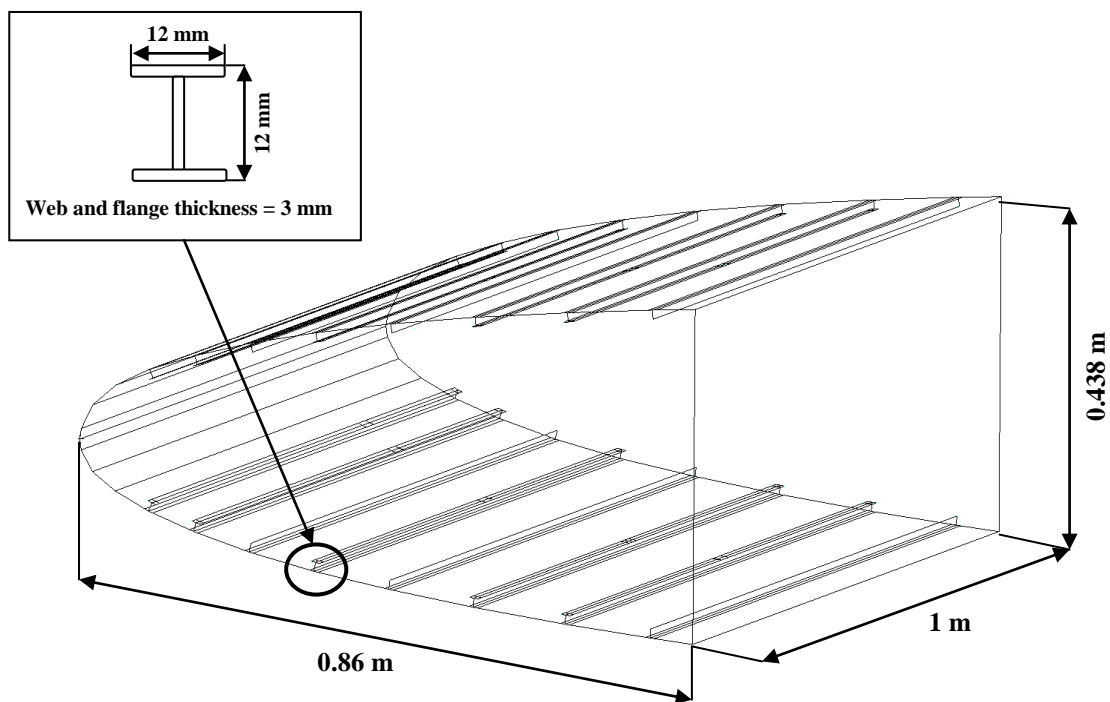
Figure 5.1 Details of the leading edge geometry at the wing reference section
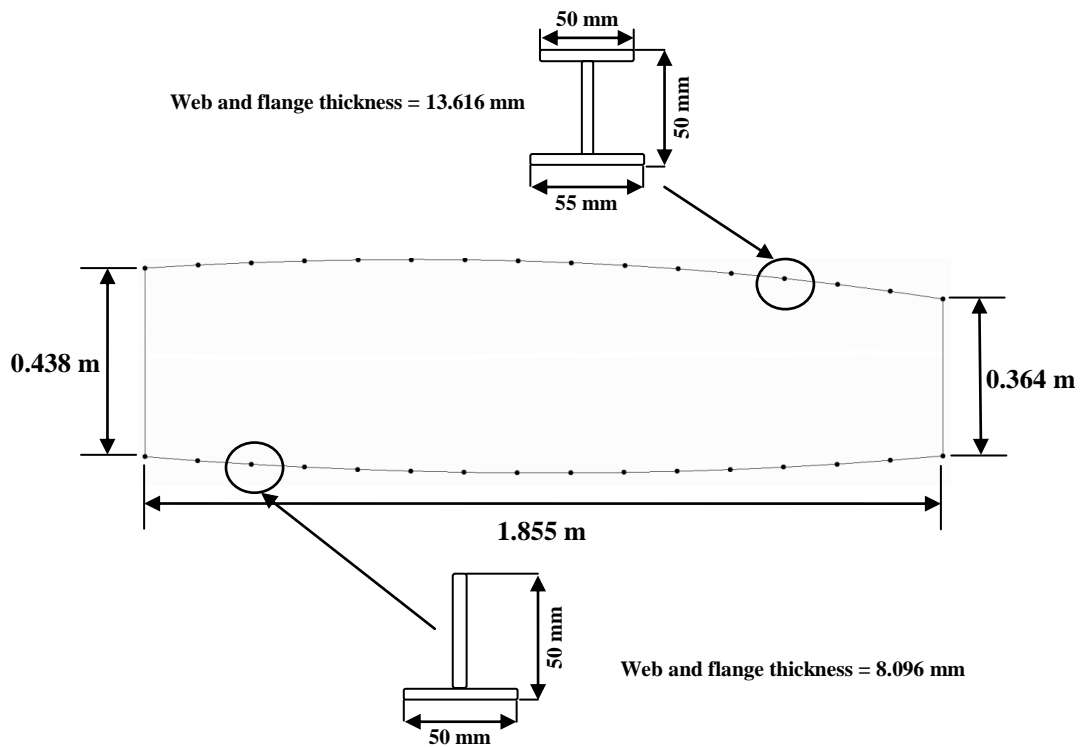
Figure 5.2 Details of the wing box geometry at the wing reference section

The 2 m wing box and leading edge section was taken from the reference point outboard. The ribs pitch was 0.655 m and the total length of the wing box and leading edge at the outer end of the section was 2.4 m as shown in Figure 5.3. The spars and ribs were made of a high strength carbon/epoxy composite laminate (M21/T800S), which properties are shown in Table 5.1, with 48 layers arranged in a symmetrical layup $[\pm45/0/\pm45/90/\pm45/\pm45/0/\pm45/90/\pm45/\pm45/0/\pm45/90/\pm45]_s$ with a total thickness of 12 mm. The cutouts at the front spar, which were needed to allow the eccentric beams to be connected to the actuator, were reinforced by composite laminated rings. As shown in Section 4.6, this method proved to be an efficient way to reduce the stresses in the spar web. The reinforcement rings were also made of the high strength carbon/epoxy composite laminate (M21/T800S) and they were 4 mm in thickness with 16 layers $[0/\pm45/90/90/\pm45/0]_s$.
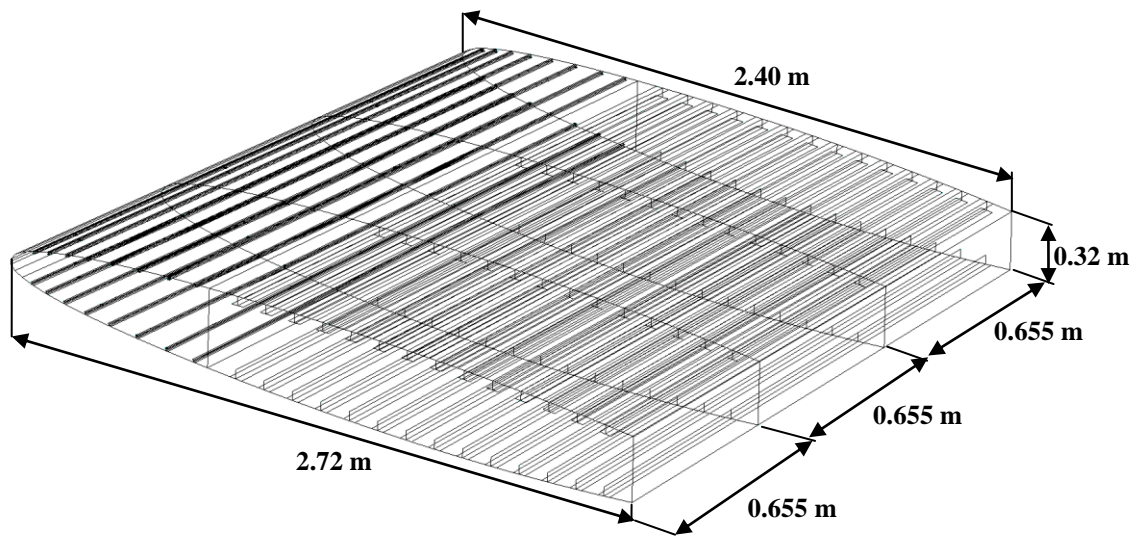
Figure 5.3 Geometrical details of the 2 m section wing box and leading edge

Table 5.1 Reference wing material properties [211 – 213]

	E_1 (GPa)	E_2 (GPa)	G_{12} (Gpa)	ν_{12}	X_t (Mpa)	X_c (Mpa)	Y_t (Mpa)	Y_c (Mpa)	S (Mpa)	ρ (kg/m^3)
GF	39	8.6	3.8	0.28	1080	620	39	128	89	2100
Al	72.4		28	0.33	450		-		295	2780
IM7	164	10	5	0.3	2723	1689	101	223	74	1780
M21	172	10	5	0.3	3939	1669	50	250	79	1580

5.1.2. Structural Requirements

Several requirements were set for the leading edge structure and its morphing deflected shape in order to ensure a laminar flow over the wing. A smooth change in curvature was necessary in the deployed position therefore the upper and lower surfaces were gapless and 12% of the leading edge was considered to be rigid, as shown in Figure 5.4. Furthermore, to avoid strong suction peaks for high angles of attack, which lead to poor high lift behaviour, the leading edge nose radius was required to increase, during deployment, to twice as large as the retracted position. The maximum vertical and

horizontal displacements needed to obtain the required lift were 6% and 1.2% of the wing chord respectively.
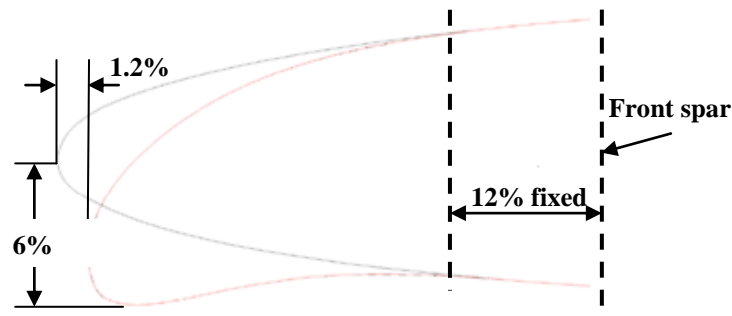
Figure 5.4 Leading edge deflection requirements

5.1.3. The Eccentric Beam Actuation Mechanism

The current actuation mechanism design was based on the concept presented in the DARPA smart wing project and the research work conducted by Muller [172-177]. In both designs an eccentric curved beam was used to convert a rotational motion generated by an actuator into a vertical displacement along the beam which deflected the wing trailing edge, as shown in Figure 5.5 (a). The required trailing edge cambered shape was determined by the beam curvature at all rotating angles. Spanwise plates were placed along the chord and cutouts were created so that the beam could go through them and push the trailing edge structure downward when it was rotated, as shown in Figure 5.5 (b). Using this bent beam concept, a rotation of 90º was enough to obtain a maximum deflection of the control surface.

(a)   **(b)**
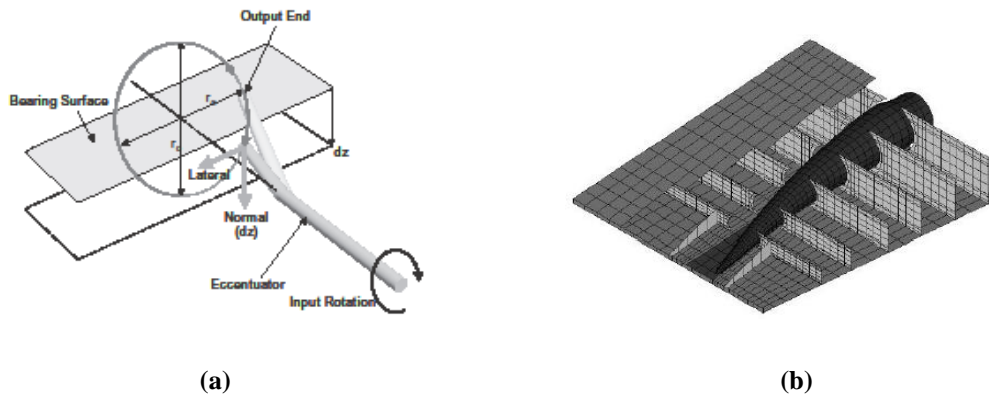
Figure 5.5 Eccentric Beam Actuation Concept: (a) Beam rotational motion; (b) Mechanism details

The original design however was not suitable to be applied for a morphing leading edge. The deployment of this control surface in fact required a change in distance between the upper and lower surface during deployment which was not possible if spanwise rigid plates were placed along the chord. A key improvement implemented in the current design was that the rigid plates were substituted by a number of different size discs, with varying radius, mounted along the bent beam, as shown in Figure 5.6 (a). The combination of the designed beam curvature and the disc dimension ensured that the leading edge skin deformed in the specified shape at any rotational angle. When the beam was rotated by the actuator, the discs connected to the stringers forced the skin to deform in the required shape as illustrated in Figure 5.6 (b).

(a)   **(b)**
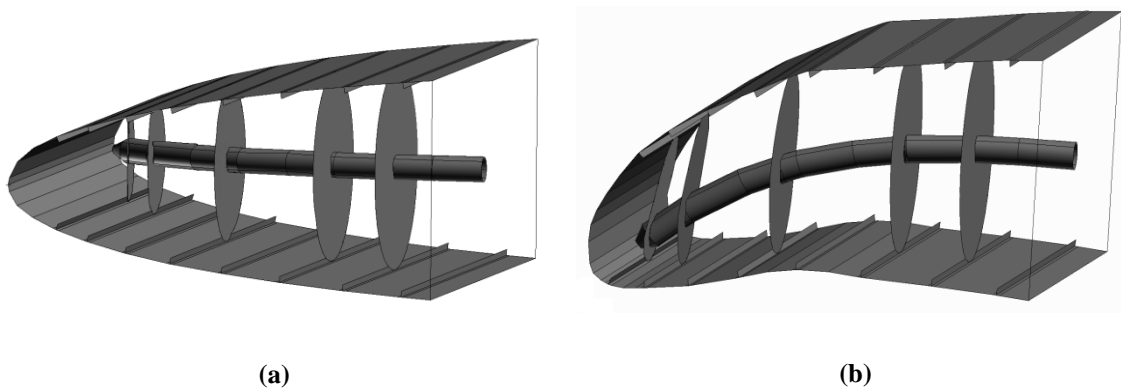
Figure 5.6 Eccentric beam auction mechanism: (a) In neutral position, (b) Fully deployed position

The eccentric beam actuation mechanisms (EBAM) therefore ensured that the desired leading edge morphing shape was reached and maintained in a certain position. The eccentric curved beam was made of aluminium (see Table 5.1 for the material properties) and the tube thickness was 5 mm. At its root the beam diameter was 0.05 m while at the tip it reduced to 0.02 m. The beam root passed the front spar through a cutout and it was connected to the actuator which was placed in the man wing box. The cutout was reinforced by circular rings placed on each side of the spar web panel in order to reduce the stress concentrations at its edges as it was discussed in Section 4.6. The rigs were made of the same material as the front spar, M21/T800S which properties are shown in Table 5.1, with a symmetrical layup [0/±45/90/90//±45/0]$_s$ and total thickness of 4 mm.

Each of the discs had continuously varying radii to allow a smooth morphing deflection. Special attention was paid to the disc close to the nose where the upper and lower skin distance from the beam changed dramatically as the leading edge deformed from the neutral to the fully deployed position. Each half of the discs were laid in a different plane and the discs were mounted at an angle with respect to the eccentric beam, as shown in Figure 5.7. This was done so that when the leading edge was deflected and the upper and lower skins moved in the chordwise direction, the discs followed a path parallel to the stringers. The stringers were in fact used as a railing to guide the discs movement and as a connection to the disc so that the leading edge skin and the EBAM were integrated.

(a)   **(b)**
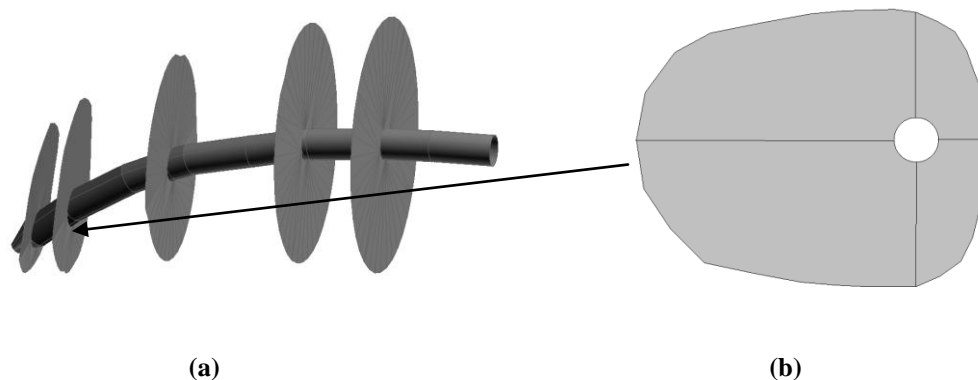
Figure 5.7 Eccentric beam actuation mechanism: (a) Discs arranged at an angle along the beam; (b) Details of the disc close to the leading edge nose

The edge of the discs had flat flanges, as shown in Figure 5.8, and rollers were used to connect the discs to the upper and lower stringers. This connection allowed the free rotation of the beam and at the same time allowed the discs to be always connected to the leading edge skin.
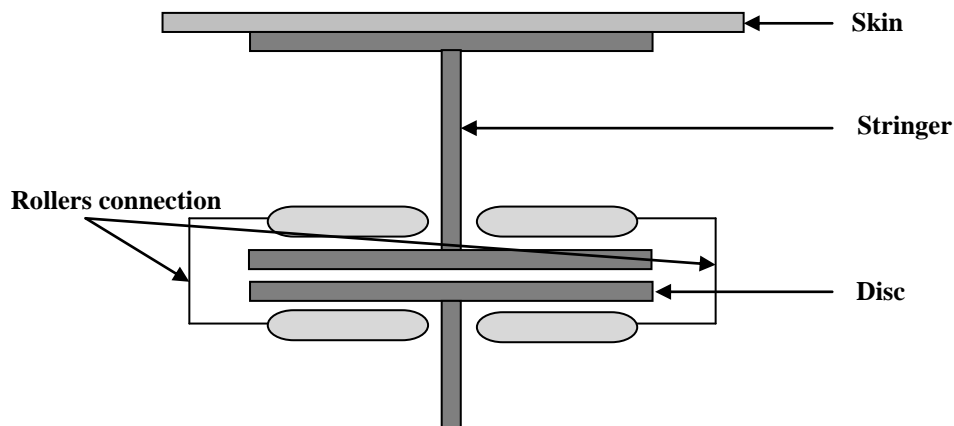
Figure 5.8 Connection between the leading edge skin and the discs

5.1.4. The Finite Element Modelling

Several finite element (FE) models were created to study the feasibility and behaviour of the morphing leading edge structure using the commercially available software PATRAN/NASTRAN. Firstly only the skin was modelled and forces were applied to deflect the structure to the target shape. Both skin and stringers were represented as shells using 3640 QUAD4 elements. The structure was fully clamped at the root where the leading edge skin met with the front spar. Considering the large deflection required, the analyses were carried out using non linear solutions. The specific skin displacements at the actuation discs location were imposed through the stringers and the aerodynamic pressure was applied to the upper and lower skins. By performing a geometric nonlinear static deformation analysis, using the NASTRAN SOL 600 solution, the reaction forces at the disc locations were obtained when the required morphing shape was achieved. Those forces were equal to the actuation forces required to deform the skin into the

morphing shape and produce the aerodynamic pressure; and were also applied to a similar leading edge model to carry out another static nonlinear analysis to obtain the skin stresses and strains using the NASTRAN SOL 106 solution.

Two types of models were instead created for the leading edge skin integrated with the eccentric beam actuation mechanism: one for the leading edge in the neutral position and one in the fully deployed configuration. The eccentric beam was modelled using shell elements while the discs were represented by beam elements connecting the eccentric beam and the upper or lower skin. A total number of 19706 and 19845 elements were used for the leading edge models in the neutral and deflected position respectively. Furthermore, a sliding constraint (sliding multipoint constrain) was set at the end of the beam connecting the eccentric beam and the stringers, as shown in Figure 5.9. This allowed the discs to have freedom in the chordwise direction with little bending constraint according to the practical design. By using the sliding effect it was possible to model more accurately the overall stiffness of the leading edge structure. The beam root at the front spar was fully clamped while the free edges of the leading edge were constrained in the chordwise and spanwise displacements and rotation with respect to the aircraft vertical direction. Both static and dynamic response analysis were carried out using these models. The solution SOL 106 was used for the non linear static analysis while the solutions SOL 103, 108 and 109 were was used for the modal, frequency response and transient response analysis.

Stringer to beam sliding connection
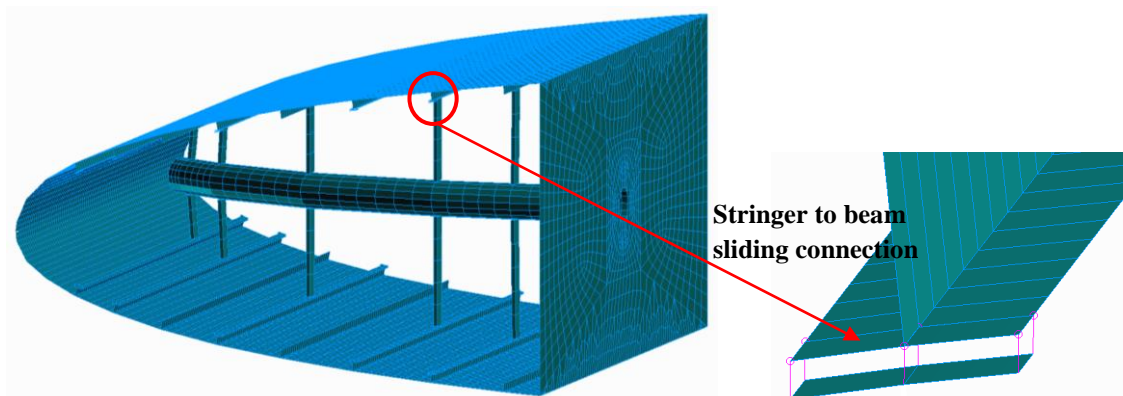
Figure 5.9 Leading edge skin with integrated eccentric beam actuation mechanism and details of the sliding connection

Finally two models of the leading edge and wing box structure were created: one for the control surface in the neutral position (199604 elements) and one in the deflected configuration (264707 elements). The wing box skin, spars, ribs and stringers were modelled as shell elements and the leading edge with the integrated actuation system was idealised as previously described. The inboard side of the wing box was fully clamped and the pressure load was applied to the leading edge and wing box upper and lower panels. The geometric non linear solution SOL 106 was used to analyse the effects of the elastic deformation on the structure at different flight conditions. Due to the large number of elements, the computation time required for these models significantly increased compared to all the other cases. It was however preferred to keep a reasonably small mesh size than decrease the computation time in order to maintain a high degree of accuracy.

5.2. The Aerodynamic Pressure Load and Leading Edge Actuation Forces

One of the main challenges in this study was to actually achieve the desired LE deflection shape. Various factors influenced the LE deformation: the number of discs mounted on the eccentric beam, their position along the chord, the stiffness of the nose skin and the aerodynamic pressure acting on the structure. All these factors were taken into account to achieve a feasible design for the LE structure to meet the morphing shape requirements.

5.2.1. The Aerodynamic Pressure Load

The aerodynamic pressure over the wing section had a significant effect on the actuation load demand and stress distribution of the structure and it was therefore necessary to obtain accurate external loads. Results obtained from a computational fluid dynamics (CFD) simulation of a 2-D airfoil were used as pressure loads to be applied to the structure [224]. According to the flight conditions three models were created. Model 1 was for the clean configuration at cruise flight; Model 2 was for a two-element configuration at landing with flap deployed and leading edge still in its neutral position

and Model 3 was for the wing with the morphing leading edge and flap deployed together, as shown in Figure 5.10.

<center>(a)</center>

<center>(b)</center>

<center>(c)</center>
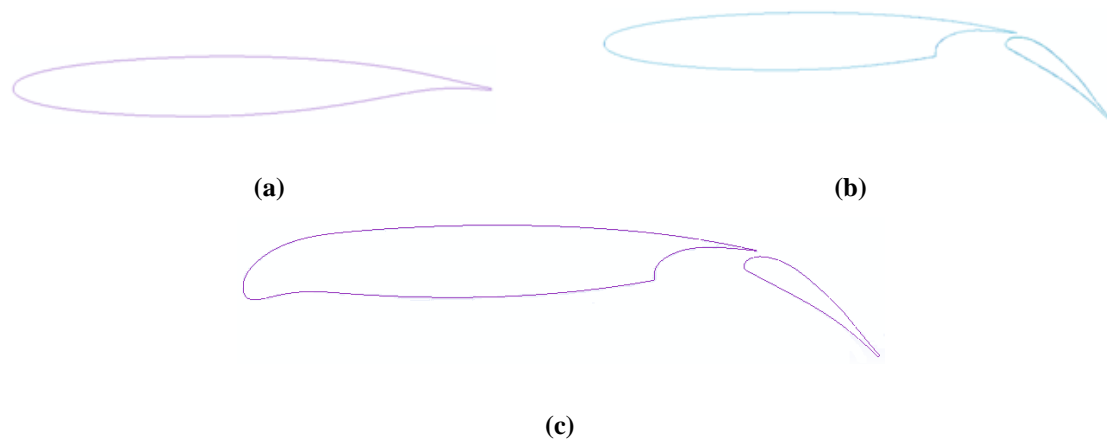
Figure 5.10 Three wing section models: (a) Clean wing at cruise; (b) Flap deployed at landing; (c) Morphing leading edge and flap deployed at landing

At cruise the aerodynamic pressure was calculated at 31000 ft and the flow velocity was at Mach 0.8. In landing condition, the wing angle of attack was set at 12 degrees with flow velocity Mach 0.15 and a Reynolds number of 7×10^6. The atmospheric conditions were taken for an altitude of 20000 ft and an air temperature of 248.6 K.

Figure 5.11 shows the pressure distribution over the 2-D airfoil at the different flight conditions. The graph shows the high suction peak at the leading edge nose and the increased lift generated by the flap for Model 3. This increase in lift is achieved by using the leading edge morphing deflection to stabilise the flow and by employing the slotted flap to increase the circulation at the aft section of the airfoil.
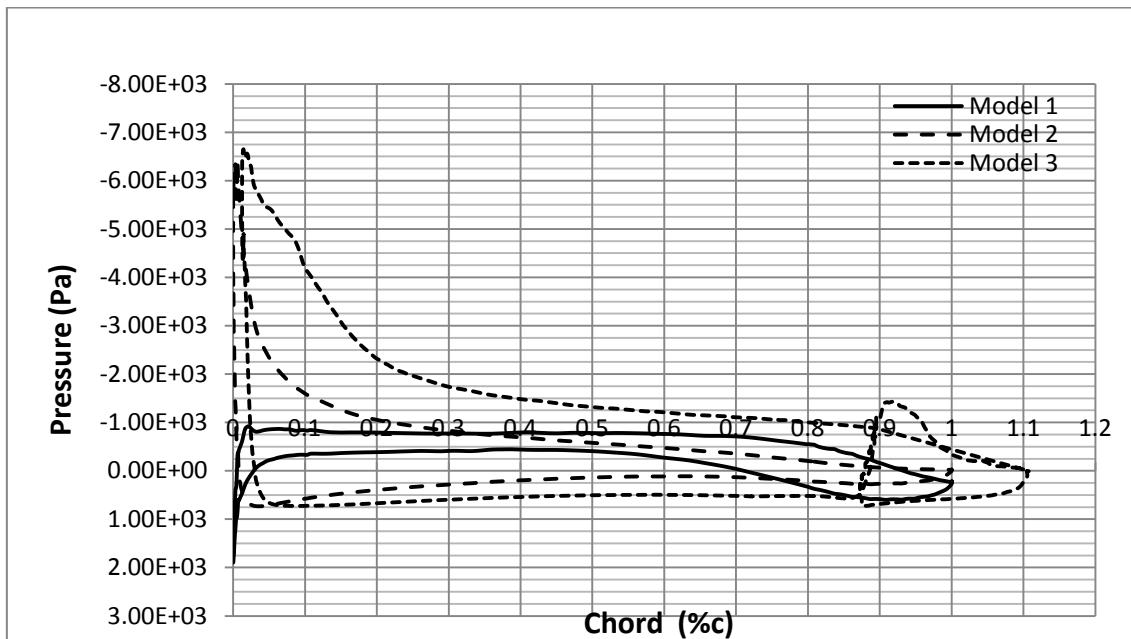
Figure 5.11 Pressure distribution of the 2-D airfoil at different flight conditions (Units Pa)

5.2.2. Internal Actuation Loads

To calculate the actuation forces required to deflect the leading edge skin to the target shape the specific displacements were imposed to the leading edge skin only FE model. The aerodynamic pressure calculated at landing condition (Model 3) was also applied the structure. By performing a nonlinear static deformation analysis the reaction forces, which were equal to the actuation forces were obtained. In the original glass fibre skin design (see Section 5.1.1 for details), the maximum total actuation force required to obtain a vertical displacement of 6% of the wing chord was 11400 N. Under this force however, the leading edge overall deformation did not actually meet the target shape. In order to achieve the required leading edge morphing shape with minimum actuation force, the nose skin thickness was reduced to 2 mm. Figure 5.12 shows the region where the skin thickness was reduced. The new layup for this region was $[\pm45/0_2]_s$, which reduced the local laminate chordwise bending stiffness by 30%. The leading edge had eight possible positions for the discs, see Figure 5.12. Fourteen different disc arrangements were analysed to find the optimum option.
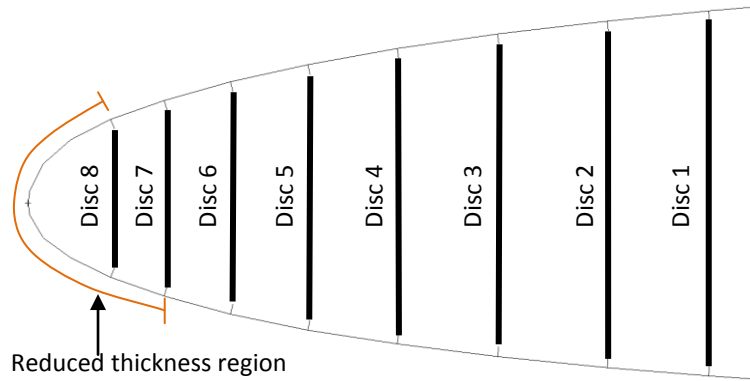
Figure 5.12 Eight options for the disc location and skin region with reduced thickness
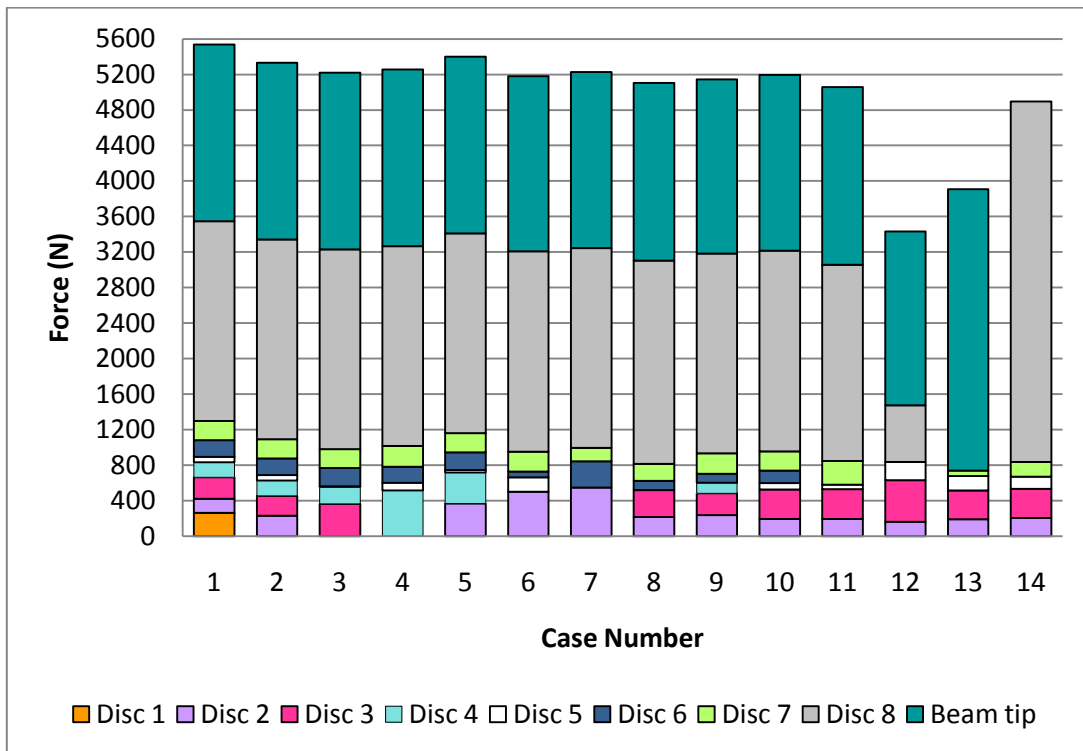
Figure 5.13 Forces required from each disc and beam tip to deflect the leading edge for the

different design cases (Units N)

Figure 5.13 shows the force required to achieve the target leading edge deflection shape from each disc and beam tip for the fourteen design cases. The graph also shows that, for all the cases, a great portion of the total actuation force was demanded by the last disc and the eccentric beam tip. The force required in the cases 12 to 14 were lower compared to the others. However, these three arrangements did not lead to the target shape. The optimum disc arrangement was case 11 where five discs and the beam tip were used to impose the required displacements. The total actuation force required to achieve the leading edge morphing shape was 5068 N with disc 2 contributing to 4% of the total force, disc 3 to 7%, disc 5 to 1%, disc 7 to 5%, disc 8 to 44% and beam tip to 39%. Case 11 was therefore chosen as the disc arrangement for the current EBAM design.

For the leading edge structure made in aluminium the nose skin thickness was reduced from 2 mm to1 mm. For the metallic option the total actuation force required using case 11 disc arrangement was 11% lower compared to the forces applied to the glass fibre skin and it was 4507 N, as shown in Figure 5.14.
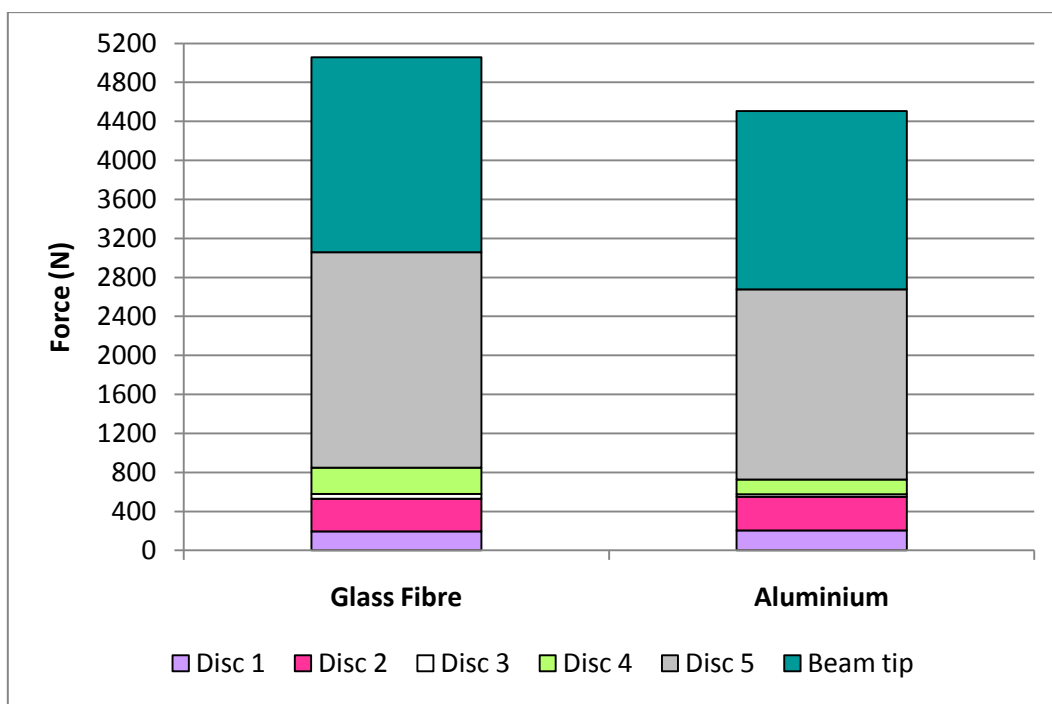
Figure 5.14 Force required from each disc and beam tip to deflect the leading edge made in glass fibre and aluminium alloy to achieve the deflected target shape (Units N)

Figure 5.15 shows the torque required by the actuator to deliver enough force to the eccentric beam and discs and deflect the aluminium leading edge structure to the required target shape. The total torque was calculated as the sum of the torque required for each disc. For a single disc, the total force was the sum of the force needed to deflect the leading edge skin, without the external pressure, and the force to counteract the effect of the aerodynamic load. This force was then multiplied by the moment arm to determine the torque. The moment arm was the distance from the centre of the disc to the centre of rotation of the eccentric beam. As the beam was bent the moment arm changed for every rotational angle and it was maximum at the beam neutral position and zero at the fully deflected position.
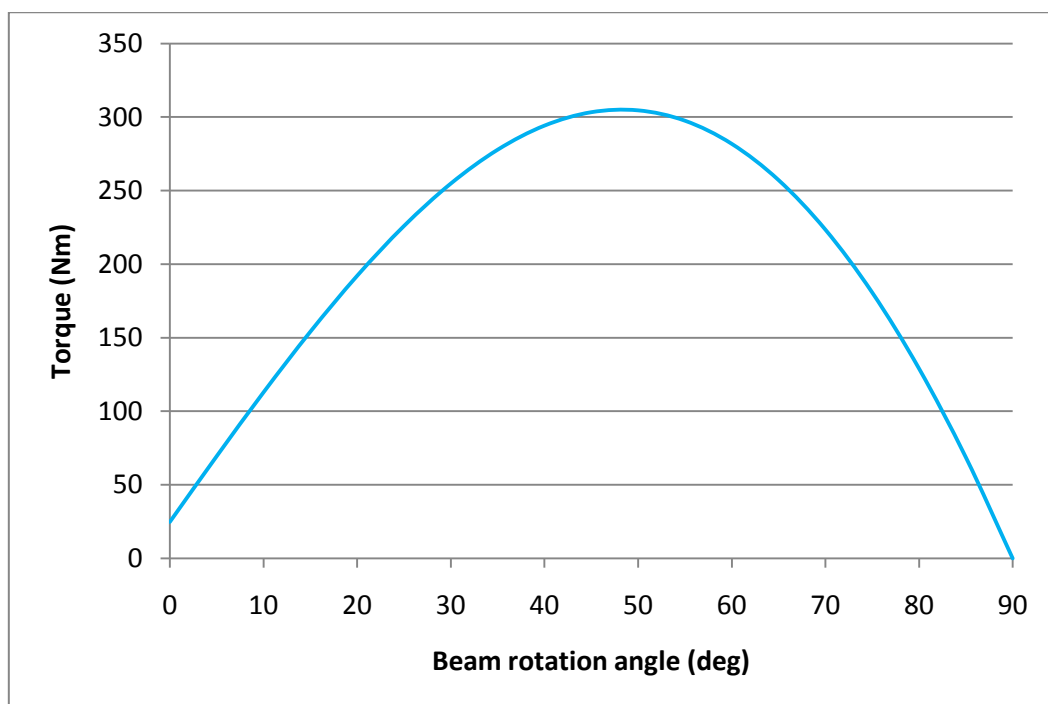
Figure 5.15 Torque required to deflect the metallic leading edge skin to the target shape (Units Nm)

5.2.3. Influence of the Aerodynamic Pressure on the Leading Edge Structure

Based on the design of the EBAM and the evaluated actuation forces to deflect the leading edge, the effect of the aerodynamic pressure on the control surface structure was studied. The overall force demand for the case without the aerodynamic load was lower, 4109 N compared to 5068 N. This showed that 81% of the actuation force was used to actually deflect the leading edge skin and 19% to overcome the pressure load.

It was noted that the forces exerted by the discs were not always acting in the direction of the displacement. Some of the forces were acting in the opposite direction in order to prevent excessive skin deformation and buckling, such as the forces F5, F8 and F9 shown in Figure 5.16 (a). In particular, the force F5 was required to maintain the upper surface shape while the forces F8 and F9 were needed to prevent the lower skin to deflect outwards. This upward load demand was lower when the aerodynamic load was applied as shown in Figure 5.16 (b). The aerodynamic load generated by the morphing leading edge had therefore a beneficial effect on the local power demand.

(a)   (b)
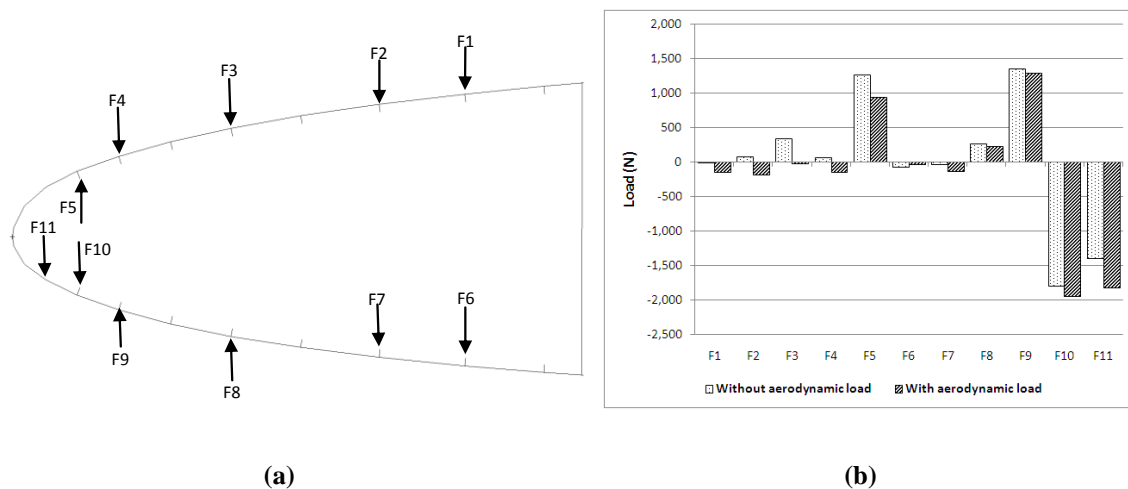
Figure 5.16 Actuation forces on the leading edge skin: (a) Force direction when the aerodynamic pressure was applied; (b) Actuation force demand for cases with and without the aerodynamic pressure (Units N)

5.3. Morphing Leading Edge Static Aeroelastic Analysis

The results presented in the previous section demonstrated that the eccentric beam actuation system is a feasible mechanism in terms of force and power demand. However, the leading edge skin material constrains were not yet considered. The structure in fact must be flexible enough to meet the large deflection demand but it also has to satisfy the strength requirements. The analysis of the leading edge structure was carried out by first calculating the stresses and strains on the skin due to the actuation forces and the aerodynamic load during deployment. This type of study allowed to assess whether the skin material was appropriate to achieve the deflection without violating the mechanical strength limitations. Following this, the behaviour of the leading edge skin with the integrated internal actuation mechanism was analysed under the aerodynamic pressure at different flight conditions. This study was necessary to ensure that the eccentric beam actuation mechanism can provide adequate support to the skin when the structure was subject to the external loads.

5.3.1. Leading Edge Skin Static Stress and Strain Analysis

A nonlinear static analysis was carried out for the leading edge structure, skin only model (as described in Section 5.1.4), in order to assess the feasibility of the materials selected. Both actuation forces and aerodynamic pressure, at landing condition, were applied and the stresses and strains were calculated. The point loads representing the actuation forces caused high stress concentration in the FE calculation which did not represent the true case. When the results were analysed these particular nodes were discarded and a slightly lower figure, obtained from a nearby node, was assumed to be a more accurate representation.
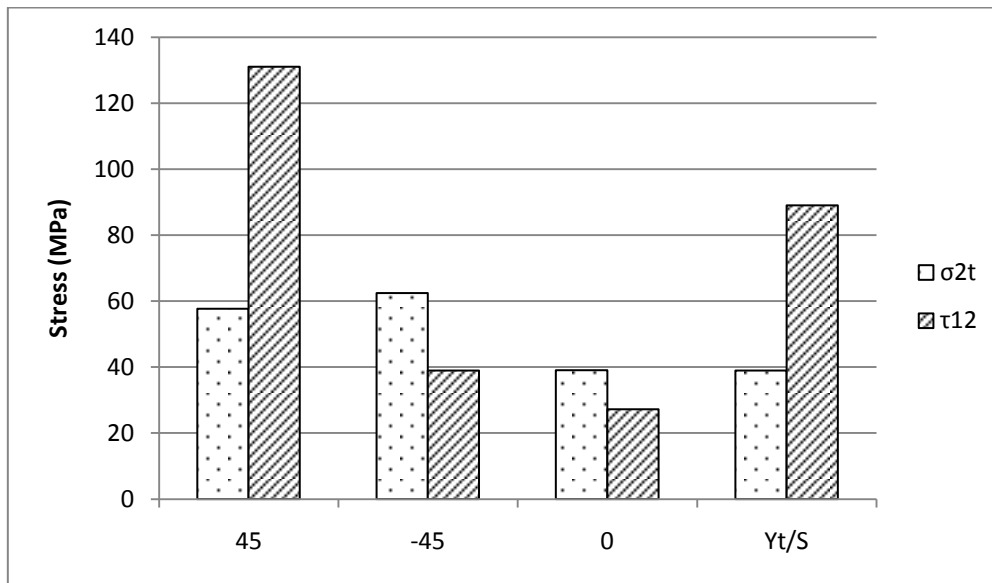
Figure 5.17 Ply by ply tensile stress in the off fibre direction and shear stress in the glass fibre skin with nose layup [±45/0$_2$]$_s$ (Units MPa)

Figure 5.17 shows the ply stresses for the case when the leading edge nose was made in glass fibre laminate with layup [±45/0$_2$]$_s$ with the 0°layers oriented in the spanwise direction. The results indicated that the 45° and -45° layers were the critical plies which caused the laminate stress failure. In particular, the tensile stress in the off fibre direction was high in both 45° and -45° ply angle, which exceeded the material strength allowable of 39 MPa. The highest stress concentration occurred in layer 7 (-45°) and 8 (45°) where the maximum tensile off fibre stresses were 62.4 and 57.7 MPa respectively. Figure 5.17 also shows that the 45° ply failed due to high in plane shear stresses. The stress levels in this ply reached 131 MPa when the allowable was 89 MPa. The highest stress was in the outer 8th ply. Both off fibre and shear stress concentration occurred at the maximum curvature region as shown in Figure 5.18 and Figure 5.19.

Figure 5.18 Leading edge tensile off fibre stress plot, layer 7 at -45° (Units Pa) (Discard highest stress where the point load is applied, actual stress 4 element away from that node)

Figure 5.19 Leading edge shear stress plot, layer 8 at 45° ((Units Pa) (Discard highest stress where the point load is applied, actual stress 4 element away from that node)

Figure 5.20 shows the ply by ply strain in the chordwise direction and in shear. Although the glass fibre allows large amount of deflection the chordwise strain required to achieve the target shape was by far beyond the material allowable. The outer layers of the laminate were particularly subject to high strain due to the large bending; in

particular the chordwise strains in the 45° and -45° ply angles were 9800 με and 7220 με, while the shear strains were 6030 με and 4360 με. For the 0° ply angle the strain levels were slightly lower 4540 με and 2790 με in the chordwise direction and in shear respectively.
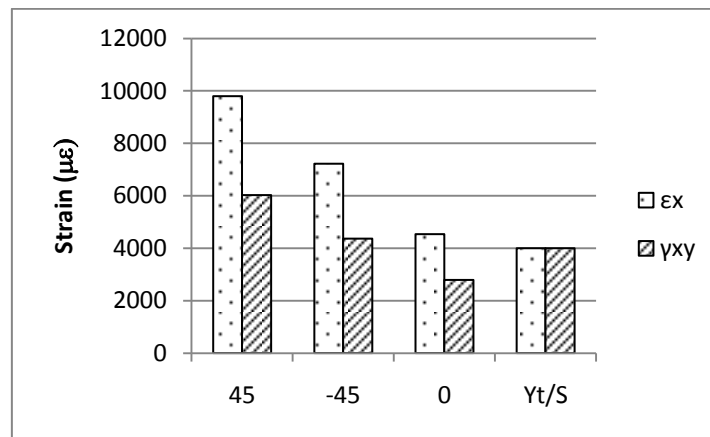
Figure 5.20 Ply by ply chordwise strain and shear strain in the glass fibre skin with nose layup [±45/0$_2$]$_s$ (Units με)

Similarly to the stress distribution, the maximum strain in both chordwise direction and shear occurred at the nose maximum curvature region where the largest deformation was required, as shown in Figure 5.21 and Figure 5.22.

Figure 5.21 Leading edge chordwise strain plot in layer 7 at -45° (Units ε) (Discard highest strain where the point load is applied, actual stress 4 element away from that node)
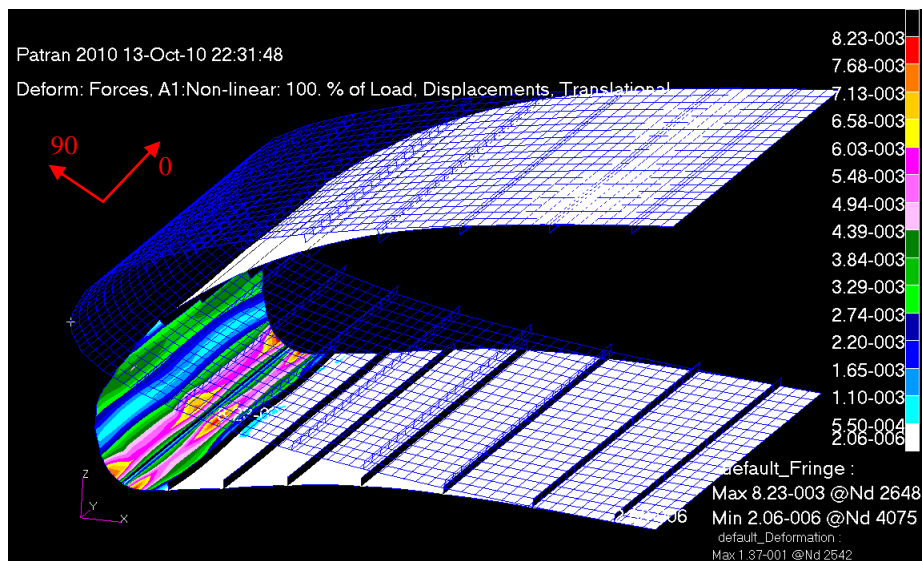
Figure 5.22 Leading edge shear strain plot in layer 8 at 45° (Units ε) (Discard highest strain where the point load is applied, actual stress 4 element away from that node)

To reduce the excessive stresses and strains at the nose region, two alternative layups, $[90/0_3]_s$ and $[30/60/0_2]_s$, were investigated. For the first layup option however, the

required shape was not reached due to the large bending stiffness of the 90° ply angle where the fibres were orientated in the same direction as the nose deployment.

Figure 5.23 shows how the leading edge nose deflected under the aerodynamic load and actuation forces when the leading edge nose stacking sequence was $[90/0_3]_s$. The upper surface followed a smooth curvature however the leading edge nose did not manage to achieve the change in curvature and consequently caused the whole of the bottom to deflect outwards. In the case when the layup $[30/60/0_2]_s$ was used the leading edge deflected target shape was achieved and therefore the stresses and strain results were compared with that of the baseline case. Figure 5.24 shows the ply stresses for the case when the leading edge nose was made in glass with layup $[30/60/0_2]_s$.
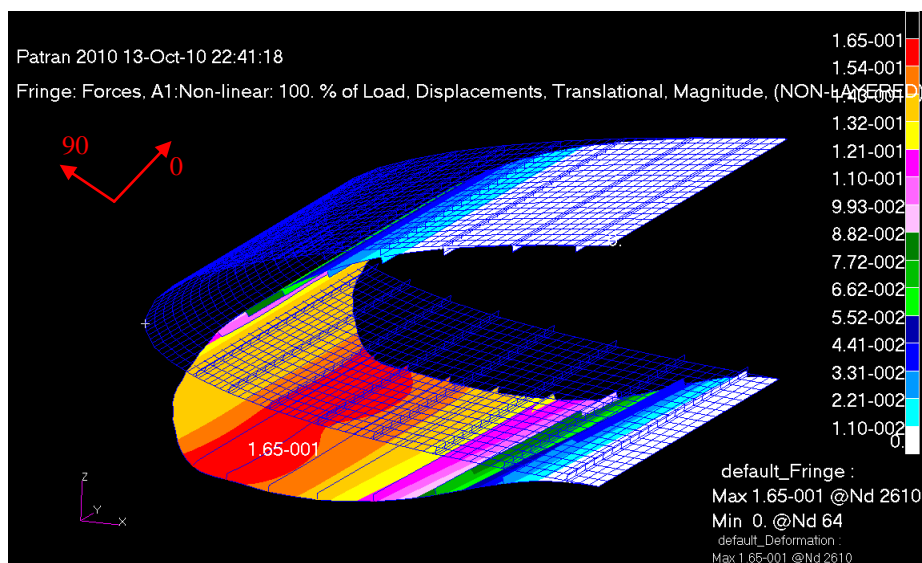
Figure 5.23 Leading edge deflection under actuation and aerodynamic loads with nose layup
$[90/0_3]_s$ (Units m)

The results indicated that the 30° and 60° plies were critical and caused the laminate failure. The tensile off fibre direction stress was high in the 30° 8th outer layer where the maximum stress was 84.7 MPa. The shear stress was instead high in the 60° 7th ply, where the maximum stress was 131 MPa. Similarly to the previous case, both tensile and shear maximum stress concentrations occurred at the maximum nose curvature region, as shown in Figure 5.26 and Figure 5.27.
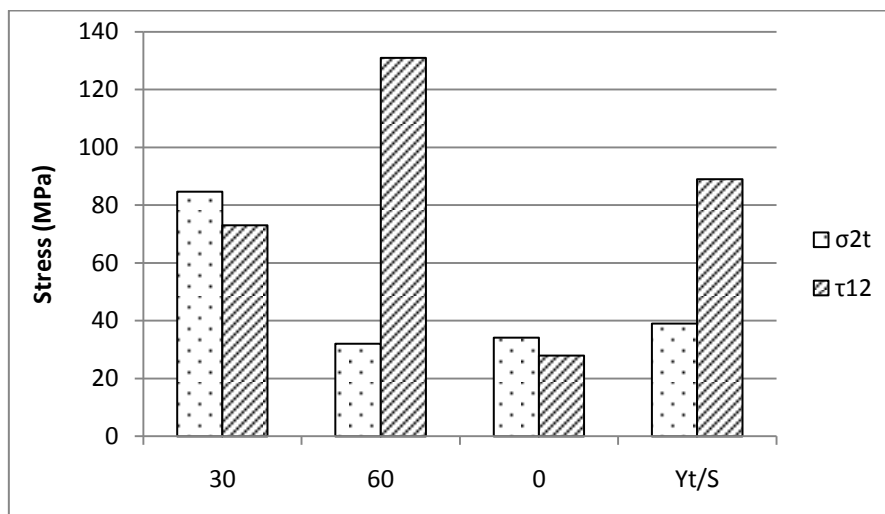
Figure 5.24 Ply by ply tensile stress in the off fibre direction and shear stress in the glass fibre skin with nose layup $[30/60/0_2]_s$ (Units MPa)
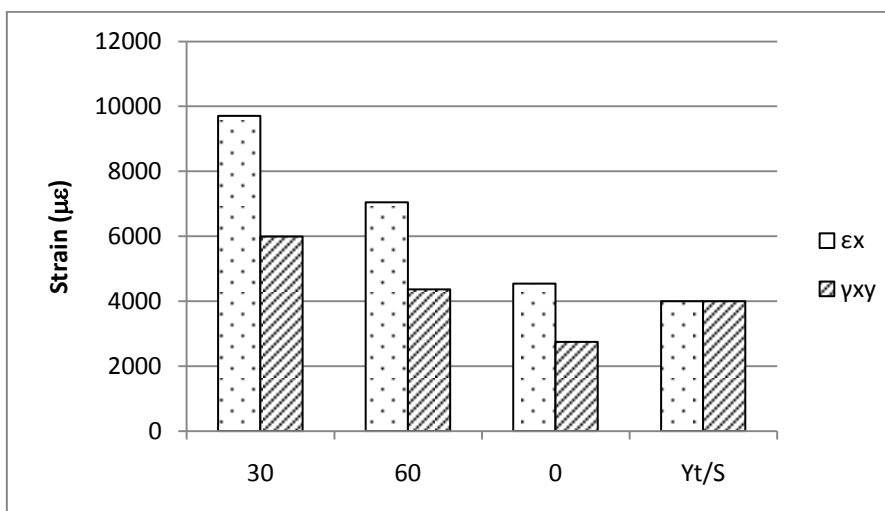
Figure 5.25 Ply by ply chordwise strain and shear strain in the glass fibre skin with nose layup $[30/60/0_2]_s$ (Units $\mu\varepsilon$)
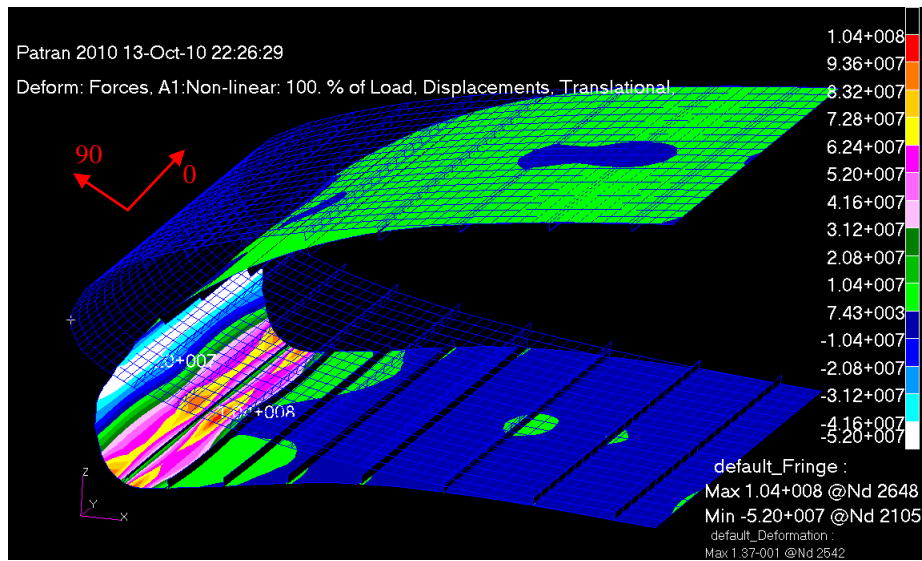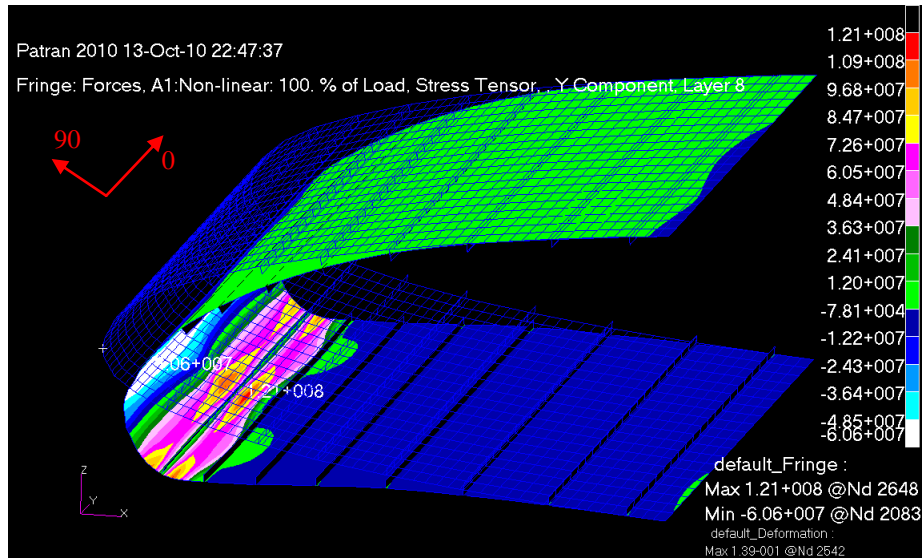
Figure 5.26 Leading edge tensile off fibre stress plot in layer 8 at 30° (Units Pa) (Discard highest stress where the point load is applied, actual stress 4 element away from that node)
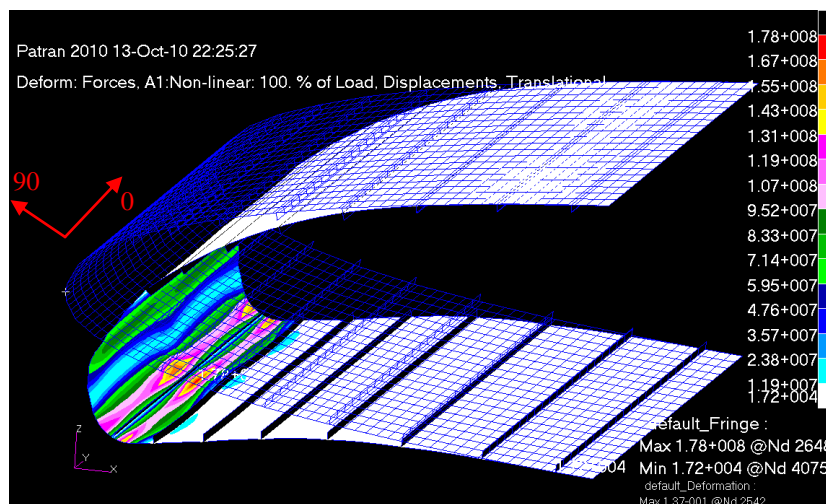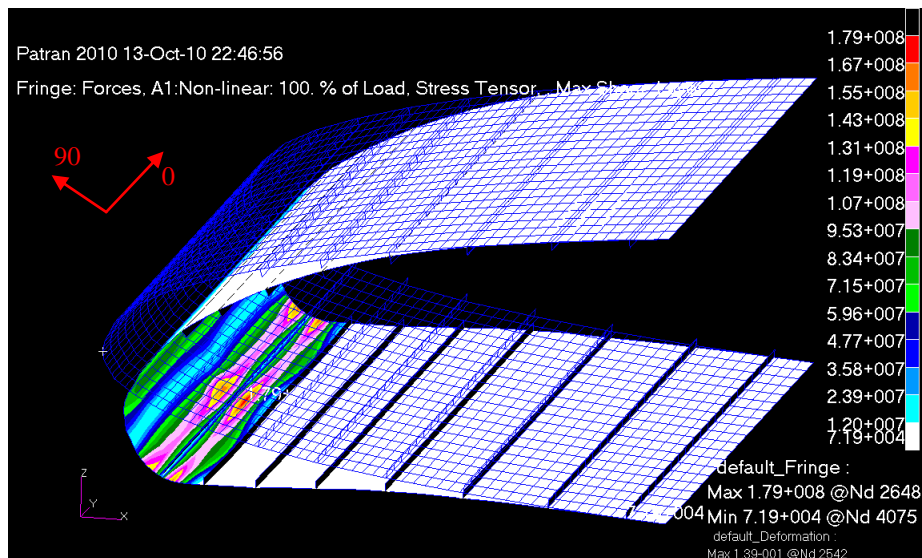

Figure 5.27 Leading edge shear stress plot in layer 7 at 60° (Units Pa) (Discard highest stress where the point load is applied, actual stress 4 element away from that node)

Figure 5.25 shows the ply by ply strain in the chordwise direction and in shear. The chordwise strain was extremely high in all layer and exceeded the design allowable of 4000 με. The strain was particularly high in the skin outer layer to the large amount of deflection imposed to the structure. The maximum chordwise strain the 30° layer was 19710 με, in the 60° layer was 7050 με and in the 0° layer was 4540 με. The shear stresses in all layers were lower than the chordwise stresses: 5990 με, 4360 με and 2750 με for the 30°, 60° and 0° layers. Similarly to the stress distribution, the maximum strain in both chordwise direction and shear occurred at the nose maximum curvature region where the largest deformation was required, as shown in Figure 5.28 and Figure 5.29.
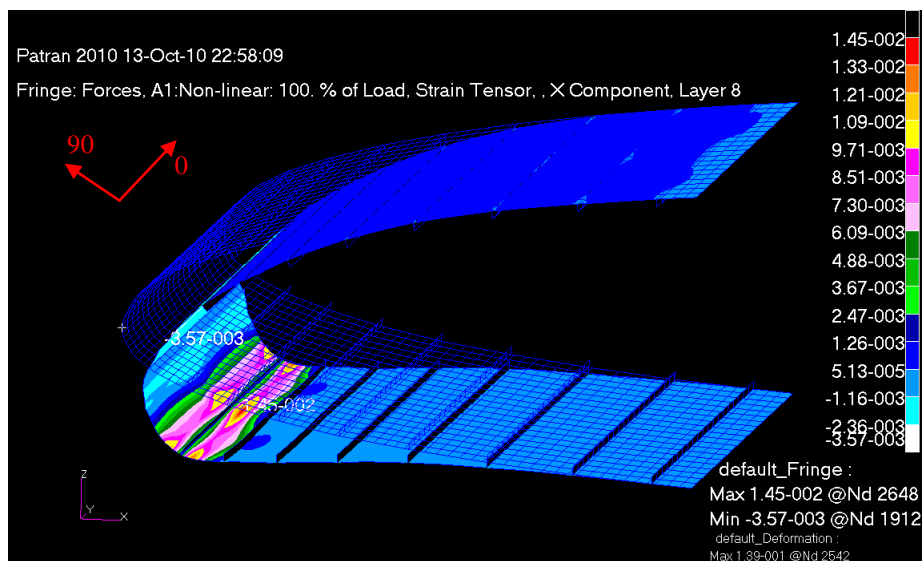
Figure 5.28 Leading edge chordwise strain plot in layer 8 at 30° (Units ε) (Discard highest strain where the point load is applied, actual strain 4 element away from that node)
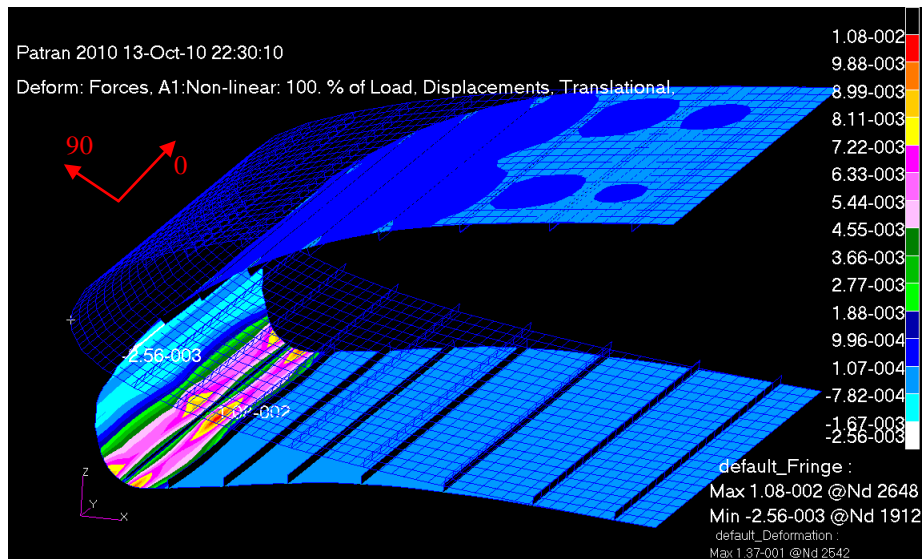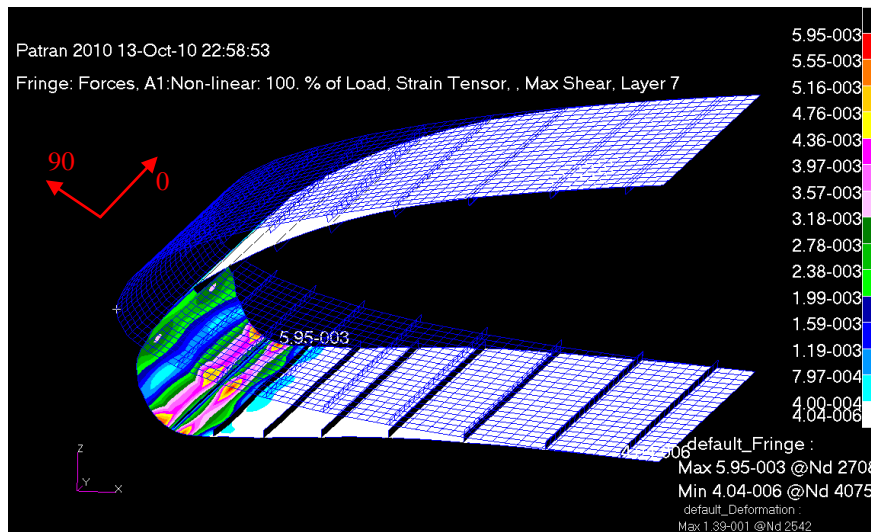
Figure 5.29 Leading edge shear strain plot in layer 7 at 60° (Units ε) (Discard highest strain where the point load is applied, actual stress 4 element away from that node)

Figure 5.30 shows a stress comparison between the two possible layups for the leading edge glass fibre skin. The outer layer stresses were compared as the previous results indicated that these were the critical plies in the laminate.
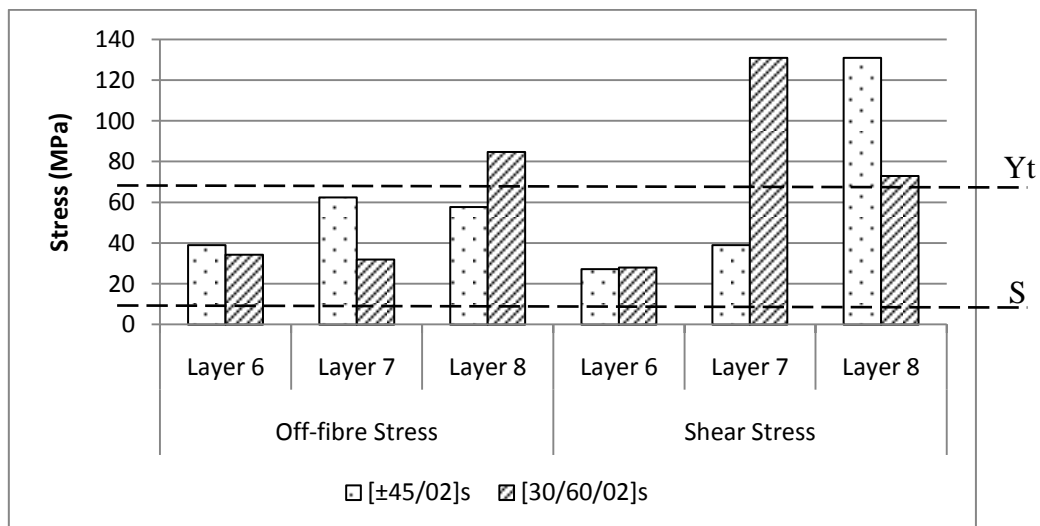
Figure 5.30 Off fibre tensile stress and shear stress comparison between the two glass fibre layups (Units MPa)

With the layup $[30/60/0_2]_s$ a generally lower off fibre stress was achieved. The tensile stresses in layer 6 and 7 were in fact 12% and 49% lower compare to the $[\pm45/0_2]_s$ layup. However the shear stress in layer 7 was 70% higher for the $[30/60/0_2]_s$ case.

The results presented above showed that the composite skin reached the required deflection shape but did not satisfy the structural strength conditions. Attention was therefore paid to the metallic skin design to meet the demanding requirements. The analysis results showed that the maximum chordwise tensile stress was 439 MPa and the maximum shear stress was 275 MPa, as shown in Figure 5.31 and Figure 5.32. Although these stresses were relatively high they were within the material allowable: 450 MPa and 295 MPa for the tensile and shear stresses respectively, as shown in Table 4.7.

The strain results also showed that the aluminium skin was a more feasible design. Both chordwise and shear strains were well below the material allowable. The chordwise strain was 331 $\mu\varepsilon$, while the shear strain was 1050 $\mu\varepsilon$, as shown in Figure 5.33 and Figure 5.34.
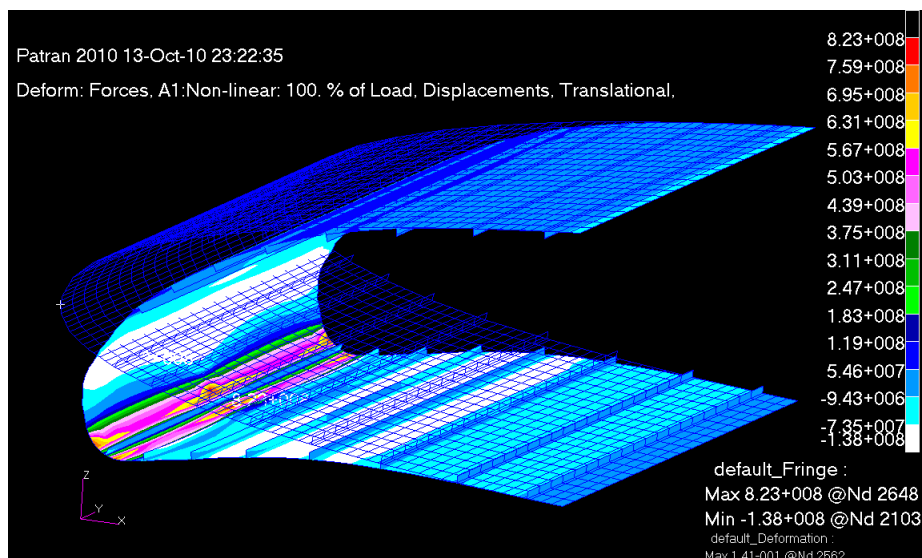
Figure 5.31 Leading edge made of aluminium alloy chordwise stress (Units Pa) (Discard highest stress where the point load is applied, actual stress 4 element away from that node)
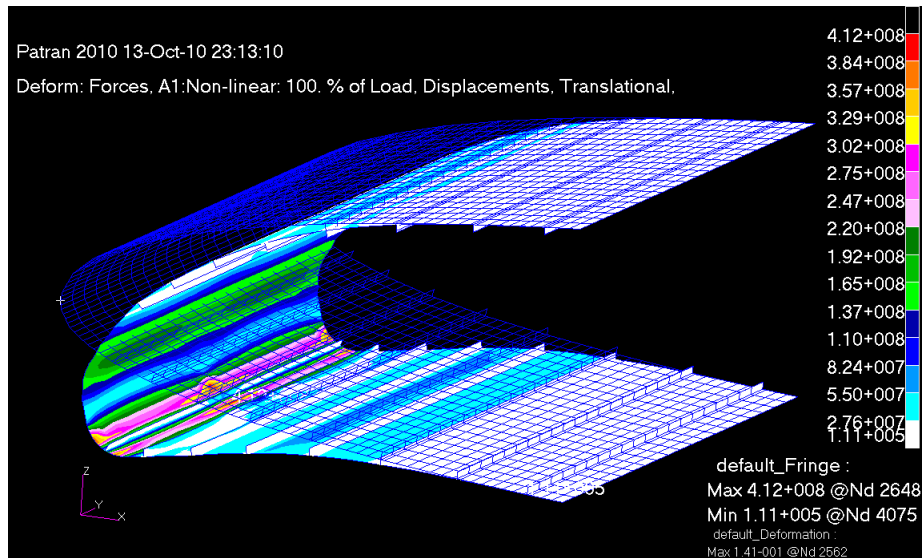
Figure 5.32 Leading edge made of aluminium alloyin plane shear stress (Units Pa) (Discard highest stress where the point load is applied, actual stress 4 element away from that node)
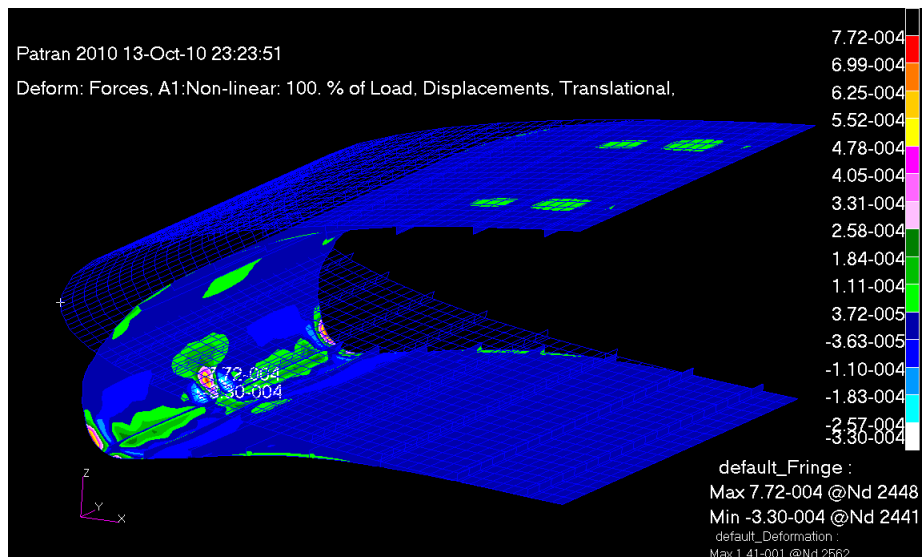
Figure 5.33 Leading edge made of aluminium alloy chordwise strain (Units ε) (Discard highest strain where the point load is applied, actual stress 4 element away from that node)

As any metallic structure the aluminium leading edge was subject to fatigue concerns. From the material S-N curve [225] it was estimated that the skin would withstand up to 3.5×10^5 load cycles when subject to the estimated high stresses during deployment. This number of cycles was higher than the number of flights required and therefore the structure met the fatigue design specifications. The metallic skin option was therefore chosen as the better solution in terms of the morphing leading edge deflected shape, actuation force demand and the strength requirements.
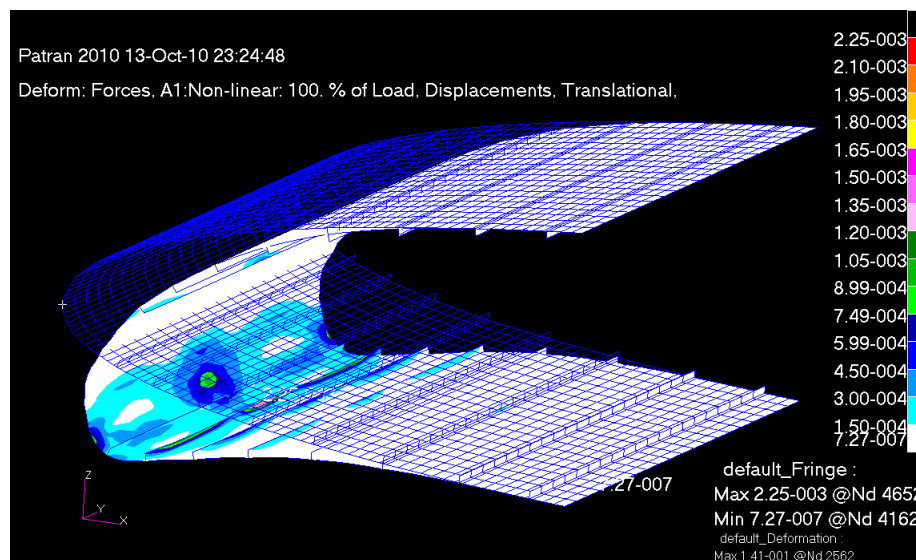
Figure 5.34 Leading edge made of aluminium alloy in plane shear strain (Units ε) (Discard highest strain where the point load is applied, actual stress 4 element away from that node)

5.3.2. Effect of the Aerodynamic Load on the Leading Edge Structure

A geometrically nonlinear static analysis of the leading edge skin with integrated eccentric beam actuation system was carried out, under the aerodynamic pressure, at both landing and cruise conditions. At landing condition, two different cases were considered: one for the LE in neutral (un-deformed) position and one for the fully deployed morphing shape, as illustrated in Section 5.2.1. At cruise condition a 2.5 g

factor (limit load) was taken into account for the worst case scenario. The skin, the actuation system and the connection between the two was represented in the FE model as described in Section 5.1.4. The effect of the stiffness of the actuator system on the overall leading edge structure was also taken into account. The effective actuator stiffness was represented by using a short beam section, 2 cm in length, at the root of the beam. The stiffness was varied from 100% to 10% of the original beam stiffness. Figure 5.35 shows the influence of this stiffness variation on the structures elastic deformation at the different flight conditions.
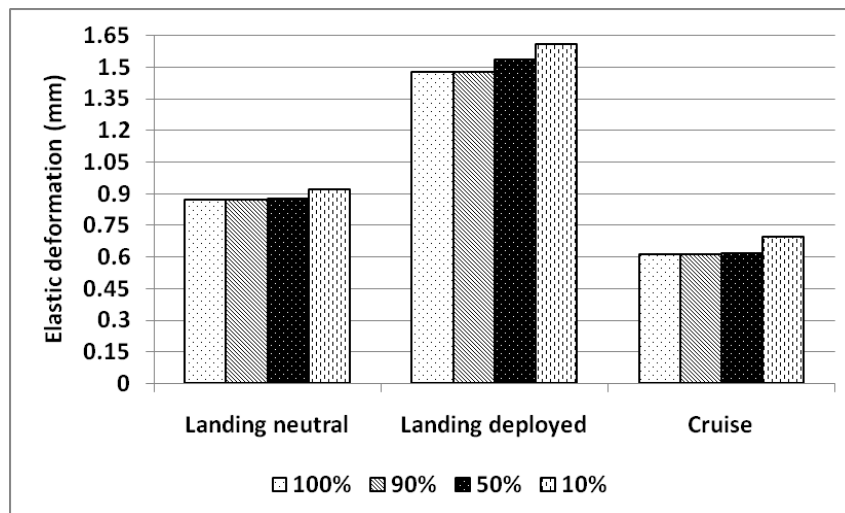
Figure 5.35 Effect of the eccentric beam stiffness on the leading edge elastic deformation at different flight conditions (Units mm)

The graph shows that the maximum elastic leading edge deformation due to the applied aerodynamic pressure was between 0.6 and 1.6 mm. This indicated that the leading edge skin integrated with the eccentric beam actuation mechanism is able to maintain the desired shape at the specific flight condition. The results also showed that the effective stiffness of the actuator mounted to the root of the eccentric beam did not have a significant influence on the overall leading edge structural stiffness. The largest impact was for the wing in the Model 1 configuration (see Figure 5.10) in cruise condition

where the skin deflection increased by 14% when the beam stiffness at the root was reduced to 10%.

Table 5.2 shows the maximum chordwise and in plane shear stresses due to the aerodynamic load at the three flight conditions. The maximum stress regions were concentrated at the root of the eccentric beam and the change in stiffness properties generally increased the stress in the structure, but did not have a significant effect.

Table 5.2 Leading edge chordwise and shear stress at different flight conditions for 100% and 10% beam root stiffness

Case	100% root stiffness				10% root stiffness			
	σ_x (MPa)		τ_{xy} (MPa)		σ_x (MPa)		τ_{xy} (MPa)	
	Skin	Beam	Skin	Beam	Skin	Beam	Skin	Beam
Landing neutral position	11.5	28.3	8.3	8.3	13.4	33.0	9.28	9.28
Landing fully deployed	18.4	43.2	18.2	18.2	19.0	45.4	19.5	19.5
Clean wing at cruise	8.1	18.2	7.5	7.5	8.5	18.9	8.26	8.26

The influence of the eccentric beam root stiffness on the leading edge structure was much more evident when a strain analysis was conducted. Both chordwise and shear strain significantly increased when the beam root stiffness was reduced, see Figure 5.36. In particular for the landing case, with the leading edge fully deployed the chordwise and shear strain increased by 460% and 293% respectively when the root stiffness was reduced to 10%.
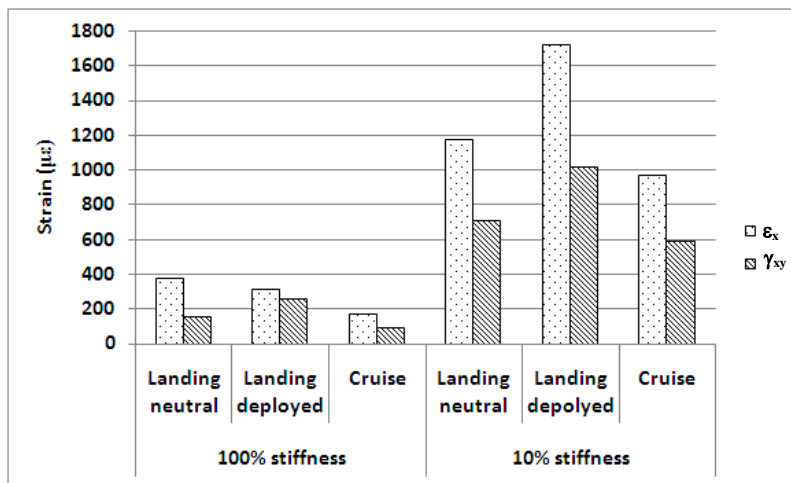
Figure 5.36 Eccentric beam chordwise and shear strain at different flight conditions for 100% and 10% beam root stiffness (Units µε)

The eccentric beam root was subject to higher strains compared to the skin. Figure 5.37 shows the maximum chordwise strain at landing condition when the beam root stiffness was reduced to 10%. Although the strain levels were relatively high they were still safely below the design allowable of 4000 µε.
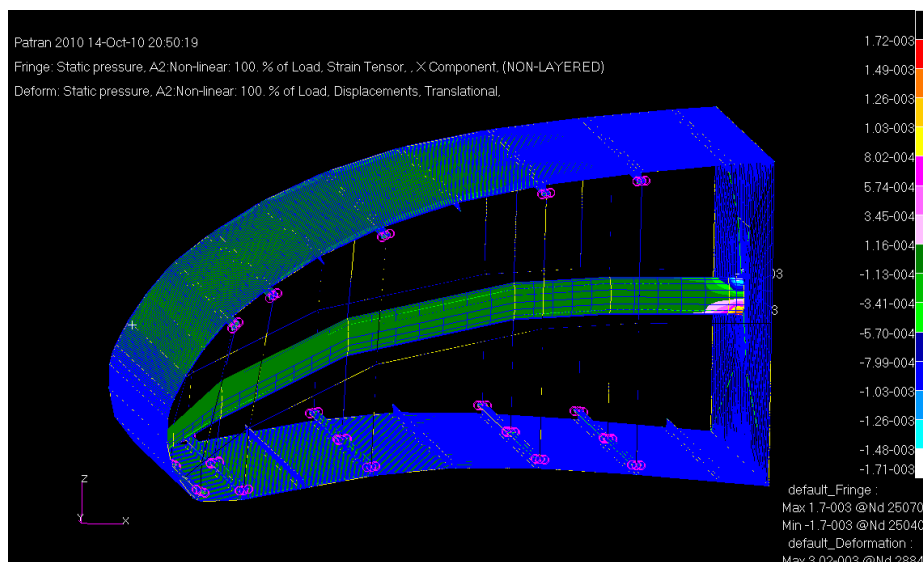
Figure 5.37 Leading edge chordwise strain at landing with reduced beam root stiffness (Units ε) (Discard highest strain where the point load is applied, actual strain 4 element away from that node)

5.4. Nonlinear Static Analysis of the Wing Box and Leading Edge Structure

A non linear static analysis was conducted considering both the wing box and the leading edge so that the effect of the flexibility and elastic deformation of the high lift device on the main wing box structure could be evaluated. The study was carried out at all the three flight conditions described in Section 5.2.1: landing with the leading edge in neutral position, landing with the fully deployed leading edge and clean cruise configuration. In order to meet the safety requirements however, an ultimate load factor of 2.5g was applied to the wing box. This part of the structure was therefore subject to a pressure load 2.5 times larger than that of the actual case.

The wing section considered for this study case was tapered, 2 m in spanwise length and it was taken from the wing reference section outwards. The geometry and materials for skin panels, stringers, ribs, spars and spar cutout reinforcements, were described in Section 5.1.1, whereas the details of the FE models were illustrated in Section 5.1.4.

The static non linear analysis focused first of all on the overall structural elastic deformation due to the aerodynamic pressure load. This was then followed by a stress evaluation in the various components of the leading edge and wing box. Finally some buckling considerations were discussed.

Table 5.3 shows the eccentric beam, leading edge and wing box maximum elastic deflection. Due to its flexible nature, the leading edge skin was subject to relatively high elastic deformation; especially at landing when the pressure was greater towards the nose in order to produce higher lift. At cruise condition the leading edge skin elastic deflection was however much smaller. On the other hand the wing box was extremely stable compared to the leading edge structure and the maximum elastic deflection was 0.23 mm in the landing configuration with the fully deployed leading edge. The reduced stiffness of the high lift device did not have any effect on the behaviour of the wing box.

Table 5.3 Elastic deflection at the three flight conditions

Flight condition	Beam deflection (mm)	Leading edge skin deflection (mm)	Wing box deflection (mm)
Landing with clean leading edge	6.83	12.10	0.10
Landing with deflected leading edge	11.90	15.00	0.23
Cruise clean configuration	2.17	2.33	0.05`

Figure 5.38 shows the leading edge structure and wing box elastic deformation at the fully deployed landing condition. The maximum leading edge skin deflection occurred on the upper surface, where the nose curvature started to increase; while the wing box skin deflection was, in comparison, extremely small.
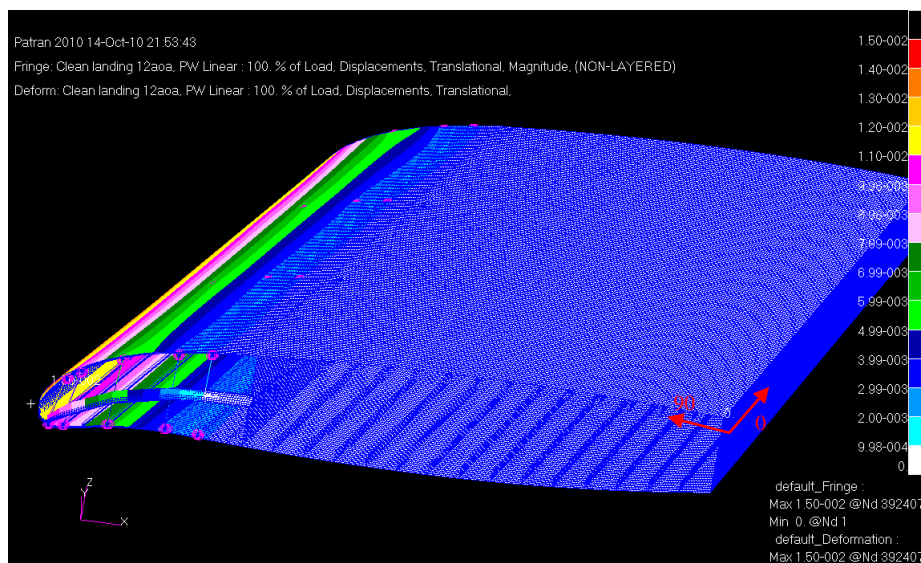
Figure 5.38 Elastic deformation at fully deployed landing condition (Units m)

The leading edge skin panel and eccentric beam chordwise, spanwise and shear stresses (σ_x, σ_y and τ_{xy}) are shown in Table 5.4. In both structural components the stress levels in all directions were safely below the material allowable shown in Table 5.1. The

eccentric beam was subject to higher stresses compared to the skin panels and the high stress concentration occurred at its root as shown in Figure 5.39. The stresses on the skin were nearly half of that of the eccentric beam and the stress concentration was at the nose maximum curvature point. The highest stress condition was reached at landing when the leading edge was fully deployed.

Table 5.4 Leading edge skin and eccentric beam stresses

Flight condition	Leading edge skin			Eccentric Beam		
	σ_x (MPa)	σ_y (MPa)	τ_{xy} (MPa)	σ_x (MPa)	σ_y (MPa)	τ_{xy} (MPa)
Landing with clean leading edge	66.8	33.4	48.3	158	50.6	105
Landing with deflected leading edge	80.9	28.8	61.4	241	56.7	132
Cruise clean configuration	38.8	17.5	17.0	53.9	17.8	27.7
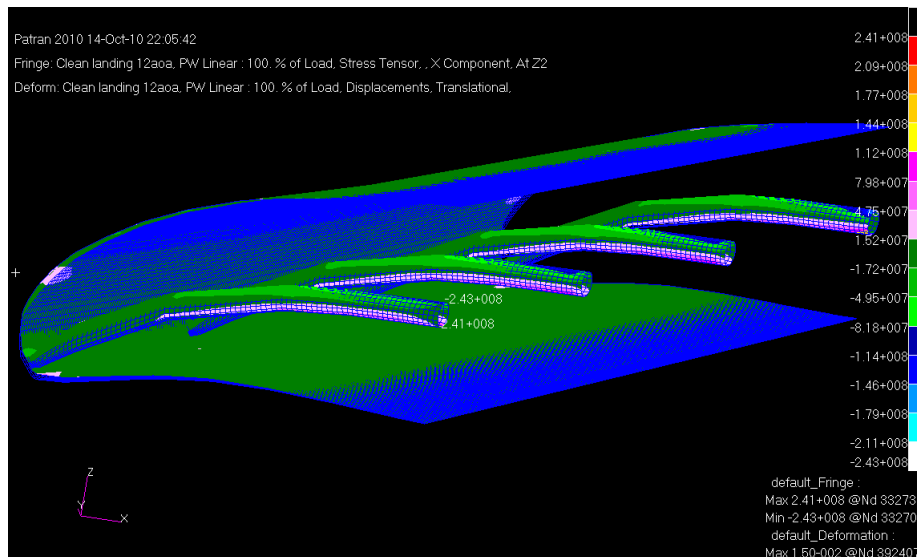
Figure 5.39 Fully deployed leading edge chordwise stress at landing (Units m)

The wing box skin stresses due to external pressure load in the fibre direction, off fibre direction and shear were low compared to the material allowable. Figure 5.40 in fact shows that the maximum stress in the material direction was 18 MPa, in the off fibre direction was approximately 2 MPa and in shear was 9 MPa when their material allowable were 2723 MPa, 101 MPa and 74 MPa respectively. The highest stresses occurred in the outer layers in the 45° or -45° plies and the worst condition was at landing with the leading edge in the neutral position.
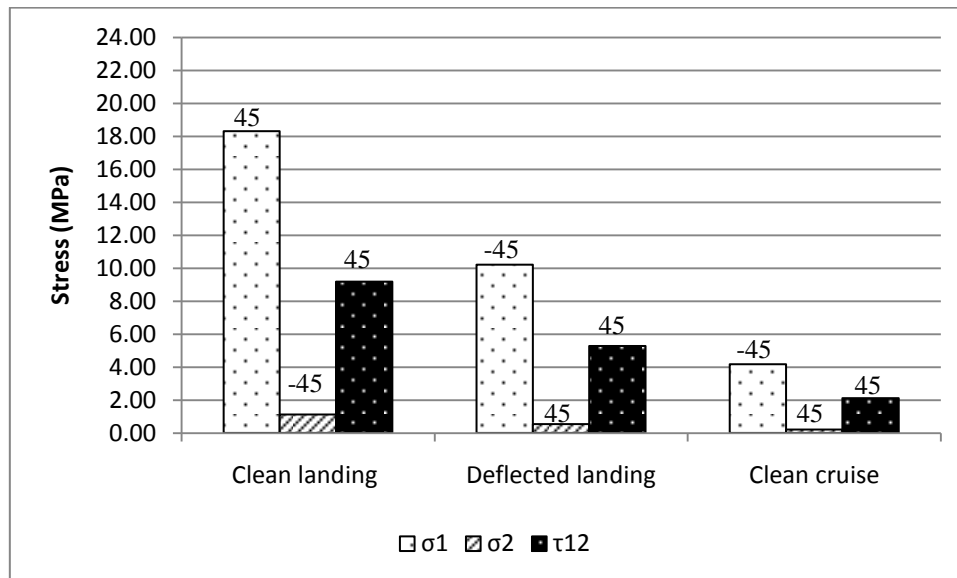
Figure 5.40 Wing box skin stress at the three flight conditions (Units MPa)

Figure 5.41 and Figure 5.42 show the fibre direction and shear stresses in the upper and lower wing box skin panels, at landing condition with the leading edge in its neutral position, and for both cases the maximum stress concentrations were near the front spar.
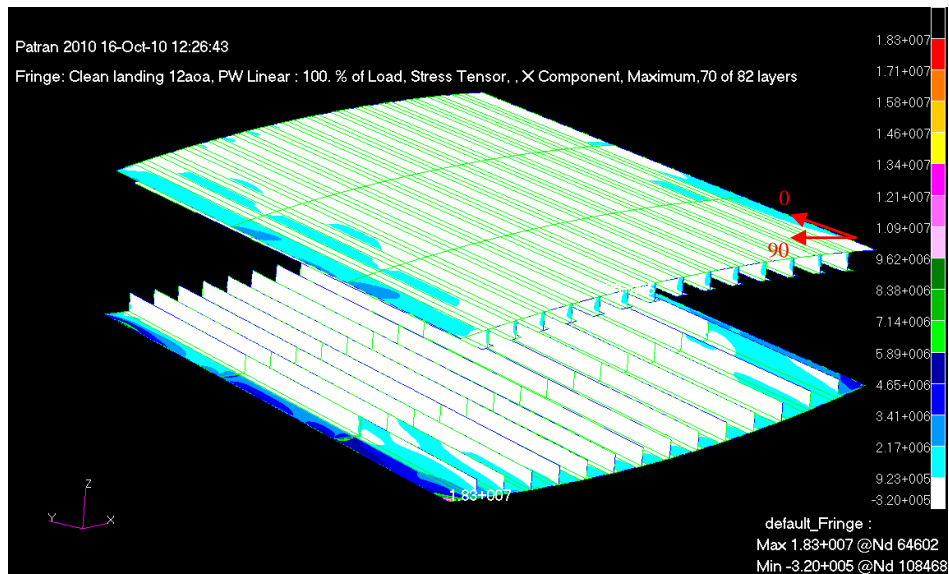
Figure 5.41 Wing box skin fibre direction stresses at landing with the leading edge in clean configuration (Units Pa)
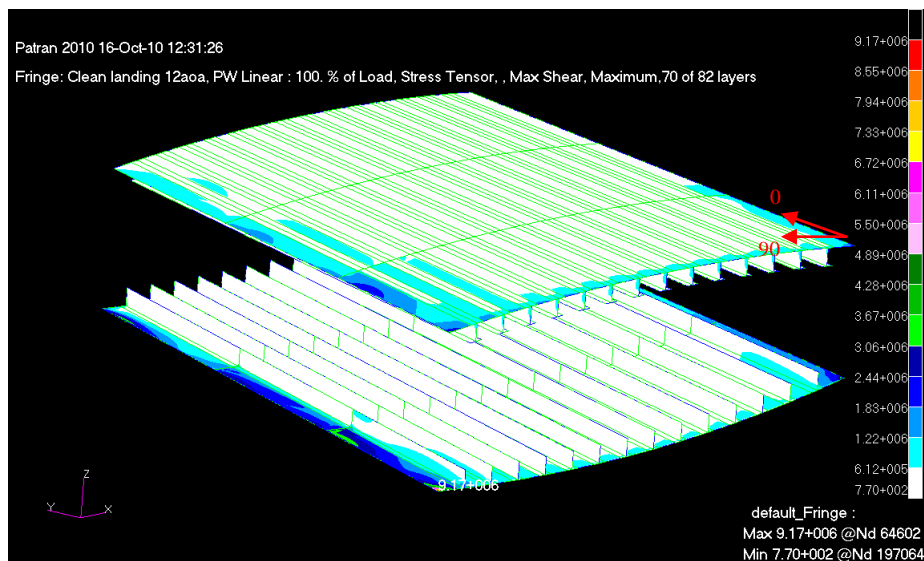
Figure 5.42 Wing box skin shear stresses at landing with the leading edge in clean configuration (Units Pa)

The stresses in the spars were higher for the front one compared to the rear due to the presence of circular cutouts needed to connect the eccentric beam and the actuator driving it. The maximum stress concentration occurred at the edges of the cutout. The reinforcement rings placed around the cutouts helped to release the stresses on the spar web reducing the stresses by up to 30%. Figure 5.43 and Figure 5.44 show the fibre

direction stresses on the spar web and reinforcement ring for the landing case with the leading edge in the clean configuration.
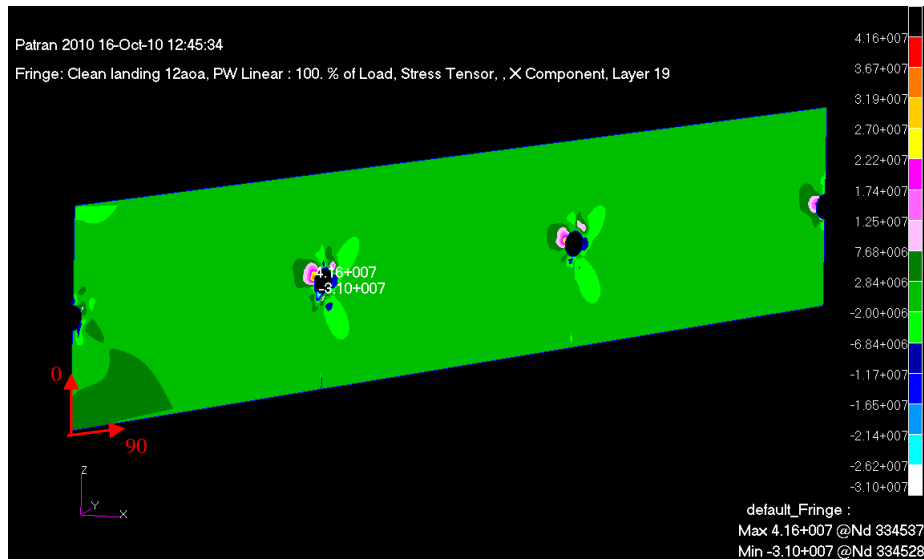
Figure 5.43 Spar web fibre direction stress contour around the cutouts at landing with the leading edge in clean configuration (Units Pa)
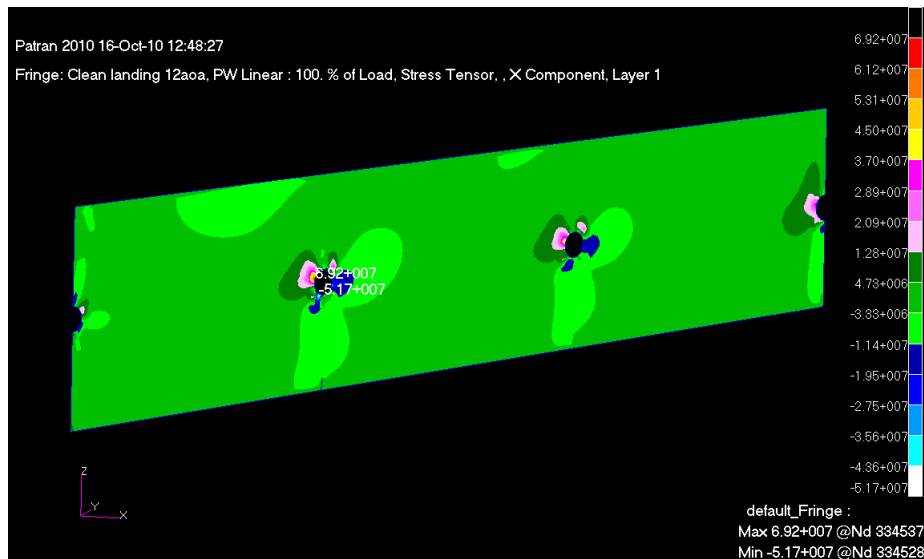
Figure 5.44 Spar cutout reinforcement fibre direction stress contour at landing with the leading edge in clean configuration (Units Pa)

The detailed comparison of the front spar reinforcement rings and spar web stresses around the cutout are shown in Table 5.5 and Table 5.6. The plies where the highest fibre direction stress and shear stress concentrations occurred were in most cases in the 0° plies where the fibres were oriented in the spanwise direction. The off fibre stresses were instead higher in the 45° or -45° plies. The failure indices also indicated that the stresses in all direction for the three flight conditions were well below the material allowable.

Table 5.5 Front spar cutout reinforcement fibre direction, off fibre direction and shear stresses

	Reinforcement rings								
	σ_1	FI	Ply	σ_2	FI	Ply	τ_{12}	FI	Ply
Landing clean	69.20	0.02	0	4.00	0.08	45	34.70	0.44	0
Landing deflected	14.70	0.004	0	0.64	0.01	-45	7.39	0.09	0
Clean cruise	4.27	0.001	0	0.19	0.004	-45	2.17	0.03	0

Table 5.6 Front spar fibre direction, off fibre direction and shear stresses

	Spar								
	σ_1	FI	Ply	σ_2	FI	Ply	τ_{12}	FI	Ply
Landing clean	41.60	0.01	0	2.54	0.05	45	27.70	0.35	0
Landing deflected	14.50	0.004	0	0.84	0.02	0	7.58	0.10	45
Clean cruise	4.13	0.001	45	0.64	0.01	45	2.30	0.03	0

The stresses on the four ribs under the aerodynamic pressure loads at the three flight conditions were low, as shown in Figure 5.45 . The highest stresses occurred in the outer layers in the 45° or -45° plies and the worst condition was at landing with the leading edge fully deployed. In this configuration the maximum fibre direction stress was 95.8 MPa, while the off fibre and shear stresses were 5.39 MPa and 49.9 MPa respectively. The failure indices for these three stress components were therefore 0.02,

0.11 and 0.63 which indicated that the stresses in the ribs were safely below the design limits.

Figure 5.45 Ribs stress at the three flight conditions (Units MPa)

Figure 5.46 Ribs fibre direction stress contour at landing condition with the leading edge fully deployed (Units Pa)
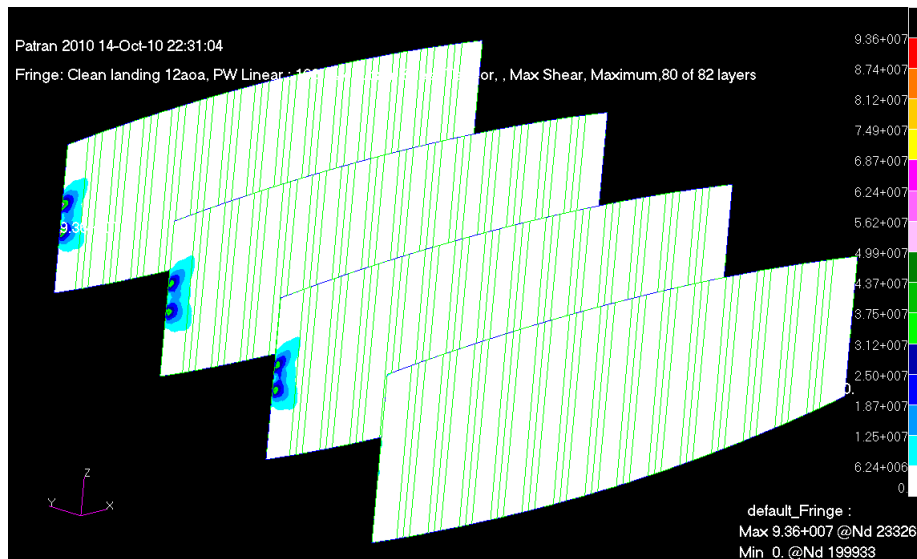
Figure 5.47 Ribs shear stress contour at landing condition with the leading edge fully deployed (Units Pa)

The maximum stress concentration occurred at the point where the ribs were connected to the front spar and in particular this position corresponded to the region where the cutouts were placed. Figure 5.46 and Figure 5.47 show these stress concentration regions for the fibre direction and shear stresses. The stress contours also showed that average stress level in the rest of the rib was much lower.

A buckling analysis was also carried out as part of the wing box and leading edge structure static study. Table 5.7 shows the buckling load factor for the first three modes, and it points out that the lowest buckling load was at landing condition when the leading edge was fully deployed.

Table 5.7 Leading edge and wing box structure bucking load factor

Mode	Landing clean	Landing deflected	Clean cruise
1	8.9	3.9	6.2
2	9.4	5.7	7.2
3	-	7.2	9.2

All these modes however, corresponded to a leading edge skin mode, as shown in Figure 5.48 Figure 5.49, indicating that the wing box skin was safely reinforced by the stringers, at all three flight conditions, against panel buckling.
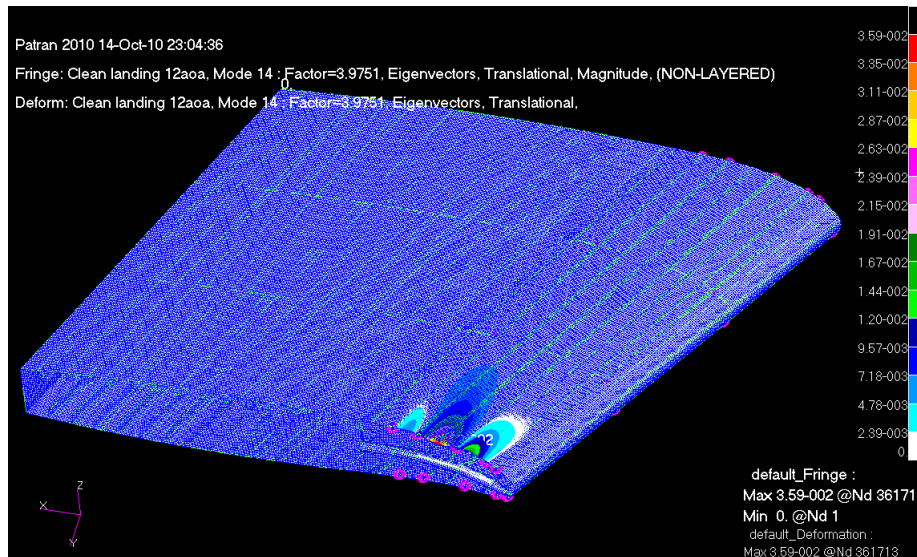
Figure 5.48 Landing condition with the leading edge fully deployed first buckling mode
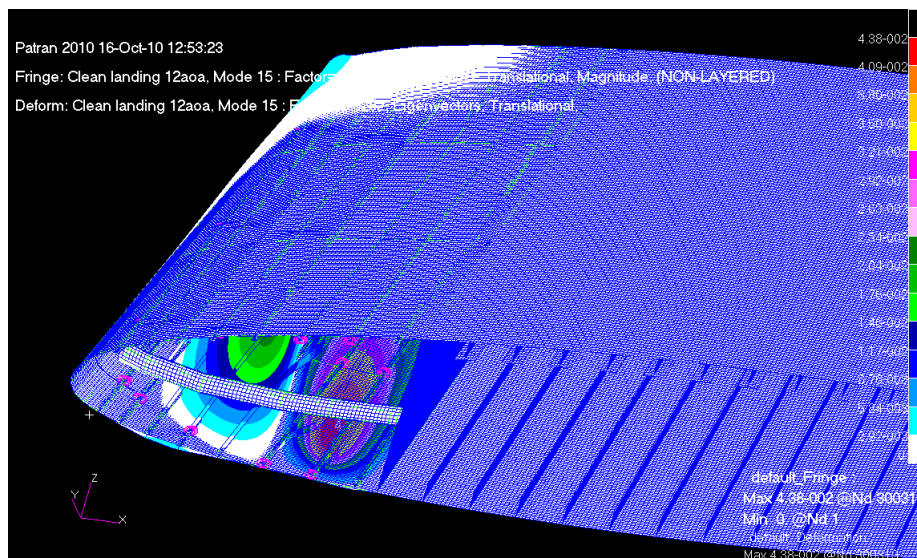
Figure 5.49 Landing condition with the leading in neutral position first buckling mode

As this study showed that the wing box skin was stable, the structures vibration analysis was carried out only for the leading edge with the integrated eccentric beam actuation mechanism, which is presented in the next section.

5.5. Morphing Leading Edge Dynamic Response Analysis

The final stage of the morphing leading edge study was to analyse its dynamic behaviour. A modal analysis was firstly conducted to obtain the natural frequencies and mode shapes of the structure with the integrated actuation system. Then, a frequency and gust response analysis, at both landing and cruise conditions, were carried out. The effect of the actuator stiffness at the root of the eccentric beam was also taken into account by changing the beam stiffness at root as explained for the static case.

5.5.1. Natural Vibration Analysis

The leading edge vibration analysis was carried out for both deployed and clean configurations.

Table 5.8 and Table 5.9 summarise the first six natural frequencies at landing, with the leading edge fully deployed, and in cruise, with the leading edge in neutral position. These results also showed how the eccentric beam root stiffness affected the dynamic characteristics of the high lift device and its actuation system.

Table 5.8 Leading edge natural frequencies in landing configuration

| Mode number | Landing with leading edge fully deployed | | | |
| | 100% stiffness | | 10% stiffness | |
	Frequency (Hz)	Mode type	Frequency (Hz)	Mode type
1	20.559	Disc	20.478	Disc
2	38.086	Disc	37.523	Disc
3	54.607	Disc	53.468	Beam
4	67.898	Disc	54.608	Disc
5	77.372	Beam	54.609	Disc
6	77.372	Skin	74.159	Skin

Table 5.9 Leading edge natural frequencies in cruise configuration

| Mode number | Cruise configuration with leading edge in neutral position | | | |
| | 100% stiffness | | 10% stiffness | |
	Frequency (Hz)	Mode type	Frequency (Hz)	Mode type
1	63.794	Beam	47.972	Beam
2	63.924	Disc	63.924	Disc
3	75.794	Skin	71.412	Skin
4	95.970	Disc	95.970	Disc
5	133.970	Skin	132.240	Skin
6	139.860	Skin	139.830	Skin

In landing configuration the first natural frequency was lower than that in cruise, and the corresponding mode was a disc vibration mode. The first beam mode at landing condition occurred at 73 Hz when the root stiffness was 100% and 53 Hz when the root stiffness was 10%. Furthermore, the first beam vibration mode at cruise condition for the 100% beam root stiffness was 64 Hz; however this was reduced by 25% when the beam root stiffness was reduced to 10%. The skin first vibration mode occurred instead at the higher modes: 77 Hz and 134 Hz when the leading edge was in the landing and cruise configurations respectively. The higher modes results showed that the eccentric beam root stiffness did not have much influence on the skin natural frequency. When the beam stiffness was reduced the skin natural frequency only reduced by 4.1% for the landing case and 1.3% for the cruise configuration. Figure 5.50 and Figure 5.51 shows the leading edge first beam and skin vibration modes at landing with the eccentric beam stiffness reduced to 10%. Figure 5.52 and Figure 5.53 shows the leading edge first beam and skin mode shapes at cruise with the eccentric beam stiffness reduced to 10%.
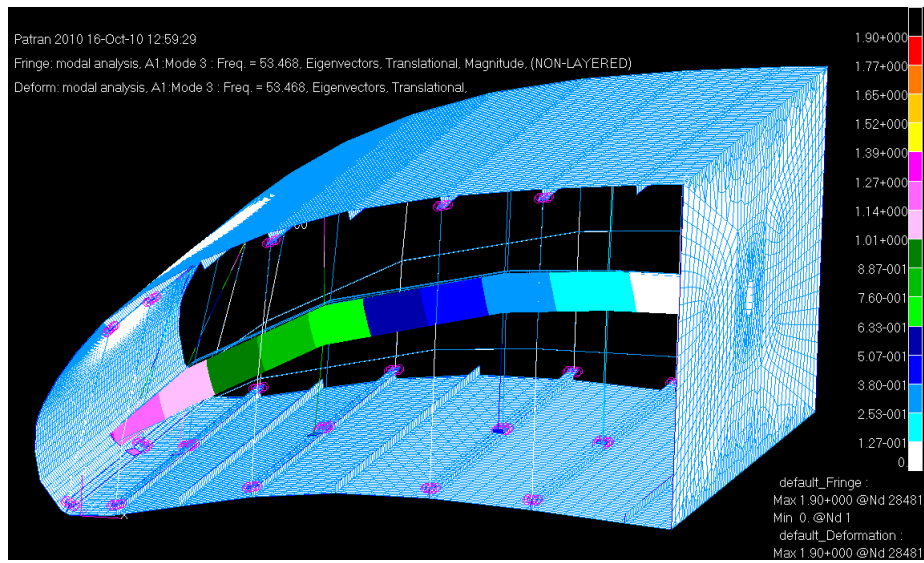
Figure 5.50 Mode 3 vibration of the fully deployed leading edge with reduced beam root stiffness: at 53.468 Hz
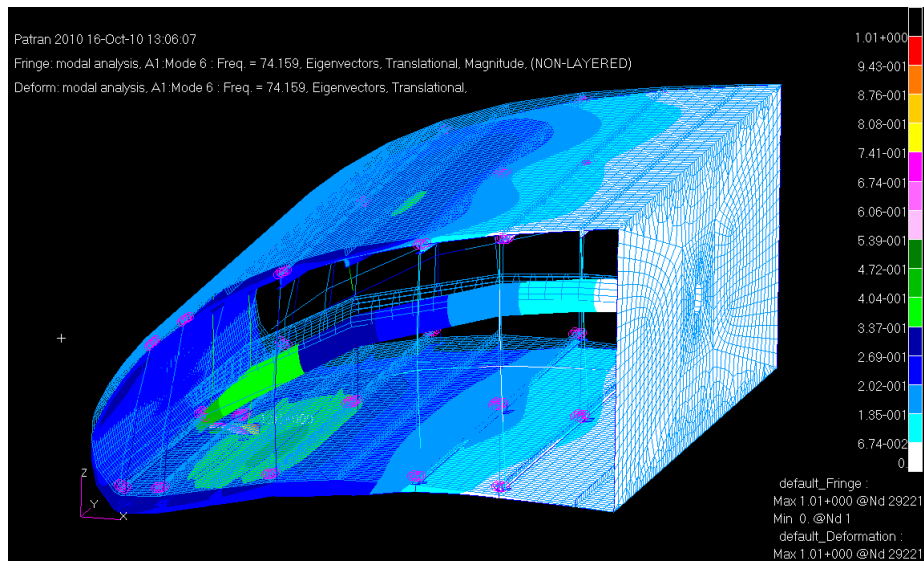
Figure 5.51 Mode 6 vibration of the fully deployed leading edge with reduced beam root stiffness: at 74.159 Hz
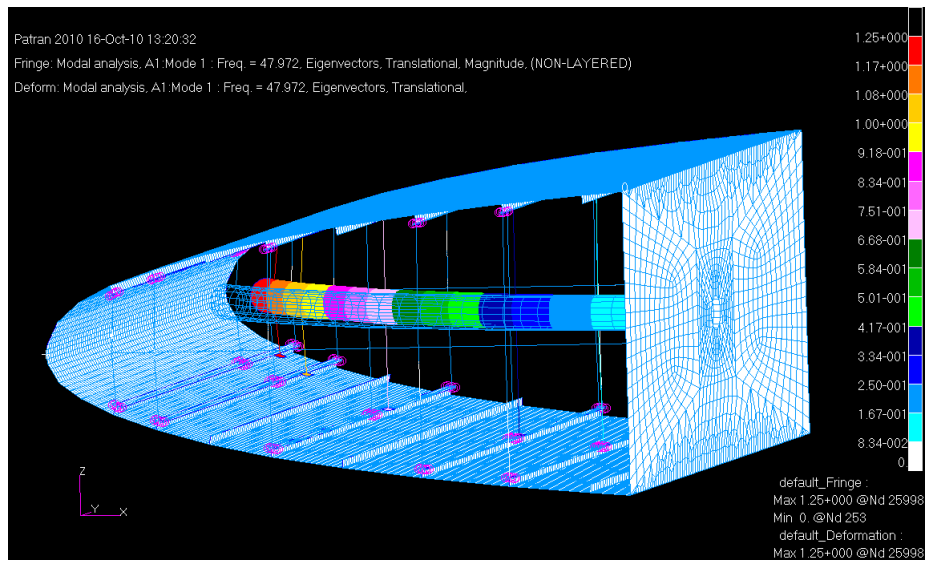
Figure 5.52 Mode 1 vibration of the leading edge in neutral position 47.972 Hz
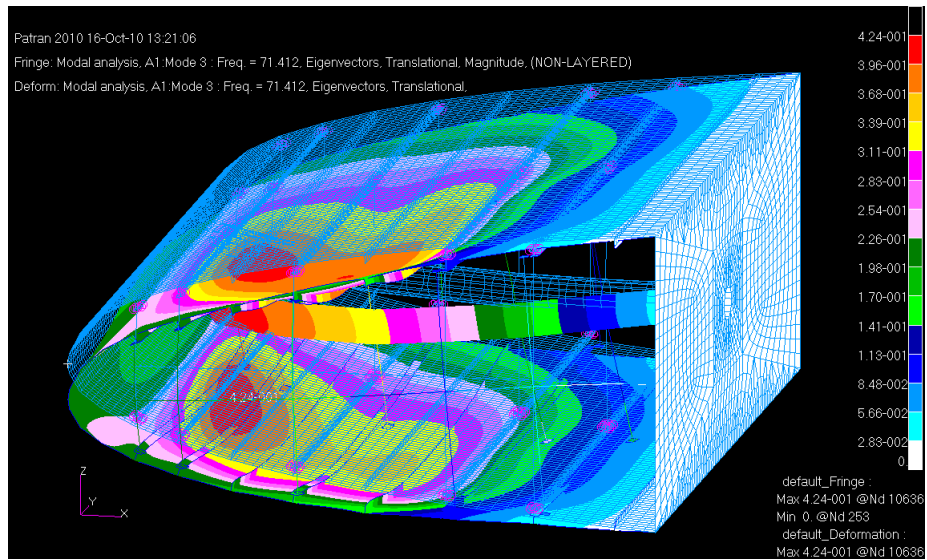
Figure 5.53 Mode 3 vibration of the leading edge in neutral position 71.412 Hz

5.5.2. Frequency Response

Before analysing the dynamic response behaviour of the morphing leading edge structure a frequency response analysis was carried out. This study allowed to predict at which frequencies the structure was subject to larger vibrations. The results were therefore used to validate the natural frequencies obtained from the modal analysis, and also to ensure that the finite element model was correctly set up for the dynamic response analysis. The frequency dependent force was an arbitrary sinusoidal point load applied at the nose of the leading edge. The structural damping coefficient was 3% of the critical damping. The study was conducted for both landing deployed (with the aerodynamic load at landing conditions) and cruise clean configurations (with the aerodynamic load at cruise conditions) and also the effect of the eccentric beam root stiffness was taken into consideration.

Figure 5.54 and Figure 5.55 show the eccentric beam frequency response when its root stiffness was varied from 100% to 10%. Both responses had the same trend however, for the 10% stiffness case the displacement at a specific frequency was higher. The first response peak was seen at 20 Hz, which corresponded to the first structural vibration mode where however, only the discs were affected. The second peak, much more evident, was at 75 Hz which corresponded to the first overall structural vibration mode.
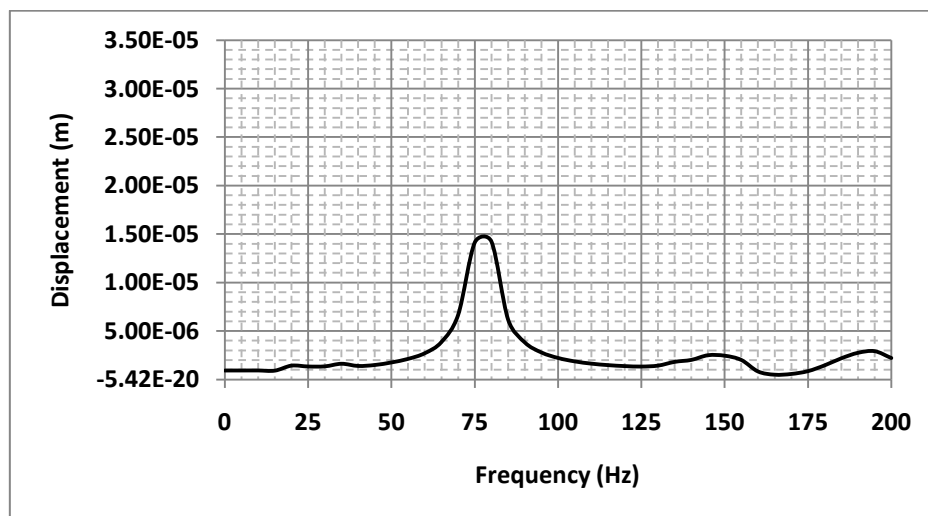
Figure 5.54 Eccentric beam frequency response with 100% beam root stiffness at landing
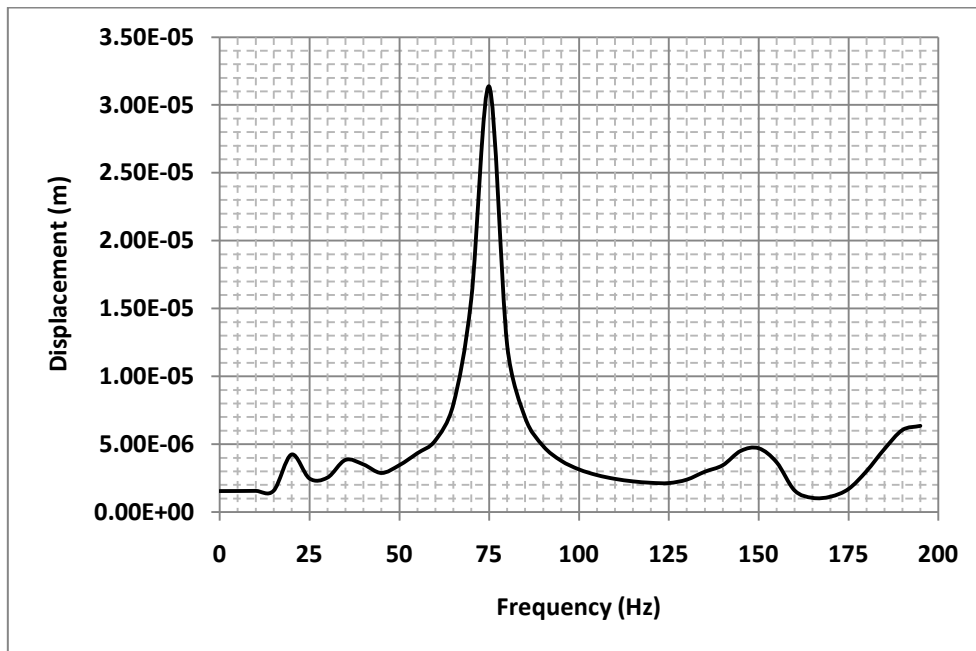
Figure 5.55 Eccentric beam frequency response with 10% beam root stiffness at landing

Figure 5.56 and Figure 5.57 show the leading edge skin frequency response when the eccentric beam root stiffness was varied from 100% to 10%. The peak response of the skin, as expected, was at the skin first natural frequency, at 75 Hz. A second peak occurred at 155 Hz, which probably corresponded to the skin second natural frequency.
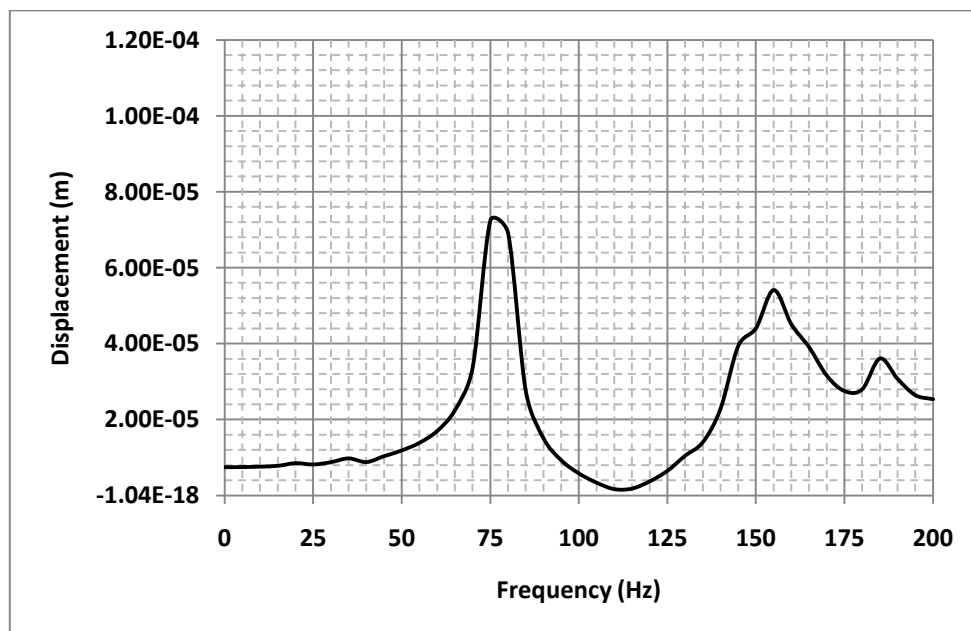
Figure 5.56 Leading edge skin frequency response with 100% beam root stiffness at landing
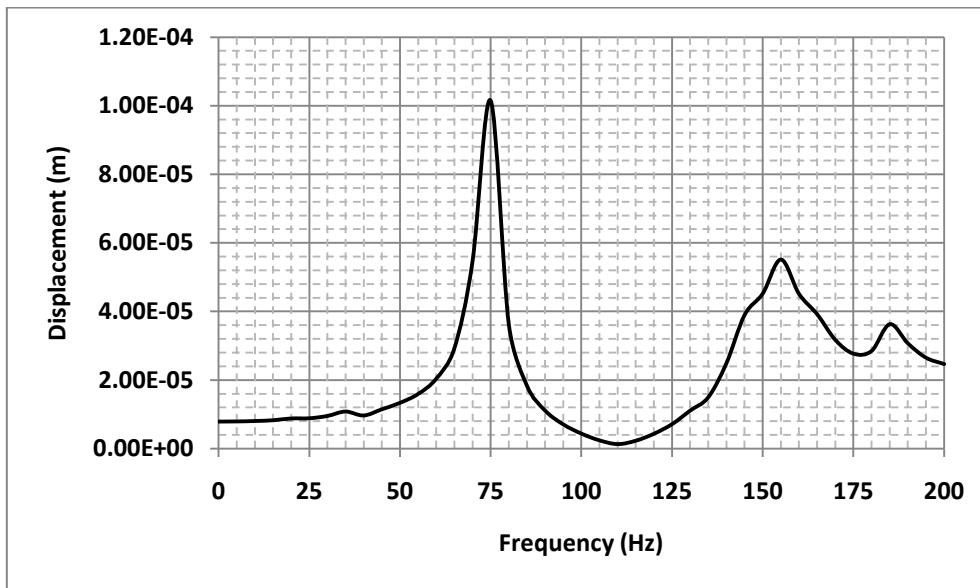
Figure 5.57 Leading edge skin frequency response with 10% beam root stiffness at landing

At cruise, the first global natural frequency of the structure was similar to that obtained for the landing condition, varying between 70 and 75 Hz. This characteristic was also seen from the frequency response results. Figure 5.58 and Figure 5.59 show the eccentric beam responses when its root stiffness was varied from 100% to 10%. A high response peak occurred at 75 Hz, whereas a smaller peak was seen at 135 Hz which corresponded to the skin second vibration mode.
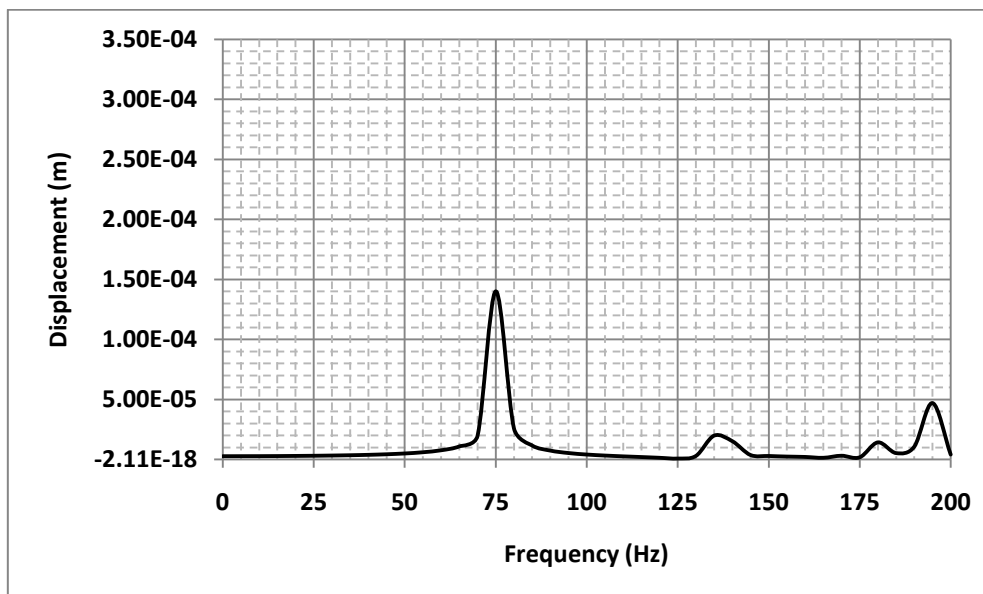
Figure 5.58 Eccentric beam frequency response with 100% beam root stiffness in cruise
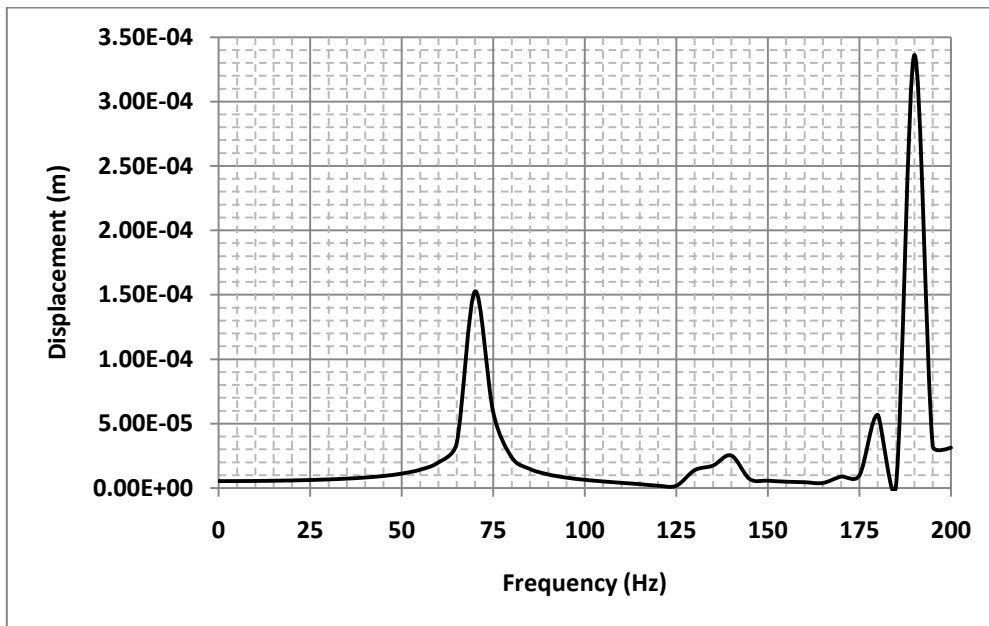
Figure 5.59 Eccentric beam frequency response with 10% beam root stiffness in cruise

When the leading edge skin frequency response was analysed, at the two response peaks, 75 and 130 Hz, the skin vibration was much higher compared to that of the eccentric beam. In this case, as shown in Figure 5.60 Figure 5.61 the second peak, corresponding to the second skin vibration mode, was more evident than the first one.
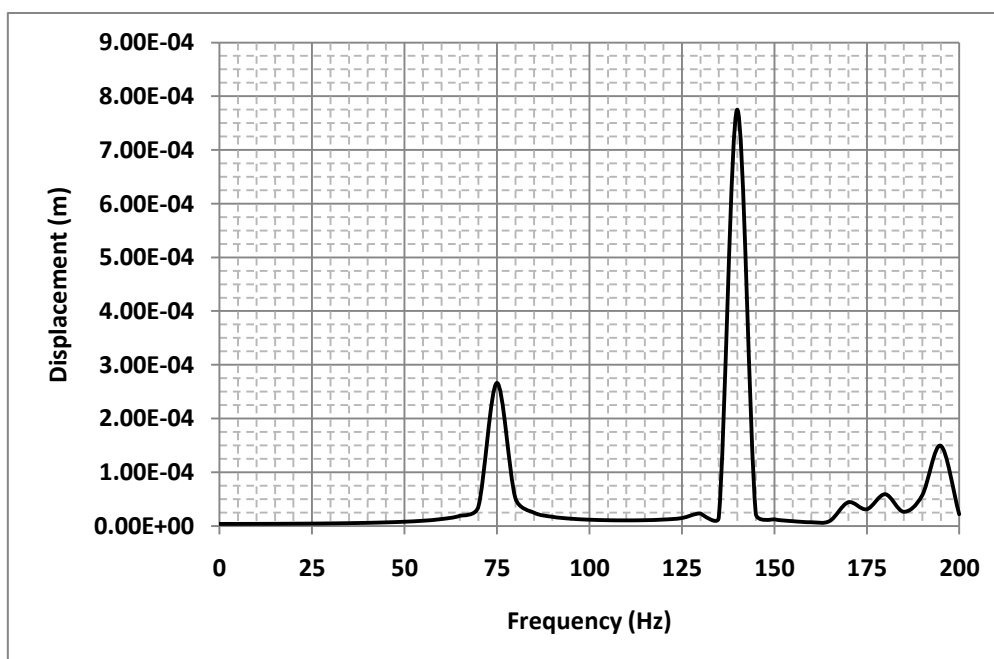
Figure 5.60 Leading edge skin frequency response with 100% beam root stiffness in cruise
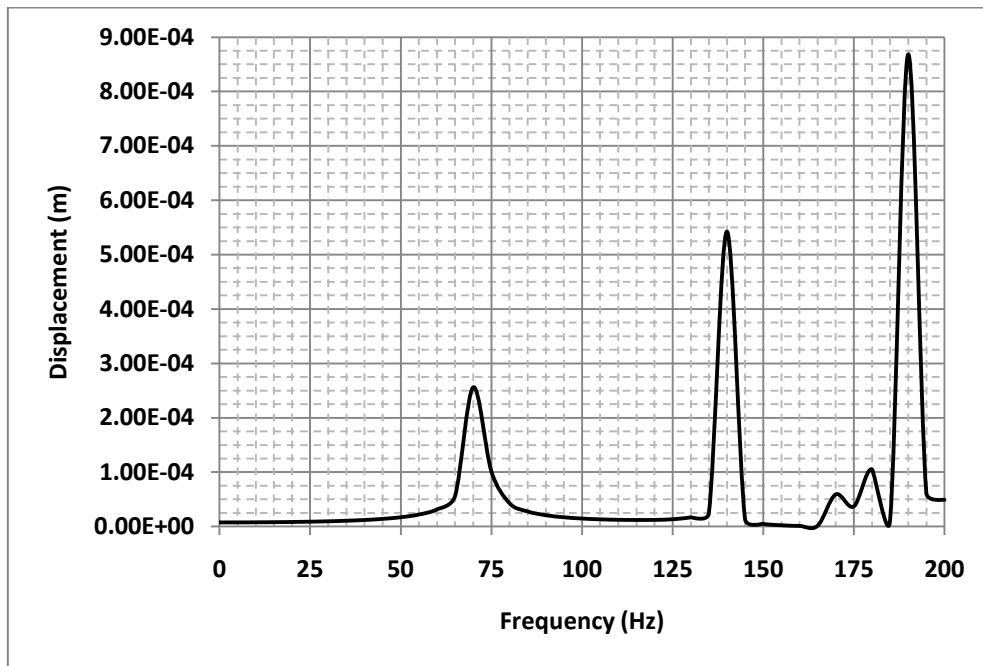
Figure 5.61 Leading edge skin frequency response with 10% beam root stiffness in cruise

When the beam root stiffness was 10% a high response peak was experienced at 190 Hz. This structural characteristic was seen in both eccentric beam and leading edge skin response, as shown in Figure 5.59 and Figure 5.61.

These results showed that when the leading edge was subject to a cyclic load, varying at a frequency near the overall structure's natural frequency, the structure was subject to high vibration peaks. This behaviour was expected, as any structure with a vibration frequency close to the natural frequency is at risk of reaching the so called resonance condition, when the structures vibration continues to diverge instead of damping out. The frequency response graphs therefore proved that the finite element model was correctly set up for a dynamic analysis and therefore they were used to study the leading edge gust response behaviour at landing and cruise conditions.

5.5.3. Gust Response Analysis

The leading edge response to a gust load was studied at landing and cruise conditions. At landing both neutral and deflected configurations were considered. For this study

case the gust shape was approximated as a discrete '1-cos' shape gust, as described in Section 2.3.2, and it was applied to the leading edge structure as a time dependent pressure in addition to the static pressure. At landing the atmospheric conditions were taken at 20,000 ft. At this altitude the aircraft equivalent airspeed was 34.6 m/s and the gust velocity 20 m/s. The gust load factor was calculated using Eq. (2-1) and it was 1.04, which meant that the magnitude of the gust load was 1.04 times the static aerodynamic pressure. The gust length at landing varied between 18 and 214 m so from Eq. (2-2) the highest gust frequency was 2.06 Hz. In the analysis, the static pressure was preloaded onto the leading edge structure and then the gust load was applied for four cycles. The structural damping coefficient was 3% of the critical damping.

Figure 5.62 and Figure 5.63 show the eccentric beam tip gust response vibration for 100% and 10% beam root stiffness at landing condition, with the leading edge structure in neutral position. The initial pressure load caused a small vertical displacement of 0.08 mm, which increased by 200% when the gust load was applied. The structure returned to its position of equilibrium almost immediately when the load was released. This phenomenon occurred because the frequency at which the leading edge was excited at was relatively low and the inertia effect was not evident. The structures response did not therefore show a slow vibration decay, as one would expect. When the structure was subject to a higher frequency vibration the effect of inertia played a role in the structures response, and therefore when the time dependent load was applied the deflection increased and few oscillations were needed before equilibrium was restored, after the load was released. If the whole wing structure was considered the inertia effect would have been more significant at the frequency used for this analysis as the natural frequency would have been much lower. The reduction in beam root stiffness also increased the deflection by 18% so that the maximum beam tip deflection was 0.26 mm.

Figure 5.62 Eccentric beam gust response at landing clean configuration, with gust frequency 2.06 Hz and gust load 1.04, with 100% beam root stiffness

Figure 5.63 Eccentric beam gust response at landing clean configuration, with gust frequency 2.06 Hz and gust load 1.04, with 10% beam root stiffness

Figure 5.64 and Figure 5.65 show the leading edge skin gust response vibration for 100% and 10% beam root stiffness at landing condition, with the leading edge structure in neutral position.
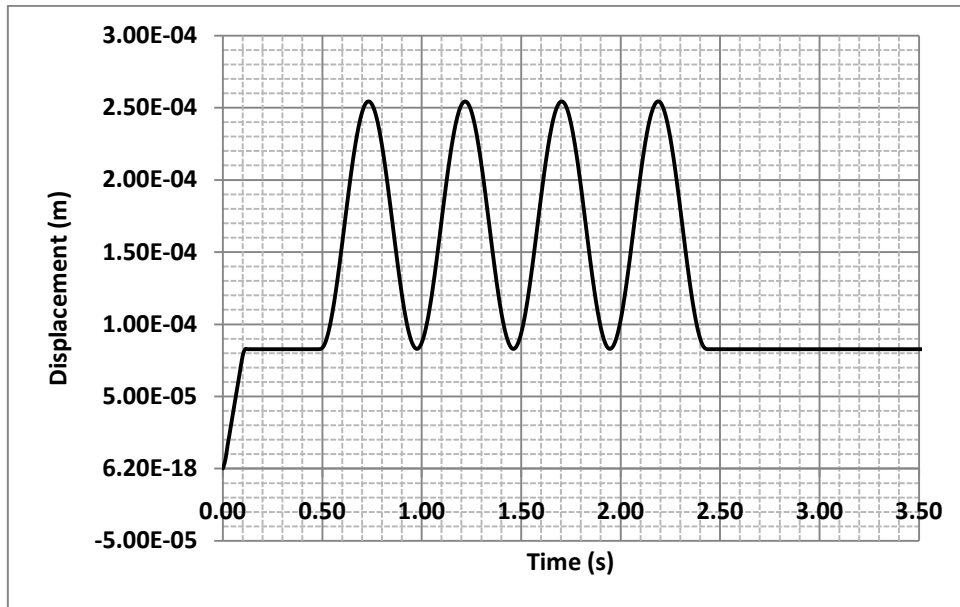
Figure 5.64 Leading edge skin gust response at landing clean configuration, with gust frequency 2.06 Hz and gust load 1.04, with 100% beam root stiffness
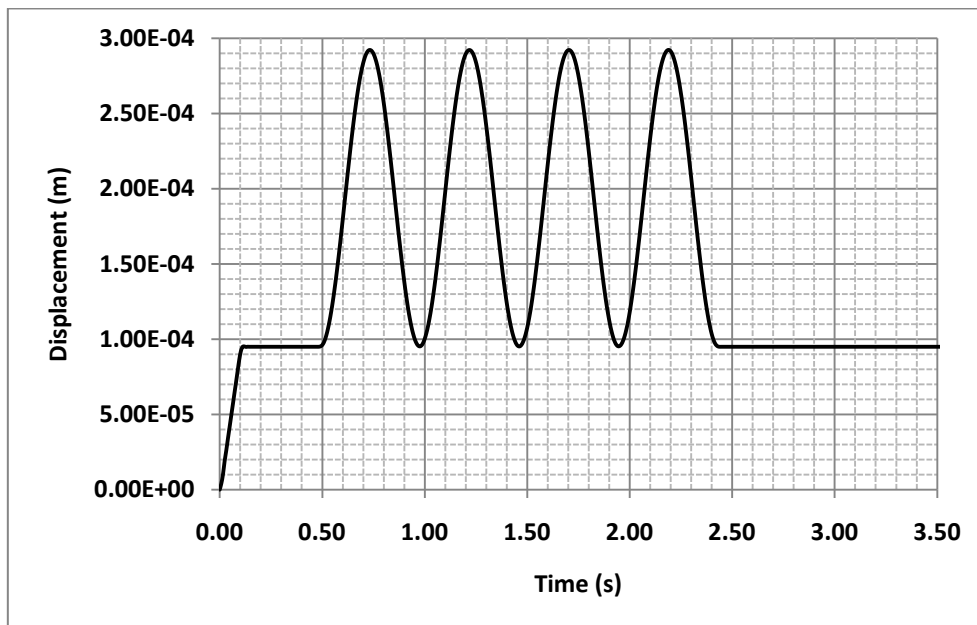
Figure 5.65 Leading edge skin gust response at landing clean configuration, with gust frequency 2.06 Hz and gust load 1.04, with 10% beam root stiffness

The initial skin deflection due to the static pressure was approximately 0.1 mm. The gust load increased this displacement up to 0.25 mm, which corresponded to a 200% increase. However, the structure returned to its original position as soon as the dynamic load was released. The decrease in eccentric beam root stiffness had a small effect on the overall structure gust response as it increased the skin deflection by only 16%.

At landing condition with the leading edge fully deployed the gust load factor and frequency were the same as the previous case however; the aerodynamic pressure on the high lift device structure was higher and therefore, the elastic deformation caused was larger. The leading edge skin displacement due to the static pressure was approximately 1.5 mm which was in fact five times higher compared to the clean case, as shown in Figure 5.66 and Figure 5.67. The gust load increased the initial displacement by 200%, up to 3.6 mm and 4 mm for the 100% and 10% beam root stiffness cases respectively. Once the dynamic load was released the structure returned to its original position almost immediately.
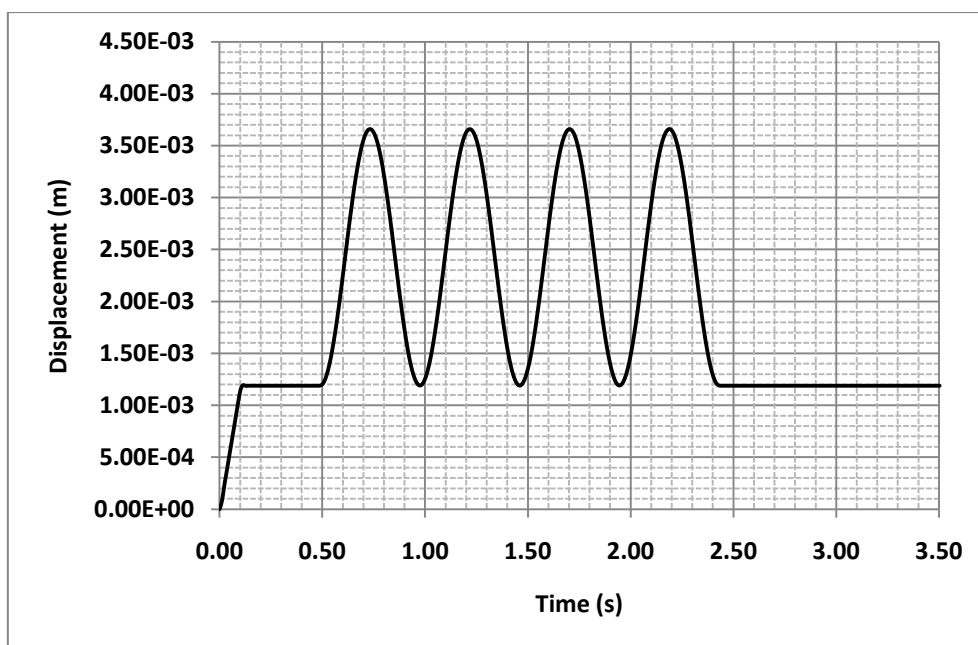
Figure 5.66 Leading edge skin gust response at landing deflected configuration, with gust frequency 2.06 Hz and gust load 1.04, with 100% beam root stiffness
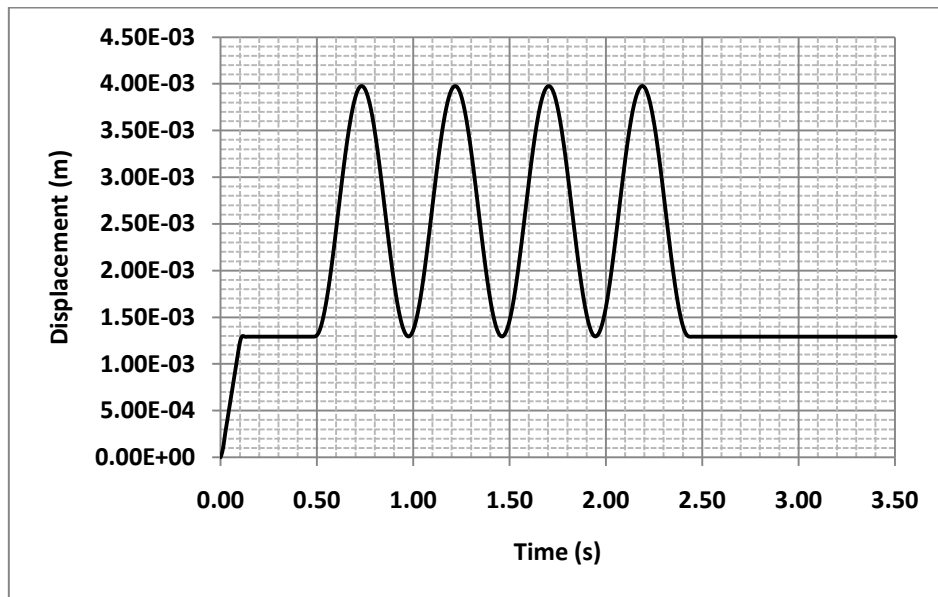
Figure 5.67 Leading edge skin gust response at landing deflected configuration, with gust frequency 2.06 Hz and gust load 1.04, with 10% beam root stiffness

Figure 5.68 and Figure 5.69 show the eccentric beam response to the gust input for both 100% and 10% root stiffness cases. The deflection due to the static load was for both cases approximately 1.5 mm. However, the deflection due to gust was higher for the reduced stiffness case and the peak displacement was 4.5 mm, which was slightly higher than the leading skin deflection at the same conditions.
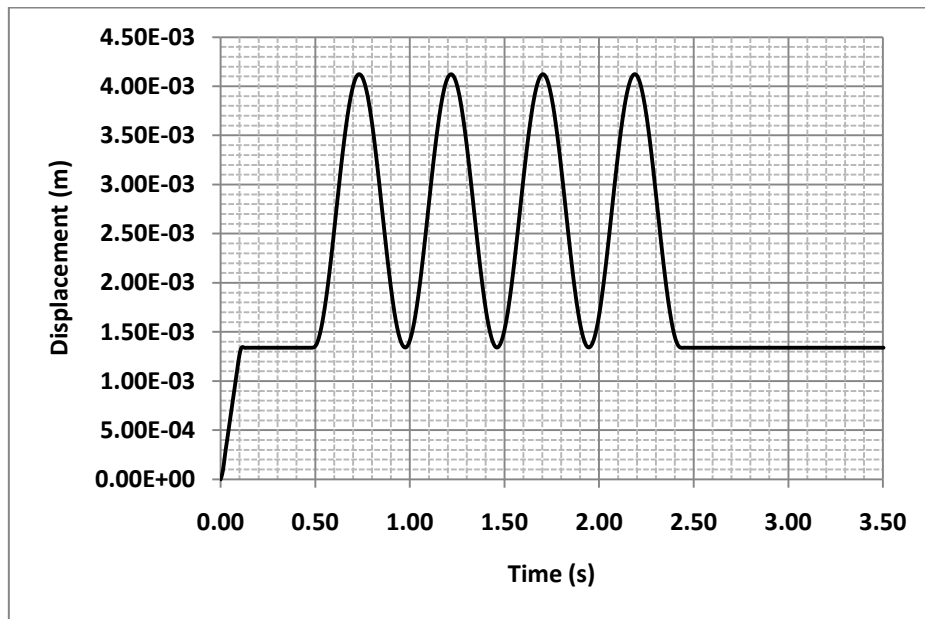
Figure 5.68 Eccentric beam gust response at landing deflected configuration, with gust frequency 2.06 Hz and gust load 1.04, with 100% beam root stiffness
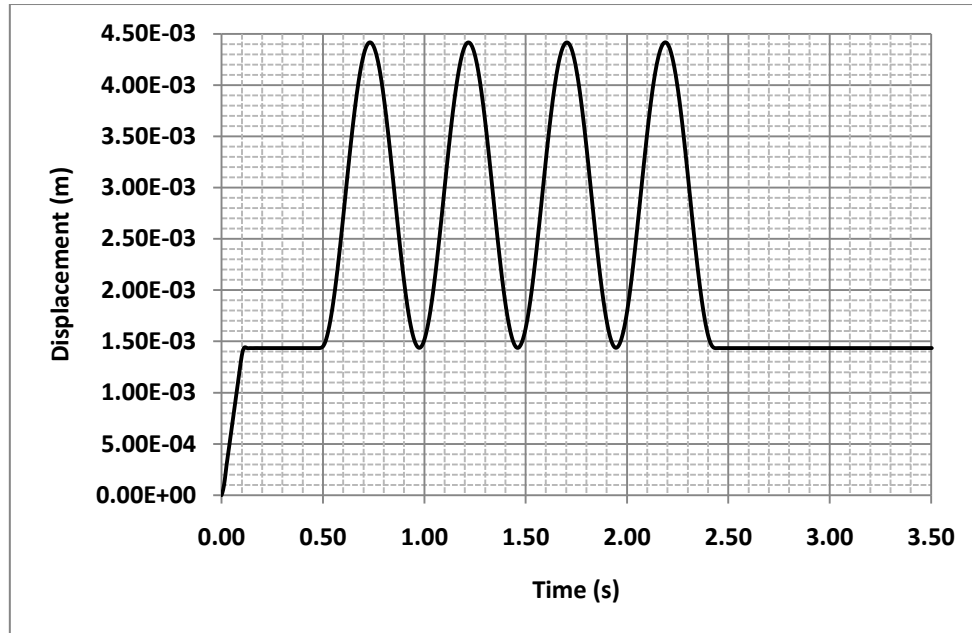
Figure 5.69 Eccentric beam gust response at landing deflected configuration, with gust frequency 2.06 Hz and gust load 1.04, with 10% beam root stiffness

At cruise condition the atmospheric data were taken at 31,000 ft, where the aircraft equivalent airspeed was 145 m/s and the maximum gust velocity was 17 m/s. The gust load factor at cruise was 2.5 and it was obtained using Eq. (2-1). Similarly to the landing case, the gust length varied between 18 and 214m so that the highest gust frequency was 14Hz. In the finite element analysis the dynamic load, which was a time depended pressure, was applied after 0.12 seconds for four cycles. This initial time shift was done so that the structure had enough time to return to a state of equilibrium after the static pressure was applied. The structural damping coefficient was 3% of the critical damping.

Figure 5.70 and Figure 5.71 shows the leading edge skin response to the applied gust load. The initial displacement was relatively small, 0.2 mm. However, the 2.5 load factor gust increased this deflection by approximately 5 times. The maximum displacements for the full and reduced beam root stiffness were 1.2 and 1.7 respectively. Once the gust load was released after four cycles the structural vibration damped out in 0.01 s.
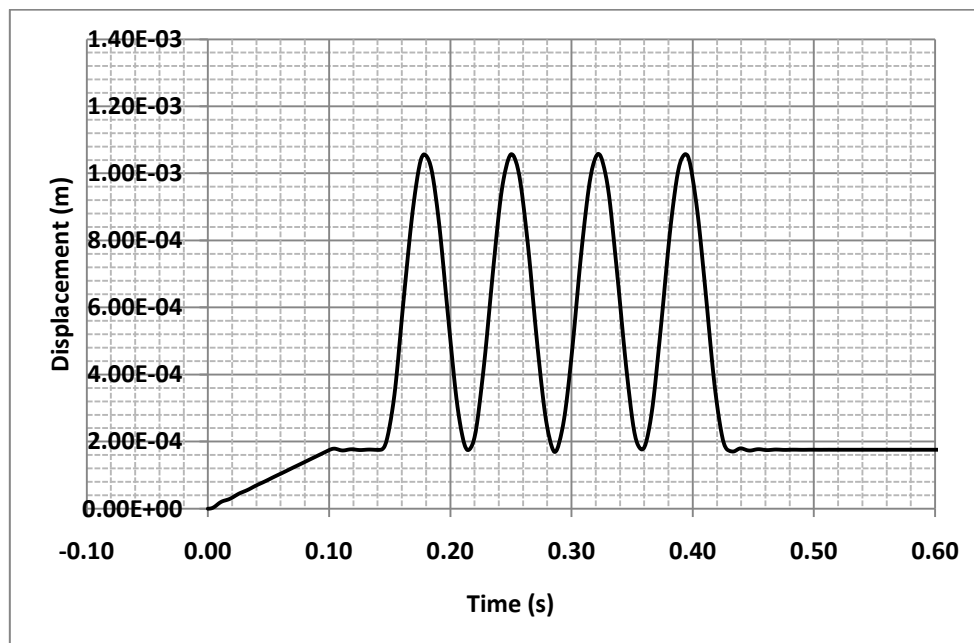
Figure 5.70 Leading edge skin gust response at cruise condition, with gust frequency 14 Hz and gust load 2.5, with 100% beam root stiffness
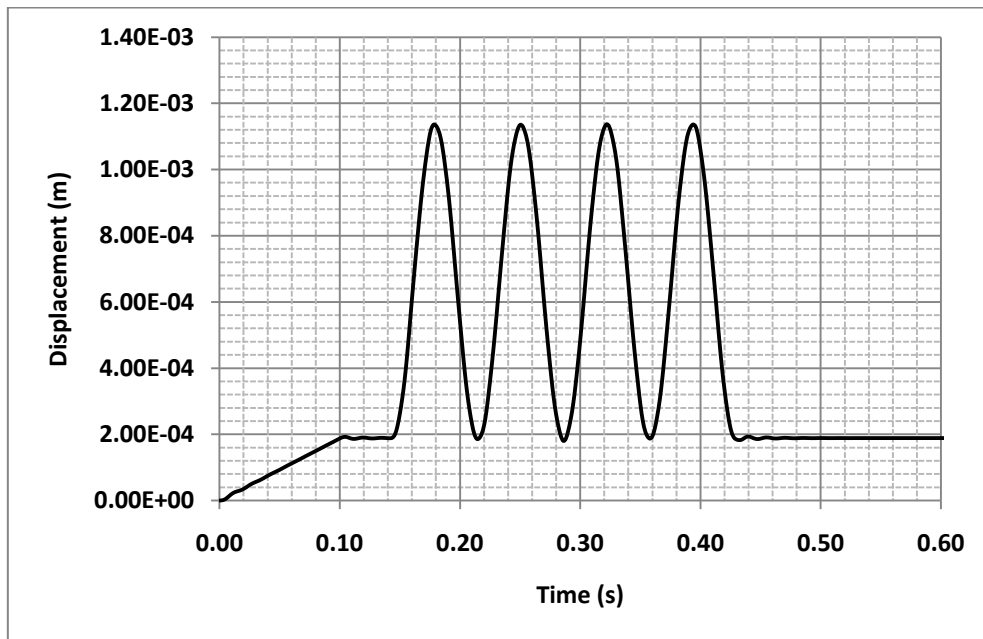
Figure 5.71 Leading edge skin gust response at cruise condition, with gust frequency 14 Hz and gust load 2.5, with 10% beam root stiffness

The eccentric beam tip responses for the 100% and 10% root stiffness cases are shown in Figure 5.72 and Figure 5.73.
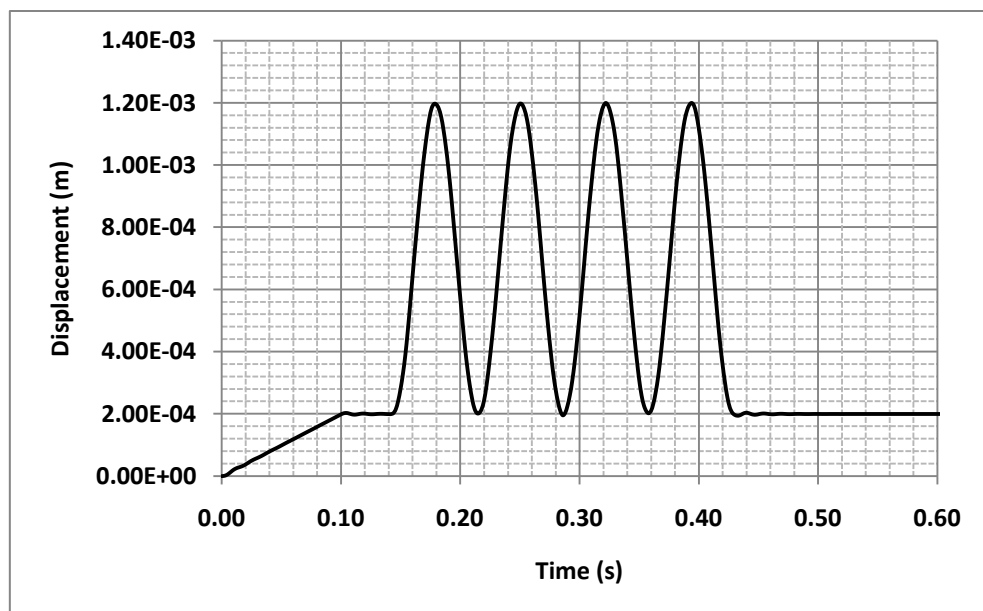
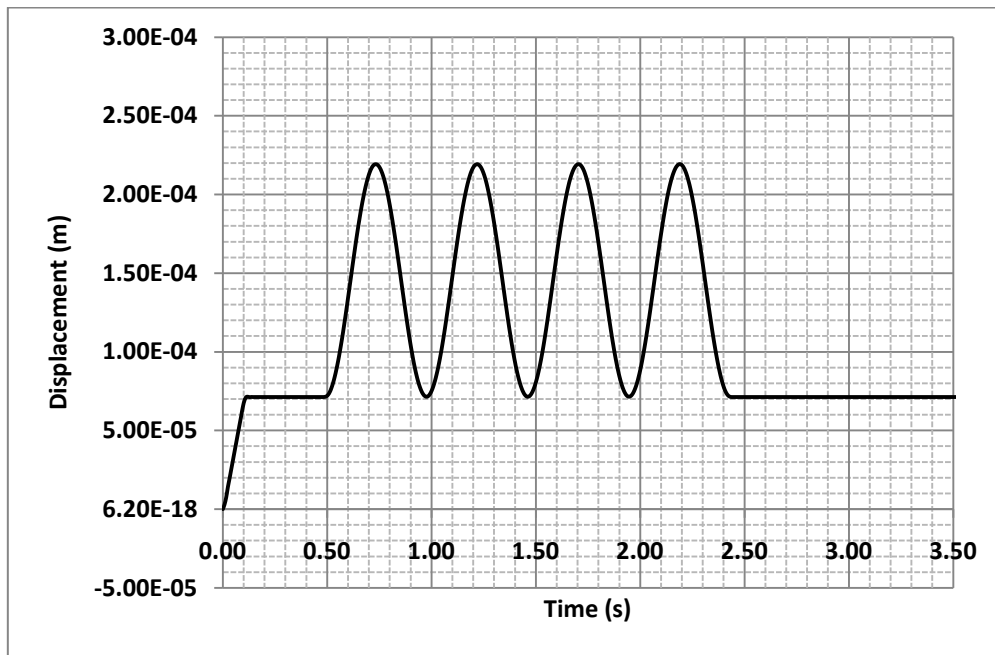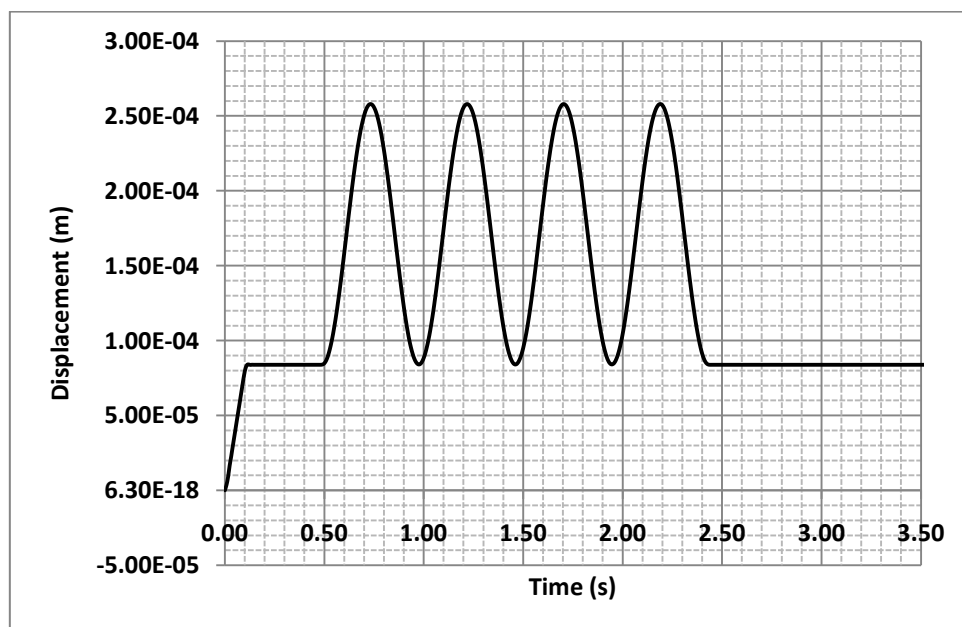**Figure 5.72 Eccentric beam gust response at cruise condition, with gust frequency 14 Hz and gust load 2.5, with 100% beam root stiffness**
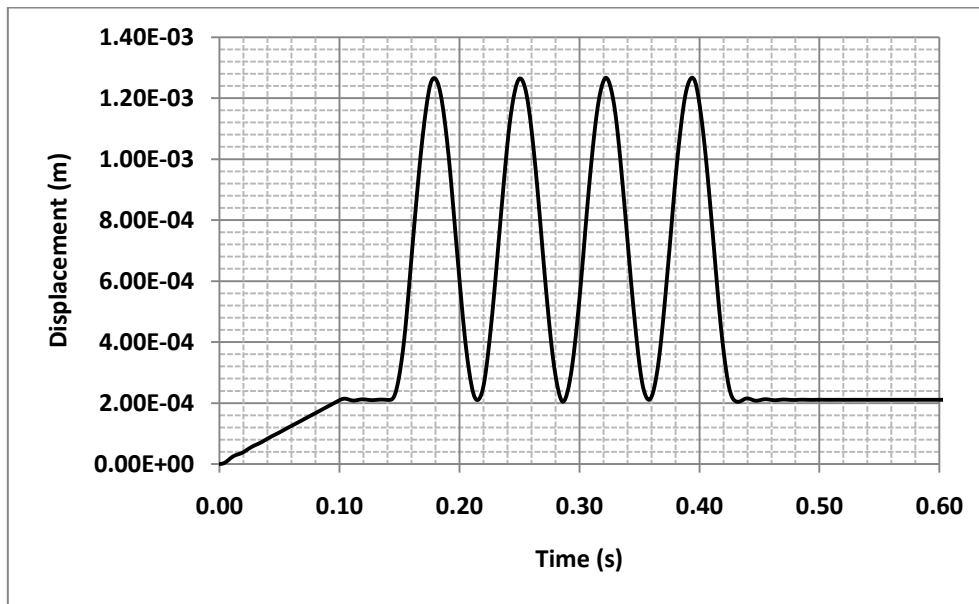
Figure 5.73 Eccentric beam gust response at cruise condition, with gust frequency 14 Hz and gust load 2.5, with 10% beam root stiffness

The vibration characteristics were almost the same as the leading edge skin: the initial beam deflection was also 0.2 mm and the gust load increased this deflection by approximately 5 times. The maximum peaks for the 100% stiffness case was 1.2 mm while for the 10% stiffness case the largest deflection was 1.6 mm. The beam vibration also damped out almost immediately after the gust load was released.

The results showed in this chapter demonstrated that by using a thin aluminium skin and an eccentric beam actuation mechanism it is possible to obtain a morphing leading edge structure that satisfies both design and structural requirements. The demanding nose deflected shape, which enhances the aerodynamic performance, was in fact achieved without violating the structural strength limits and without affecting the stability and stiffness of the main wing box structure. By analysing the whole leading edge skin with the integrated actuation system was also possible to show that the eccentric beam and discs provide adequate stiffness to the structure. The actuation mechanism in fact minimised the overall elastic deformation under the aerodynamic pressure and also helped the leading edge skin to maintain the required shape when deflected. The dynamic analysis also proved that the leading structure is able to maintain a high degree of stability in the event of gust encounter.

Chapter 6

6. Conclusions and Future Work

6.1. Composite Structural Analysis

The research on the design and analysis of the next generation wing concept started with the study of the composite wing box of the chosen reference wing. As the main configuration did not vary from a conventional box type structure the design process was kept at a preliminary stage, setting some key parameters which can be used for future studies. The attention instead, was focused on how this structure can be improved by increasing its strength and load carrying capability without adding significant weight penalty. In particular the following solutions were found:

1. The stress concentrations on spars and ribs webs, caused by the presence of cutouts, can be reduced by optimising the cutout shape or by bonding reinforcement rings around the edges of the cutout.

2. Significant stress reduction is achieved by using these reinforcement rings and their effectiveness depends on their stiffness. In particular, the use of carbon fibre tow placements enables to maximise the ratio of stress reduction and added structural weight.

3. The reinforcement rings also have the capability of increasing the web buckling stability.

4. In order to increase the strength of a composite joint in pulling the stiffness of the base panel must be maximised and good quality bonding must be used between the web and base panels in order to maximise the load transfer.

5. For a composite joint in both pulling and shear it is of paramount importance to carefully choose the outer layers ply orientation. In particular by laying the outer layers fibres in the direction of the applied force it is possible to maximises the load at which laminate matrix failure occurs.

By implementing these findings in the design of the reference composite wing box, it was possible to obtain a failsafe design supporting the morphing leading edge structure. It was important to ensure that the wing box was stiff enough to withstand the aerodynamic loads as the leading edge did not contribute in adding stiffness to the overall wing.

6.2. Eccentric Beam Actuation Mechanism

An actuation mechanism concept has been developed for a short range commercial aircraft's leading edge device, which enables a large morphing deflection with a gapless structure. The main characteristic of this actuation mechanism are described below.

1. The actuation mechanism consists of an actuator mounted onto the front spar, an eccentric beam and five discs with varying radii. The actuator rotates the eccentric beam which is designed with a curvature that meets the leading edge target shape. The combination of the designed beam curvature and the disc dimension ensure that the LE skin deforms to the target deflected shape

2. Each half of the discs is laid in a different plane and the discs are mounted at an angle with respect to the eccentric beam. This is done so that when the leading edge is deflected and the upper and lower skins move in the chordwise direction, the discs follow a path parallel to the stringers. The stringers are in fact used as a railing to guide the discs movement.

3. The edge of the discs had flat flanges and rollers were used to connect the discs to the upper and lower stringers. This connection allowed the free rotation of the

beam and at the same time allowed the discs to be always connected to the leading edge skin.

As previous work on a similar type of high lift device was not available, both structural analysis and modelling techniques were novel aspects of this research. With the modelling methodology adopted it was in fact possible to demonstrate that the designed actuation mechanism was an efficient and feasible design solution. The study steps used to carry out the analysis can be summarised as follows:

1. A finite element model of the leading edge skin was created and the imposed deflections to achieve the target deflected shape were set at the locations of the actuation discs. The actuation loads were therefore obtained as the reaction forces to the enforced deflection.

2. The stresses and strains were obtained by applying both actuation and aerodynamic loads to the leading edge skin structure. This process was essential to select a suitable material for the leading edge which allowed to achieve the target shape as well as to meet the strength requirements.

3. A finite element model of the leading edge structure with the integrated actuation mechanism was then created to calculate the elastic deformation at different flight conditions, with the leading edge fully deflected and in neutral position. This study demonstrated the actuation mechanism could replace the conventional rigid ribs and support the leading edge skin during the various flight stages.

4. Finally, a dynamic response analysis was carried out to test that the leading edge skin, with the integrated actuation mechanism, was stiff enough to withstand gust loads at both low and high altitude at takeoff/landing and cruise.

The main research objective of obtaining a feasible design for a next generation large aircraft wing morphing leading edge actuation mechanism was therefore achieved. The actuation system was designed in such a way that the target shape was reached with minimum actuation force demand. For the current study aluminium was selected as the most suitable material for this application. The results showed that the skin when

deflected met the target shape without violating the strength limits and also that the designed actuation mechanism provides adequate stiffness to the leading edge structure to overcome the aerodynamic pressure at different flight conditions and also to maintain a high degree of stability in the event of gust encounter.

6.3. Contribution to Knowledge

The research work conducted contributed in adding new knowledge in the area of composite aircraft structures and morphing wing design and analysis.

1. The effectiveness of using composite fibre tow rings to reduce the stress concentrations due to cutouts in ribs and spars webs has been demonstrated.

2. Methods to increase the buckling stability of spar like beams have been investigated and it was shown that using reinforcement stringers on the beam flanges is a simple but efficient solution.

3. The effect of the stiffness of the base panel in a sandwich composite structure was discussed. It was proved that the strength of the joint, under a pulling load, was dependent on the stiffness of the base panel, which was subject to large bending, and the bonding quality between the web and base panel. It was also demonstrated that, when a composite joint is loaded in both pulling and shear, the outer layer matrix failure can be delayed by laying the outer layer fibres in the same direction as the applied force.

4. The already existing actuation concept based on an eccentric beam has been improved and modified in order to be applicable to a morphing leading edge device. New design features were implemented in order to achieve a large vertical deflection and also change in nose radius.

5. A detailed structural analysis of a morphing leading edge was provided. This study showed, for the first time, the effect of a morphing deformation on the static and dynamic behaviour of a leading edge structure. In this research it was therefore possible to demonstrate that the eccentric beam concept was feasible from a design perspective, which is the usual approach of the previous studies

available in the literature, but also to show that it was a practical concept satisfying the structural strength requirements.

6.4. Future Work

1. Composite wing box optimisation – the skin, stringer, spars and ribs layup can be optimised to make the structure more efficient, reducing the overall structural weight and increasing its strength.
2. A solution for a morphing leading edge skin in glass fibre using fibre layup optimisation or fibre steering can be explored.
3. Create a kinematic model of the actuation mechanism and show the details of the connection between the leading edge skin and actuation systems discs.
4. Create a simple physical model of the leading edge with the actuation mechanism to show the concept's feasibility.
5. Carry out a simple static aeroelastic analysis.
6. Couple the wing CFD and the structural models and carry out a full high fidelity aeroelastic analysis
7. Model the whole wing including the eccentric beam actuation mechanism distributed along the span and carry out a high fidelity aeroservoelastic analysis.

Reference

1   Science how stuff works. How air traffic control works. *Citing Internet Source*. (WWW document). http://science.howstuffworks.com/transport/flight/modern/air-traffic-control1.htm. (Accessed 30th March 2011).

2   Soutis, C. Fibre reinforced composite in aircraft construction. *Progress in Aerospace Science*, 41, 2005, p. 143-151.

3   Harris, C. H., Starnes, J. H. Jr., Shuart, M. J. Design and manufacturing of aerospace composite structures, state –of-the-art assessment. *Journal of Aircraft*, 39 (4), 2002, p. 545-560.

4   Ravi, B. D., Starnes, J. H. Jr., Holzwarth, R. C. Low-cost composite materials and structures for aircraft applications. *In: Meeting on "Low Cost Composite Structures"*, Loen, Norway, May 7-11 2001.

5   Quilter, A. *Composites in aerospace applications*. An IHS White Paper

6   New Scientist. Aviation-the shape of wings to come. *Citing Internet Source*. (WWW document). http://www.newscientist.com/article/dn7552-aviation--the-shape-of-wings-to-come.html?full= true. (Accessed 22nd June 2010).

7   Engineering News. Airbus to star manufacturing parts for new A350 XWB in late '09. *Citing Internet Source*. (WWW document). http://www.engineeringnews.

co.za/article/airbus-to-start-manufacturing-parts-for-new-a350-xwb-in-late-09-2009-05-11 (Accessed 22nd June 2010).

8   Boeing. Boeing 787 Dreamliner will provide new solutions for airliners, passengers. *Citing Internet Source*. http://www.boeing.com/commercial/ 787family/ background. html. (Accessed 22nd June 2010).

9   Razzaq, Z., Prabhakaran, R., Sirjani, M.M. Load and resistance factor design (LRFD) approach for reinforced-plastic channel beam buckling. *Composites Part B: Engineering*, 27 (3-4), 1996, p. 361-369.

10   Lee, J., Kim, S. Lateral buckling analysis of thin-walled laminated channel-section beams. *Composite Structures*, 56 (4), 2002, p. 391-399.

11   Shan, L., Qiao, P. Flexural–torsional buckling of fiber-reinforced plastic composite open channel beams. *Composite Structures*, 68 (2), 2005 p. 211-224.

12   Mohammad, Z. K., Archibald, N. S. Optimal fibre orientation in lateral stability of laminated channel section beams. *Composites Part B: Engineering*, 29 (1), p. 81-87.

13   Tosh, M.W., Kelly, D.W. Fibre steering for a composite C-beam, *Composite Structures*, 56 (2), 2001, p. 133-141.

14   Wu, H., Mu, B. On stress concentrations for isotropic/orthotropic plates and cylinders with a circular hole. *Composites Part B: Engineering*, 34B (2), 2003, p. 127-134.

15   Henshaw, J. M., Sorem Jr, J. R., Glaessgen, E. H. Finite element analysis of ply-by-ply and equivalent stress concentrations in composite plates with multiple holes under tensile and shear loading. *Composite Structures*, 36 (1), 1996, p. 45-58.

16   Arjyal, B. P., Katerelos, D. G., Galiotis, C., Filiou, C. Measurement and modeling of stress concentration around a circular notch. *Experimental Mechanics*, 40(3), 2000, p. 248-255.

17 Ukadgaonker, V. G., Rao, D. K. N. A general solution for stresses around holes in symmetric laminates under inplane loading. *Composite Structures*, 49(3), 2000, p. 339-354.

18 Rezaeepazhand, J., Jafari, M. Stress analysis of perforated composite plates. *Composite Structures*, 71 (3-4), 2005, p. 463-468.

19 Whitworth, H. A., Mahase, H. Failure of orthotropic plates containing a circular opening. *Composite Structures*, 46 (1), 1999, p. 53-57.

20 Bailey, R., Wood, J. Stability characteristics of composite panels with various cutout geometries. *Composite Structures*, 35 (1), 1996, p. 21-31.

21 Ghannadpour, S. A. M., Najafi, A., Mohammadi, B. On the buckling behaviour of cross-ply laminated composite plates due to circular/elliptical cutouts. *Composite Structures*, 75 (1-4), 2006, p. 3-6.

22 Jain, P., Kumar, A. postbuckling response of square laminates with a central circular/elliptical cutout. *Composite Structures*, 65 (2), 2004, p. 179-185.

23 Bailey, R., Wood, J. Postbuckling behaviour of square compression loaded graphite epoxy panels with square and elliptical cut-outs. *Thin-Walled Structures*, 28 (3-4), 1997, p. 373-397.

24 Nemeth, M. P. Buckling and postbuckling behaviour of laminated composite plates with a cutout. *NASA Technical Paper*, 3587, 1996.

25 Liu, Y., Jin, F., Li, Q. A strength-based multiple cutout optimization in composite plates using fixed grid finite element method. *Composite Structures*, 79 (4), 2006, p. 403-412.

26 Falzon, B. G., Steven, G. P., Xie, Y. M. Shape optimization of interior cutouts in composite panels. *Structural and Multidisciplinary Optimization*, 11 (1-2), 1996, p. 43-49.

27 Guo, S. Stress concentration and buckling behaviour of shear loaded composite panels with reinforced cutouts. *Composite Structures*, 80(1), 2007, p. 1-9.

28 Zemlyanova, A. Y., Sil'vestrov, V. V. The problem of the reinforcement of a plate with a cutout by a two-dimensional patch. *Journal of Applied Mathematics and Mechanics*, 71 (1), 2007, p. 40-51.

29 Engels, H., Hansel, W., Becker, W. Optimal design of hole reinforcements for composite structures. *Mechanics of Composite Materials*, 38 (5), 2002, p. 417-428.

30 De Boos, C., Guo, S., Zhou, L. The effect of core to skin thickness ratio and cutout reinforcements on composite sandwich panels. In: *15th International Conference on Composite/Nano Engineering (ICCE-15)*, Haikou, China, July 15-21 2007.

31 Guo, S., Zhou, L., Cheung, C. W. Cutout reinforcements for shear loaded laminate and sandwich composite panels. In: *International Journal of Mechanics and Materials in Design*, 2008, Vol. 4, p. 157-171.

32 Engels, H., Becker, W. Optimization of hole reinforcements by doublers. *Structural and Multidisciplinary Optimization*, 20 (1), 2000, p. 57-66.

33 Eiblmeier, J., Loughlan, J. The influence of reinforcement ring width on the buckling response of carbon fibre composite panels with circular cut-outs. *Composite Structures*, 38 (4), 1997, p. 609-622.

34 J. Eiblmeier, J., Loughlan, J. The buckling response of carbon fibre composite panels with reinforced cut-outs. *Composite Structures*, 32 (1-4), 1995, p. 97-113.

35 Oterkus, E., Barut, A., Madenci, E. Buckling of composite plates with a reinforced circular cutout subjected to uniform and non-uniform compression. In: *45th AIAA/ASME/ASCE/AHS/ASC Structures, Structural Dynamics and Materials Conference*, Palm Springs, CA, 19-22 April.

36 Jegley, C. D., Tatting, B.F., Adoptech, J., Gürdal, Z. Optimization of elastically tailored tow-placed plates with holes. In: *AIAA-2003-1420 44th AIAA /ASME /ASCE / AHS/ASC Structures, Structural Dynamics, and Materials Conference*, Norfolk, Virginia, 7-10 April 2003.

37 Jegley, C. D., Tatting, B. F., Gürdal, Z. Tow-steered panels with holes subjected to compression or shear loading. In: *American Institute of Aeronautics and Astronautics*, 2005, p. 1-14.

38 Hyer, M. W., Lee, H. H. The use of curvilinear fiber format to improve buckling resistance of composite plates with central circular holes. *Composite Structures*, 18 (3), 1991, p. 239-261.

39 Lopes, C. S., Camanho, P. P., Gürdal, Z., Tatting, B. F. Progressive failure analysis of tow-placed, variable-stiffness composite panels. *International Journal of Solids and Structures*, 44 (25-26), 2007, p. 8493-8516.

40 Huang, J., Haftka, R. T. Optimization of fiber orientations near a hole for increased load-carrying capacity of composite laminates. *Structural and Multidisciplinary Optimization*, 30 (5), 2005, p. 335-341.

41 Legrand, X., Kelly, D., Crosky, A., Crépin, D. Optimisation of fibre steering in composite laminates using a genetic algorithm. *Composite Structures*, 75 (1-4), 2006, p. 524-531.

42 Temmen, H., Degenhardt, R., Raible, T. Tailored fibre placement optimization tool. In: *25th International Congress of the Aeronautical Sciences*, 2006, p. 1-10.

43 Yap, J. W. H., Scott, M. L., Thomson, R. S., Hachenberg, D. The analysis of skin-to-stiffener debonding in composite aerospace structures. *Composite Structures*, 57 (1-4), 2002, p. 425-435.

44 Kesavan, A., Deivasigamani, M., John, S., Herszberg, I. Damage detection in T-joint composite structures. *Composite Structures*, 75 (1-4), 2006, p. 313-320.

45 Blake, J. I. R., Shenoi, R. A. House, J., Turton, T. Progressive damage analysis of tee joints with viscoelastic inserts. *Composites Part A: Applied Science and Manufacturing*, 32 (5), 2001, p. 641-653.

46 Vijayaraju, K., Mangalgiri, P. D., Dattaguru, B. Experimental Study of Failure and Failure Progression in T-Stiffened Skins. *Composite Structures*, 64 (2), 2004, p. 227-234.

47 Kumari, S., Sinha, P. K. Finite element analysis of composite wing T-joints. *Journal of Reinforced Plastics and Composites*, 21 (17), 2002, p. 1561-1585.

48 Shenoi, R. A., Violette, F. L. M. A study of structural composite tee joints in small boats. *Journal of Composite Materials*, 24 (6), 1990, p. 644-666.

49 Zhou, D. W., Louca, L. A., Saunders, M. Numerical simulation of sandwich T-joints under dynamic loading. *Composites Part B*, 39, 2008, p. 973-985.

50 Theotokoglou, E. E. Study of the numerical fracture mechanics analysis of composite T-joints. *Journal of Reinforced Plastics and Composites*, 18 (3), 1999, p. 215-223.

51 Theotokoglou, E. E. Strength of composite T-joints under pull-out loads. *Journal of Reinforced Plastics and Composites*, 16 (6), 1997, p. 503-518.

52 Theotokoglou, E. E., Moan, T. Experimental and numerical study of composite T joints. *Journal of Composite Materials*, 30 (2), 1996, p. 190-209.

53 Shenoi, R. A., Read, P. J. C. L., Jackson, C. L. Influence of joint geometry and load regimes on sandwich tee joint behaviour. *Journal of Reinforced Plastics and Composites*, 17 (8), 1998, p. 725-740.

54 Turaga, U. V. R. S., Sun, C. T. Failure modes and load transfer in sandwich T-joints. *Journal of Sandwich Structures and Materials*, 2 (3), 2000, p. 225-245.

55 Bannister, M. K. Development and application of advanced textile composites. *Proceedings of the Institution of Mechanical Engineers, Part L: Journal of Materials: Design and Applications*, 218 (3), 2004, p. 253-260.

56 Cartié, D. D. R., Dell'Anno, G., Poulin, E., Partridge, I. K. 3D reinforcement of stiffener-to-skin T-joints by Z-pinning and tufting. *Engineering Fracture Mechanics*, 73 (16), 2006, p. 2532-2540.

57 Stickler, P. B., Ramulu, M., Van West, B. P. Transverse stitched T-joints in bending with PR520 resin: initial results. *Journal of Reinforced Plastics and Composites*, 20 (1), 2001, p. 65-75.

58 Stickler, P. B., Ramulu, M. Investigation of mechanical behavior of transverse stitched T-joints with PR520 resin in flexure and tension. *Composite Structures*, 52 (3-4), 2001, p. 307-314.

59 Stickler, P. B., Ramulu, M., Johnson, P. S. Experimental and numerical analysis of transverse stitched T-joints in bending. *Composite Structures*, 50 (1), 2000, p. 17-27.

60 Yang, Q. D., Rugg, K. L., Cox, B. N., Shaw, M. C. Failure in the junction region of T-stiffeners: 3D-braided vs. 2D tape laminate stiffeners. *International Journal of Solids and Structures*, 40 (7), 2003, p. 1653-1668.

61 Vlasov, V. Z. *Thin-walled elastic beams*. 2nd ed. Jerusalem, Israel: Israel Program for Scientists Translation, 1961.

62 Gjelsvik, A. *The theory of thin-walled bars*. New York: John Wiley and Sons Inc, 1981.

63 Kim, J. H., Kim, Y. Y. Thin-walled multicell beam analysis for coupled torsion, distortion, and warping deformations. *ASME Journal of Applied Mechanics*, 66 (4), 1999, p. 904-912.

64 Jonsson, J. Distortional warping function and shear distribution in thin-walled beams. *Journal of Thin-Walled Structures*, 33, 1999, p. 245-268.

65 Boswell, L. F., Li, Q. Consideration of the relationship between torsion, distortion and warping of thin-walled beams. *Journal of Thin-Walled Structures*, 21, 1995, p. 147-161.

66 Shakourzadeh, H., Guo, Y. Q., Batoz, J. L. A torsion bending element for thin-walled beams with open and closed cross sections. *Journal of Computers and Structures*, 55 (6), 1995, p. 1045-1054.

67 Kollar, L. P., Pluzsik, A. Analysis of thin-walled composite beams with arbitrary layup. *Journal of Reinforced Plastics and Composites*, 21 (16), 2002, p. 1423-1465.

68 Vo, T. P., Lee, J. Flexural-torsional behaviour of thin-walled closed-section composite box beam. *Engineering Structures*, 29, 2007, p. 1774-1782.

69 Chandra, R., Stemple, A. D., Chopra, I. Thin-walled composite beams under bending, torsional, and extensional loads. *Journal of Aircraft*, 27 (7), 1990, p. 619-626.

70 Librescu, L., Song, O. *Thin-walled composite beams*. Dordrecht, the Netherlands: Springer, 2006.

71 Shadmehri, F., Haddadpour, H., Kouchakzadeh, M. A. Flexural-torsional behaviour of thin-walled composite beams with closed cross-section. *Journal of Thin-Walled Structures*, 45, 2007, p. 699-705.

72 Qui, Z., Librescu, L. On a shear-deformable theory of anisotropic thin-walled beam: further contribution and validation. *Journal of Composite Structures*, 56, 2002, p. 345-358.

73 Zienkiwwicz, O. C., Taylor, R. L. *The finite element method*. 5th ed. Oxford, UK: Butterworth-Heinemann.

74 Sarawit, A. T., Kim, Y., Bakker, M. C. M., Pekoz, T. The finite element method for thin-walled members-applications. *Journal of Thin-Walled Strucutres*, 41, 2003, p. 191-206.

75 Yu, W., Hodges, D. H., Volovoi, V. V. Fuchs, E. D. A generalised Vlasov theory for composite beams. *Journal of thin-walled structures*, 43, 2005, p. 1943-1511.

76 Smeltzer, S. S., Lovejoy, A. E., Satyanarayana, A. *Numerical characterisation of a composite bonded wing-box*. NASA Technical Report 2080015750, 2008.

77 Taylor, R. M., Weisshaar T. A. Improved structural design using evolutionary finite element modelling. In: *RTO AVT Symposium "Reduction of Military Vehicle Acquisition Time and Cost through Advanced Modelling and Virtual Simulation"*, Paris, France, 22-25 April, 2002.

78 Morris, A. J. Introduction to finite element basics. In: *AGARD Lecture Series 147"Practical Application of Finite Element Analysis to Aircraft Structural Design"*, 1986.

79 Schuhmacher, G., Murra, I., Wang, L., Laxander, A., O'Leary, O. J., Herold, M. Multidisciplinary design optimization of a regional aircraft wing box. In: *9th AIAA/ISSMO Symposium and Exhibit on Multidisciplinary Analysis and Optimization*, Atalanta, GA, 4-6 September, 2002.

80 Anhalt, C., Monner, H. P., Breitbach, E. Interdisciplinary wing design-structural aspects. *SAE International*, 112 (1), 2003, p. 521-530.

81 Gantois, K., Morris, A. J. The multi-disciplinary design of a large-scale civil aircraft wing taking account of manufacturing costs. *Structures Multidisciplinary Optimisation*, 28, 2004, p. 31-46.

82 Emero, D. H., Spunt, L. Wing box optimization under combined shear and bending. *Journal of Aircraft*, 3 (2), 1966, p. 130-141.

83 York, C. B., Williams, F. W., Kennedy, D. A parametric study of optimum designs for benchmark stiffened wing panels. *Composites Engineering*, 3 (7-8), 1993, p. 619-632.

84 Seresta, O., Gurdal, Z., Adams, D. B., Watson, L. T. Optimal design of composite wing structures with blended laminates. *Composites: Part B*, 38, 2007, p. 469-480.

85 Liu, B., Haftka, R.T., Akgun, M. A. Two-level composites wing structural optimization using response surface. *Structures Multidisciplinary Optimisation*, 20, 2000, p. 87-96.

86 Hodges, D. H., Pierce, G. A. *Introduction to structural dynamics and aeroelasticity*, 1st ed. Cambridge: Cambridge University Press, 2002.

87 Wright, J. R., Cooper, J. E. *Introduction to aircraft aeroelasticity and loads*. 1st ed. Southern Gate: John Wiley & Sons Ltd, 2007.

88 Livne, E., Weisshaar, T. A. Aeroelasticity of nonconventional airplane configurations-past and future. *Journal of Aircraft*, 40 (6), 2003, p. 1047-1065.

89 Livne, E. Future of airplane aeroelasticity. *Journal of Aircraft*, 40 (6), 2006, p. 1066-1092.

90 Scanlan, R. H., Rosenbaum R. *Aircraft vibration and flutter*. 1st ed. New York: The Macmillan Company, 1951.

91 Bisplinghoff, R. L., Ashley, H., Halfman, R. L. *Aeroelasticity*. 2nd ed. Reading: Addison-Wesley Publishing Company, Inc., 1957.

92 Fung, Y. C. *An introduction to the theory of aeroelasticity*. New York: Dover Publications, Inc., 1969.

93 Dowell, E. H., Crawley, E. F., Curtiss Jr, H. C., Peters, D. A., Scanlan, R. H., Sisto, F. *A modern course in aeroelasticity*. 3rd ed. Dordrecht: Kluwer Academy Publishers Group, 1995.

94 Battoo, R. S. *A beginners guide to literature in the field of aeroelasticity*. College of Aeronautics Report No. 9712, 1997.

95 Battoo, R. S. An introductory guide to literature in aeroelasticity. *The Aeronautical Journal*, 103 (1029), 1999, p. 511-518.

96 Weisshaar, T. A. *Aeroelasticity' role in innovative UAV design and optimization. Citing Internet Source*. (WWW document). engg.kau.edu.sa/.../057_Technological %20Hurdles_Baabad_formatted.pd. (Accessed 24th June 2010).

97 Weisshaar, T. A., Foist, B. L. Vibration tailoring of advanced composite lifting surfaces. *Journal of Aircraft*, 22(2), 1985, p. 141-147.

98 Mansfield, E. H. The stiffness of a two-cell anisotropic tube. *Aeronautical Quarterly*, 32 (4), 1981, p. 338-353.

99 Hodges, D. H., Atilgan, A. R., Fulton, M. V., Rehfield, L. W. Free-vibration analysis of composite beams. *Journal of American Helicopter Society*, 36 (3), 1991, p. 36-47.

100 Eslimy-Isfahany, S. H. R., Banerjee, J. R. Dynamic response of composite beams with application to aircraft wings. *Journal of Aircraft*, 34 (6), 1997, p. 785791.

101 Qui, Z., Marzocca, P., Librescu, L. Aeroelastic instability and response of advanced aircraft wings a subsonic flight speeds. *Aerospace Science and Technology*, 6, 2002, p. 195-208.

102 Qui, Z., Librescu, L. Aeroelastic stability of aircraft wings modelled as anisotropic composite thin-walled beams in incompressible flow. *Journal of Fluids and Structures*, 18, 2003, p. 43-61.

103 Banerjee, J.R. Explicit frequency equation and mode shaped of a cantilever beam coupled in bending and torsion. *Journal of Sounds and Vibration,* 224 (2), 1999, p. 267-281.

104 Banerjee, J. R., Su, H., Jayatunga, C. A dynamic stiffness element for free vibration analysis of composite and its application to aircraft wings. *Journal of Computers and Structures*, 86, 2008, p. 573-579.

105 Chandra, R., Chopra, I. Structural behavior of two-cell composite rotor blades with elastic coupling. *AIAA Journal*, 30 (12), 1992, p. 2914-2921.

106 Armanios, E. A., Badir, A. M. Free vibration analysis of anisotropic thin-walled closed-section beams. *AIAA Journal*, 33 (10), 1905-1910.

107 Badir, A. M. Analysis of two-cell composite beams. In: *36th AIAA Conference on Structures, Structural Dynamics and Materials*, New Orleans, LA, 95-1208-CP, p. 419-24.

108 Marur, S. R., Kant, T. Free vibration analysis of fiber reinforced composite beams using higher order theories and finite element modelling. *Journal of Sounds and Vibrations*, 194 (3), 1996, p. 337-351.

109 Chen, W. Q., Lv, C. F., Bian, Z. G. Free vibration analysis of generally laminated beams via state-based differential quadrature. *Journal of Composite Strucutres*, 63, 2004, p. 417-425.

110 Na, S. Librescu, L. Vibration and dynamic response control of elastically tailored non uniform adaptive aircraft wings. In: *41st AIAA/ASME/ASCE/AHS/ASC Structures, Structural Dynamics, and Materials*, Atlanta, GA, 3-6 April, 2000, p. 217-227.

111 Seigler, T. M., Neal, D. A., Inman, D. J. Dynamic modelling of large-scale morphing aircraft. In: *47th AIAA/ASME/ASCE/AHS/ASC Structures, Structural Dynamics, and Materials*, Newport, Rhode Island, 1-4 May, 2006, p. 1-11.

112 Park, G. J. Nonlinear dynamic response structural optimisation of a joined-wing using equivalent loads. *Final Report FA4869-07-1-4087*, 2008.

113 Ameri, N., Lowenberg, M. H., Friswell, M. I. Modelling the dynamic response of a morphing wing with active winglets. In: *AIAA Atmospheric Flight Mechanics Conference and Exhibit*, Hilton Head, South Carolina, 20-23 August, 2007, p. 1-19.

114 Shokrieh, M. M., Behrooz, F. T. Wing instability of a full composite aircraft. *Journal Composite Structures*, 54, 2001, p. 335-340.

115 Zbrozek, J. K. *The relationship between the discrete gust and power spectra presentations of atmospheric turbulence, with a suggested model of low-altitude turbulence*. Aeronautical Research Council Reports and Memoranda No. 3216, 1961.

116 *Certification specifications for large aeroplanes*. European Aviation Safety Agency, Amendment 5, Subpart C, 2008.

117 Pastel, R. L., Caruthers, J. E., Frost, W. *Airplane wing vibration due to atmospheric turbulence*. NASA Contractor Report No. 3431, 1981.

118 Abdulwahab, E. N., Hongquan, C. Aircraft response to atmospheric turbulence at various types of the input excitation. *Space Research Journal*, 1 (1), 2008, p. 17-28.

119 Hoblit, F. M. *Gust loads on aircraft: Concepts and applications*. AIAA Education Series, 1988.

120 Azoulay, D., Karpel, M. Characterization of methods for computation of aeroservoelastic response to gust excitation. *47th AIAA/ASME/ASCE/AHS/ASC Structures, Structural Dynamics, and Materials*, Newport, Rhode Island, 1-4 May, 2006, p. 1-15.

121 Qin, Z., Librescu, L. Dynamic aeroelastic response of aircraft wings modelled as anisotropic thin-walled beams. *Journal of Aircraft*, 40 (3), 2003, p. 522-543.

122 Rodrigues, E. A., Kamiyama, M. T. *Computation of dynamic loads on aircraft structure due to continuous gust using MSC/NASTRAN. Citing Internet Source.* (WWW document). www.mscsoftware.com/support/library/conf/auc97/p00797. pdf. (Accessed 29th June 2010).

123 Cesnik, C. E. S., Hodges, D. H., Patil, M. J. Aeroelalstic analysis of composite wings. In: *37th Structures, Structural Dynamcis and Materials Conference*, Salt Lake City, Utah, 15-17 April, 1996.

124 Gern, F. H., Inman, D. J., Kapania, R. K. Structural and aeroelastic modelling of ceneral planform wings with morphing airfoils. *AIAA Journal*, 40 (4), 2002, p. 628-637.

125 Zimmermann, H. Aeroservoelasticity. *Computer Methods in Applied Mechanics and Engineering*, 90, 1991, p. 719-735.

126 Brenner, M. J. *Actuator and aerodynamic modelling for high angle of attack aeroservoelasticity*. NASA Technical Memorandum, No. 4493, 1993.

127 Buttrill, C. S., Bacon, J., Heeg, J., Houck, J. A., Wood, D. V. *Aeroservoelastic simulation of an active flexible wing wind tunnel model*. NASA Technical Paper 3510, 1996.

128 Henderson, J. A. Global Optimization Method for Aeroservoelastic Concepts. In: *43rd AIAA/ASME/ASCE/AHS/ASC Structures, Structural Dynamics, and Materials Conference*, Denver, Colorado, 22-25 April, 2002.

129 Karpel. M., Moulin, B. Models for aeroservoelastic analysis with smart structure. *Journal of aircraft*, 41 (2), 2004, p. 314-321.

130 Yoo, J.H., Park, Y. K., Lee, I., Han, J. H. Aeroelastic analysis of a wing with freeplay in the subsonic/transonic regions. *JSME International Journal Series B*, 48 (2), 2005, p. 208-211.

131 Patil, N. J., Hodges, D, H. On the importance of aerodynamic and structural geometrical nonlinearities in aeroelastic behaviour of high-aspect-ratio wings. *Journal of Fluids and Structures*, 19, 2004, p. 905-915.

132 Shi, G., Renaud, G., Yang, X., Zhang, F., Chen, S. Integrated wing design with three disciplines. In: *9th AIAA/ISSMO Symposium on Multidisciplinary Analysis and Optimization*, Atlanta, Georgia, 4-6 September, 2002.

133 Chen, S., Zhang, F., Renaud, G., Shi, G., Yang, X. A preliminary study of wing aerodynamic, structural and aeroelastic design and optimisation. In: *9th AIAA/ISSMO Symposium on Multidisciplinary Analysis and Optimization*, Atlanta, Georgia, 4-6 September, 2002.

134 Taylor, W. S. *CFD Data Transfer to Structural Analysis*. *Citing Internet Source.* (www document) www.mscsoftware.com/support/library/conf/wuc96/04a_tayl.pdf (accessed 30th June 2010).

135 Beckert, A. Coupling Fluid (CFD) and Structural (FE) Models Using Finite Interpolation Elements. *Aerospace Science and Technology*, 4, 2000, p. 13-22.

136 Taylor, N. V., Allen, C. B., Gaitonde, A., Jones, D. P., Fenwick, C. L., Hill, G. F. J., Lee, V. Moving Mesh CFD-CSD Aeroservoelastic Modelling of BACT Wing with Autonomous Flap Control, In: *23rd AIAA Applied Aerodynamics Conference*, Toronto, Ontario, 6-9 June, 2005.

137 Cooper, J. Adaptive aeroelastic structures. In: *Adaptive Structures Engineering Applications* edited by Wagg, D., Bond, I., Weaver, P., Friswell, M. Southern Gate, Chichester: John Wiley & Sons Ltd., 2007, p. 137-162.

138 Kuzmina, S., Amiryants, G., Schweiger, J., Cooper, J., Amprikidis, M., Sensberg, O. Review and outlook on active and passive aeroelastic design concepts for future

aircraft. In: *23rd International Congress of Aeronautical Sciences*, 2002, p. 432.1-432.10.

139 Weisshaar, T. A. Morphing aircraft technology – new shapes for aircraft design. *Meeting Proceedings RTO-MP-AVT-141*, 2006, p. O1-1 – O1-20.

140 Weisshaar, T. A., Duke, D. K. Induced drag reduction using aeroelastic tailoring with adaptive control surfaces. *Journal of Aircraft*, 43 (1), 2006, p. 157-164.

141 Weisshaar, T. A. Aeroelastic tailoring of forward swept composite wings. *Journal of Aircraft*, 18 (8), 1981, p. 669-676.

142 Guo, S. Aeroelastic optimization of an aerobatic aircraft wing structure. *Aerospace Science and Technology*, 11 (5), p. 396-404.

143 Guo, S., Cheng, W., Cui, D. Aeroelastic tailoring of composite wing structures by laminate layup optimization. *AIAA Journal*, 44 (12), 2006, p. 3146-3150.

144 Guo, S., Cheng, W., Cui, D. Optimization of composite wing structures for maximum flutter speed. In: *46th AIAA/ASME/ASCE/AHS/ASC Structures, Structural Dynamics and Materials Conference*, Austin, Texas, 18-21 April, 2005.

145 Librescu, L., Meirovitch, L., Na, S. S. Control of cantilever vibration via structural tailoring and adaptive materials. *AIAA Journal*, 8, 1997, p. 1309-1315.

146 Parker, H. F. The variable camber wing. *National Advisory Committee for Aeronautics*, Report No. 77, 1920.

147 Perry III, B., Cole, S. R. Miller, G. D. *A summary of the active flexible wing program*. NASA Technical Memorandum 107655, 1992.

148 Pendleton, E. W., Bessette, D., Field, P. B., Miller, G. D., Griffin, K. E. Active aeroelastic wing flight research program: technical program and model analytical development. *Journal of Aircraft*, 37 (4), 2000, p. 554-561.

149 Heeg, F., Spain, C. V., Florance, J. R., Panetta, A., Tumwa, V. Experimental results from the active aeroelastic wing wind tunnel test program, In: *46th*

AIAA/ASME/ASCE/AHS/ASC Structures, Structural Dynamics & Materials Conference, Austin, Texas, 18 - 21 April, 2005, Austin, p. 1-16.

150 Voracek, D., Pendleton, E., Reichenbach, E., Griffin, K., Welch, L. *The active aeroelastic wing phase I flight research through January 2003*. NASA/TM-2003-210741, NASA, 2003.

151 Wlezien, R. W., Horner, G. C., McGowan, A. R., Padula, S. L., Scott, M. A., Silcox, R. J., Simpson J. O. The aircraft morphing program. In: 39th AIAA Structures, Structural Dynamics, and Materials Conference and Exhibit, Long Beach, California, 20-23 April, 1998.

152 Schweiger, J., Suleman, A., Kuzmina, S. I., Chedrik, V. V. MDO concepts for an european research project on active aeroelastic aircraft. In: *9th AIAA/ISSMO Symposium on Multidisciplinary Analysis and Optimization*, Atlanta, Georgia, 4-6 September, 2002.

153 Elber, W. *Means for controlling aerodynamically induced twist*, Patent B64C 3/52, United States, 1982.

154 Bae, L. S., Seigler, T. M., Inman, D. I. Aerodynamic and static aeroelastic characteristics of a variable-span morphing wing. *Journal of Aircraft*, 42 (2), 2005, p. 528-534.

155 Bae, L. S., Seigler, T. M., Inman, D. I. Aerodynamic and aeroelastic considerations of a variable-span morphing wing. *45th AIAA/ASME/ASCE/AHS/ASC Structures, Structural Dynamics & Materials Conference*, Palm Springs, California, 19-22 April, 2004.

156 Amprikidis, M., Cooper, J. E., Rogerson, D., Vio, G. On the use of adaptive internal structures for wing shape control. In: *46th AIAA/ASME/ASCE/AHS/ ASC Structures, Structural Dynamics and Materials Conference*, Austin, Texas, 18-21 April, 2005.

157 Vos, R., Siddaramaiah, V. H., Cooper, J. E. Aeroelastic flight control for subscale UAVs. In: *48th AIAA/ASME/ASCE/AHS/ASC Structures, Structural Dynamics and Materials Conference*, Honolulu, Hawaii, 23-26 April, 2007.

158 Ricci, S., Scotti, A., Terraneo, M. Design, manufacturing and preliminary test results of an adaptive wing camber model. *48th AIAA/ASME/ASCE/AHS/ASC Structures, Structural Dynamics, and Material Conference*, Newport, Rhode Island, 1-4 May, 2006.

159 Ricci, S., Terraneo, M. Conceptual design of an adaptive wing for a three-surface airplane. In: *46th AIAA/ASME/ASCE/AHS/*ASC *Structures, Structural Dynamics and Materials Conference*, Austin, Texas, 18-21 April, 2005.

160 Campanile, L. F., Anders, S. Aerodynamic and aeroelastic amplification in adaptive belt-rib airfoils. *Journal of Aerospace Science and Technology*, 9 (1), 2005, p. 55-63.

161 Bolonkin, A., Gilyard, G. B. *Estimated benefits of variable-geometry wing camber control for transport aircraft*. NASA Report NASA/TM-1999-206586, 1999.

162 Szodruch, J., Hilbig, R. Variable wing camber for transport aircraft. *Progress in Aerospace Science*, 25, 1988, p. 297-328.

163 Dowell, E. H., Bliss, D. B., Clark, R. L. Aeroelastic wing with leading and trailing edge control surfaces. *Journal of Aircraft*, 40 (3), 2003, p. 559-565.

164 Andersen, G., Forster, E., Kolonay, R. Multiple control surface utilization in active aeroelastic wing technology. *Journal of Aircraft*, 34 (4), 1997, p. 552-557.

165 Carlsson, M., Cronander, C. Efficient roll control using distributed control surfaces and aeroelastic effects. *Aerospace Science and Technology*, 9 (2), 2005, p. 143-150.

166 Sanders, B., Eastep, F. E., Forster, E. Aerodynamic and aeroelastic characteristics of wings with conformal control surfaces for morphing aircraft. *Journal of Aircraft*, 40 (1), 2003, p. 94-99.

167 Gujjulaa, S., Singh, S. N., Yim, W. Adaptive and neural control of a wing section using leading- and trailing-edge surfaces. *Aerospace Science and Technology*, 9 (2), 2005, p. 279-291.

168 Plantanitis, G., Strganac, T. W. Analyses and experiments of suppression of control reversal using a wing section with multiple control surfaces. In: *44th AIAA/ASME/ASCE/AHS/ASC Structures, Structural Dynamics and Materials Conference*, Norfolk, Virginia, 7-10 April 2003.

169 Niu, M. C. Y. *Aircraft structural design*. 7th ed. Hong Kong: Conmilt Press Ltd., 1993.

170 Rudolph, P. K. C. *High-lift systems on commercial subsonic airliners*. NASA Contractor Report 4746, 1996.

171 Monner, H. P., Sachau, D., Breitbach, E. Design aspects of the elastic trailing edge for and adaptive wing. *RTO AVT Specialists' Meeting on Structural Aspects of Flexible Aircraft Control*, Ottawa, Canada, 18-20 October, 1999, p 14.1-14.8.

172 Cho, J. D. B., Wang, D. P., Martin, C. A., Kudva, J. N., West, M. N. Development of high-rate, adaptive trailing edge control surface for the smart wing phase 2 wind tunnel model. *Journal of Intelligent Material Systems and Structures*, 15 (4), 2004, p. 279-291.

173 Musgrove, R. G. *Eccentric actuator*. International Patent WO 81/01396, 1979.

174 Jardine, A. P., Bartley-Cho, J., Flanagan, J. Improved design and performance of SMA torque tube for the DARPA smart wing program. In: *SPIE Conference on Industrial and Commercial Applications of Smart Structures Technologies*, Newport Beach, California, 1999.

175 Perera, M., Guo, S. Optimal design of a seamless aeroelastic wing structure. In: 50th *AIAA/ASME/ASCE/AHS/ASC Structures, Structural Dynamics, and Material Conference*, Palm Springs, California, 4-7 May, 2009.

176 Muller, D. *Das Hornkonzept*. Stuttgart University PhD Thesis, 2000, Private Correspondence.

177 Kudva, J. N., Martin, C. A., Scherer, L. B., Jardine, A. P., McGowan, A. R., Lake, R. C., Sendeckyj, G., Sanders, B. Overview of the DARPA/AFRL/NASA smart wing program. In: *SPIE Conference on Industrial and Commercial Applications of Smart Structures Technologies*, Newport Beach, California, 1999.

178 Statkus, F. D. *Continuous skin, variable camber airfoil edge actuating mechanism. Citing Internet Source.* (www document) http://www.wikipatents.com/4351502.html, United States Patent, No 4351502, 1980, (accessed 5th July 2010).

179 Monner, H. P., Kintscher, M., Lorkovski, T., Storm, S. Design of a smart droop nose as leading edge high lift system for transport aircrafts. . In: *50th AIAA/ASME/ASCE/AHS/ASC Structures, Structural Dynamics, and Material Conference*, Palm Springs, California, 4-7 May, 2009.

180 Heap. H., Crowther, B. A review of current leading edge device technology and of options for innovation based on flow control. *RaES Conference*, London, 2003.

181 Reckzeh, D. *Aerodynamci design of Airbus high lift wings. Internet Source*. (www document) www.dlr.de/as/.../5/.../reckzeh_aero-design_of_high-lift-wings.pdf, (accessed 5th July 2010).

182 Lajux, V. *Methodology for the design of leading edge devices applied to variable camber*. Cranfield University PhD Thesis, 2007.

183 Thill, C., Etches, J., Bond, I., Potter, K., Weaver, P. Morphing skins. *The Aeronautical Journal*, 112 (1129), 2008, p. 117-139.

184 Loewy, R. G. Recent developments in smart structures with aeronautical applications. *Smart Materials and Structures*, 6 (5), 1997, p. 11-42.

185 McGowan, A. R., Horta. L. G., Harrison, J. S., Raney, D. L. *Research activities within NASA's morphing program*, NASA Technical Report, 1999.

186 Giurgiutiu, V. Review of smart-materials actuation solutions for aeroelastic and vibration control. *Journal of Intelligent Material Systems and Structures*, 11 (7), 2000, p. 525-544.

187 Forster, E., Livne, E. Integrated structural/actuation synthesis of strain actuated devices for shape control. In: *46th AIAA/ASME/ASCE/AHS/ASC Structures, Structural Dynamics and Materials Conference,* Seattle, Washington, 16-19 April, 2000.

188 Cho, M., Kim, S. Structural morphing using two-way shape memory effect of SMA. *International Journal of Solids and Structures*, 42 (5-6), 2005, p. 1759-1776.

189 Pinkerton, J. L., Moses, R. W. A feasibility study to control airfoil shape using THUNDER. *NASA Technical Memorandum*, No. 4767, 1997.

190 Kim, D. H., Han, J. H., Lee, I. Application of fiber optic sensor and piezoelectric actuator to flutter suppression. *Journal of Aircraft*, 41 (2), 2004, p. 409-411.

191 Ardelean, E. V., McEver, M. A., Cole, D. G., Clark, R. L. Active flutter control with V-stack piezoelectric flap actuator. *Journal of Aircraft*, 43 (2), 2006, p. 482-486.

192 Rocha, J., Ccosta, P. A., Suleman, A. On active aeroelastic control of and adaptive wing using piezoelectric actuators. *Journal of Aircraft*, 41 (1), p. 278-282.

193 Chopra, I. Review of State of Art of Smart Structures and Integrated Systems. *AIAA Journal*, 40 (11), 2002, p. 2145-2187.

194 Banks, H.T., Smith, R. C., Wang. Y. Smart materials technology and control applications. In: *Smart Material Structures, Modelling, Estimation and Control.* New York: John Wiley and Sons, 1996, p. 1-26.

195 Kollar, L. P., Springer, G. S. *Mechanics of composite structures*, 1st ed. New York: Cambridge University Press, 2003.

196 ESDU 85001. Elastic stress and strain distributions around circular holes in infinite plates of orthotropic materials (applicable to fibre reinforced composites). November, 1985.

197 ESDU 03001. Elastic buckling of long, flat, symmetrically-laminated (AsBoDf), composite stiffened panels and struts in compression. ESDU International, 2003.

198 Megson, T. H. G. *Aircraft structures for engineering students*, 3rd ed. Woburn: Butterworth-Heinemann, 2001.

199 Yu, W. Manual of VABS. *Citing Internet resources* (WWW document). http://hifi-comp.com/VABS.aspx, (accessed 15th July 2010).

200 Yu, W., Volvoi, V. V., Hodges, D. H., Hong, X. Validation of the variational asymptotic beam sectional analysis. *AIAA* Journal, 40 (10), 2002, pp 2105-2113.

201 Guo, S. *User's guide for program TWboxdc*. Unpublished document.

202 Zienkiewicz, O. C., Taylor, R. L. *The finite element method, Volume 1: the basis*, 5th ed. Woburn: Butterworth-Heinemann, 2000.

203 Zienkiewicz, O. C., Taylor, R. L. *The finite element method, Volume 1: solid mechanics*, 5th ed. Woburn: Butterworth-Heinemann, 2000.

204 MSC Software. *MSC Nastran 2007 r1, implicit nonlinear user's guide*.

205 MSC Software. *MSC Nastran 2003, linear static analysis user's guide*.

206 MSC Software. *MSC Nastran version 68, basic dynamic analysis user's guide*

207 *SADE-flexible high lift structures aerodynamic requirement*. Unpublished document.

208 Guo, S. *Programs for airframe preliminary sizing and stressing*. Unpublished document.

209 Hexcel. HexForce and HexPly aerospace selector guide. *Citing Internet resources* (WWW document). http://www.hexcel.com/Products/Selector+Guides/. (Accessed 16th July 2010).

210 Philips, B. J. *Multidisciplinary optimisation of CFRP wing cover*. Cranfield University EngD Thesis, 2009.

211 Hexcel. *Citing Internet resources* (WWW document). http://www.hexcel.com/Products/Downloads/Carbon+Fiber+Data+Sheets.htm?ds=Continuous. (Accessed 16th July 2010).

212 E-glass properties. *Citing Internet resources* (WWW document). http:// composite.about. com/od/data/l/blg_egepoxy.htm. (Accessed 19th July 2010).

213 Aluminium 2024-T81 properties. *Citing Internet resources* (WWW document). http://www.matweb.com/search/datasheet.aspx?matguid=6441f805a3bb42758ab5b 15752343138&ckck=1. (Accessed 19th July 2010).

214 Guo, S., Morishima, R., Zhang, X, Mills, A. Cutout and flange reinforcement of a composite C-section beam against stress concentration and buckling. In: *49th AIAA/ASME/ASCE/AHS/ASC Structures, Structural Dynamics and Materials Conference*, Schaumburg, IL, 7-10 April, 2008.

215 Guo, S., Morishima, R., Zhang, X, Mills, A. Cutout shape and reinforcement design for composite C-section beam under shear load. *Composite Structures*, 88 (2), 2009, p 179-187.

216 M21/T800 data sheet. *Citing Internet resources* (WWW document). http://www.hexcel.com/Products/Downloads/Prepreg%20Data%20Sheets/.(Access ed 19th July 2010).

217 T300 series stainless steel properties. *Citing Internet resources* (WWW document). http://www.matweb.com/search/datasheet.aspx?MatGUID=abc4415b0f8b490387e3 c922237098da. (Accessed 19th July 2010).

218 Guo, S., Morishima, R. Design, analysis and testing of composite sandwich T-joint structures. In: *50th AIAA/ASME/ASCE/AHS/ASC Structures, Structural Dynamics and Materials Conference*, Palm Springs, California, 4-7 April, 2009.

219 Guo, S., Morishima, R., Wei, P. Sandwich T-joint structures with and without cut-out under shear loads. In: *17th ICCE Conference*, Honolulu, Hawaii, 26-31 July, 2009.

220 Morishima, R., Guo, S., Dhande, R., Mills, A. Design improvement of a sandwich T-joint structure. In: *51st AIAA/ASME/ASCE/AHS/ASC Structures, Structural Dynamics and Materials Conference*, Orlando, Florida, 12-15 April, 2010.

221 Morishima, R., Guo, S., Ahmed, S. A composite wing structure with a morphing leading edge. In: *51st AIAA/ASME/ASCE/AHS/ASC Structures, Structural Dynamics and Materials Conference*, Orlando, Florida, 12-15 April, 2010.

222 Morishima, R., Guo, S. Optimal design of a composite wing with a morphing leading edge. In: *17th ICCE Conference*, Honolulu, Hawaii, 26-31 July, 2009.

223 Morishima, R., Guo, S. Optimum design of a composite morphing leading edge for high lift wing. In: *4th SEMC Conference*, Cape Town, South Africa, 6-8 September 2010.

224 Ahmed, S. *Aeroelastic analysis and tailoring of morphing high lift devices.* 21 Months Progress Review Report, August 2010, Private correspondence.

225 Military Handbook. *Metallic materials and elements for aerospace vehicle structures*. MIL-HDBK-5H, December 1998.